UNIVERSITY OF SOUTHAMPTON

FACULTY OF PHYSICAL AND APPLIED SCIENCES

Electronics and Computer Science

Development and Implementation of a Deflection Amplification Mechanism for Capacitive Accelerometers

by

Ioannis Zeimpekis

A Thesis for the degree of Doctor of Philosophy

January 2012

UNIVERSITY OF SOUTHAMPTON

ABSTRACT

FACULTY OF PHYSICAL AND APPLIED SCIENCES
ELECTRONICS AND COMPUTER SCIENCE

Doctor of Philosophy

Ioannis Zeimpekis

Micro-Electro-Mechanical-Systems (MEMS) and especially physical sensors are part of a flourishing market ranging from consumer electronics to space applications. They have seen a great evolution throughout the last decades, and there is still considerable research effort for further improving their performance. This is reflected by the plethora of commercial applications using them but also by the demand from industry for better specifications. This demand together with the needs of novel applications fuels the research for better physical sensors.

Applications such as inertial, seismic, and precision tilt sensing demand very high sensitivity and low noise. Bulk micromachined capacitive inertial sensors seem to be the most viable solution as they offer a large inertial mass, high sensitivity, good noise performance, they are easy to interface with, and of low cost. The aim of this thesis is to improve the performance of bulk micromachined capacitive sensors by enhancing their sensitivity and noise floor.

MEMS physical sensors, most commonly, rely on force coupling and a resulting deflection of a proof mass or membrane to produce an output proportional to a stimulus of the physical quantity to be measured. Therefore, the sensitivity to a physical quantity may be improved by increasing the resulting deflection of a sensor. The work presented in this thesis introduces an approach based on a mechanical motion amplifier with the potential to improve the performance of mechanical MEMS sensors that rely on deflection to produce an output signal.

The mechanical amplifier is integrated with the suspension system of a sensor. It comprises a system of micromachined levers (microlevers) to enhance the deflection of a proof mass caused by an inertial force. The mechanism can be used in capacitive accelerometers and gyroscopes to improve their performance by increasing their output signal. As the noise contribution of the electronic read-out circuit of a MEMS sensor is, to first order, independent of the amplitude of its input signal, the overall signal-to-noise ratio (SNR) of the sensor is improved.

There is a rather limited number of reports in the literature for mechanical amplification in MEMS devices, especially when applied to amplify the deflection of inertial sensors. In this study, after a literature review, mathematical and computational methods to analyse the behaviour of microlevers were considered. By using these methods the mechanical and geometrical characteristics of microlevers components were evaluated. In order to prove the concept, a system of microlevers was implemented as a mechanical amplifier in capacitive accelerometers.

All the mechanical structures were simulated using Finite Element Analysis (FEA) and system level simulations. This led to first order optimised devices that were used to design appropriate masks for fabrication. Two main fabrication processes were used; a Silicon on Insulator (SOI) process and a Silicon on Glass (SoG) process. The SOI process carried out at the University of Southampton evolved from a one mask to a two mask dicing free process with a yield of over 95%, in its third generation. The SoG is a well-established process at the University of Peking that uses three masks.

The sensors were evaluated using both optical and electrical means. The results from the first prototype sensor design (1HAN) revealed an amplification factor of 40 and a mechanically amplified sensitivity of 2.39V/g. The measured natural frequency of the first mode of the sensor was at 734Hz and the full-scale measurement range was up to 7g with a maximum nonlinearity of 2%. The measurements for all the prototype sensor designs were very close to the predicted values with the highest discrepancy being 22%. The results of this research show that mechanical amplification is a very promising concept that can offer increased sensitivity in inertial sensors without increasing the noise. Experimental results show that there is plenty of room for improvement and that viable solutions may be produced by using the presented approach. The applications of this scheme are not restricted only to inertial sensors but as the results show it can be used in a broader range of micromachined devices.

Contents

List of figures

List of tables

List of abbreviations

AC	Alternating Current
BEM	Boundary Element Method
DC	Direct Current
DOF	Degree of Freedom
DRIE	Deep Reactive Ion Etching
ESP	Electronic Stability Program
FEA	Finite Element Analysis
FEM	Finite Element Method
GA	Genetic Algorithm
HAN	High Amplitude No spring
HAS	High Amplitude with Springs
HF	Hydrofluoric Acid
ICP	Inductively Coupled Plasma
IPA	Isopropanol Alcohol
KOH	Potassium Hydroxide
LAN	Low Amplitude No springs
LAS	Low Amplitude with Springs
LIGA	Lithographie, Galvanoformung, Abformung
MEMS	Micro-Electro-Mechanical-Systems
MSA	Micro System Analyser
PCB	Printed Circuit Board
PECVD	Plasma Enhanced Chemical Vapour Deposition
PZT	Lead Zirconate Titanate
RIE	Reactive Ion Etching
RMS	Root Mean Square
SEM	Scanning Electron Microscopy
SIMP	Solid Isotropic Material with Penalisation
SNR	Signal-to-Noise Ratio
SoG	Silicon on Glass
SOI	Silicon On Insulator
VPE	Vapour Phase Etching

Declaration of authorship

I, **Ioannis Zeimpekis**, declare that the thesis entitled "**Development and Implementation of a Deflection Amplification Mechanism for Capacitive Accelerometers**" and the work presented in the thesis are both my own, and have been generated by me as the result of my own original research. I confirm that:

- this work was done wholly or mainly while in candidature for a research degree at the University of Southampton;
- where any part of this thesis has previously been submitted for a degree or any other qualification at this University or any other institution, this has been clearly stated;
- where I have consulted the published work of others, this is always clearly attributed;
- where I have quoted from the work of others, the source is always given. With the exception of such quotations, this thesis is entirely my own work;
- I have acknowledged all main sources of help;
- where the thesis is based on work done by myself jointly with others, I have made clear exactly what was done by others and what I have contributed myself;
- parts of this work have been published as:

1. I. Zeimpekis, I. Sari, M. Kraft, "Characterization of a Mechanical Motion Amplifier Applied to a MEMS Accelerometer," JMEMS, (doi:10.1109/JMEMS.2012.2196491) in press.
2. I. Sari, I. Zeimpekis, M. Kraft, "A full wafer dicing free SOI process for MEMS devices," *Microelectronic engineering Journal, Vol. 95, pp.121-129, 2012.*
3. I. Zeimpekis, I. Sari, M. Kraft, "Deflection amplification mechanism in a capacitive accelerometer," *Transducers 2011*, pp. 1096-1099, 2011.
4. I. Sari, I. Zeimpekis, M. Kraft, "A full wafer dicing free dry release process for MEMS devices," Procedia Engineering, Vol. 5, Eurosensors XXIV, Pages 850-853, 2010.
5. I. Zeimpekis, M. Kraft, "Single stage deflection amplification mechanism in a SOG capacitive accelerometer," *Procedia Chemistry*, Volume 1, Issue 1, Eurosensors XXIII, Pages 883-886, 2009.
6. I. Zeimpekis, M. Kraft, "Displacement amplification mechanism in a capacitive accelerometer," *MME 2008*, vol. 19, pp.291-294, 2008.

Signed: ………………………………………………………………………..

Date:………………………………………………………………………….

Acknowledgements

I would first like to thank Professor Michael Kraft for giving me the opportunity to carry out research in a field that I love. I consider myself privileged working with Michael. His continuous help, motivation and support are the aspects that kept me going. They say that you must be very lucky if you still talk with your supervisor by the end of your studies. I consider myself very lucky. Michael treats us as equals and his friendly approach eases the burden of research. I must specifically thank him for never letting me run out of funding for my research and living expenses.

The success of Cleanroom facilities is not based solely on a good selection of tools. In the same manner, an office environment is not only good because of the building it is housed. It is people who make the difference. People that make the working environment friendly, that accompany you in lunch time, help you in your research, or simply listen to your most subtle problem can really make a research facility of high standard distinguish from others. I was privileged enough to work with people that are excellent scientists as well being excellent friends. I would like to thank all of them from the deepest of my heart. Badin, Mike, Greg, Haitao, Kian, Prassana, Reuben, Stuart B., Stuart P., Mehdi, Petros, Evans, Harold, Owain, Tristan, Asa, Ali, Bader, Steffen, Pej, Mujde, and Sue Ann thank you for everything and I am sorry for my grumpiness. Special mention has to be made to my friend Ibrahim Sari. Ibrahim helped me out in every aspect. We evolved a fabrication process together from scratch. Without him I would still be fighting with Pegasus and stuck devices. He served as a colleague, a co-traveller, an assistant, an advisor, but foremost a dear friend. Special thanks also for the invaluable help from our secretaries Lucia and Glenys.

My family. What is most important than family? Without them I would not even be here. They gave everything they could and more and they never stopped giving. Thank you Mum, Dad, Mary, and Rena. My close friends are family as well, so I want to thank Panos, Alex, Christos, Aggelos, Dionysis, Nasia, Vasko, and Nikos for helping put up with a foreign country but also for putting up with me. Kostas and Pantelis for being my oldest friends always waiting for me to come back in my hometown. Gogo, I mention you last as nothing would be possible without you. No one ever managed to put up with me and support me the way you do. My sincere gratitude and love to you.

This work is dedicated to
the memory of my
grandparents
Γιάννης and Μαρίκα.

Chapter 1 Introduction

1.1 Overview of research

Since the introduction of micromachining, a new field of mechanics has been evolving. Micro-electro-mechanical systems (MEMS) are being developed to provide new applications and solutions at the micro-scale. Applications such as pressure measurement, motion detection, and biomedical sensing can now utilise micro-scale devices to reduce cost while simultaneously increasing practicality, accuracy, and reliability. These benefits created a vast field for research and development. Although most applications maintain their basic operating principles at the micro-scale, not all rules that they abide by are valid at these dimensions. One example is the behaviour of parallel plate capacitors when those move at micron dimensions. This makes the research on scaling-down mechanisms of the macro-world even more challenging.

The field of MEMS is a very fast growing market, which is expected to thrive in every day applications in the upcoming years [1, 2]. Currently, the automobile industry is the dominant user of MEMS technology. Sensors vital for the safety, handling and convenient operation of vehicles can be realised using this technology. Safety and control systems mostly rely on inertial sensors since they have the ability to sense motion by utilising inertial forces. The advantages that MEMS inertial sensors have, like most micromachined devices, are reduced size and cost while at the same time increased efficiency and reliability. Examples of automotive safety systems relying on inertial sensors are rollover protection, Electronic Stability Programs (ESP), vehicle dynamics control, and short-term navigation. Other applications that inertial sensors are used for include tactical guidance, control systems, human motion analysis and interfacing, and device stabilization. Such applications would often be impossible to realise at the small scale necessary to make them viable solutions, without the use of micromachining.

Although more complex combinations of inertial sensors are emerging, the most common ones are accelerometers and gyroscopes. Accelerometers and gyroscopes in their simplest form use a suspended proof mass to measure acceleration or rate of rotation. The motion of the proof mass due to a change in its kinematic state is detected through readout mechanisms that employ capacitive, piezoresistive, or electromagnetic methods to translate this motion to an electrical signal that is easier to measure. The miniature nature of micromachined inertial sensors results in low inertial forces due to the small size of the inertia mass (few milligrams), which also makes sensitivity an inherent problem.

1.2 Motivation and contributions

There have been plenty of approaches explored to increase the sensitivity of inertial sensors. Research in micromachined physical sensors has focused on all aspects of their implementation. These are the mechanical design, the fabrication technology, the electronic interface, and the packaging of the sensor. Improvements in the mechanical design are being introduced in the form of compliant and rigid mechanisms with the common goal of increased sensitivity. Examples include, improved suspension systems, and advanced structures to provide large deflection or force. The fabrication process serves design requirements such as tolerances and often provides improvements by allowing for larger proof masses, more compliant suspension systems, and higher transductance through improved structures such as reduced comb-finger gaps. Advanced interface circuits aim to provide high amplitude outputs of low noise, and frequently control the mechanical part through closed loop arrangements. Packaging is one of the most expensive parts of the sensor and provides isolation from the environment. Improvements on the performance of the sensor can be achieved through packaging with the use of vacuum encapsulation.

The research work presented in this thesis has aimed to increase the sensitivity of bulk micromachined accelerometers. Bulk micromachined capacitive sensors offer a large inertial mass, high sensitivity and good noise performance [3], hence, they are highly advantageous in applications such as inertial, seismic, and precision tilt sensing.

Current research work on inertial sensors primarily aims to increase the sensitivity and improve the noise floor. The sensitivity of a capacitive sensor can be increased by increasing the effective proof mass, the nominal capacitance, or by maintaining low damping and high compliance along the sense axis [4-8]. For a bulk micromachined device operating at ambient pressure, the electronic interface is typically the dominant noise source[1]. There are therefore numerous research examples where performance increase mechanisms of the mechanical sensing element are coupled with advanced interface circuits [9-13]. There is also extended, on-going, research that exclusively aims to improve the noise floor of the electronic pick-off circuits for such sensors [14-17].

MEMS physical sensors typically rely on force coupling and the resulting deflection of a proof mass or membrane to produce an output proportional to a stimulus of the physical quantity to be measured. They typically have compliant mechanisms [18], such as flexible beams, to implement spring structures in order to provide suspension and mobility along desired axes. The geometry of conventional suspension mechanisms is usually a limiting factor for sensitivity by restricting the motion according to their stiffness.

The work presented in this thesis introduces an approach based on a mechanical motion amplifier with the potential to improve the performance of mechanical MEMS sensors that rely on deflection to produce an output signal. To achieve this, a scheme is proposed where the suspension system is integrated with a mechanical amplifier. The mechanical amplifier comprises a system of micromachined levers (microlevers) to enhance the deflection of a proof mass caused by an inertial force. The mechanism can be used in capacitive accelerometers and gyroscopes to improve their performance by increasing their output signal. Compared to a conventional accelerometer of the same sense mode natural frequency and proof mass a mechanically amplified accelerometer deflects more for the same excitation as it will be shown in this thesis. If the bandwidth is considered to be limited by the natural frequency of the sensor, the mechanically amplified accelerometer has an increased sensitivity within the same bandwidth compared to the conventional design. As the noise contribution of the electronic read-out circuit of the MEMS sensor is, to first order, independent of the amplitude of its

---

[1] Brownian noise is very low due to the size of the mass without the need for vacuum packaging

input signal, the overall signal-to-noise ratio (SNR) of the mechanically amplified sensor is improved. The output of an accelerometer is proportional to its deflection. Thus, the SNR of the amplified accelerometer is higher than a conventional sensor by a factor defined by the ratio of their output deflections, for the same nominal capacitance and circuit.

In order to explore the concept of mechanical amplification, microlevers are first analysed mathematically to explore the geometrical and mechanical characteristics. The next step involves the implementation of microlevers in capacitive accelerometers in order to evaluate their use in inertial sensors. Through system level and Finite Element Method (FEM) simulations, amplified sensors were designed and fabricated for experimental evaluation. The results from the investigation show that mechanical amplification using microlevers is an advantageous concept that can be used in various MEMS devices.

1.3 Document structure

This report describes the mechanical approach to amplification in inertial sensors, how it was implemented using microlevers in capacitive accelerometers, and the results from using this approach.

The literature review (Chapter 2) details the current methods used for analysing and designing mechanisms that can be used for mechanical amplification in MEMS devices. In this review, some of the most interesting mechanisms are presented.

In Chapter 3, microlevers are evaluated using mathematical analysis based on the stiffness of the structures. The results are compared to system level and FEM simulations in order to verify their accuracy.

Chapter 4 describes the implementation of microlevers in four single axis accelerometers. It starts with the design of the mechanism and its implementation with a proof mass. Specific performance-defining structural parameters are discussed. The chapter concludes with an evaluation of the designs by simulation.

Chapter 5 describes the fabrication processes developed for the accelerometer. It starts by describing an initial Silicon on Insulator (SOI) process and Silicon on Glass (SoG) process. It then presents an improved SOI process developed at the University of

Southampton. The chapter concludes with some remarks on experiments carried out with the fabrication processes.

Chapter 6 gives a brief introduction to the pick-off circuit used in this study while Chapter 7 presents results on the experimental evaluation of the fabricated sensors. Chapter 8 presents conclusions and a summary of future work that can be carried out to improve the implemented sensors.

Chapter 2 Literature review

2.1 Introduction to mechanical amplification

Mechanical amplification has been applied in a variety of MEMS devices. The aim is to achieve higher force or deflection. There are three general approaches in the literature for applying mechanical amplification in MEMS devices. These are: parametric resonance amplification [19], dual mass systems based on the mechanical absorber principle [20], and compliant mechanisms based systems [21]. Parametric resonance amplification utilises parametric amplification using variable force actuators that operate according to the non-linear Mathieu equation. The work presented in this thesis aims to use a linear, non-resonant, passive amplification mechanism that is applicable to a wide range of sensors and actuators hence parametric amplification is not suitable. The concept of a mechanical dynamic vibration absorber [22] based system has already been effectively applied in MEMS sensors and in particular gyroscopes. According to the mechanical absorber principle, the natural frequencies of a two degrees of freedom (2-DOF) system can be tuned such that maximum dynamic mechanical amplification is achieved for a specific frequency or a frequency range [23]. A mechanical absorber is therefore a resonating system with an amplified deflection at a specified frequency or a limited bandwidth range. It is applicable to resonant[2] accelerometers and gyroscopes but not translational accelerometers, thus it is not applied in this study.

Mechanisms with compliant members (compliant mechanisms) are included in most MEMS devices in many different forms. Specific arrangements of a compliant mechanism can provide mechanical amplification for force or displacement. Many studies focus on optimisation techniques such as topological optimisation to achieve an

---

[2] "resonant" here implies that they operate at a specific frequency, not necessarily at their natural frequency

amplified result [24, 25]. The research groups concentrated on the topology optimisation of compliant mechanisms have produced various amplifying mechanisms that are specific to certain applications. With this method, the entire structure is designed by an optimisation algorithm. The focus of the work in this thesis is to implement a mechanism that can be applied in a variety of MEMS devices. To achieve that, a design framework based on a sensor was formed. This was based on simple compliant elements such as micromachined levers (microlevers), rather than topologically optimised structures. In this way, the mechanism is effective, simple to design and fabricate, and its operation can be intuitively understood. Nevertheless, it can be further improved by using optimisation algorithms, such as a genetic algorithm. Therefore, structural parameter optimisation may be performed according to the specific needs and performance requirements of the application. This was considered during the composition of the simulations by creating parametric models so that optimisation can be implemented later. However, structural optimisation was not the main goal for this thesis.

The remainder of this chapter discusses the advantages of compliant mechanisms and flexure hinges in MEMS devices, research on implementing amplifying mechanisms in different devices, and the application of such mechanisms in MEMS sensors.

2.2 Introduction to compliant mechanisms

A compliant mechanism is a mechanical device that has the ability to translate or transform motion, force, or energy [18]. What makes those devices distinct from rigid-link devices that use bearings or other types of rigid joints is the feature of energy storage along their flexible members. This provides the advantage of extended motion abilities, such as the return to the initial position after external loads stop being applied. Figure 2-1 shows two mechanisms that use rigid-links, whereas Figure 2-2 a mechanism designed with compliant links [18].

Removed for copyright reasons.

Please find image on the cited source.

Figure 2-1 Two mechanisms based on rigid-links (mechanisms with rigid parts that are connected through rigid links such as bearings). Reproduced from [18].

Removed for copyright reasons.

Please find image on the cited source.

Figure 2-2 Compliant microgripper (most of the rigid-links have been replaced by flexible links). Taken from [18].

The advantages of compliant mechanisms are mainly low cost and high performance. In contrast to mechanisms that use rigid-links for their joints, compliant mechanisms do not need assembly of complex structures. As a result, they have a much simpler fabrication process and an improved performance in terms of reliability, precision, and wear. It would be completely impractical for a MEMS device to need lubrication and to have a high chance of failure when poorly maintained. In addition, fabricating a MEMS device with parts in all three dimensions has proven to be an expensive and quite difficult task. Compliant mechanisms offer the advantages of in-plane fabrication, no assembly or lubrication, reduced susceptibility to friction and wear, and provide high precision and energy storage [18, 26].

Considering the advantages of compliant mechanisms, designers use them in different ways and forms to achieve the desired motion characteristics for their devices. One of the simplest forms of a flexure part is a cantilever beam that is used to suspend a structure. In this thesis, the commonly used cantilever-beam suspension mechanism is replaced by a system of microlevers. This mechanism aims to both suspend the structure and amplify the deflection of the device. Research on amplifying mechanisms using compliant members has been carried out before for MEMS devices. This chapter aims to present the most important of these devices and correlate them with the work presented in this thesis.

2.3 Flexure hinges

In the analysis of compliant mechanisms, the most important element is the flexure hinge. Figure 2-3 shows different types of flexure hinges. The flexure hinge is the “compliant” part of a compliant mechanism, which serves as a connecting link between rigid parts. Paros and Weisbord [27] gave exact and simplified equations for the compliances of circular flexure hinges. Lobontiu et al. presented different types of flexure hinges in [28-30] providing closed-form compliance equations. In [31] they introduced two analysis procedures; one based on the strain energy method, and another constructed on the loop-closure theory.

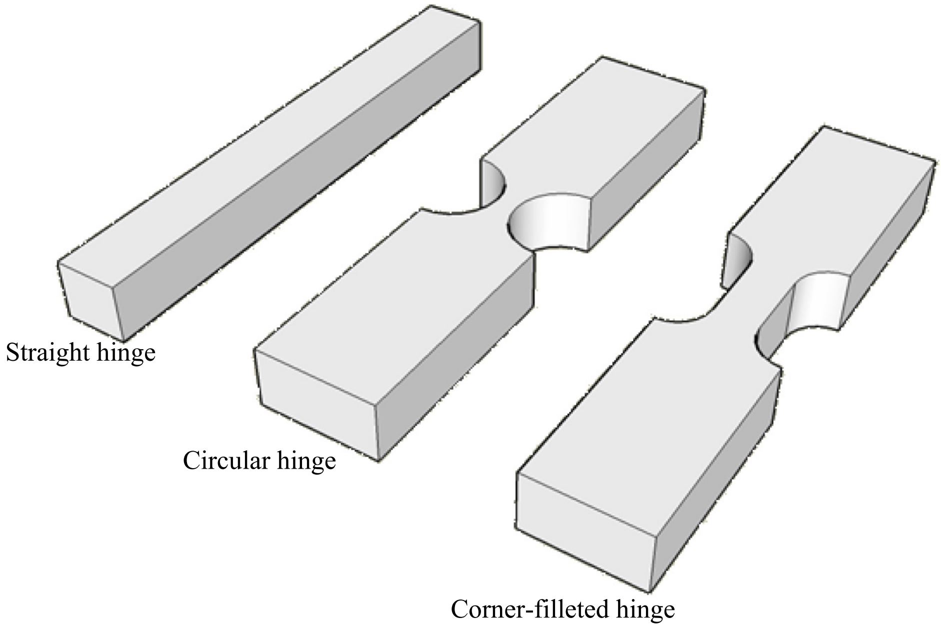

Figure 2-3 Different flexure hinges. A straight hinge is the simplest. Circular and corner-filleted hinges can handle more stress and present motion that is more accurate.

The pseudo-rigid-body approach (Figure 2-4) was presented in detail in [18]. This method models the flexure hinge as a torsional spring. This analysis is also valid for large deflections since there is no assumption for small deformations in the derivation of the formulas. For the analysis and synthesis of mechanisms using compliant joints the authors of [32] also developed a loop closure theory. Other methods used in the analysis and design of compliant mechanisms include dynamic analysis [33, 34] inverse kinematic analysis [35], direct-bending stiffness analysis [36], and topology optimisation [37, 38]. The operation of a mechanism employing compliant joints can be accurately predicted by these methods. The choice of method used is based on the kind of analysis, results, or mechanism synthesis required.

Removed for copyright reasons.
Please find image on the cited source.

Figure 2-4 Flexure substituted by a torsional spring in a pseudo-rigid-body model, *l* is the flexure length and *F* the applied force. The pseudo-rigid-body model represents the flexure with a torsional spring. Reproduced from [18].

Most of these approaches act as an intermediate between first approximations and finite-element simulations in the design, analysis, and evaluation of compliant mechanisms. Although they may not present the highest possible precision, they provide a framework for analysis and understanding of the mechanisms working principles, while saving the time taken from rigorous simulations.

2.4 Mechanical amplification mechanisms in MEMS devices

This part of the literature review aims to present different amplifying mechanisms applied to micromachined devices. The literature was extensively studied and the work presented in this chapter influenced how the mechanical amplifier in this thesis was implemented.

2.4.1 Piezoelectric micropositioning stage with high resolution and amplitude

In order to achieve maximum deflection and rigidity for a micropositioning stage a compliant amplification mechanism was used by [39]. This micropositioning stage, schematically shown in Figure 2-5, is driven by a piezoelectric actuator. The output motion of the actuator is translated by a compound displacement amplifying lever mechanism. The advantages of using flexures include: negligible backlash, no bearing noise, low friction, and no need for lubricants. Although this mechanism is made from a metal blank (10x10x2cm^3), which is much larger than a typical MEMS device, it is presented here as its operation is relevant to the micromachined mechanism used in this thesis.

Removed for copyright reasons.

Please find image on the cited source.

Figure 2-5 Schematic of the micropositioning stage design. The ratios $R1/R$ and $R3/R2$ determine the gain in an ideal system. Reproduced from [39].

The proposed design should have maximum mechanical displacement gain and rigidity while taking into account flexure stretching and bending, allowable stresses for the piezoelectric elements, and lever arm bending. In the first model it was assumed that all levers are rigid and all flexures do not stretch or compress. The output deflection of this model is expressed as $d = m_1 m_2 d_p$ with d_p being the input deflection and m_1, m_2 the amplification factors of stages one and two, respectively. If there is no external load applied at the output the force applied at the stack from the input is due to the bending moment needed to bend the flexure pivots. The rotational stiffness used in this model was first described by Paros and Weisbord [27] for a right circular hinge, such as the one shown in Figure 2-6.

Removed for copyright reasons.

Please find image on the cited source.

Figure 2-6 Schematic of a right circular flexure hinge and definitions of the geometrical parameters used in its analysis. Reproduced from [39].

By using force equilibrium equations, the reaction force at the connecting link between the stages and the overall reaction at the input were derived. The purpose of this model was to calculate the maximum deflection and stiffness of the mechanism. Comparison with the fabricated designs showed that the model was highly inaccurate. The amplification factor that the model predicted was much larger than that of the fabricated device. The model was further improved by adding the strains induced at the pivots. The fabricated device presented smooth linear outputs as a function of the applied voltage. Although the displacement was linear relative to the input voltage there was an offset upon return to zero voltage of about 1% of the maximum displacement, as shown in Figure 2-7. Unfortunately, this problem was not addressed or further explained by the authors.

Removed for copyright reasons.

Please find image on the cited source.

Figure 2-7 Displacement versus voltage curve for the output member of the stage. Displacements measured interferometrically. Further cycling reduces hysteresis offset to levels less than shown here. Reproduced from [39].

This work [39] uses a compound mechanism to amplify displacement. In the work presented in this thesis, compound mechanisms were designed and simulated but were not fabricated since they added complexity with no practical advantage as shown in Appendix E.

2.4.2 Electrostatic parallelogram actuators

Another compliant mechanism able to amplify motion but based on a different principle is presented in [40]. Surface micromachined actuators composed of polysilicon are able to transform the direction and magnitude of an electrostatic force developed between the drive electrodes. Figure 2-8 illustrates the working principle of the parallelogram mechanism. The operation of this mechanism was verified by a fabricated prototype device.

Removed for copyright reasons.

Please find image on the cited source.

Figure 2-8 Working principle of the parallelogram actuators a) Initial position, b) deflection of the parallelogram actuators. Reproduced from [40].

When a potential difference is applied to the electrodes, a force is generated at the free-moving electrodes of the parallelogram structure. This results in motion of the free-moving electrodes along the X-axis. The deflection *dx* can be approximated by

$$dx = \frac{FL^3}{6EI} sin^2\theta \qquad \text{eq. 2-1}$$

Here, L is the length of the parallelogram, θ is the angle shown in Figure 2-8, E is the Young's modulus, and I is the moment of inertia. The deflection at the axis of actuation (x) is proportional to the square of applied force. The deflection at the perpendicular axis can be calculated by eq. 2-2.

$$\frac{dy}{dx} = 2cot\theta \qquad \text{eq. 2-2}$$

This relationship shows that, depending on the angle θ, the parallelogram structure can either redirect and amplify motion that happens along the X-axis to the Y-axis when $\theta<45^o$, or redirect and reduce the motion when $\theta>45^o$.

This method of motion translation is suitable for motion amplification in actuators. It cannot be directly applied to a MEMS accelerometer since it needs actuation along two different directions. This means that such a design requires two proof masses moving in opposite directions, hence it was not further considered in this thesis.

2.4.3 Micromotion amplifier

In [41] another way of amplifying the motion of an actuator is presented. This method is based on the buckling of beams. Motion amplification is achieved through axial loading of straight beams. Gradual transition of the deformation from straight to buckled is achieved through the introduction of a geometrical asymmetry implemented by hinge-like structures. Since this transition is gradual, precise control over displacement is possible. In this design, the loading actuators provide a force larger than the critical force for buckling the beams. They are separated from the amplification stage to ensure stability of the loading actuators while the amplified displacement increases. The high aspect ratio (12:1) of the device ensures that buckling will only occur along the desired axis. The operation of the device is stable when the above specifications are met. Devices using the micromotion amplifier were fabricated in single crystal silicon.

The operating principle of the micromotion amplifier can be described with the help of Figure 2-9. The long slender beam has one fixed end and one free to move along the axial direction. When the load applied at the free end exceeds the critical value P_{cr} the beam starts to buckle.

Removed for copyright reasons.
Please find image on the cited source.

Figure 2-9 Schematic of the buckling of an axially loaded beam. P is the applied force, $2L$ is the length of the beam, δ the horizontal deflection, and Δ the transverse amplitude. Taken from [41].

The maximum transverse amplitude *Δ* can be obtained by the Euler buckling equation for a straight rectangular beam, as shown in eq. 2-3, where *2L* is the length of the beam and δ the horizontal deflection.

$$\mathit{\Delta} = \frac{2}{\pi}\sqrt{L\delta} \qquad \text{eq. 2-3}$$

eq. 2-3 also shows that the operation of the mechanism is non-linear. Following the presented theory for buckling beams, a higher amplification can be achieved by replacing the buckling beam by rigid beams and flexure hinges connected at the actuators. A micromotion amplifier working under this principle is schematically presented in Figure 2-10.

Removed for copyright reasons.
Please find image on the cited source.

Figure 2-10 Schematic of the micromotion amplifier (top: before loading; bottom after loading). Taken from [41].

The transverse amplitude for actuation on one side is given by eq. 2-4. When the actuation is applied equally at both sides of the amplifier the amplitude is given by eq. 2-5.

$$\mathit{\Delta} \approx Lsin[cos^{-1}\left(1-\frac{\delta}{L}\right)] \approx \sqrt{2L\delta} \qquad \text{eq. 2-4}$$

$$\Delta \approx 2\sqrt{L\delta} \qquad \text{eq. 2-5}$$

For stable buckling, the cross section of the beam must ensure a minimum moment of inertia about the axis perpendicular to the desired direction of motion. The force provided by the actuator must be much larger than the critical load, so that the stability of the actuator remains unaffected by the motion of the buckling beams. According to the authors, introduction of a properly designed asymmetry[3] ensures buckling in the desired direction, while preventing a sudden uncontrolled motion of the actuator.

It must be noted here that the last two specifications make the micromotion amplifier unusable for an inertial sensor. The force supplied by the motion of a MEMS proof mass at low accelerations is very low; therefore, the critical force needed for the force amplifier would introduce a mechanical limit to the sensitivity if it were used in a MEMS sensor. Furthermore, the asymmetry introduced restricts buckling to a certain direction whereas the motion of an inertial sensor must be along both directions of an axis. This issue could of course be alleviated by the inclusion of two mechanisms. However, this would increase the stiffness of the mechanism, and introduce uncontrollable motions due to the oppositely directed asymmetries of the dual mechanism. Finally, as indicated by eq. 2-3, the mechanism is non-linear, thus it would not be sensible to use it in an inertial sensor requiring a linear output response, without a special dedicated pick-off circuit that compensates for the non-linearity.

The results from the evaluation of a quasi-buckling beams-based amplifier show that high amplitudes can be achieved using this method. The displacement amplification achieved in this design was 55. As mentioned above, this design is not suitable for inertial sensors, but is more suitable in applications where displacement amplification is desired for the output of an actuator.

2.4.4 Two-axis scanner array driven by a force amplifying leverage mechanism

The authors of [42] reported the design, fabrication, and characterisation of a high fill-factor, large scan-angle, two-axis scanner array. The two-axis micromirror is driven electrostatically by vertical comb-drive actuators through four motion-amplifying

---

[3] The authors do not report on the exact form of a properly designed asymmetry

levers. The maximum rotational angles achieved are ±6.7^{o}. In contrast to [43] and [44], who used a complex bulk micromachining process, these micromirrors use a simpler surface micromachining process. In addition, the four-lever system enables these micromirrors to rotate about two axes, while similar micromirrors reported by [45] and [46] are limited to one axis.

Figure 2-11 shows a schematic of the micromirror and its principle of operation. Each micromirror is supported by four microlevers. The inputs of the microlevers are attached to the comb-drive. In order to achieve displacement amplification, the fulcrum of the lever is positioned closer to the actuator. The joint that connects the output of the microlever to the micromirror is a flexure joint with 2-DOF. In this way, the differential vertical displacement is translated into two-dimensional tilting of the mirror. The four levers can move independently to offer two-dimensional tilting, or all equally to offer piston-like motion. The large force requirements of this mechanism and the low fill-factor make it less suitable for application in a micromachined accelerometer.

Removed for copyright reasons.
Please find image on the cited source.

Figure 2-11 a) Schematic structure of the two-axis mirror b) Operating principle of the two-axis scanner. Taken from [42].

Special attention was given in [42] to the design of the 2-DOF joint between the mirror and the levers. Based on their previous study [47], a serpentine compliant joint was used. This offers a high rotational compliance and it does not reduce the scan angle (θ). The use of highly compliant serpentine joints is particularly advantageous. This is because a stiffer joint would also cause elevation (Δ) on the opposite side, which would reduce the range of the scan angle, as shown in Figure 2-12.

Removed for copyright reasons.
Please find image on the cited source.

Figure 2-12 Dependence of the mirror scan angle on the compliance (relative to the torsion spring constant of the lever fulcrum) of the 2-DOF joints. a) Stiff joints, b) Compliant joints. Taken from [42].

Although a serpentine like joint in an inertial sensor would increase the rotational compliance, it would also increase the axial compliance. This is highly undesirable since the expected displacement would mainly be lost in the deformation of the joint.

2.4.5 Bridge-type flexure mechanism

A very common structure used as a compliant mechanism for displacement amplification is the bridge-type flexure hinge. This kind of flexure mechanism finds most of its applications in amplifying the displacement of piezo-stacks. There are four more types of displacement mechanisms used in piezo-stacks. These are lever-, Moonie-, Rainbow- and Cymbal-type structures, as shown in Figure 2-13 [48]. The bridge-type amplification mechanism is more recent than the other four mechanisms, and is commonly used in applications that use piezo-stacks.

Removed for copyright reasons.

Please find image on the cited source.

Figure 2-13 Topology of different flexure amplification mechanisms. Taken from [48].

The structure of a bridge-type flexure mechanism is shown in Figure 2-14. It comprises eight rigid members connected by eight flexure hinges. One of the first micromachined bridge structures was presented by [49]. It was fabricated using the Lithography, Electroplating, Moulding (Lithographie, Galvanoformung, Abformung, LIGA) process [50]. This mechanical amplifier is designed so that a strain input from a piezoelectric material is increased through the leverage structure that is formed by rigid arms connected with elastic pivots. The ideal amplification ratio for the displacement r is presented in eq. 2-6, with reference to Figure 2-15.

Removed for copyright reasons.

Please find image on the cited source.

Figure 2-14 Bridge-type amplifying mechanism. Taken from [48].

Removed for copyright reasons.

Please find image on the cited source.

Figure 2-15 Quarter kinematic model of bridge-type amplification mechanism. Taken from [48].

$$R_{amp} = \left|\frac{\sin(a) - \sin(a - \partial a)}{\cos(a) - \cos(a - \partial a)}\right| \qquad \text{eq. 2-6}$$

From eq. 2-6 [48], it can be shown that an input strain will change the angle between the initial value $(a - \partial a)$ and final value a [49], resulting in a variable amplification ratio for this structure. This translates to a change in the natural frequency of the system as the amplitude varies. In high amplitude excitations, the angular dependence of the amplification factor is more obvious. Since the microamplifier is not an ideal mechanism, energy is stored in its elastic link during deformation, resulting in a strain transmission efficiency loss and reduction of the maximum amplification ratio. A stiffer mechanism or high modulus of elasticity can improve the efficiency of the mechanism [49, 50]. The stiffness of the leverage mechanism is inversely proportional to the amplification factor and proportional to the strain transmission efficiency.

The bridge-type structures have been closely analysed using geometric relations [51], elastic beam theory [52], and kinematic theory [28].

2.5 Mechanical amplification in inertial sensors

There is little published work describing the implementation of mechanical amplification in inertial sensors. From the open literature it seems that only few groups of researchers such as [36] and [55], have presented analyses and results of microlever-based mechanical amplification in inertial sensors. Some of the more pertinent results are presented in the following sections, together with devices using alternative methods for mechanical amplification.

2.5.1 Non-resonant micromachined gyroscope with structural mode decoupling

The authors of [23] describe a methodology to design a 4-DOF non-resonant micromachined gyroscope with structural mode decoupling. The aims of this design are to eliminate the mode matching required for gyroscopes, and minimise instability and drift due to mechanical coupling between the drive and sense mode. In order to satisfy these requirements, a mechanical dynamic vibration absorber [22] is applied on both the drive and the sense mode of the gyroscope. Apart from eliminating the mode matching requirement and minimising mode coupling, the applied concept also results in a mechanically amplified sensor.

The design approach of [23] comprises a system of three masses. The first mass (m_1) is restricted to move only in the drive direction. The second (m_2) and third mass (m_3) are fixed with respect to each other in the drive direction (x) as shown in Figure 2-16.

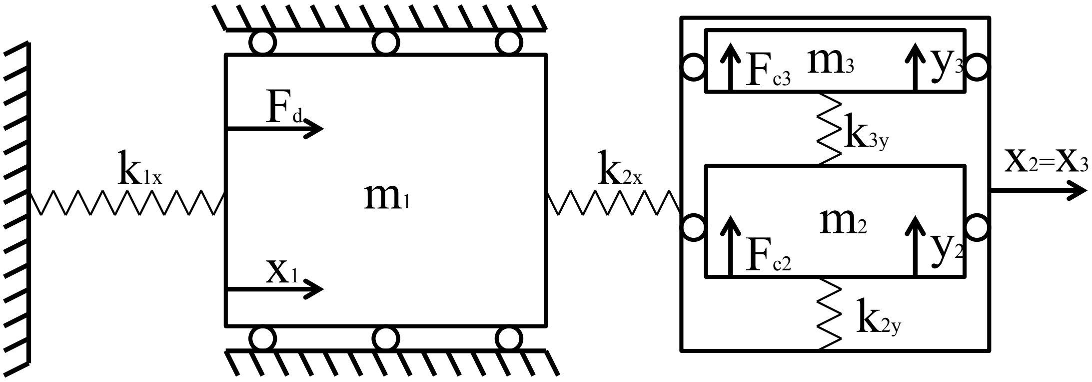

Figure 2-16 Schematic of the 4-DOF micromachined gyroscope of [23]. Reproduced from [23].

The design can be described by two 2-DOF systems; one in the drive direction (x) and a second in the sense direction (y). The 2-DOF system in the drive direction is composed of m_1 and the combination m_2+m_3. The rotation induced Coriolis force on m_2 (F_{c2}) is proportional to its deflection (x_2) along the drive direction. In order to maximise F_{c2}, x_2 has to be maximised. A mechanical dynamic absorber system achieves maximum amplification of the passive mass (m_2+m_3) when the drive frequency of force F_d is matched to the natural frequency of the isolated passive mass-spring system [56]. The natural frequency of the isolated passive mass-spring system is the natural frequency of m_2+m_3 when the spring that connects m_2+m_3 to m_1 is simply anchored from the side that it would be connected to m_1. The resonance frequency ω_{2x} of the isolated passive mass-spring system is dictated by the driving frequency specifications of the gyroscope, but also from the fact that larger Coriolis forces are induced at lower frequencies. When ω_{2x} is fixed, the optimal drive direction mass ratio ($m_x=(m_2+m_3)/m_1$) defining m_1 is dictated by how sensitive the response bandwidth and amplitude of oscillation are to damping. The amplification factor of the system depends on the resonance frequency ratio of the isolated active and passive mass-spring systems. This is optimised to achieve high mechanical amplification and high oscillation amplitudes of the passive mass. When the parameters of the drive mode 2-DOF system have been obtained, the sense mode parameters are calculated in a similar manner. Since m_2 is significantly larger than m_3, the Coriolis force (F_{c2}) induced on m_2 is the dominant driving force of the system. Such as in the drive mode, when the frequency of this force matches the oscillation frequency of the isolated mass-spring system comprising m_3, the dynamic amplification is maximised.

The proposed approach in [23] achieves mechanical amplification using the mechanical dynamic absorber principle. It is evident that this principle is applicable to resonating structures and hence it is not considered in this thesis as a mechanical amplifier for translational accelerometers. It has to be noted that coupling the mechanical absorber principle with a mechanical amplifier based on microlevers could achieve further amplification for vibrating devices. This will be considered in future work when the mechanical amplifier presented in this thesis is implemented in other micromachined devices, such as gyroscopes.

2.5.2 Mechanical amplification in MEMS devices based on topology, shape and size optimisation

Topology, shape, and size optimisation are methods that aim to solve the basic engineering problem of designing a device to fit within a confined space that achieves specific requirements [57]. As their names imply, the three methods solve the optimisation problem from different perspectives and have all been applied in MEMS devices to improve their performance. The main aim of these methods in MEMS devices is to achieve maximum deflection or force within a device.

The report presented in [24] serves as a review of topology-optimised structures and introduces a methodology for designing topology-optimised capacitive accelerometers. The authors of [24] aim to introduce a method that simplifies the problem of a mechanically amplified sensor. This method is based on a spring-mass-lever system rather than a spring-mass system. The reason behind this is that a design implementing mechanical amplification has an input where a force or displacement is applied and an output where the amplified displacement is read. This is different to a design with no mechanical amplification where the input and the output are at the same point. The main reason it is different is that the amplifying mechanism cannot be simply considered as a rigid lever. The ratio of the input and output deflection is different when the force is applied at the input or the output.

The lumped spring-mass lever model includes the following parameters: a) the inherent amplification defined as the ratio of the output versus the input deflection; b) the input stiffness defined as the ratio of a force applied at the input versus the resulting deflection; c) the output stiffness similarly defined but also including a parameter to make it dependant on the input stiffness and the inherent amplification; d) the input, and e) the output inertia masses that are defined from the natural frequency of the device.

This model is useful for comparing accelerometers that use different mechanical amplifiers. It also proves useful in the synthesis of a mechanically amplified accelerometer. The interested reader can find more information in [24].

The authors of [24] compare different mechanical amplification mechanisms. Those mechanisms have distributed compliance rather than flexure hinges. In order to perform a comparison, size normalisation is performed on the designs to constrain them in the same design space and fabrication technology. The topology and shape of the devices is not affected by the size optimisation. The figure of merit for the comparison of the mechanisms is the ratio of the deflection of the device with the mechanical amplifier attached to the deflection of the device with the mechanical amplifier detached. This is denoted as the net amplification. Additional criteria for the performance of a mechanism are the inherent amplification, the unloaded output sensitivity, the natural frequency, and the cross-axis sensitivity. None of the mechanisms that authors reported met all the set criteria. A topology optimisation problem was defined to achieve the desired criteria. The objective function of the problem had as the main goal to maximise the net amplification and keep the cross-axis sensitivity as low as possible. Table 2-1 shows the specification and design constraints. The resulting mechanism achieved an inherent amplification of 3.2 and cross-axis sensitivity of 0.02% and it is shown in Figure 2-17.

Table 2-1 Specification for the accelerometer optimisation problem [24]

Quantity	*Specification for the accelerometer*
Size of the grid	1500x1500μm^2
Thickness of each element	3.5μm
Lower bound for the element width	10μm
Force at the input	1μN
Value of sensor stiffness k_s	5N/m
Value of the proof mass m_s	5mg
Value of the comb suspension	1.25N/m
Value of the cross-axis stiffness SE_{cross}	Better than 0.025%

Removed for copyright reasons.
Please find image on the cited source.

Figure 2-17 Optimised deflection amplification mechanism in conjunction with a proof mass and suspension. Reproduced from [24].

The most important contribution of [24] is the justification that a mechanically amplified design cannot be compared to a conventional design by employing simple spring-mass models. Design constraints from the available device space and fabrication technology have to also be taken into account when comparing devices. The authors state that there has to be a global figure of merit for the comparison of different design concepts. In the study for this thesis, the design approach differs substantially. Rather than relying on a computer generated design the sensor is based on flexure hinges and the amplifier is based on microlevers and flexure hinges. Therefore, the comparison to a conventional design, as will be seen in Chapter 4, is performed on the deflection natural frequency product. Further optimisation of the sensor can include cross-axis stiffness and a design space constraint but those are not considered in this thesis.

2.5.3 Topology optimisation of a force amplifier on a resonant accelerometer

The work presented in [55] deals with the optimisation of a compliant force amplifier mechanism in a surface micromachined resonant accelerometer. The force amplifier is optimised such that the noise floor is minimised while the scale factor is maximised. The optimisation constraints are set by the device geometry and the fabrication process limitations. Results were extracted using a continuum topology optimisation depending on the size of the design space, output and input stiffness and boundary conditions. Those were subsequently converted to beam element models that were used for further shape and size optimisation. Through the optimisation procedure, force amplification factors of a 100 were achieved. [55]

Since in resonant accelerometers the scale factor of the device is directly proportional to the force coupled, a compliant microleverage mechanism based on force amplifying microlevers was implemented in a resonant accelerometer in order to amplify the force induced by inertial forces. The optimisation offers an improved SNR versus previous designs [58].

The resonant accelerometer shown in Figure 2-18 consists of a proof mass coupled to four resonant force sensors through a compliant leverage mechanism [55]. Assuming a quarter model, the force acting at the tuning fork is $F_{out}=K_{out}\,u_{out}$ where K_{out} and u_{out} are the output stiffness and axial displacement of the fork respectively. The input force for one fork is then: $F_{in,1} = \frac{1}{4}m\ddot{u}$. In the linear elastic region, where the design is independent of the input force size, the objective of the optimisation is to maximise the amplification, A, of the mechanism. The amplification factor of such a mechanism is the ratio of the output versus the input force. According to eq. 2-7, the deflection at the output must be maximised in order to maximise the amplification factor [55].

$$\begin{aligned}\max(A) &= \max\left(\frac{F_{out}}{F_{in,1}}\right) = \max\left(\frac{K_{out}u_{out}}{F_{in,1}}\right)\\ &= \frac{K_{out}}{F_{in,1}}\max(u_{out})\end{aligned} \qquad \text{eq. 2-7}$$

Removed for copyright reasons.

Please find image on the cited source.

Figure 2-18 A) The resonant accelerometer. B) The subsystem containing the compliant amplifier mechanism which is optimised. The spring stiffnesses in the X-direction, K_{in} and K_{out}, model the stiffness of the resonant accelerometer. The input force $F_{in,1} = \frac{1}{4}m\ddot{u}$, is one quarter of the inertial force for the proof mass m. The output force F_{out} is the axial force applied to one of the excited beams measuring the axial force F_{out}. C) Due to symmetry, only half of the resonant accelerometer is analysed and symmetry supports are applied. Taken from [55].

In order to optimise the individual microlevers a topology optimisation method was applied in a predefined domain Ω. The Solid Isotropic Material with Penalisation (SIMP) method [57] combined with a mesh-independency filter [59] was used for this purpose. Because the flexure-hinges of the microlevers were contained in this domain, there were violations of the fabrication constraints during optimisation. Then the shape and size were optimised based on the results from the topology optimisation to give maximum deflection. Finally, the amplifying mechanism was included in a half model of the resonant accelerometer and modelled using ABAQUS [60] for validation. The details of this work and results are presented in [55].

2.5.4 Single stage amplification in a resonant accelerometer

Work in the field of mechanical amplification by using discrete microlevers has mainly been carried out by X.-P.S. Su [36]. The authors of [36] present the application of a single-stage microleverage mechanism in a resonant accelerometer. In the presented device, a force amplification microleverage system was implemented in a resonant accelerometer. The proof mass is the input of this device while the output system comprised two double-ended tuning forks. The inertial force from the proof mass is amplified by the leverage system and the output of the microlevers shifts the frequency of the tuning forks providing in this way a high sensitivity (50Hz/g) accelerometer.

Removed for copyright reasons.
Please find image on the cited source.

Figure 2-19 Layout of the resonant mechanically amplified accelerometer. Taken from [36].

The levers that were used by [36] for the resonant accelerometer are force amplifying levers. This means that the output lies between the input and the pivot and that the ratio of the output to pivot distance versus input to pivot distance is less than one. In order to perform an analysis of the force characteristics for this kind of lever they assumed that all deformations are within the linear region, the lever arm is rigid, the displacement at the output due to output system deformation is negligible, and that all horizontal forces are negligible for a vertical input. Under these assumptions and by applying the force and moment equilibrium to the model shown in Figure 2-20 they extracted the amplification factor shown in eq. 2-8. In this model, F_{in} and F_{out} are the input and output force respectively, L is the length of the lever arm, l is the distance of the output from the pivot, θ is the angle of rotation and δ the axial deformation. The axial stiffness of the output arm and the pivot are K_{vvo} and K_{vvp}, respectively, whereas $K_{\theta mo}$ and $K_{\theta mp}$ are the respective rotational stiffness components.

Removed for copyright reasons.

Please find image on the cited source.

Figure 2-20 a) Force amplifying microlever, b) Model of microlever under loading. Taken from [36].

$$A = \frac{F_{in}}{F_{out}} = \frac{K_{vvo}(\delta + l\theta)}{F_{in}} = \frac{\frac{1}{K_{vvp}}\left(K_{\theta mo} + K_{\theta mp}\right) + lL}{\left(\frac{1}{K_{vvo}} + \frac{1}{K_{vvp}}\right)\left(K_{\theta mo} + K_{\theta mp}\right) + l^2} \qquad \text{eq. 2-8}$$

By finding the relative difference of the ideal amplification factor and the one extracted by the analysis of the structure they defined the amplification coefficient, A^*, shown in eq. 2-9. As can be noted from eq. 2-8 and eq. 2-9, the amplification factor increases as the amplification coefficient decreases.

$$A^* = \left(\frac{1}{K_{vvo}} + \frac{1}{K_{vvp}}\right)(K_{\theta mo} + K_{\theta mp}) \qquad \text{eq. 2-9}$$

As a conclusion, the amplification factor of such a microlever depends on the ideal amplification factor (*L/l*), the geometry of the pivot, and the axial and torsional spring constants of the output system. Finally, it was noted that the largest bending spring constant and the smaller axial spring constant, among the stiffness constants, are those that have the greater influence on the amplification factor.

2.5.5 Dual stage mechanical amplification

Further amplification stages may be used to improve the results of mechanical amplification. In a MEMS device, this can be achieved by stacking microlever structures in a compound assembly. In addition to a higher amplification factor multi-stage microlevers also offer the advantage of a more efficient space occupation. One of the most extensive examples of multi stage mechanical amplification in an inertial sensor is by the authors of [61] who continued the work that they had presented in [36] and extended their structure by implementing two-stage force amplification microlevers. The new amplification factor was simply extracted by the product of the amplification factors of the individual stages. The two-stage amplification mechanism was optimised for a resonant accelerometer using both analytical and FEM methods. The results showed that in order for a two-stage microlever mechanism to provide efficient force amplification the compliance between the two microlevers has to be distributed properly [61], meaning that the microlever stage closest to the output has to be much stiffer in its axial dimension than the one connected at the input. Figure 2-21 presents the designed resonant accelerometer with a dual stage force amplification mechanism.

For this thesis, compound mechanisms were considered but not fabricated since through simulations (Appendix E) it was shown that they add complexity without further improving the sensitivity of a displacement amplifier.

Removed for copyright reasons.

Please find image on the cited source.

Figure 2-21 Schematic of the two-stage microleverage mechanism in a resonant accelerometer. Reproduced from [61].

2.6 Conclusions on the literature review

The design approaches and mechanisms presented in this chapter set the grounds for the implementation of a mechanically amplified accelerometer. From the mechanisms presented, microlevers offer an intuitive design approach and wide application spectrum. Therefore, the design of the mechanical deflection amplifier is based on microlevers. For proof-of-concept, it is sensible to use a simple structure that can be easily modified. The mathematical approach for the initial evaluation and design has to provide means of identifying how different design parameters affect performance. From the analysis presented in this chapter the method presented in [36] provides the most intuitive insight into the mechanism. The reason is that individual device components are distinguished in the equation hence identifying the performance-defining parameters is straightforward. Since in [36] the method is presented for a force amplifier, this has to be amended to be applicable for a deflection amplifier. Therefore, the final equations describing the static operation of the mechanism include the deflection or deformation of each individual part of the mechanism. The deflection parameters are based on the stiffness of each component. This provides a clear view as to which parameter needs to be modified to meet specific requirements. Although topology, shape, and size optimisation techniques may result in an overall better device, the result is a structure that is specific for an application. Furthermore, the complexity of the resulting mechanism constitutes the distinction of individual performance defining parameters and components virtually impossible. This is a point where the design methodology is divided into two approaches. The more traditional approach is based on intuition. The modern approach is based on computer-generated and optimised designs. A middle ground approach is followed in this thesis. This is to base the design on a well-known mechanism, such as a lever, but make the design such that it can be easily optimised by a computer. To achieve that, fully parameterised simulation models of the amplified accelerometer were created. Finally, since the design prototypes are not optimised within a confined space or a specific application, a figure of merit is created to compare them with conventional devices. This is based on the fact that mechanical amplification is implemented with the aim to improve the sensitivity of inertial sensors. The figure of merit is created to compare the deflection of devices of the same natural frequency. This effectively highlights, to a first order, the improvement that a mechanical amplifier brings to inertial sensors as will be shown in the following chapters.

Chapter 3 Microlevers

3.1 Introduction

The mechanical amplifying mechanism for this thesis consists of microlevers. These are considered the most appropriate of the mechanisms presented in the previous chapter, due to their topology, mechanical characteristics, and simplicity. Furthermore, a mechanism based on microlevers has an intuitive structure with a well-understood operation. This is preferred over optimisation-generated mechanisms with a complicated distributed compliance.

Microlevers present similar characteristics to macro world levers, but with a major difference; there is no practical way to produce micromachined bearings. Microlevers are instead constructed using compliant flexures in the place of bearings, with the result that microlevers are classified as compliant mechanisms. The practical difference is that compliant mechanisms present a finite compliance along the operation axis. This results in energy storage along the flexible parts of the mechanism, which is a vital aspect for the operation of the mechanism within an inertial sensor. Taking into account the flexure nature of microlevers, this chapter discusses methods of static modelling for preliminary design evaluation. More specifically, the analysis methods presented are based on the pseudo rigid body method, stiffness model analysis, system level analysis using commercial software, and finally, FEA. For comparison reasons the lever used in all three methods is the same Type 3 microlever.

3.2 Types of microlevers

Microlevers comprise an input, an output, and an anchored pivot. They are able to amplify either force or deflection; these functions are referred to as mechanical and geometrical advantage, respectively. An additional advantage that microlevers offer is inversing the direction of the output respective to the input.

Mechanical advantage can be achieved by trading off displacement for larger force. If the pivot of a microlever is closer to the output than the input, the ratio of the input distance from the pivot versus that of the output is greater than one. This means that the displacement at the output will be smaller than the deflection at the input, but also that the force at the output will be greater than that applied to the input. The amplification factor for an ideal force-amplifying microlever is defined as the ratio of the input versus the output distance to the pivot as in eq. 3-1. Conversely, if the pivot is closer to the input than to the output, the output force will be lower than that applied to the input. In this arrangement the displacement at the output will be greater than that at the input; thus providing geometrical advantage. The amplification factor for the geometrical advantage in an ideal lever is defined as the output versus the input distance from the pivot in eq. 3-2. [62]

$$A_m = \frac{b_m}{a_m} \quad \text{eq. 3-1} \qquad\qquad A_g = \frac{a_g}{b_g} \quad \text{eq. 3-2}$$

There are three types of microlevers that can provide either mechanical or geometrical advantage according to the ratio of the output versus the input distance to the pivot [62]. A microlever is considered a Type 1 lever (Figure 3-1, a.) when the pivot lies between the input and the output. This is the most common type and it can be used for both deflection and force amplification. The second type (Figure 3-1, b.) has its output lying between the input and the pivot and it provides force amplification. Finally, the third kind of microlever (Figure 3-1, c.) has its output lying between the output and the pivot, so that it can only amplify deflection. The three microlever types are shown in Figure 3-1.

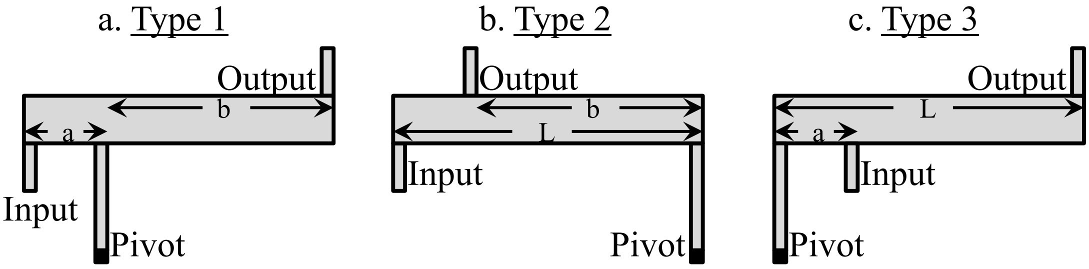

Figure 3-1 The three types of levers: a) Type 1 can amplify either force or deflection since the ratio of *b* versus *a* can be smaller, greater, or equal to 1. It is also an inverting lever since the input always moves in the opposite direction to the output; b) Type 2 can only be used in force amplification since *L* is always greater or equal to *b* and it is non-inverting; c) Type 3 can only be used in deflection amplification since *L* will always be greater or equal to *a* and it is non-inverting.

As this thesis aims to amplify deflection and consequently increase the sensitivity of translational inertial sensors, the microlevers used could be either Type 1 or Type 3. Type 1 microlevers are directionally inversing and thus the output would move in the opposite direction to the input. This is an undesirable effect for an accelerometer because it introduces masses moving in opposite directions. Therefore, Type 3 microlevers were implemented in this thesis. The choice of the type of microlever is further discussed in the next chapter, where its function is more evident when implemented on an accelerometer. The analyses that follow are based on Type 3 microlevers.

3.3 Microlever model analysis

The most common ways to analyse the static behaviour of a microlever and that of a flexure mechanism in general are the loop-closure theory [32], the pseudo rigid body model [18], the inverse kinematic-model [35], and stiffness based modelling [36]. In this thesis, the methods used are the pseudo rigid body method and the stiffness based model analysis. As discussed in Chapter 2 those methods offer simplified models that give a direct insight in the operation of microlevers. The pseudo rigid body method provides precise results for large deflections when the microlever arm is considered rigid. Modelling based on the individual stiffnesses of the components of a microlever gives an intuitive insight on how the different components contribute to the operation of the mechanism, thus it is the preferred method in this thesis.

3.3.1 Pseudo rigid body model

The pseudo rigid body model method can be described by example of a cantilever beam with two segments. If one of the segments is short and flexible (i.e. short flexure pivot), while the other is long and rigid, the mechanism can be described by two rigid links connected at a pin point. This point is called the characteristic pivot and can be any point on the flexible beam as long as this is at least an order of magnitude shorter than the rigid segment, without loss of accuracy. For a moment acting at the end of the rigid segment, the angle of rotation can be found by considering a torsional spring at the centre of the flexural pivot. [18]

Removed for copyright reasons.
Please find image on the cited source.

Figure 3-2 Pseudo rigid body model, *L*>>l in the model the short flexure has been substituted by a torsional spring. Reproduced from [32].

The simplest flexure that this model can describe is the small length flexural pivot. Figure 3-2 shows a short flexure pivot connected to a rigid arm. In order for the analysis to be valid, the short (l) flexible part has to be 10 times smaller than the rigid arm. So if $L >> l$ then the deflection equations for the X and Y axes (δ_x and δ_y) for the flexible segment with a moment M_o at its end are:

$$\theta_0 = \frac{M_o l}{EI} \qquad \text{eq. 3-3}$$

$$\frac{\delta_y}{l} = \frac{1 - cos\theta_o}{\theta_o} \qquad \text{eq. 3-4}$$

$$\frac{\delta_x}{l} = 1 - \frac{sin\theta_o}{\theta_o} \qquad \text{eq. 3-5}$$

In these equations, E is Young's Modulus, I the moment of inertia of the flexible part, and θ_o the angle of rotation. As the flexible pivot is short, the system can be modelled as two rigid links joined at a pin joint. This pin point is called the characteristic pivot and it is located at the centre of the flexure pivot. This point could be any point on the flexure pivot without affecting the accuracy since the deflection occurs at the small flexure and it is small compared to the length of the rigid arm. For this model, the angle of rotation is the same as the angle at the end of the flexure pivot. The stiffness K of this rigid-link is calculated by considering a torsional spring. Thus by modelling the resistance to deflection by the flexible part (eq. 3-6):

$$K = \frac{(EI)_l}{l} \qquad \text{eq. 3-6}$$

This model is not accurate if the bending moment is smaller than the axial or transverse loading. It also assumes that the arm is rigid and so will not give accurate results for flexible bending arms. The pseudo rigid body method is useful for large deflections of rigid arms connected to flexible members. Although investigated and initially used in this thesis, it proved unnecessary since the deflections studied here are at least ten times smaller than the dimensions of the flexures and rigid parts. This method provides precise results for large deflections of microlevers, when the microlever arm is rigid. Therefore, it is referenced at this point for future use in large deflection analysis if this proves necessary.

3.3.2 Static analysis using a model based on stiffness, deflections and deformations

A simple model that can be used in the first steps of the analysis may be constructed using the stiffness of the individual members of a microlever. By employing the free-body diagram method to isolate the different parts of a microlever and finding their deflections and deformations, a model that can describe the overall deflection at every point may be obtained. At this point, the principle of super-position can be used to include the various loads. The following assumptions are made:

a) The input force is always perpendicular to the input
b) The axial deformation of the input arm is not considered
c) Horizontal forces are considered negligible
d) The microlever is anchored at one point and hence it is considered a structurally determinate structure
e) There is no load at the output of the microlever

The deflection of the microlever may then be found by substituting the pivot with a torsional spring representing the angle of the curvature, and an axial spring representing the axial stiffness. The model is schematically shown in Figure 3-3.

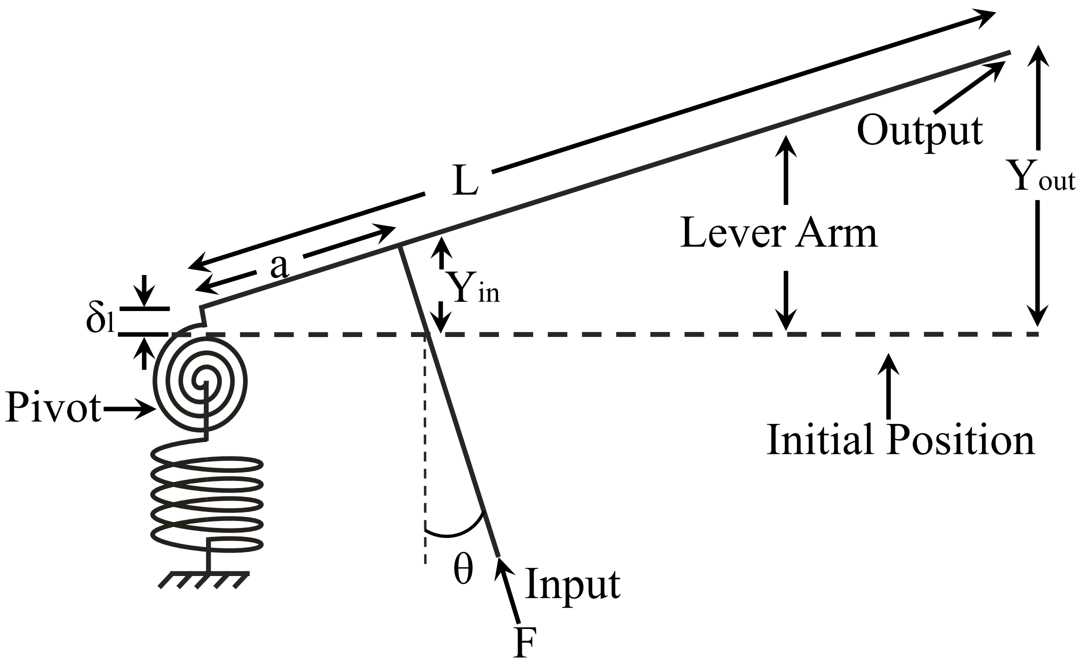

Figure 3-3 Stiffness model for a Type 3 microlever; *a* is the distance from the input to the pivot while L is the distance from the output to the pivot. The pivot has been replaced by a torsional and an axial spring.

Employing the stiffness model that was constructed using the principles of statics and strength of materials theory [63], a first order model of a Type 3 microlever was formulated. The equations used are shown as a Matlab script in Appendix A. This model considers a Type 3 microlever, where the rotational stiffness of the pivot, the axial deformation of the pivot, and the deformation of the arm are taken into account. The angle of rotation is calculated as the angle of the curvature at the point where the pivot is connected to the arm. This is valid as the arm retains its orthogonal position with the end tip of the pivot, at least for small deflections, so that the angle of rotation of the lever coincides with the angle of the curvature at the end tip of the pivot. The deflection at the input and the output can be calculated by the angle of rotation if we consider that the input arm retains its shape with the application of a force.

The resistance of the pivot to rotation is modelled by a torsional spring with stiffness K_{tor}. In order to deflect this torsional spring by an angle θ, a torque T must be applied at the end of the pivot (eq. 3-7). In the case of the Type 3 lever, a force is applied at the input of the lever. This force is translated to a torque through the lever arm, which is initially considered rigid, to the torsional spring.

$$T = K_{tor}\theta \qquad \text{eq. 3-7}$$

According to the Bernoulli-Euler equation, the curvature of a beam with a bending moment M_0 applied at its free end abides by eq. 3-8, where s is approximately equal to the length l of the beam for small angles, E is Young's Modulus and I is the moment of inertia of the beam.

$$\frac{d\theta}{ds} = \frac{M_0}{EI} \qquad \text{eq. 3-8}$$

The angle by which the end of the beam is deflected can be found by integrating the above equation. This gives:

$$\theta = \frac{M_0 l}{EI} \qquad \text{eq. 3-9}$$

This equation gives the bending moment when rearranged:

$$M_0 = \frac{EI}{l}\theta \qquad \text{eq. 3-10}$$

Since the moment at the end of the pivot equals the torque applied, by comparing eq. 3-9 and eq. 3-10, the torsional stiffness of the spring is:

$$K_{tor} = \frac{EI}{l} \qquad \text{eq. 3-11}$$

The moment at the pivot can be found by multiplying the input force with its distance from the pivot.

The axial deflection of the pivot can be calculated by Hooke's Law, as shown in the equations below.

$$\sigma = E * \varepsilon \qquad \text{eq. 3-12}$$

$$\frac{F}{A} = E\frac{\delta l}{l} \qquad \text{eq. 3-13}$$

$$\delta l = \frac{Fl}{AE} \qquad \text{eq. 3-14}$$

Where σ is the stress normal to the pivot cross section, ε the strain along the axis normal to the pivot, F is the applied axial force, A the area of cross section, l the total length of the pivot, and δl the elongation.

The deflection at the input and output of the microlever due to the rotation and axial deflection of the pivot is given by eq. 3-15 and eq. 3-16, respectively.

$$Y_{pout} = L \cdot \sin(\theta) + \delta_l \qquad \text{eq. 3-15}$$

$$Y_{pin} = a \cdot \sin(\theta) + \delta_l \qquad \text{eq. 3-16}$$

Although very small compared to the pivot deformation, the lever arm bending can be included in the model. The deflection of the arm at the output and the input is shown in eq. 3-17 and eq. 3-18, respectively. This deflection is only due to the bending of the arm subjected to an input force F.

$$D_{aout} = \frac{F \cdot a^2 \cdot [2 \cdot a + 3 \cdot (L - a)]}{6 \cdot E \cdot Ia} \qquad \text{eq. 3-17}$$

$$D_{ain} = \frac{F \cdot a^3}{3 \cdot E \cdot Ia} \qquad \text{eq. 3-18}$$

Where D_{aout}, D_{ain} are the deflections of the arm at the output and input accordingly, and I_a is the moment of inertia of the microlever arm. At the end tip of the arm the overall deflection is as shown in eq. 3-19, while at the point where the arm is connected to the input, it is as shown in eq. 3-20.

$$Y_{out} = Y_{pout} + D_{aout} \qquad \text{eq. 3-19}$$

$$Y_{in} = Y_{pin} + D_{ain} \qquad \text{eq. 3-20}$$

An ideal lever presents infinite compliance along its axis of rotation. Due to this infinite compliance, its amplification factor is the ratio of the output distance from the pivot to that of the input, which equals the ratio of the output deflection d_{out} relative to the input deflection d_{in} as shown in eq. 3-21.

$$A_{ideal} = \frac{L}{a} = \frac{d_{out}}{d_{in}} \qquad \text{eq. 3-21}$$

Microlevers are not ideal levers since their pivot introduces stiffness along its axis of rotation. Additionally, the microlever arm is not ideally rigid. For a non-ideal Type 3 microlever, the amplification factor can be derived as the ratio of the output deflection Y_{out} relative to the input deflection Y_{in}. By combining eq. 3-14 to eq. 3-20, eq. 3-22 was derived to describe the amplification factor of a Type 3 microlever using its structural dimensions.

$$A_d = \frac{Y_{out}}{Y_{in}} = \frac{Y_{pout_l} + D_{aout}}{Y_{pin} + D_{ain}} = \frac{L \cdot \sin(\theta) + \frac{F \cdot l}{A \cdot E} + \frac{F \cdot a^2 \cdot [2 \cdot a + 3 \cdot (L - a)]}{6 \cdot E \cdot Ia}}{a \cdot \sin(\theta) + \frac{F \cdot l}{A \cdot E} + \frac{F \cdot a^3}{3 \cdot E \cdot Ia}} \qquad \text{eq. 3-22}$$

A method similar to that applied in this thesis was applied for the force amplifier by [64] and is presented in Appendix B applied to a Type 3 microlever. The model given in eq. 3-22 describes well the deflection of a Type 3 microlever, as a stand-alone deflection amplifier. When a microlever is used in an inertial sensor, the assumption of a following force is not valid (the input force is not always perpendicular to the microlever arm). In addition, when the sensor is subjected to acceleration, the microlever and anything attached to its output are also subjected to acceleration. This affects its deflection and amplification ratio. The later effect can be introduced into the model by including a load at the output of the microlever, as described in the next paragraph.

The model of eq. 3-22 is of a single microlever with a force F applied at its input. The Force F in the model represents the force applied by a proof mass to the lever. When a mechanical structure consisting of capacitive comb-fingers is attached to the output of the microlever an additional force F_C is introduced when the sensor is subjected to acceleration. Force F_C results in additional deflections at the input and the output of the microlever. These are Y_{prinC} and Y_{proutC} due to rotation of the pivot, θ_C, elongation of the pivot, δ_{lC}, and D_{ainC} and D_{aoutC}, due to bending of the arm. Those deflections were derived in a similar manner to the deflections due to the input force F and are shown in eq. 3-23 to eq. 3-28.

$$\theta_C = \frac{F_C \cdot L \cdot l}{E \cdot I} \qquad \text{eq. 3-23}$$

$$\delta_{lC} = \frac{F_C \cdot l}{A \cdot E} \qquad \text{eq. 3-24}$$

$$Y_{prinC} = a \cdot \sin(\theta_C) \qquad \text{eq. 3-25}$$

$$Y_{proutC} = L \cdot \sin(\theta_C) \qquad \text{eq. 3-26}$$

$$D_{ainC} = \frac{F_C \cdot a^2 \cdot (3L - a)}{6 \cdot E \cdot Ia} \qquad \text{eq. 3-27}$$

$$D_{aoutC} = \frac{F_C \cdot L^3}{3 \cdot E \cdot Ia} \qquad \text{eq. 3-28}$$

By including the additional deflections, eq. 3-22 can be refined to the model represented by eq. 3-29.

$$A_{dC} = \frac{Y_{out}}{Y_{in}} = \frac{Y_{prout} + \delta_l + D_{aout} + Y_{proutC} + \delta_{lC} + D_{aoutC}}{Y_{prin} + \delta_l + D_{ain} + Y_{prinC} + \delta_{lC} + D_{ainC}} =$$

$$\frac{L \cdot \sin(\theta) + \frac{F \cdot l}{A \cdot E} + \frac{F \cdot a^2 \cdot [2 \cdot a + 3 \cdot (L - a)]}{6 \cdot E \cdot Ia} + L \cdot \sin(\theta_C) + \frac{F_C \cdot l}{A \cdot E} + \frac{F_C \cdot L^3}{3 \cdot E \cdot Ia}}{a \cdot \sin(\theta) + \frac{F \cdot l}{A \cdot E} + \frac{F \cdot a^3}{3 \cdot E \cdot Ia} + a \cdot \sin(\theta_C) + \frac{F_C \cdot l}{A \cdot E} + \frac{F_C \cdot a^2 \cdot (3L - a)}{6 \cdot E \cdot Ia}} \qquad \text{eq. 3-29}$$

The terms of eq. 3-29 are the deflection components of each building block of the microlever. This allows an intuitive insight into the behaviour of the structure. Furthermore, as can be seen from the results presented in Chapter 4 and Chapter 7, the analytical model closely predicts the amplification factor found by simulations and measurements on the fabricated devices.

When a system of microlevers is implemented in an accelerometer, it constitutes a statically indeterminate mechanism. The analysis of such mechanisms is commonly carried out by the superposition of statically determined structures [63], or by the deflection method [65]. These analyses produce unwieldy equations where the behaviour of individual building blocks is not apparent. For this reason, such an analysis is considered beyond the scope of this thesis.

The amplification factor predicted by eq. 3-29 is higher than the ideal (A_{ideal}). For the parameters given in Table 3-1, a mechanical amplification factor of 38.23 is estimated by eq. 3-29. The deviation of the results from the estimated amplification factor is due to the non-ideal behaviour of the microlever. Two effects are taken into account in eq. 3-29: i) The finite stiffness of the microlever arm, leading to the terms D_{ain}, D_{aout}, D_{ainC} and D_{aoutC}, and ii) the axial deformation of the pivot arm, leading to the terms δ_l and δ_{lC}. The former effect leads to an increase in the amplification factor compared to the ideal; the second to a decrease. For the geometrical parameters in the discussed devices, the combination of the two effects leads to an approximately 4.7% higher amplification factor predicted by eq. 3-29 compared to A_{ideal}.

3.3.3 Analytical evaluation of design parameters for microlevers

With the help of the above equations and by knowing the input force F from a proof mass and the output load F_C from a comb-finger structure, the output deflection and amplification can be easily calculated. Using a Type 3 microlever, such as the one used in the actual devices with the parameters shown in Table 3-1, the deflection at the output for an input force of 18μN and a load of 622nN using the method presented above is 2.439μm.

Table 3-1 Type 3 test lever parameters

Parameter	*Value*
Structure thickness	50μm
Pivot width	10μm
Pivot length	110μm
Input distance from pivot	100μm
Arm length	3650μm
Arm width	50μm
Input force	18μN
Output load force	622nN

The pivot is the compliant feature that defines the amplification and deflection of the microlever mechanism in the model presented. In order to obtain an estimate of how the amplification factor and output deflection changes relative to the pivot width, value sweeps were performed using the analytical model. The graph shown in Figure 3-4 shows the change in the amplification, when the thickness of the pivot varies from 2μm to 15μm, while the graph in Figure 3-5 shows the change of the deflection at the output for the same change of pivot width for the microlever of Table 3-1.

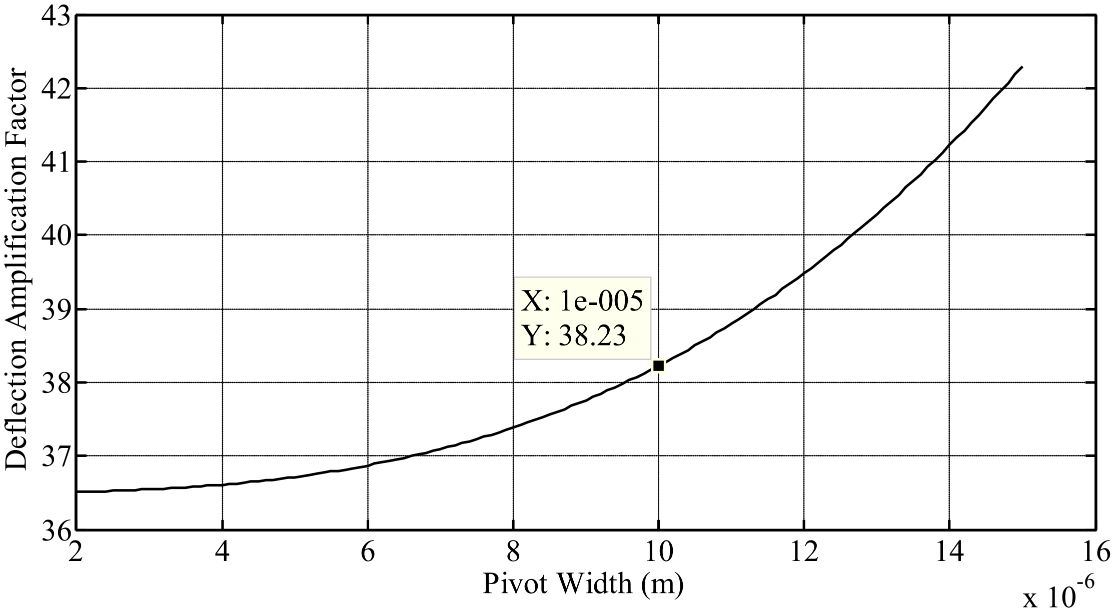

Figure 3-4 Graph based on the analytical model of eq. 3-29 showing the relationship between the deflection amplification factor and the width of the pivot for a Type 3 microlever.

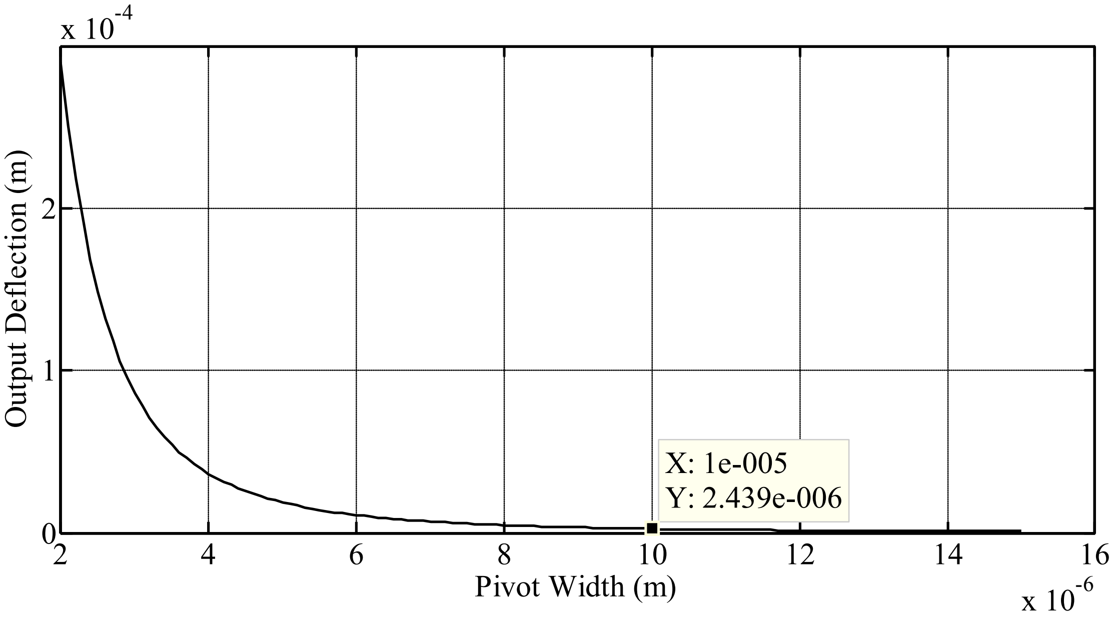

Figure 3-5 Graph based on the nominator of eq. 3-29 showing the relationship between the output deflection and the width of the pivot for a Type 3 microlever.

These graphs reveal that the wider the pivot, the higher the amplification but the lower the output deflection. The change in amplification with the width is very subtle, as shown in Figure 3-6, whereas the change in deflection is affected more as shown in Figure 3-7.

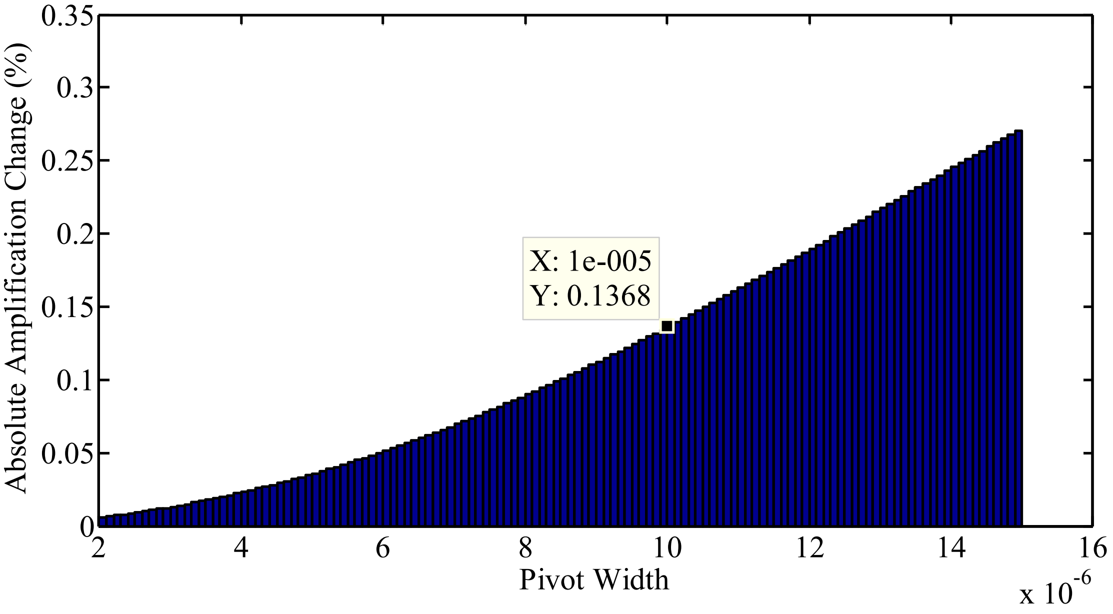

Figure 3-6 Histogram of the percentage of amplification change for width change of 0.1μm.

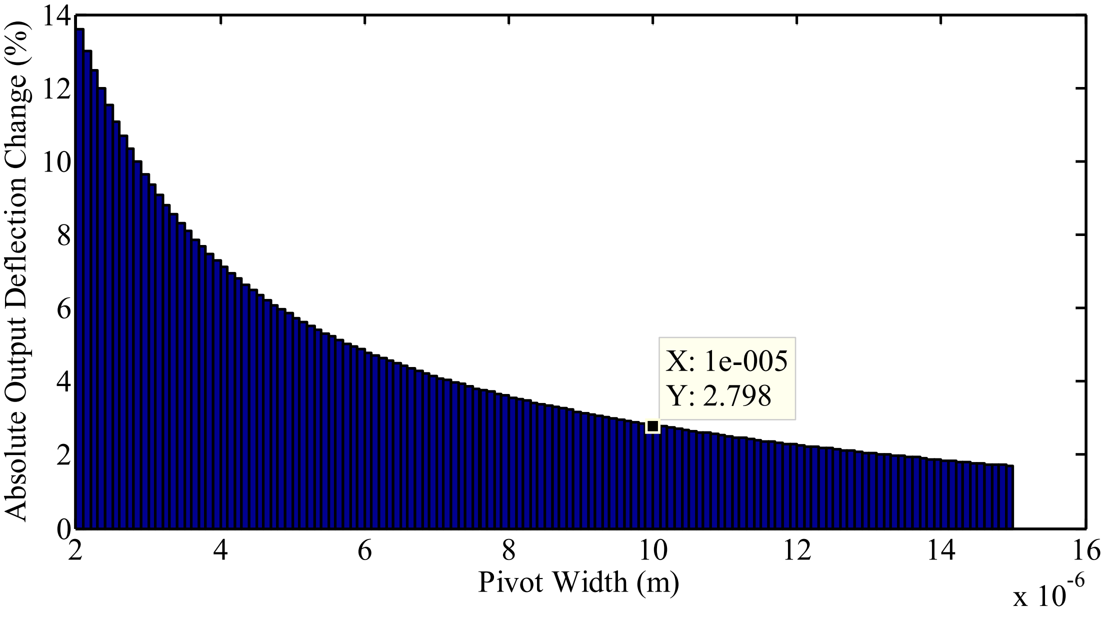

Figure 3-7 Histogram of the percentage of output deflection change for width change of 0.1μm.

The length of the pivot also has an effect on the amplification factor and the output deflection. Plots in Figure 3-8 and Figure 3-9 show the change of the amplification and the output deflection, respectively. As it is shown in these graphs, a longer pivot has similar effects on the amplification factor and output deflection as a narrower pivot. The amplification factor reduction starts to saturate at about 100μm and therefore the choice of a pivot length near this value is considered to give a good compromise between output deflection, amplification factor, and structural rigidity.

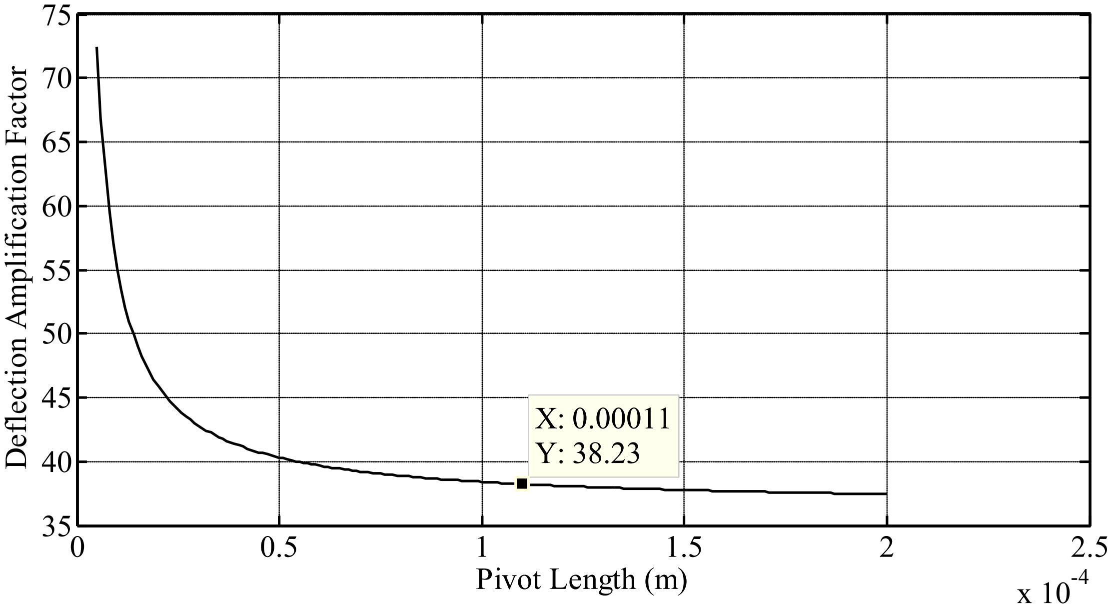

Figure 3-8 Graph based on the analytical model showing the relationship between the deflection amplification factor and the length of the pivot for a Type 3 microlever.

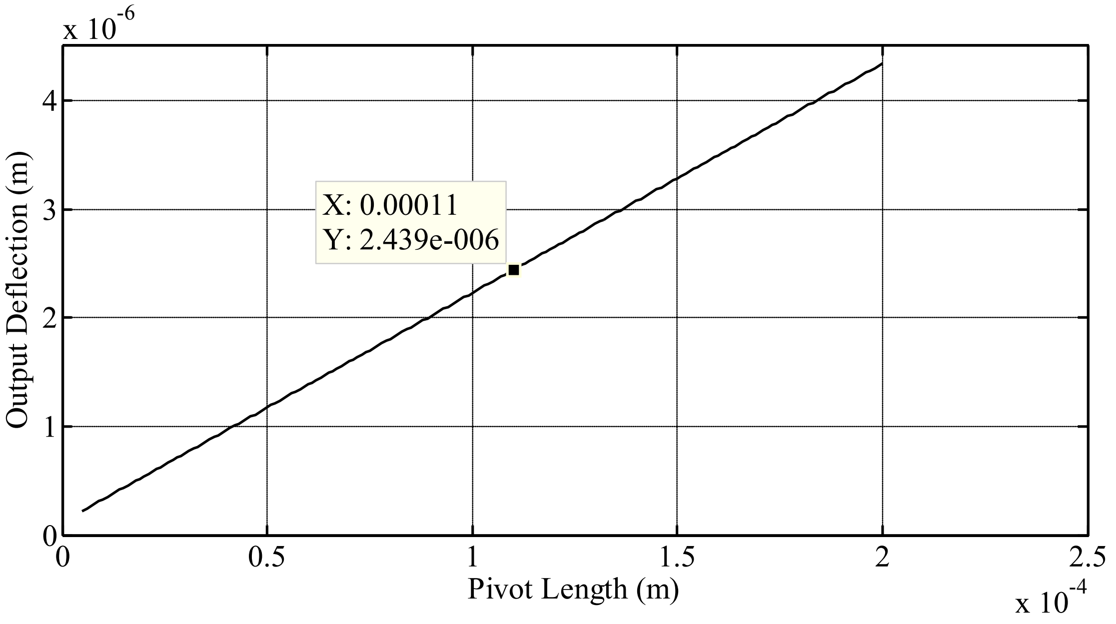

Figure 3-9 Graph based on the analytical model showing the relationship between the output deflection and the length of the pivot for a Type 3 microlever.

The graphs shown in this section present how a change in the pivot stiffness affects the deflection and the mechanical amplification. Although it is evident that a change in the pivot stiffness would greatly affect the deflection of the mechanism, it is not initially apparent why it affects the amplification factor, because this is ideally only related to the geometrical parameters of the arm of the microlever. The reason is that the stiffness of the pivot affects the amplification factor indirectly. In the model of eq. 3-29, an increase of the rotational stiffness of the pivot, by increasing its width w or reducing its length l, results in a subsequent increase of the amplification factor. For a pivot with higher rotational stiffness, bending of the microlever arm has a higher impact on the amplification factor. However, if the bending of the microlever arm is omitted in eq. 3-29, the increase of the rotational stiffness of the pivot by increasing its width, results in a decrease of the amplification factor. This is due to the two components (θ and θ_C) contributing to the overall angle of rotation of the microlever being inversely proportional to w^3, whereas the two components of axial deformations (δ_l and δ_{lC}) are inversely proportional to w. Varying the length of the pivot has a weak effect on the amplification factor, due to the terms $sin(\theta)$ and $sin(\theta_C)$ in eq. 3-29. If the axial deformation of the pivot is omitted as well, the amplification factor will be equal to the ideal regardless of any change in the rotational stiffness of the pivot. This verifies that the stiffness of the pivot does not directly affect the amplification factor. The simulation and measurement results of Chapter 4 and Chapter 7 indicate a higher amplification factor than the ideal. Based on the discussion of this section this is attributed to the low stiffness of the arm of the microlever.

From the initial evaluation of the microlevers presented in this chapter, their structural parameters could be chosen before implementing them with a proof mass. The choice of their structural parameter dimensions was based on the amplification factor and the order of deflections achieved. It has to be noted that the structural parameters are restricted by the fabrication process. Additional restrictions are imposed by the need for a robust prototype that will be easy to interface with and without which tests are bound to fail due to fracture. Those were the specifications that led to the microlever of Table 3-1.

3.4 Static analysis using system level simulations

System level simulation tools use parametric libraries to simulate a given element. The parametric libraries contain models of elements with their behaviour expressed by reduced order equations. This method is advantageous over FEM since there is no need for computing the behaviour of finite elements. The complete model behaviour is simulated and thus the speed and flexibility of the simulations is increased. In this particular thesis, Coventor Architect [66] is used as a system level simulation tool offering the ability to run simulations on variations of the same model. This is particularly useful for the optimisation of the device under development.

For further verification of the validity of eq. 3-29, the same parametric sweeps were run with the model of Table 3-1 implemented in Architect as shown in Figure 3-11, Figure 3-12, Figure 3-13, and Figure 3-14. The model shown in Figure 3-10 is the highly parameterised model used for this verification. A change in any parameter in this model will be reflected in all its elements effectively adjusting them so that the model remains functional. It consists of a reference frame, an anchor, an angled linear beam model, a straight linear beam model, and two constant force elements. The angled linear beam element models the pivot and the arm of the microlever up to the point where the input force is applied. The straight beam element models the arm of the microlever from the point where the input force is applied to the point where the load is applied. In this particular simulation, accelerations and rotations are set to zero in the reference frame. The loads are applied through constant force sources as shown in Figure 3-11.

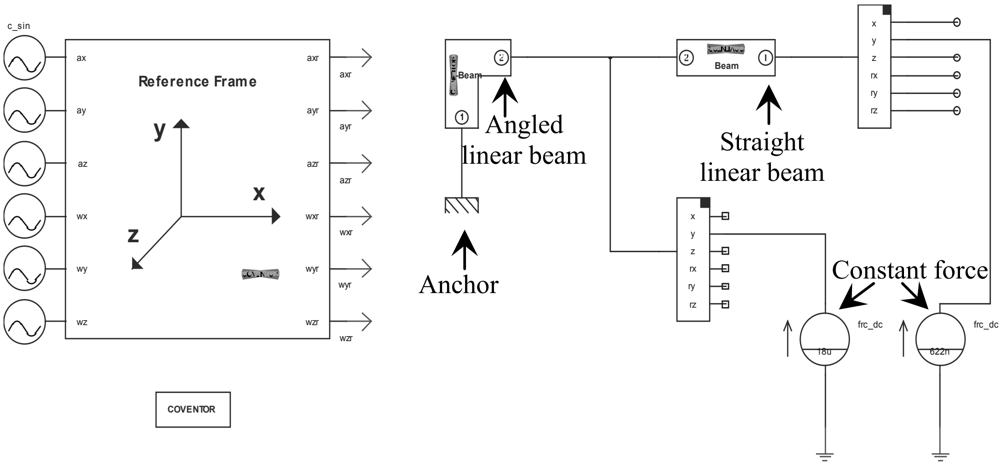

Figure 3-10 Architect model of a Type 3 microlever based on Table 3-1. It consists of a reference frame, an anchor, an angled linear beam model, a straight linear beam model, and two constant force elements.

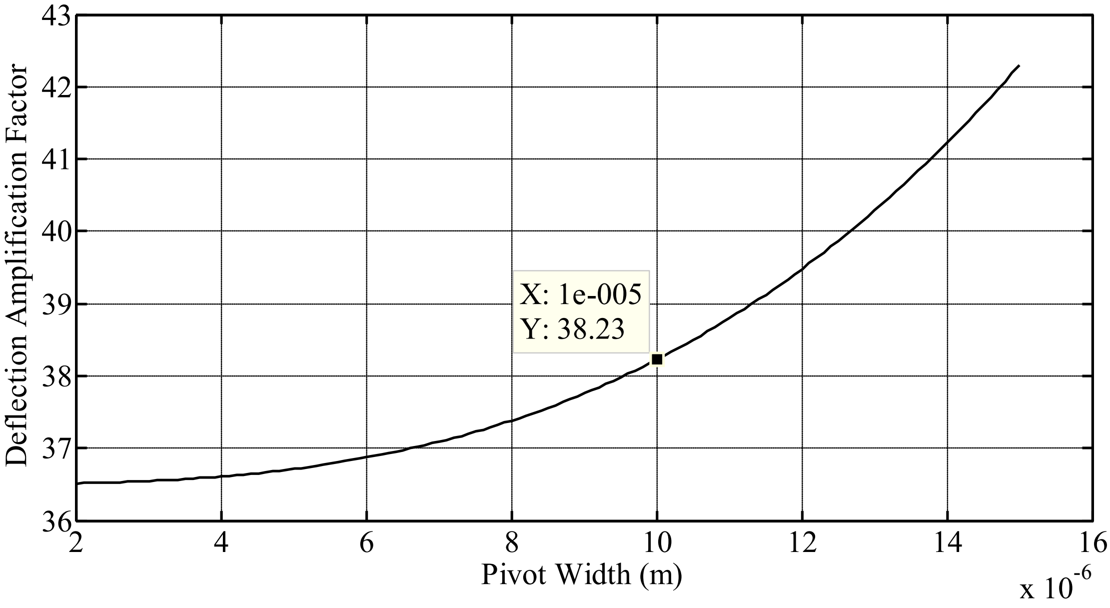

Figure 3-11 Graph produced using the parametric model defined in Architect showing the relationship between the deflection amplification factor and the width of the pivot for a Type 3 microlever.

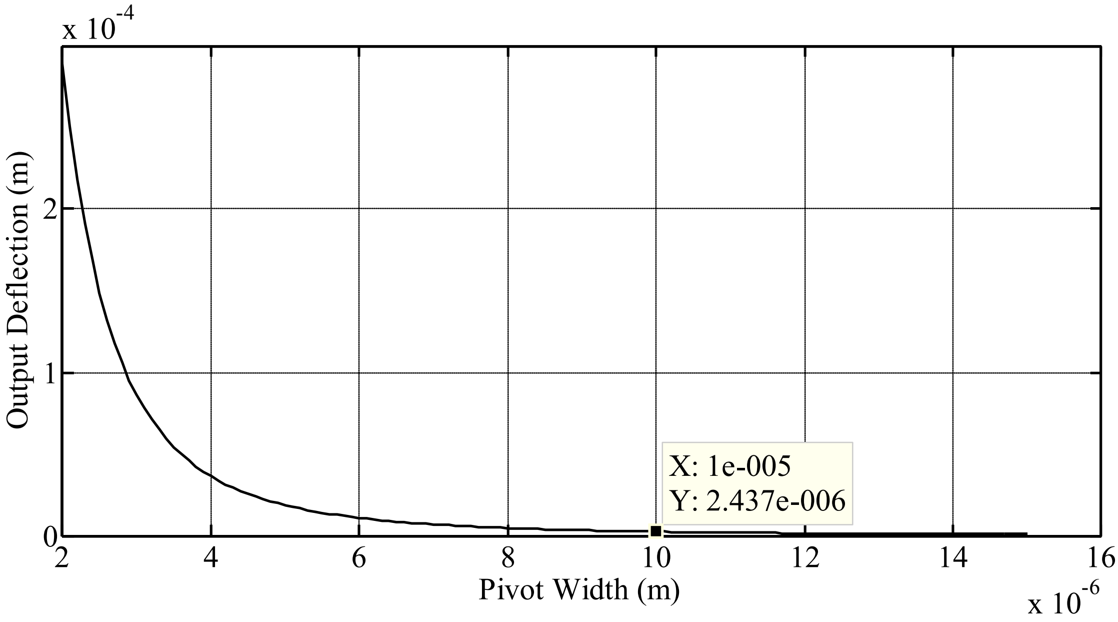

Figure 3-12 Graph produced using the parametric model defined in Architect showing the relationship between the output deflection and the width of the pivot for a Type 3 microlever.

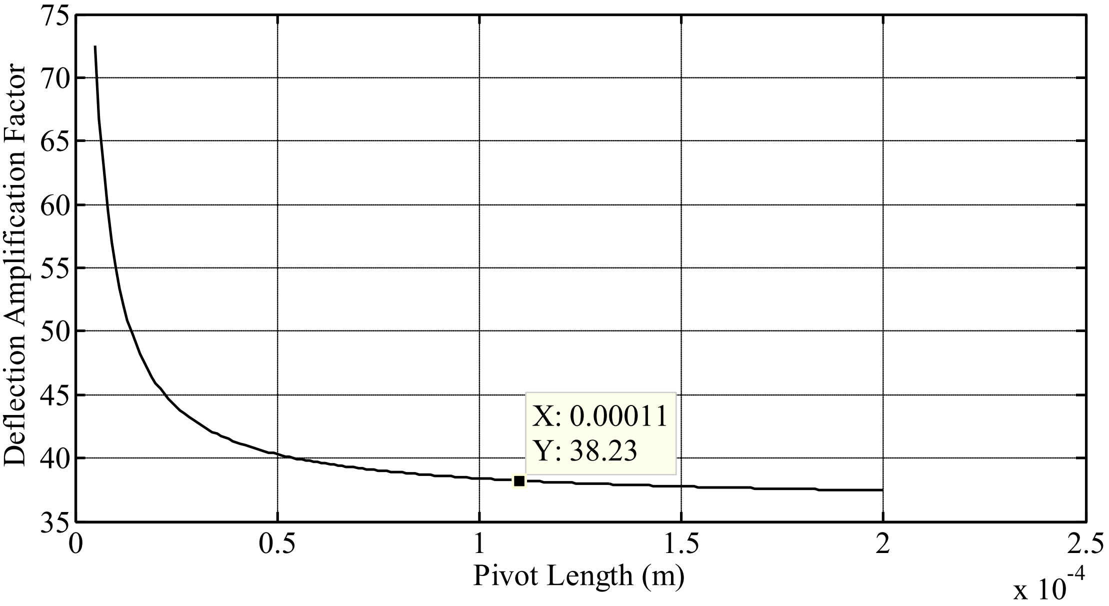

Figure 3-13 Graph produced using the parametric model defined in Architect showing the relationship between the deflection amplification factor and the length of the pivot for a Type 3 microlever.

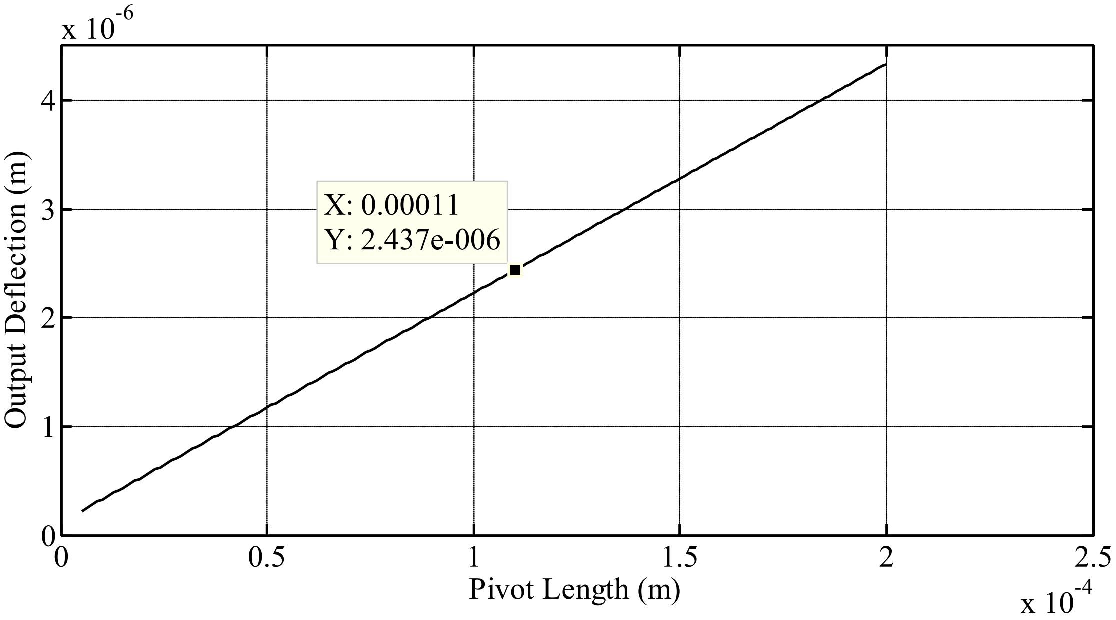

Figure 3-14 Graph produced using the parametric model defined in Architect showing the relationship between the output deflection and the length of the pivot for a Type 3 microlever.

As can be seen by the comparison of the figures above to the graphs obtained by the analytical model, the latter matches the results of the parametric model made in Architect. This proves that the derived equations for the Type 3 microlevers are accurate and can be used to obtain fast results.

3.5 Type 3 microlevers FEM static analysis

Coventorware was used to perform a comparative finite element analysis on the microlevers. The model of Table 3-1 was designed and a 3-dimensional model was built such as the one shown in Figure 3-15. In order to apply forces on the FEM model an input and an output arm had to be implemented. The introduction of the small arms was needed to provide the surfaces that the loads were applied. To avoid introducing more deformations into the model, which are not included in the analytical and system analysis model the arms were designed to be 1μm long and 2μm wide. A linear Manhattan mesh geometry was used for the model. The results showed 2.408μm deflection at the microlever output and an amplification factor of 38.8. The analytical model results deviate less than 1.5% from the FEM model. This proves that the analytical model describes the microlever behaviour under load accurately.

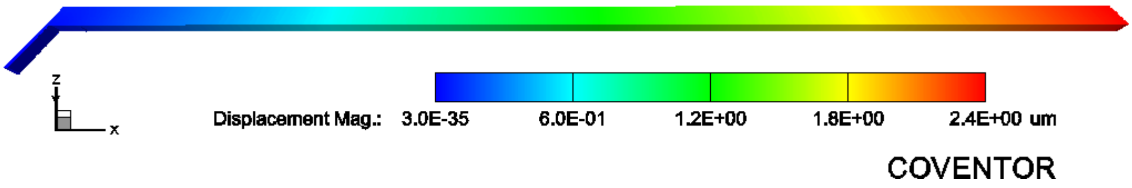

Figure 3-15 FEM model of a Type 3 microlever. The microlever was loaded with a 18μN force at the input arm and a 622nN force at the output. The results from the simulation show a 2.408μm deflection at the output of the microlever and an amplification factor of 38.8. The results from the FEM are in agreement with the analytical results within 1.5%.

3.6 Dual stage compound levers evaluation

In order to investigate the application of compound microlevers consisting of two levels of amplification, different combinations of microlever types were compared using FEM simulation. The results from this comparison are presented in Appendix C. Since Type 3 microlevers prove to have the highest amplification when combined in multiple stages, these were chosen for the subsequent designs. In order to investigate how the different components of these affect the amplification factor, sweep simulations were performed using system level simulations. The results are shown in Appendix D. Appendix E presents a preliminary study on the application of mechanical amplification in micromachined accelerometers using dual stage microlever systems. The added complexity and results from this study did not justify the improvements that dual stages might bring; hence, the devices were not further assessed or fabricated.

3.7 Conclusions in the analytical evaluation of microlevers

The analytical evaluation of microlevers has proven vital for the preliminary study of their use. The analytical model presented in this chapter describes the deflections and amplification factor of microlevers accurately matching system level and FEM simulations. The analytical model can be used to obtain optimal values for the pivot dimensions by running value sweep or optimisation algorithms according to the application. The description of a mechanical amplifier consisting of several microlevers implemented on an accelerometer proved to produce unwieldy equations, therefore, for the subsequent evaluation, FEM and system level simulations are employed. One of the most important outcomes of this chapter is the description of the dependency of the output deflection and amplification factor to the overall stiffness of the mechanism. The pivot stiffness defines the compliancy of the mechanism. Ideally, the amplification factor is the ratio of the output over the input distance from the pivot. In reality though, it is indirectly related to the stiffness of the pivot. When structural components such as the arm of the microlever deform, the amplification factor deviates from the ideal ratio. This effect is more prevalent when the pivot is stiffer, as its deflection becomes comparable to the deformation of the arm.

Chapter 4 Mechanically amplified capacitive accelerometers

4.1 Introduction

As seen in the previous chapters, mechanical amplification is a very promising scheme that may offer improvements in important aspects of MEMS devices. This thesis explores these potential improvements for capacitive inertial sensors. Since capacitive inertial sensors rely on displacement to produce an output, their sensitivity is limited by the amplitude of the deflection of their sensing elements along the sense axis. Achieving a higher deflection by amplifying it, can improve the output signal level; thereby reduce the gain requirements for the interface circuit. This effectively results in a reduced noise floor, as the mechanical amplifier, unlike electronic signal amplification, to first order approximation does not actively add noise. Through this approach, a higher SNR compared to a conventional accelerometer can be achieved. Figure 4-1 presents a conceptual block diagram of an accelerometer with a mechanical amplifier acting between the accelerometer sensing element and the electronic interface. Electronic noise is introduced after the mechanical amplifier and thus is not amplified by it. As the device is realised using bulk micromachining, Brownian noise typically is lower than electronic noise. Therefore, the additional mechanical amplifier does not significantly alter the overall noise level at the output.

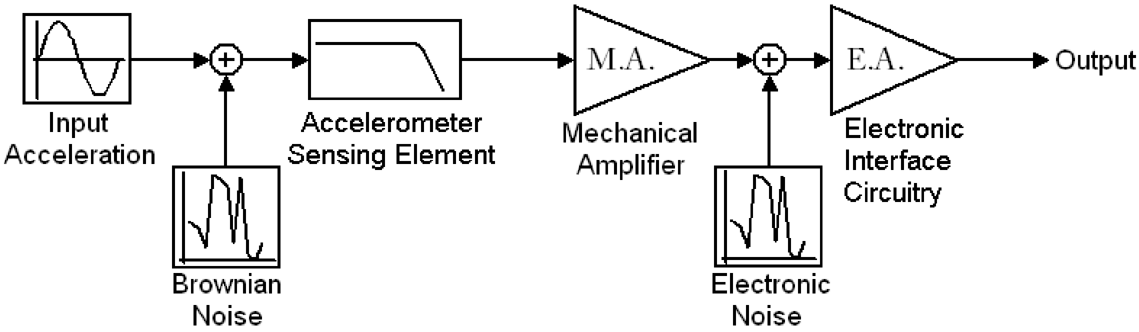

Figure 4-1 Block diagram showing a conventional accelerometer sensing element with an additional mechanical amplification stage. The mechanical amplifier enhances the deflection of the comb-fingers by the M.A. (Mechanical Amplification) factor, while the electronic circuit amplifies the signal picked-off from the comb-fingers by the E.A. (Electronic Amplification) factor. The electronic noise introduced by the interface circuit is not amplified by the mechanical amplifier.

Considering the promising improvements that mechanical amplification may provide, this thesis aims to explore their usage in inertial sensors. The concept of displacement amplification is evaluated through its implementation with single axis capacitive accelerometers. Various structures were designed and simulated including single and dual stage mechanical amplifiers. This chapter discusses the most successful designs. The four designs presented here implement two amplification factors an order of magnitude apart. Two of the designs include an out-of-plane motion suppressing mechanism. The results from the analysis in Chapter 3 on microlevers are used here as a guide for the design of the structural parameters of the mechanism. The ultimate goal of this thesis is to provide a generic framework for the application of mechanical amplification using microlevers in inertial sensors. This also allows the application of mechanical amplification to more sophisticated sensors, such as gyroscopes.

4.2 Assembly of an amplified accelerometer

As mentioned earlier, four different accelerometer designs will be presented in this chapter. In the following, these are referred to 1HAN (high amplitude, no springs), 2LAN (low amplitude, no springs), 3HAS (high amplitude with extra springs), and 4LAS (low amplitude with extra springs). The difference between 1HAN and 2LAN is that the lever ratio, and therefore the mechanical amplification, in the former is an order of magnitude higher than in the latter. The reasoning behind choosing these two different designs was to evaluate how the amplification ratio can affect the overall stiffness and the overall output deflection of the device. The difference between 3HAS and 1HAN, and 4LAS and 2LAN is the inclusion of an out-of-plane motion suppressing mechanism implemented by four folded springs. Those are 800μm long and 5μm wide, yielding an overall stiffness of 4.12N/m. All other structural parameters are the same for all four designs. For brevity, in the following the design parameters will be presented only for 1HAN.

The results from the analysis of the microlevers presented in the previous chapter provide a good foundation to start building an accelerometer that uses microlevers as an amplifying mechanism. The device comprises a system of microlevers, a proof mass, and comb-fingers. This section starts by describing the individual components of the mechanically amplified accelerometer. Following this, it presents the assembled design, and, finally, concludes with a discussion on individual performance-defining elements of the design.

4.2.1 Microlevers design for a capacitive accelerometer

In non-resonant capacitive accelerometers, the higher the deflection at the capacitive readout stage for a given acceleration, the larger the signal for this acceleration is. The purpose of the microlever is to amplify the proof mass deflection in order to achieve a higher deflection at the capacitive output of the accelerometer. Type 1 and 3 microlevers can amplify deflection while Type 2 ones can only amplify force.

Whilst Type 1 levers are probably most frequently used in macro-world devices, they have a fundamental disadvantage in an inertial sensor. This is mainly due to the respective direction of motion of the input and output of the lever but also due to the direction of motion of the mass of the lever. Type 1 levers are inverting the motion so that the output moves in the opposite direction of the input (inverting function). In an amplified capacitive accelerometer, the proof mass would be connected to the input of the microlever making it deflect under acceleration. This deflection would be amplified through the microlever and measured at its output. In order to capacitively pick-off the motion a comb-finger structure has to be connected at the output of the microlever. The comb-fingers add substantial mass to the system. As Type 1 levers invert the motion, if applied, the system would have two masses moving in opposite directions in the same inertial frame. The effective mass of Type 1 levers also adds to this effect, as the larger part of the lever moves in the opposite direction to the direction of motion of the proof mass.

The topology of a Type 3 microlever is much more suitable in this case, since the entire mass of the lever and any mass connected to its input and output move in the same direction. For this reason, Type 3 microlevers are chosen to compose the amplifying mechanism of the accelerometer.

4.2.2 Proof mass of the accelerometer

The choice of the proof mass is straightforward. It should be as large as the design specifications allow, for example determined by the out-of-plane stiffness, and overall chip size. This will provide adequate force to the input of the microlevers when it is subjected to acceleration. It has to be noted that very large proof masses (larger than 5000 x 5000μm^2) are difficult to fabricate, introduce high stress and are not a viable solution for MEMS devices. This was verified during experimentation with fabricated large proof masses. It was found that large proof masses (larger than 5000 x 5000μm^2) tend to bend or warp severely affecting the operation of the sensors.

Normally, the proof mass of inertial sensors is suspended through anchored beams acting as springs that provide compliance along the desired axis. In the devices presented in this thesis, however, springs would add unnecessary stiffness and reduce, to some extent, the effect provided by using microlevers. Considering this, the proof mass was chosen to be suspended solely by four microlevers, thus preserving the symmetry and avoiding the use of springs.

The proof mass size was determined based on three basic requirements; it needs to be large enough, without inducing high stresses, and able to accommodate a large number of comb-fingers and long microlever arms. Its shape can be contained in a 4500x4750x50μm^3 cuboid. It comprises 14524 hexagonally arranged round etch holes for release. The diameter of the holes is 20μm and overall they reduce the mass by 20.4%. The designed effective mass including the mass of the attached comb-fingers is 1.9mg. This is further reduced due to over-etching during fabrication to 1.8mg.

4.2.3 Comb-fingers for capacitive pick-off design

Differential parallel comb-finger mechanisms are chosen to capacitively measure the motion of the accelerometer. Their design and number not only defines the nominal capacitance of the system but also the damping. Eq. 4-1 gives the capacitance C between parallel plates of overlap area A and separation d, where ε_0 is the permittivity of free space and ε_r the relative permittivity of the dielectric.

$$C = \frac{\varepsilon_0 \varepsilon_r A}{d} \qquad \text{eq. 4-1}$$

According to eq. 4-1, the larger the overlap area of the plates and the smaller the distance between them, the higher the capacitance is. Although the gap between the parallel plates is inversely proportional to the nominal capacitance, for a small perturbation $x<<d$, as shown in eq. 4-2 it is the square of the gap that is inversely proportional to the change in capacitance, ΔC:

$$\Delta C = \frac{\varepsilon_0 \varepsilon_r A x}{d^2} \qquad \text{eq. 4-2}$$

This leads to the initial conclusion that the gap between the parallel plate comb-fingers should be minimum. As can be seen in eq. G-4 of Appendix G (or its simplified form eq. G-5), damping is directly proportional to the length and to the cube of the width of the comb-fingers, while it is inversely proportional to the cube of the comb-finger gap. Damping is generally considered one of the most difficult to determine parameters, due to its high dependence on many different structural and environmental parameters. During the preliminary design stage of the accelerometer, gaps as small as 4μm were used. This resulted in very high damping values as discussed in Appendix G where a study on damping is presented. The designs presented here use a gap of 10μm for the comb-fingers. This produces a relatively low nominal capacitance, but it also ascertains that the device will not be over-damped. In fact, even if the damping coefficient predicted is an order of magnitude different from the actual value, the device will still operate in the under-damped region. Comparison of the measurement results to the predicted values gives a better insight to further optimise the ratio of nominal capacitance and damping.

The large gap also facilitates another aspect of the device. Having a large gap at the output comb-fingers of the device allows for large motions. This is very important since large amplification factors could be implemented, and the motion of the proof mass would still be measurable. In large amplifications, the proof mass moves much less than the output (a maximum of 40 times in the current designs). The test equipment used in this study is limited to the minimum motion it can detect. Hence, a large gap at the output comb-fingers would also allow the proof mass to move more and be measured by the measurement tools.

The overall number of comb-finger pairs at the output, determined from the available space, is 304 (both differential sides) with a length of 200μm and overlap of 190μm. In early-fabricated prototypes, it was found that long and thin comb-fingers bent when electrostatically excited. This dictated their size. Comb-fingers were also implemented at the proof mass for comparative signal pick-off; those contribute to the overall damping, but not to the overall amplified output capacitance. They share the same dimensions as the output comb-fingers but their number is approximately half (148).

4.2.4 Mechanical amplification in capacitive accelerometers

As shown in Figure 4-2, four symmetrically arranged microlevers were used for the amplifying mechanism, in order to preserve a symmetrical design. The pivots of the microlevers were anchored at the anchor points of the chip. The input arms were connected to the proof mass while the output arms were connected to comb-finger structures. Since the proof mass is connected to the microlevers and the microlevers are anchored, the proof mass can be suspended by them without the need of additional springs. This has to be considered carefully to minimise tilt motion. Nevertheless, the suspension design is different to traditional springs. Due to the long nature of the microlevers, if the proof mass was to be suspended by its four corners the device would be very large with a very poor design space occupation. In the designs considered here the proof mass is suspended through four points that are close to a line along the sense axis that passes through the centre of the proof mass. This arrangement allows higher amplification factors to be achieved and provides a much denser space occupation. The main disadvantage imposed is that, in this way, the proof mass has a lower rotational stiffness leading to out-of-plane tilt motions. A further issue is, since compliant links are used, the microlevers are compliant in-plane, but also out-of-plane. Therefore, although tilting is in the out-of-plane direction, it will effectively be amplified by the ratio of the microlever. The differential amplifier of the pick-off circuit will reject the common mode out-of-plane motion for a static acceleration. In dynamic operation though, the sensitivity will be modulated by an out-of-plane motion as the nominal capacitance changes. This means that measurement values in the time domain will have a different scale factor when the sensor is subjected to an out-of-plane acceleration.

The overall designed structure comprises a proof mass, which provides the input deflection to the microlevers, a system of four microlevers that are used to amplify the deflection of the proof mass and suspend it, and a system of parallel differential comb-fingers that provide the capacitive output of the sensor. Figure 4-2 illustrates the structure of the single-stage amplified accelerometer.

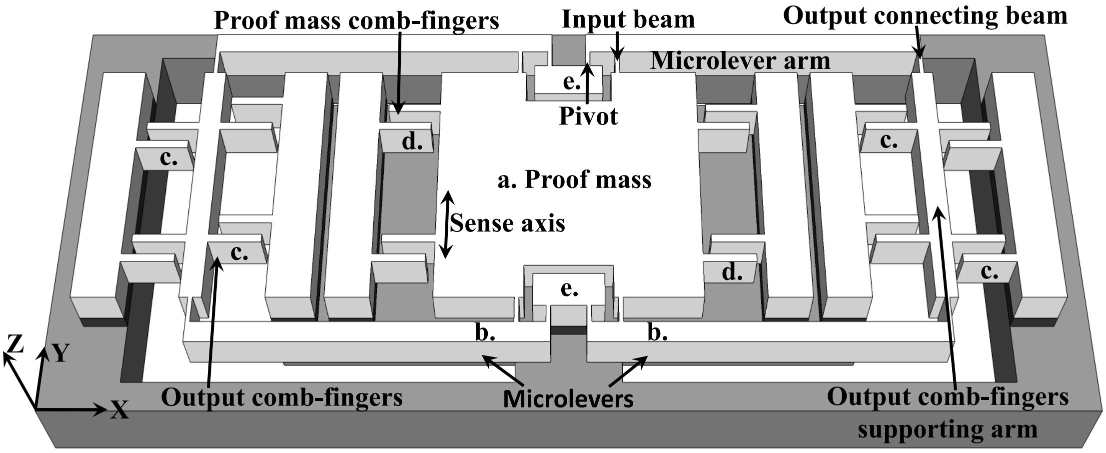

Figure 4-2 Schematic of the single stage mechanically amplified capacitive accelerometer showing. a.) Proof mass, b.) Microlevers, c.) Output comb-fingers, d.) Proof mass comb-fingers, e.) Anchors. The direction of motion is along the Y-axis.

As it can be seen in Figure 4-2 the device also contains comb-fingers attached to the proof mass (Figure 4-2 d.). The comb-fingers at the proof mass can be used for feedback when the accelerometer operates in closed loop operation. In the current study, they were used for comparative signal pick-off. This function is vital in the proof-of-concept since it is used to measure the input deflection, which can then be compared to the output deflection and hence gives an evaluation for the gain of the mechanism.

4.2.5 Design of the individual performance-defining structural parameters

The static analysis of the microlevers presented in Chapter 3 provided an estimate for the size of the microlever components. Those were then implemented with the proof mass and the output system, while they were optimised using both analytical and FEM results. Since the amplification factor of a microlever depends on the stiffness of its elements, those had to be optimised. At the same time, they also had to comply with the limits of materials and fabrication process. Initial design parameters were pushed to the limits of the employed fabrication process. Although this is safe for a well-known design, it could result in serious issues for an experimental prototype. The sensors were later redesigned to have more relaxed geometrical parameters. Therefore, the presented designs do not achieve the maximum potential of the approach. Nevertheless, they are suitable for proving the concept and robust enough to withstand rigorous testing.

The equations from the previous chapter imply that the pivots rotational stiffness has to be as low as possible in order to gain higher deflections. The thickness of the structure was defined by the structural layer thickness of the SOI wafers used in the fabrication process (which is 50μm). The length and width of the pivots were optimised for the mechanical amplifier. Evidently, the most important parameter between those two is the width of the pivot, since rotational stiffness is proportional to the width cubed. A pivot with narrower width delivers higher rotational compliance and therefore larger deflection at the output. For this reason, it has to be as narrow as possible. The width of the minimum feature size is restricted by the aspect ratio that the fabrication process can achieve. Considering that in a Deep Reactive Etching (DRIE) process, aspect ratios up to 20:1 are easily achieved, the aspect ratio was conservatively chosen to be 10:1. The minimum feature size for a SOI wafer with a structural layer of 50μm and a DRIE aspect ratio of 10:1 is 5μm. As mentioned earlier, in order to achieve a sensor of good structural rigidity and, where possible, increase out-of-plane stiffness, the pivot width was designed to be 10μm throughout all working designs. Through parameter variation simulations performed with Coventor Architect, the length of the pivots was designed to be 110μm long. This length proved to give the best compromise between sense axis compliancy, out-of-plane stiffness, and rigidity. The thickness of the input arm that connects the proof mass to the amplifying mechanism has the same thickness as the pivot, while its length is 150μm, designed through parameter variation.

The output deflection of the accelerometer is measured by the change in capacitance of differential comb-fingers. These comb-fingers have to be rigidly connected at the output of microlevers. The motion of the microlevers follows an arc with a maximum length at the amplified output of the microlevers. This arc is part of a circular motion and for this reason it has components along both in-plane axes. An infinite compliance of the mechanism connecting the microlevers to the output comb-fingers would alleviate this issue. Such a mechanism would have to be implemented using bearings that are unsuitable for MEMS devices. Since bearings cannot be used in this design, in order to keep the cross-axis motion low and at the same time the compliance along the sense axis high, the connecting beam between the output of microlevers and the comb-fingers has to ensure a low rotational stiffness. To achieve that, the connecting beam was designed to be 5µm wide. The cross-axis motion is reduced since the comb-fingers structure is connected at both ends perpendicular to the sense axis at the output of the microlevers thus suppressing any circular motion. In contrast to the pivot and the input arm the output arm does not affect the out-of-plane motion. Therefore, reducing its width will not adversely affect the performance of the device. It was shown through simulation that reducing the thickness of the output arm not only reduces the rotational motion, but also greatly increases the output deflection. An example for the remaining rotational motion is given for a deflection of 626nm (which is the deflection of the microlevers output for 1g acceleration obtained by FEM for the design 1HAN): the difference of deflection for two comb-finger tips from opposite sides is only 6pm, which can be neglected for all practical considerations.

4.3 Operating principle of the mechanically amplified capacitive accelerometer

The operation of the accelerometer is as follows: When the sensor is subjected to acceleration along its sensitive axis (Y-axis in Figure 4-2) the proof mass is displaced along the same axis. This motion is amplified and transferred to the output through the microlevers. Each pair of microlevers has its output connected to a differential comb-finger stage, where the amplified motion can be capacitively measured. This configuration allows amplification of the proof mass deflection through the microlevers, with a ratio defined by the design geometry parameters.

4.4 Simulations of the mechanically amplified capacitive accelerometers

The sensors were simulated using commercially available FEM software and system level simulation packages. Although various simulation programmes were tried, the final simulations were carried out using Coventor suite [66]. The simulation designs were implemented in Tanner L-Edit [67] in which the photolithography masks were also designed. Coventorware allows FEM simulations to be crosschecked with its system level simulator, Architect. It also offers means to verify the electrostatics and damping calculated analytically using simulation tools.

4.4.1 Mechanical simulations

As mentioned earlier, the devices were simulated using two methods; FEM and system level simulations. Although the simulations were run simultaneously, the FEM will be presented first, followed by the system level and a comparison of their results.

The designs had to be modified to comply with FEM simulation restrictions. Comb-fingers are small structures in high numbers that would render the simulations computationally too intensive. For this reason, their mass was lumped at the proof mass and amplified output mechanism. Similarly, as etch holes would make the simulation impractical, they were combined in 9 larger holes distributed along the proof mass. The anchors were omitted and the boundary condition “fixed” was set at the edges of the anchored features. One of the most crucial elements to be optimised for an FEM simulation is the size and type of the mesh. A linear (non-parabolic) Manhattan geometry was chosen. This geometry provides accurate results for linear bending problems. The size of the individual elements was chosen to be 50 x 50 x 50μm^3 with a minimum of 4 features along the X-axis, 20 features along the Y-axis, and 1 feature along the Z-axis of any element. Finer meshes were found to give converging results at an exponentially longer time. After a thorough mesh study, this geometry was found to give the best ratio of accuracy versus time. The large 50 x 50 x 50μm^3 features are mainly used for the proof mass, where fine elements are not necessary. The directives for minimum features along the X and Y axes ascertain that there will be 4 elements along the width and 20 along the length of the pivot and the input/output arms. Those are the most compliant elements and for this reason they need to be simulated with the highest accuracy. It must be noted that since the simulations are mostly concerned with simple in-plane linear bending, the mesh does not need to be fine along the Z-axis. Thus, the mesh elements were set to have the wafer thickness size. Figure 4-3 shows the simulation model of 1HAN used in Coventorware.

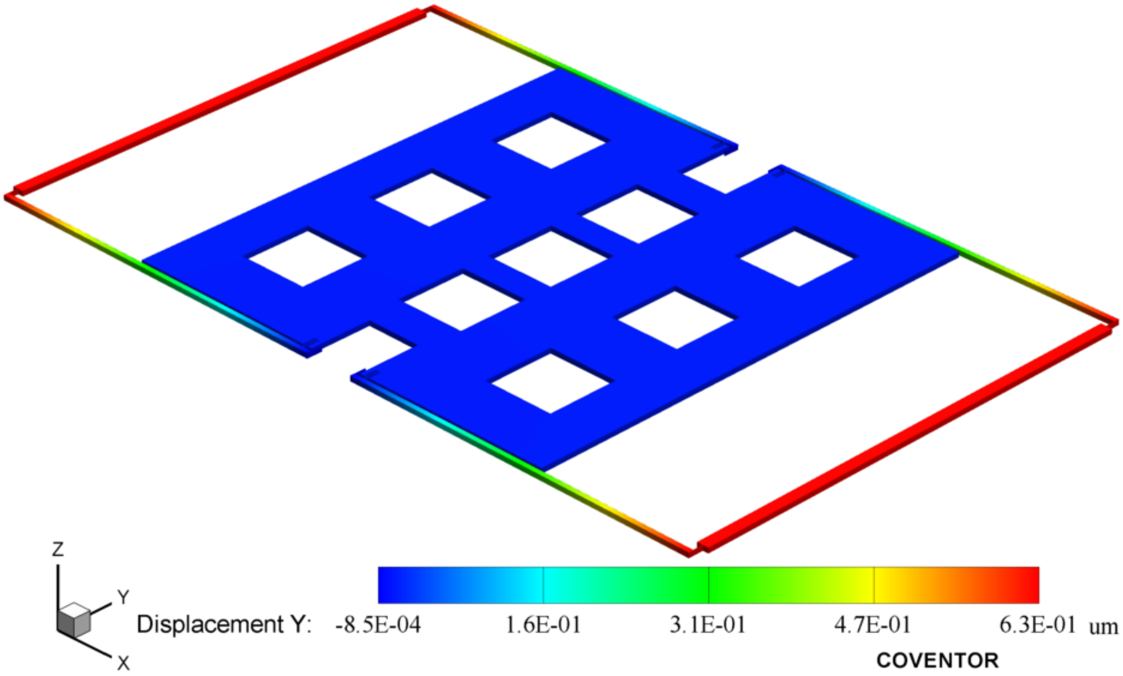

Figure 4-3 FEM simulation example for the 1HAN design. This is the result from a static simulation where 1g constant acceleration was applied at the accelerometer. The colour bar shows the amplitude of the in-plane deflection of the accelerometer.

Architect is a system level simulation tool built on top of Synopsys Saber [67] with a set of parametric libraries. The Architect libraries include electromechanical, magnetomechanical, damping, optical, and fluidic parts. With these building components, the user may synthesise a MEMS device by defining parameters and connecting different components rather than designing from scratch. This gives the ability to run highly accurate simulations much quicker than FEM. Parametric studies, and interfacing with an electronic system are additional advantages of system level simulations. Architect was used to simulate the mechanically amplified accelerometers in addition to FEM. Its ability to run parametric sweeps on structural values was employed to optimise the accelerometers. Figure 4-4 shows one of the models used. This model includes all the mechanical components of the device, including comb-fingers and, as will be shown in Chapter 6, it can be directly connected to a pick-off circuit model. The results from the simulations are shown in Table 4-1, Table 4-2, Table 4-3, and Table 4-4 in comparison to the results from the FEM simulations. The tables show the deflection of the proof mass and the amplified output for 1g constant acceleration. The maximum deflection for 1g along the three axes is always at the amplified output in all sensors and is included in the tables. Finally, the first three bending modes of the sensors are presented for the two methods of simulation.

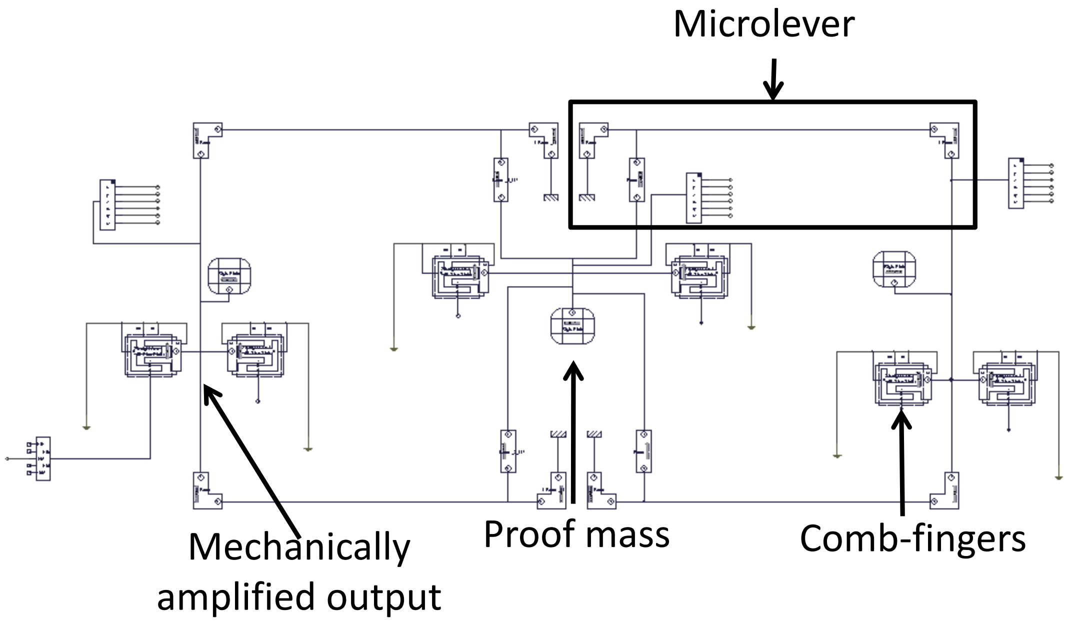

Figure 4-4 Architect system level model of the 1HAN mechanically amplified accelerometer. This model can be directly coupled with electronics to give results from the entire micro-electro-mechanical system.

Table 4-1 FEM and system level simulations results for the 1HAN accelerometer

Property	***Value FEM***	***Value Architect***
Proof mass deflection for 1g (sense axis)	15nm	16nm
Amplified deflection for 1g (sense axis)	626nm	640nm
Maximum X deflection for 1g	21.5nm	2nm
Maximum Y deflection for 1g	627nm	640nm
Maximum Z deflection for 1g	415nm	521nm
Mode 1	740Hz (in-plane)	731Hz (in-plane)
Mode 2	786Hz	806Hz
Mode 3	914Hz	----

Table 4-2 FEM and system level simulations results for the 2LAN accelerometer

Property	***Value FEM***	***Value Architect***
Proof mass deflection for 1g (sense axis)	504nm	515nm
Amplified deflection for 1g (sense axis)	1.82µm	1.86µm
Maximum X deflection for 1g	63nm	2nm
Maximum Y deflection for 1g	1.82µm	1.86µm
Maximum Z deflection for 1g	1.11µm	1.47µm
Mode 1	530Hz	553Hz (in-plane)
Mode 2	561Hz (in-plane)	625Hz
Mode 3	724Hz	---

Table 4-3 FEM and system level simulations results for the 3HAS accelerometer

Property	***Value FEM***	***Value Architect***
Proof mass deflection for 1g (sense axis)	4.5nm	5.6nm
Amplified deflection for 1g (sense axis)	162nm	208nm
Maximum X deflection for 1g	5.8nm	1.3nm
Maximum Y deflection for 1g	163nm	208nm
Maximum Z deflection for 1g	11.6nm	17nm
Mode 1	1456Hz (in-plane)	1285Hz (in-plane)
Mode 2	2303Hz (in-plane tilt)	4443Hz
Mode 3	2648Hz	---

Table 4-4 FEM and system level simulations results for the 4LAS accelerometer

Property	***Value FEM***	***Value Architect***
Proof mass deflection for 1g (sense axis)	160nm	194n
Amplified deflection for 1g (sense axis)	492nm	627nm
Maximum X deflection for 1g	19nm	1.33nm
Maximum Y deflection for 1g	494nm	627nm
Maximum Z deflection for 1g	51nm	52nm
Mode 1	1047Hz (in-plane)	936Hz (in-plane)
Mode 2	2200Hz	2311Hz
Mode 3	2417Hz	---

As it can be seen from the tables above, a higher amplification does not mean a higher deflection at the output. The designs with a lower amplification produce a higher deflection due to the lower overall stiffness of the mechanism that the proof mass faces. This can be visualised by considering a simple mechanism with a rigid beam attached to a rotational spring at one end. The force needed to rotate this mechanism is higher closer to the spring. This, in effect, is a force amplifier. Although this result may initially seem to counteract the scope of using a deflection amplifier, it provides a very important advantage of the mechanism. This is the higher deflection over a wider bandwidth, which is inherent to the mechanism and is presented in more detail in section 4.4.4. When designing with such a mechanism, careful considerations have to be made based on the application. The design framework presented in this chapter proves to be a valuable tool for the application of mechanical amplification to inertial sensors.

The designs with the additional springs provide a reduced out-of-plane motion. From the tables above, the ratio of reduction of the out-of-plane deflection is an order of magnitude higher than the reduction of the in-plane deflection. For applications where the sensor is subject to out-of-plane motions, the additional springs would offer increased stability in the amplitude of the output signal.

Sensitivity to structural parameters

Parametric sweeps were used for the amplification ratio and the pivot, input and output beam length and width. The structural parameters of the fabricated devices were determined through these sweeps. Rather than only providing parametric sweeps, Architect can also be used to run sensitivity to structural parameters analyses. This gives a very good insight as to which structural parameters have more effect on the design. Table 4-5 shows the results from the sensitivity analysis. The most important parameters of the device were varied within 1% of their nominal value. The sensitivity column shows the percentage of output deflection change for each parameter perturbation. As noted before, the pivot width is the most influential parameter. The pivot to input distance, which defines the amplification factor, is affecting the output much less for such a small perturbation.

Table 4-5 Sensitivity of output deflection to parameters change using Architect

Parameter	*Nominal Value*	*1% perturbation*	*Sensitivity%*
Pivot width	10μm	0.1μm	-1.3
Input beam width	10μm	0.1μm	-1.24
Input beam length	150μm	1.5μm	1.16
Pivot length	110μm	1.1μm	-0.824
Output beam width	5μm	0.05μm	-0.214
Pivot to input distance	100μm	1μm	0.207
Output beam length	125μm	1.25μm	0.0544

4.4.2 Electrostatic simulations

The sensors use differential parallel plate capacitive comb-fingers to convert deflection to capacitance variation such as the ones shown in Figure 4-5. There are 74 (plus 74 on the second differential side) parallel comb-fingers for the proof mass and 152 (plus 152 on the second differential side) of the amplified output. The length L_c of the fingers is 200µm, the thickness t_c is 50µm, and the width w_c is 10µm. The overlap L_o between fingers is 190µm, with a small gap g_a of 10µm, and a large gap g_b of 30µm. The small gap g_a was chosen to be 10µm to reduce squeeze film damping and facilitate large motions while the large gap g_b was chosen to be 3 times larger to reduce its negative effect to the overall capacitance change when the sensors are subjected to acceleration.

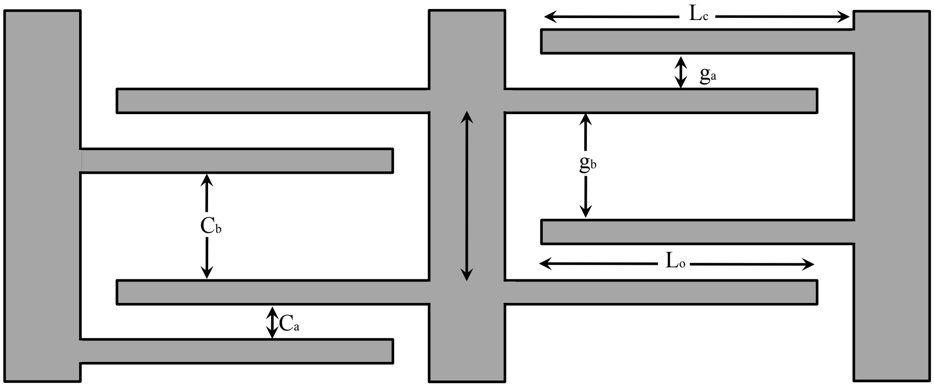

Figure 4-5 Model of differential comb-fingers used in the accelerometer. C_a is the capacitance of the small gap g_a while C_b is the capacitance of the large gap g_b. L_o is the overlap length of the fingers.

The overall capacitance can be calculated analytically by the parallel plate equation eq. 4-1 and by multiplying it with the number of comb-fingers. The useful capacitor in Figure 4-5 is formed by the gap g_a and, whereas C_b contributes to the overall capacitance, but acts in a detrimental way during operation, and is therefore considered parasitic. The overall capacitance for the proof mass comb-fingers is 0.84pF and that for the amplified output is 1.73pF. It must be noted that this way of calculating capacitance does not include fringe fields capacitance and, for this reason, it is normally 20-40% [68] lower than the actual one, depending on geometry.

The Memelectro module of Coventorware was also used to calculate the overall output capacitance. The capacitance for the output was found to be 2.93pF whereas for the proof mass it was 1.44pF. It can be seen that, as expected, the values from the

Boundary Element Method (BEM) are 40% larger than the analytical ones. The reason for this deviation is that the BEM method used includes the calculation of fringe fields in the derivation of capacitance.

Architect also has the ability to model electrostatic components. It achieves that by introducing electrostatic comb-finger models in the Saber library. This is a very useful component since the comb-fingers can then be connected to a pick-off circuit model implementing in this way the entire MEMS structure. For the devices discussed here, the model predicts 2.55pF for the output and 1.23pF for the proof mass comb-fingers capacitance. Those values are 14% lower than the BEM and 32% higher than the analytical results.

The measured nominal capacitance of the device is at least an order of magnitude larger than the values presented here. This is due to large parasitic capacitances, with the largest of those being the proof mass to handle wafer capacitance. Additionally, it is difficult to predict how the parasitic and fringe field capacitances vary when the sensor moves. For these reasons, the models for the electrical evaluation that will be presented proved to give the closest results by using the nominal capacitance calculated analytically and by compensating for the parasitics in the circuit simulation.

4.4.3 Damping of mechanically amplified capacitive accelerometers

The miniature nature of MEMS devices constitutes air damping a governing parameter on their dynamic operation. During the design phase of the amplified accelerometer, a thorough study on damping was carried out on a preliminary prototype. This is presented in Appendix G. Using eq. G-4, the overall squeeze film damping of the devices including all the comb-fingers was calculated to be 1.27×10^{-4}N/(m/s). The accelerometers are made in an SOI process and the handle wafer behind the proof mass is not removed, hence they experience additional slide film damping. Due to the large area of the mass, the slide film damping is in the same order of magnitude as the squeeze film damping of the comb-fingers. It therefore adds significantly to the overall damping. Since the sensors operate at a frequency below $f_d = \mu/(2 \cdot \pi \cdot h^2)$, where μ is the kinematic viscosity of air and $h=2\mu m$ is the gap between the proof mass and the handle wafer, the slide film damping can be calculated from eq. 4-3 in which A is the effective area of the proof mass [69].

$$D_{slide} = \frac{\mu_{eff} \cdot A}{h} \qquad \text{eq. 4-3}$$

$$\mu_{eff} = \frac{\mu}{1 + 2 \cdot K_n} \qquad \text{eq. 4-4}$$

The effective viscosity of air including the rarefaction effect on air present in gaps of size comparable to the mean free path of air, is given in eq. 4-4. K_n is the Knudsen number as described in Appendix G. The slide film damping of the accelerometers is calculated from eq. 4-3 to be 1.34x10^{-4}N/(m/s). The overall damping of the devices is therefore 2.61x10^{-4}N/(m/s).

It is important to calculate the damping ratio ζ to obtain a measure for the damping, which can be compared to measurement results. This will be performed here using the 1HAN mechanically amplified accelerometer but it equally applies to the other designs. The damping ratio is the ratio of the overall damping to the critical damping. The equivalent mass m_{eq} has to be found at a reference point. The reference point in the amplified accelerometers is at the output of the microlevers where measurements are performed. The proof mass can be lumped at the output by dividing it by the deflection amplification factor. This is correct since the force at the output due to the inertia force of the proof mass is attenuated by the microlevers by the inverse of the deflection amplification factor. The equivalent mass of the proof mass at the microlevers output is 5.233x10^{-2}mg.

The mass of the microlevers is substantial and it contributes to the overall equivalent mass as well. In order to find the equivalent mass of the microlevers, their mass has to be found by integrating along their length. The integral has to include the attenuation factor (inverse of the deflection amplification factor). The mass of the lever for a length dx is $d_a \cdot w_a \cdot t_a \cdot dx$. Where d_a is the density of silicon, w_a is the width of the lever arm and t_a is the thickness of the arm. Each mass part of each dx contributes to the equivalent mass at the tip of the microlever an amount of mass divided by the deflection amplification factor for this point (L_a/L_a-x). The integral for lumping the mass of the microlever is shown in eq. 4-5.

$$m_{levereq} = \int_{0}^{La} d_a \cdot w_a \cdot t_a \cdot \frac{L_a - x}{L_a} dx \qquad \text{eq. 4-5}$$

The overall equivalent mass including the proof mass, the comb-fingers, the output comb-finger supporting arms, and the four microlevers is therefore 0.219mg. This value was calculated for the microlevers of 1HAN with w_a=t_a=50µm and L_a=3650µm.

In addition to the equivalent mass an equivalent spring constant needs to be found for the reference point of measurement. This can be simply calculated using the natural frequency of the accelerometer and the equivalent mass from eq. 4-6.

$$k_{eq} = m_{eq} \cdot \omega^2 \qquad \text{eq. 4-6}$$

where ω is the un-damped natural frequency (740Hz for 1HAN) of the sensor. The critical damping calculated from eq. 4-7 is 2x10^{-3}N/(m/s).

$$D_c = 2 \cdot \sqrt{K_{eq} m_{eq}} \qquad \text{eq. 4-7}$$

The ratio of the overall damping (2.61x10^{-4}N/(m/s)) versus the critical damping (2x10^{-3}N/(m/s)) gives a damping coefficient for the 1HAN accelerometer of 0.128. This is in accordance to the under-damped behaviour for which the sensors were designed. In Chapter 7 those results are compared to experimental data.

4.4.4 *Figure of Merit definition*

Since the designed accelerometers use an unconventional suspension system, defining a comparison measure to conventional devices is a rather challenging task. Maximum sensitivity versus space occupation could be one figure, but this would complicate the comparison and it would lead to out-of-scope space and shape optimisation. For this reason a conventional capacitive accelerometer based on work presented in [70] was designed. The conventional accelerometer uses 4 straight beams to suspend the proof mass, which weighs the same as the proof mass of the mechanically amplified accelerometer. The minimum feature size is set to 10µm for both conventional and mechanically amplified accelerometers. The aim is to compare the deflection of the sensors for the same natural frequencies. To compare sensors of various natural frequencies the lever ratio of the mechanically amplified accelerometer was varied by varying the input to pivot distance (therefore varying the amplification without changing the size of the sensor) and keeping all the other parameters constant. To perform this, the Architect system level simulation model of 1HAN shown in Figure 4-4 was employed. The width of the beams that connect the microlever output to the comb-fingers was changed from 5μm to 10μm to comply with the minimum feature size requirement. For the conventional accelerometer, the length of the suspension beams was varied to provide the same range of natural frequencies, while the rest of the parameters were kept constant. The conventional accelerometer was simulated analytically using the Matlab script of Appendix F. Figure 4-6 shows the variation in the deflection for 1g constant acceleration with respect to the natural frequency for the conventional accelerometer for different lengths of the suspension beams. Figure 4-7 shows the same figure for the amplified accelerometer[4] for different amplification factors. Although both graphs have a declining trend, their shape is different. Figure 4-8 shows the ratio of the two graphs. It is evident that the amplified accelerometer deflects more for the same natural frequencies. This means that the mechanically amplified accelerometers are more sensitive within the same bandwidth[5] compared to conventional accelerometers. It is therefore sensible to define the Figure of Merit as the product of 1g deflection and natural frequency. The most important information in the graph of Figure 4-8 is the maximum, which is attributed to the unconventional spring-mass-lever-damper system that the mechanical amplifier forms. At the maximum ratio, the mechanically amplified accelerometer deflects 2.34 times more for the same natural frequency as the conventional accelerometer. At this point, the input to pivot length for the mechanically amplified accelerometer is set to 750μm, which gives an amplification ratio of 4.6. Using this method of comparison, the sensor can be optimised to operate at the maximum deflection bandwidth product compared to a conventional accelerometer of the same mass. These results indicate that the real performance improvement that the mechanical amplifier offers is a combination of larger deflection along a wider

---

[4] The design used here is based on 1HAN with a varying amplification factor.

[5] For an optimised critically damped sensor the bandwidth can be extended up to the natural frequency. Although the sensors presented here are not critically damped, the word “bandwidth” is used, as for an optimised sensor this would extend to the natural frequency.

bandwidth. Appendix F presents the Matlab script describing the operation of the conventional accelerometer. This accelerometer was fabricated as part of this study and accompanied the measurements as a reference sensor.

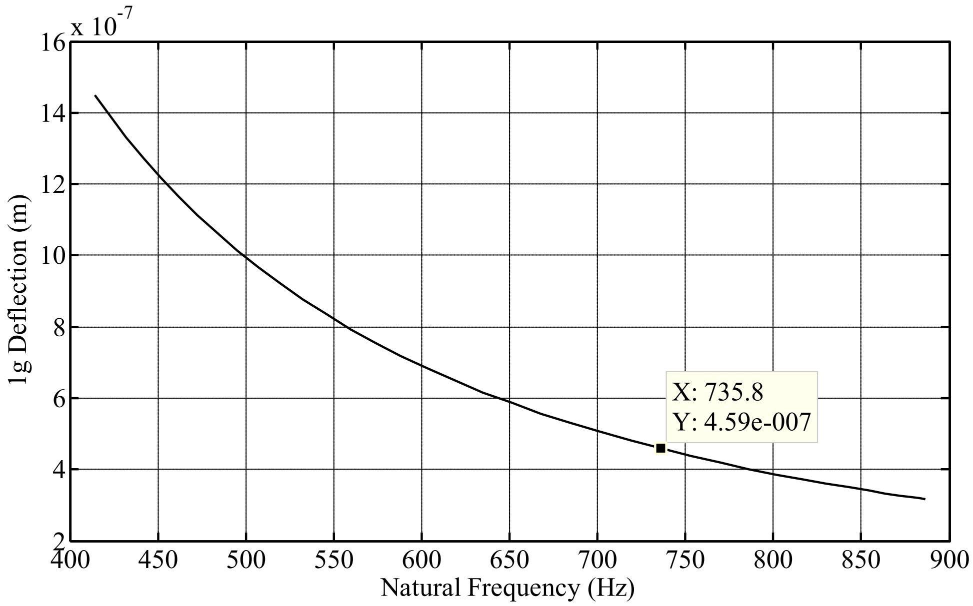

Figure 4-6 Variation of deflection for 1g constant acceleration with respect to the natural frequency for the conventional accelerometer. The natural frequency was varied by varying the length of the supporting spring system while the width remained constant. The analytical model used is implemented in a Matlab script and it is presented in Appendix F.

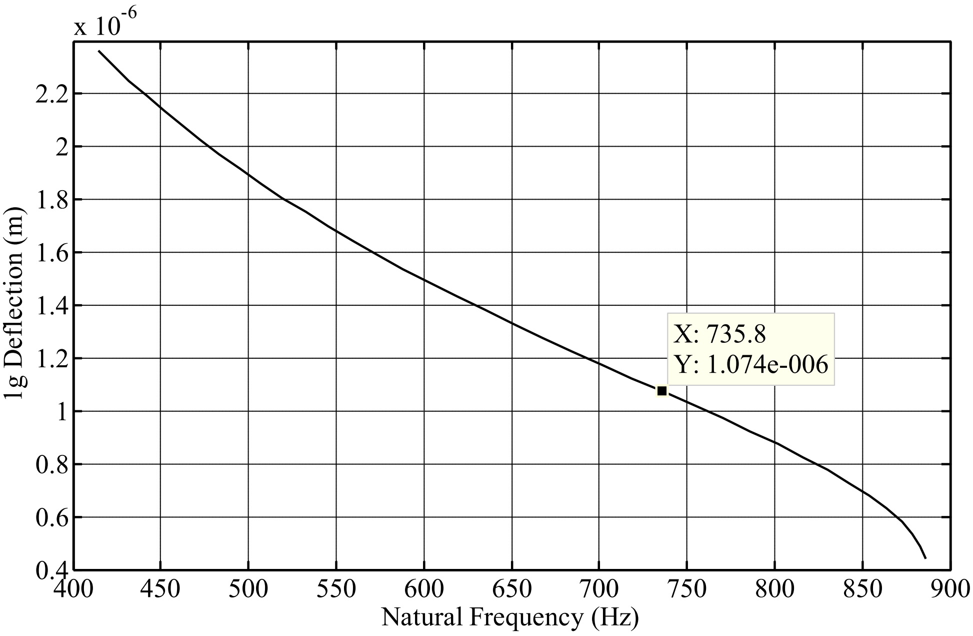

Figure 4-7 Variation of deflection for 1g constant acceleration with respect to the natural frequency for the amplified accelerometer. The variation of the natural frequency was achieved by varying the input to pivot distance hence varying the amplification factor. The simulation was performed using the parametric model of Figure 4-4 in Architect.

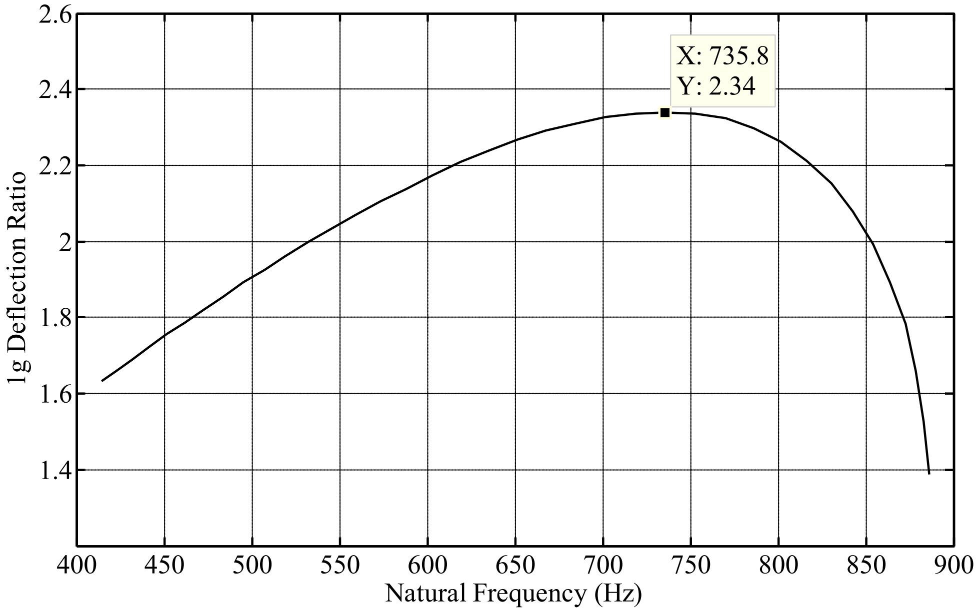

Figure 4-8 Amplified accelerometer deflection versus conventional accelerometer deflection for 1g constant acceleration over the same natural frequencies. The amplified accelerometer provides higher deflection for the same natural frequencies range. The graph has a maximum of 2.34 at 735.8Hz where the amplified accelerometer (system level simulation in Architect, Figure 4-4) gives the highest deflection for the same natural frequency as the conventional design (analytical calculations in Matlab, Appendix F.

The table that follows summarises the most important parameters of the accelerometers discussed in this chapter. The full design layout for 1HAN is presented in Figure 5-8 of Chapter 5 where the fabrication process is described.

Table 4-6 Mechanically amplified accelerometers parameters

Property	***Value***
Die area	11380x7553(μm)^2
Proof mass + comb-fingers mass	1.91mg
Proof mass + comb-fingers (including over-etch)	1.797mg
Nominal capacitance at microlevers (analytical)	1.73pF
Nominal capacitance at proof mass (analytical)	0.84pF
1HAN	
Deflection amplification (FEM)	41.7
Lever Ratio (Ideal Amplification)	36.5
Comb-fingers deflection for 1g (FEM)	626nm
In-plane proof mass deflection for 1g (FEM)	15nm
Out-of-plane deflection of comb-fingers for 1g (FEM)	415nm
In-plane resonance (FEM)	740Hz
Differential static sensitivity (0.5μm over-etch)	114fF/g
Figure of Merit	463 (μm Hz)
2LAN	
Deflection amplification (FEM)	3.61
Lever Ratio (Ideal Amplification)	3.65
Comb-fingers deflection for 1g (FEM)	1.82μm
In-plane proof mass deflection for 1g (FEM)	504nm
Out-of-plane deflection of comb-fingers for 1g (FEM)	1.11μm
In-plane resonance (FEM)	561Hz
Differential static sensitivity (0.5μm over-etch)	334fF/g
Figure of Merit	1021 (μm Hz)
3HAS	
Deflection amplification (FEM)	36
Lever Ratio (Ideal Amplification)	36.5
Comb-fingers deflection for 1g (FEM)	162nm
In-plane proof mass deflection for 1g (FEM)	4.5nm
Out-of-plane deflection of comb fingers for 1g (FEM)	11.6nm
In-plane resonance (FEM)	1456Hz
Differential static sensitivity (0.5μm over-etch)	30fF/g
Figure of Merit	235 (μm HZ)
4LAS	
Deflection amplification (FEM)	3.08
Lever Ratio (Ideal Amplification)	3.65
Comb-fingers deflection for 1g (FEM)	492nm
In-plane proof mass deflection for 1g (FEM)	160nm
Out-of-plane deflection of comb fingers for 1g (FEM)	51nm
In-plane resonance (FEM)	1047Hz
Differential static sensitivity (0.5μm over-etch)	90fF/g
Figure of Merit	515 (μm Hz)

4.5 Conclusions on the design towards a mechanically amplified accelerometer

This chapter presented the design considerations of a mechanical amplifier based on microlevers in a micromachined capacitive accelerometer. The mechanical amplifier was based on Type 3 microlevers. Those are the most appropriate for the application, due to their non-inverting nature. Four different designs were presented, with amplification factors spanning an order of magnitude (36.5 and 3.65), while two of them have additional springs for suppressing the out-of-plane motion. The structural parameters of the designs were discussed, revealing that the most important parameters are the widths of the pivot and the input beams. The additional springs proved to reduce the out-of-plane motion to an order of magnitude less than the in-plane motion and therefore are useful to applications that undergo undesired out-of-plane vibrations. The sensors were compared to a conventional accelerometer, which led to the formulation of a Figure of Merit. This is the deflection natural frequency product for 1g constant acceleration. The amplified accelerometers have a higher Figure of Merit along the natural frequency range that was examined compared to the conventional design. This significant result brings forward the improvements in the sensitivity/bandwidth trade off that the mechanically amplified accelerometers offers.

The system level simulation of 1HAN presented here forms a framework for the application of mechanical amplification in inertial sensors. The parameters of the model can be easily changed to meet the specifications of a particular application. As Saber is based on powerful scripting languages, further work on the simulation file can couple it with optimisation algorithms to produce optimum designs for specific applications in reduced time. This is out of the scope of this thesis but nonetheless demonstrates potential for further exploration and improvement of the concept proven here.

Chapter 5 Fabrication

5.1 Introduction to fabrication

When this study was initiated, there was no stable in-house MEMS process for the fabrication of such devices at the University of Southampton. In fact, there were no permanent cleanroom facilities either. During the transition to the new cleanroom facilities of the University (Southampton Nanofabrication Centre) the fabrication process underwent considerable development until a suitable and robust process was standardised. Since the development of the fabrication process was a large part of this project, some of the iterations will be presented in this chapter.

5.1.1 First generation fabrication process

The sensors were initially designed to be fabricated in a single mask SOI process. For this reason etch holes were used in the proof mass and microlevers for the subsequent release of the structure from the silicon dioxide layer. The maximum releasable size was set to 30µm (15µm from each side) while the minimum safe size for the anchors was set to 70µm. The maximum releasable size may be assigned a relatively wide range of values within the design constraints (typically from as low as 1µm to as high as 100µm). The minimum anchor size has to be set such that they remain rigid even if the silicon dioxide layer is over-etched. It was experimentally found that a minimum anchor size of 70µm produced rigid anchors when the maximum releasable feature size was set to 30µm.

The wafers used in the fabrication process were 6 inch in diameter double-side polished SOI wafers. The device layer is n-type phosphorous-doped silicon with a resistivity of 0.001-0.0015Ωcm and a thickness of 50±5µm. The buried silicon dioxide layer is 2µm thick and was used as a sacrificial layer. The fabrication process steps are as follows:

1. The wafers were first cleaned of organic residues using nitric acid.
2. A 2.5μm thin photoresist (AZ9260) was then deposited on the top side of the wafer and was patterned using the structural mask (Figure 5-1a).
3. The structures were then defined by a DRIE process performed in the SPTS Pegasus tool [71] (Figure 5-1b). Table 5-1 shows the recipe used.
4. The chips were then diced using a dicing saw. The dicing was performed before the final etching of the silicon dioxide in order to prevent braking or sticking of the sensitive parts such as the comb-fingers.
5. The release was performed from the front side using a 48% Hydrofluoric Acid (HF) solution for 7 minutes (Figure 5-1c).
6. After the release, the devices were stirred for a few minutes in Isopropyl alcohol (IPA). This cleaned the devices of HF and water while it helped preventing the stiction problem usually met after the release procedure.
7. Then the chips were removed from the IPA and left in Cyclohexane for 10 minutes.
8. The final step was to remove the sensors from the solvent carefully and dry them on a hot plate at 70°C.

The most important steps are shown in Figure 5-1. Figure 5-2 shows a detail from a device under the microscope while Figure 5-3 shows a side view SEM image of an anchor and comb-finger. The sidewall angles evaluated with SEM pictures such as Figure 5-3 were found to be 88° in the worst case. This varied considerably with the gap size. By fixing the gaps to a certain value where the profile is crucial, the process can be optimised to produce sidewalls with less than 1° deviation from the vertical.

Table 5-1 DRIE recipe used in the SPTS Pegasus for 50µm deep etching

	Etch cycle	**Deposition cycle**
Sf$_6$ flow rate (sccm)	390	-
O$_2$ flow rate (sccm)	39	-
C$_4$f$_8$ flow rate (sccm)	30->0	250
Coil power (W)	2800	2000
380kHz LF Platen power (W)	60	-
Pressure (mT)	30	24
Time duration (s)	2.3	2.0
Chiller temperature (^{o}C)	5	5

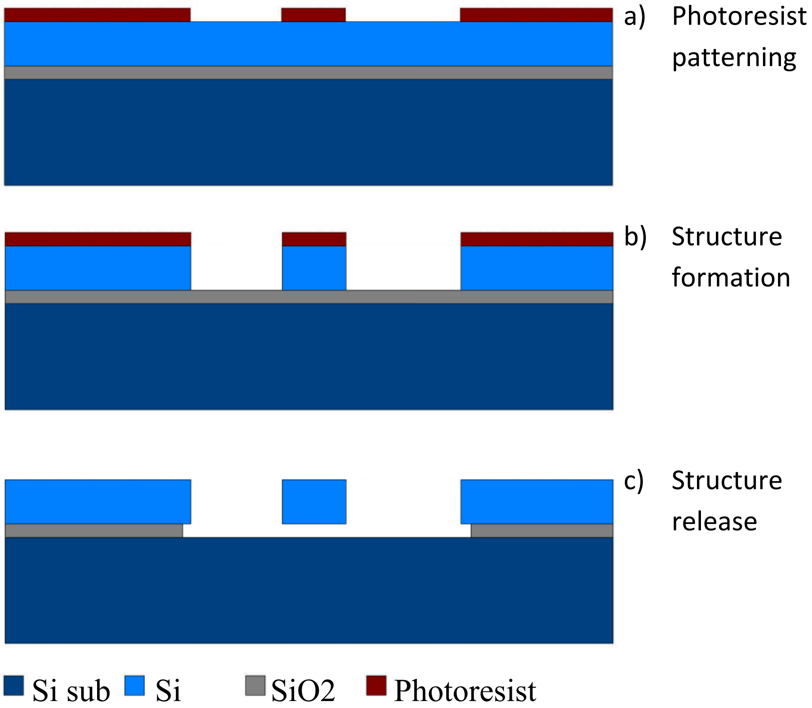

Figure 5-1 Simple SOI process used to fabricate the prototypes

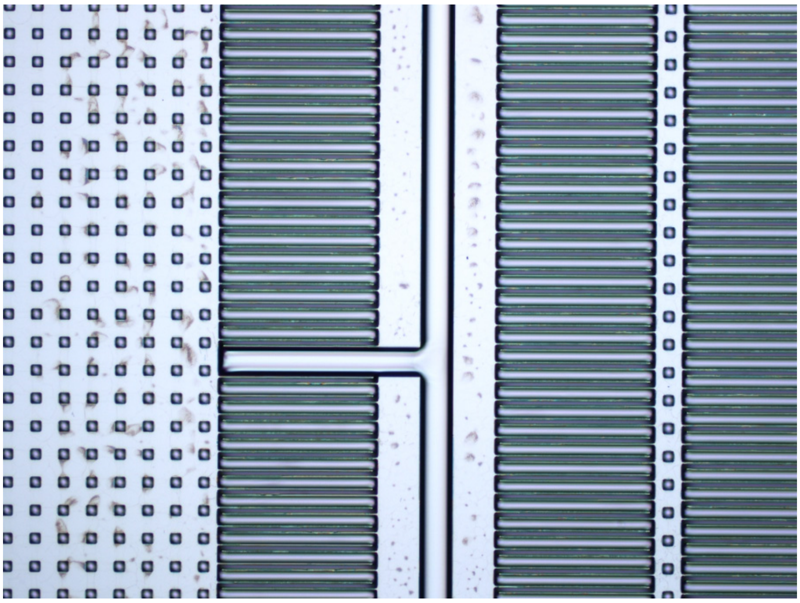

Figure 5-2 Microscope detail from the SOI fabricated device. The detail shows part of the proof mass and comb-fingers as well part of the output.

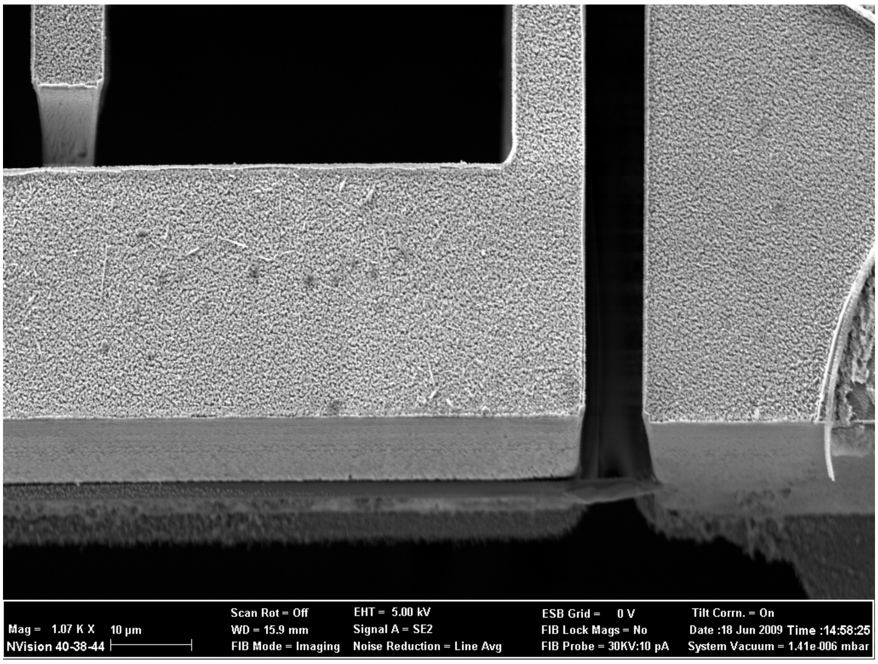

Figure 5-3 SEM image showing the profile of the sidewalls achieved on the anchors and comb-fingers

The first generation of the SOI process offered a good foundation but had many problems. The main issue was stiction. The devices had to be immersed into the release solution individually with a modest success rate. Furthermore, it proved impractical to release devices one by one. The dicing saw used for the separation of the dice produced a considerable amount of debris so the surfaces had to be protected with photoresist, which added complexity to the process. Although this was a multi-project process that produced some working samples it never resulted in a fully working mechanically amplified accelerometer. This was mainly due to the high compliancy of the first prototype sensor but also due to the small gap (5µm) and large surface of the comb-fingers (300 x 50μm^2). Compliant features were mainly stuck or broken. Therefore, alternative fabrications processes were developed.

5.1.2 Silicon on Glass process

The initial prototypes were also designed for a three-mask SoG process. This fabrication process was performed at the University of Peking, China. The silicon wafers used in this process were 4 inches wide and highly doped with a resistivity of 0.01~0.03Ωcm. The glass wafers were Pyrex 7740 wafers that have a thermal expansion coefficient close to that of silicon. The process proceeded as follows:

1. The first step involved a backside DRIE etching of the silicon wafers to leave 20µm high anchor areas (Figure 5-4a). The depth of this etch defined the gap between the moving structures and the glass substrate and hence defined the squeeze film damping between these components.

2. The backside anchors were then doped by implanting phosphorous ions to obtain a good Ohmic contact with the substrate (Figure 5-4c).

3. At the same time, a 200nm thick Ti/Pt/Au layer was patterned by a lift-off process to form the electrical interconnections at the glass wafer (Figure 5-4b).

4. The two wafers were then anodically bonded (Figure 5-4d).

5. Using potassium hydroxide (KOH), the silicon front side was then thinned to leave a 60µm thick layer from which the accelerometers were to be formed (Figure 5-4e).

6. The structures were then formed by the DRIE process (Figure 5-4f).

7. Finally, the devices were separated by dicing.

The process is shown in Figure 5-4 [72], whereas Figure 5-5 and Figure 5-6 show SEM images of the SoG fabricated devices.

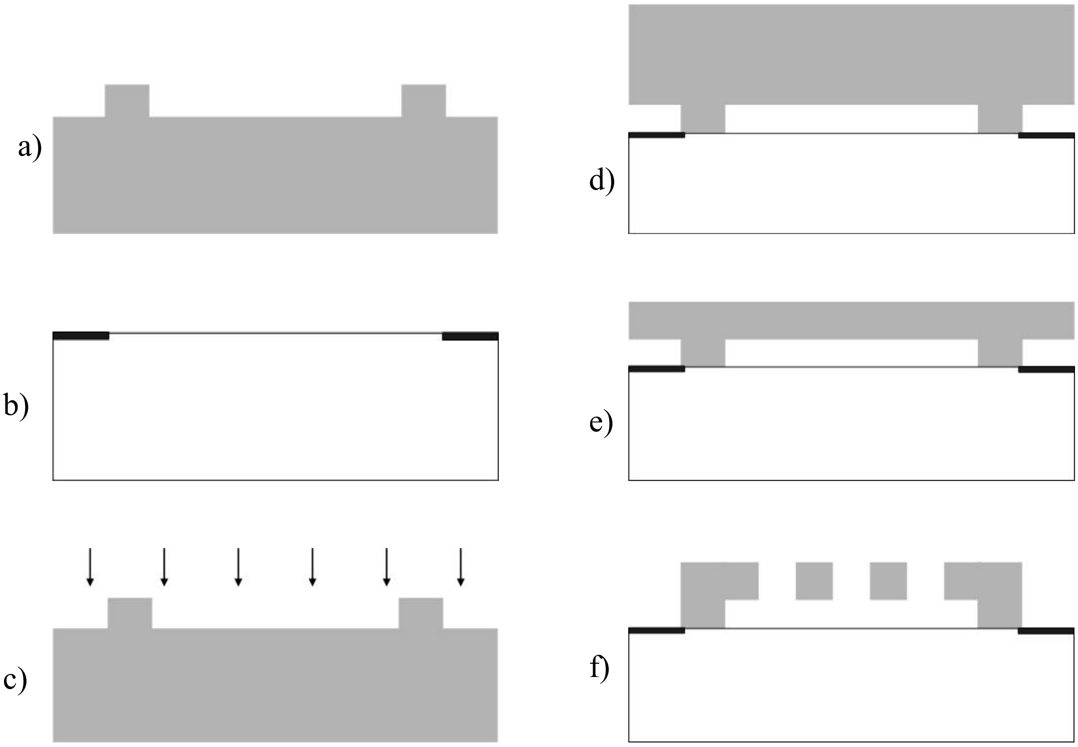

Figure 5-4 SoG process used to fabricate the mechanically amplified accelerometer: a) Backside DRIE etching of the silicon wafer; b) Ti/Pt/Au interconnect layer patterning on the glass wafer; c) Doping of the backside of the silicon wafer; d) Anodic bonding of the two wafers; e) Thinning of the silicon wafer by KOH etching; f) Device formation by DRIE.

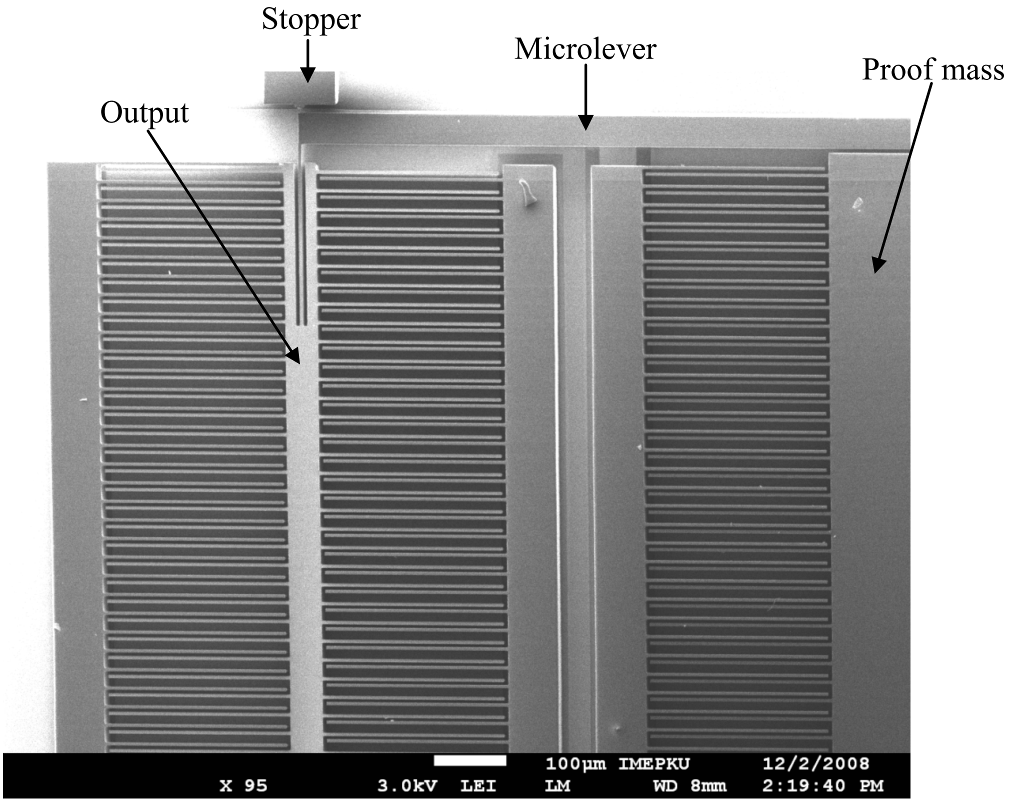

Figure 5-5 SEM detail from the SoG fabricated device. This image shows a detail from one output (left side) and part of the proof mass (right side)

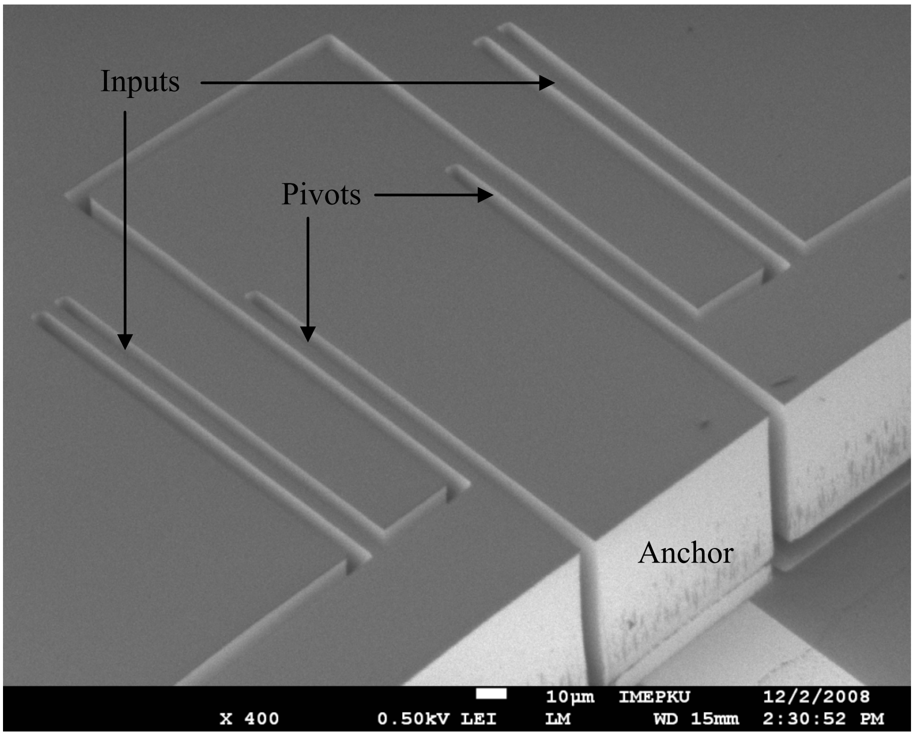

Figure 5-6 SEM image showing a detail from the SoG accelerometer. The image shows an anchor and the pivot and input of two microlevers.

The particular SoG process is a well-established process that produced working accelerometer samples. The early prototypes fabricated in this process offered useful information on the performance of the mechanically amplified accelerometers. This knowledge was used to produce the fully functioning samples presented in this work.

5.1.3 Second generation SOI fabrication process

The second generation of the SOI process was developed at the Southampton Nanofabrication Centre to improve on the issues such as low yield and impracticality of the release of first generation. One of the improvements included introducing an additional mask for etching the backside of the SOI wafers. By introducing another etching step, the area behind the proof mass could be removed. This helped to prevent stiction of the proof mass to the handle substrate whilst decreasing the release time and allowing for a 10-20% increase in the proof mass since there was no need for etch holes. An additional improvement that the second iteration of the process offered was to introduce features for chip separation on the backside of the wafer in the form of small bridges between the dice. The dice could be easily separated with a pair of tweezers after successful fabrication. This addition eliminated the need for dicing.

The introduction of a second mask to the process proved to be a major change and brought improvements as well as new challenges to the process. One of the challenges involved the order the sides being processed. After spinning, exposing and developing the photoresist on one side this side, had to be etched using DRIE. The second side had to be processed accordingly. When the second side was being etched using DRIE, the first side was initially placed upside-down on the chuck in the chamber of the SPTS Pegasus tool. When this was done without a handle wafer, the helium used to cool the substrate flowed uncontrollably, due to the non-smooth surface of the already etched side. This caused the wafer to overheat and eventually the process failed. An additional issue was that when the etch from the side that was etched second reached the underlying oxide, the wafer broke in the process chamber due to the large area of the thin oxide exposed to a high pressure difference between the front and back sides.

The use of a handle wafer was thus inevitable but introduced another complication to the process. A method was required to attach the two wafers together sufficiently strong so that they would not separate in the chamber but at the same time it should be possible to separate the wafers afterwards, without breaking either wafer or leaving excessive residues. Additionally, the adhesion method should offer a good thermal path between bonded wafers so that the processed wafer could be cooled during processing. Three methods were tried for attaching the two wafers: Stiction tape, crystal bond, and photoresist. The stiction tape was good enough to keep the two wafers together but it was very hard to separate them afterwards. The crystal bond kept the two wafers together well enough and then it was easy to separate them using heat and methanol but the crystal bond residues were excessive and they were very hard to clean off since they were also found in-between etched structures. The final solution was to use photoresist and then clean it off with acetone and IPA. This worked very well and the remaining residues were cleaned with O_2 in the Oxford Instruments Plasmalab 80 plus Reactive Ion Etching (RIE) tool [73]. Photoresist provided an acceptable heat path so the masking photoresist was not burnt during the process.

It is reasonable that for such a process the device layer should be left to be processed last to prevent harming sensitive structures. When the device layer is processed last, the backside layer is stuck on the handle wafer. Although between the chips there are air paths, this is not true for the cavities behind the proof mass. In these cavities, there is trapped air at ambient pressure. Unfortunately, when this method was used the wafers ruptured in the chamber of the DRIE tool due to the pressure difference (there is a low pressure in the chamber of the DRIE tool). For this reason, the backside layer was processed last giving acceptable results when the process and handling wafers were carefully separated afterwards.

In the absence of a dry release process, the release from the sacrificial oxide still presented difficulties, mainly due to stiction. In order to alleviate this problem a technique based on a bath process [74] was introduced. The chips were dipped in a shallow and small Teflon container containing a 48% HF solution. The container was then placed in a large beaker. The beaker was slowly filled with water up to the point beyond which the small container would float in the beaker. After 7 minutes of etching, water was poured slowly into the small Teflon container, overflowing the HF solution into the larger beaker. An aspirator was then used to remove the diluted acid from the beaker while at least two litres of water were poured in, significantly reducing the concentration of the solution. The transition from HF to water in this way is vital since the dehydration of the devices is completely prevented and hence surface tension is reduced and induced stress on the devices is eliminated. In the same manner, the water was substituted by acetone, then IPA and finally cyclohexane or pentane. These liquids were used in order of descending surface tension. Since cyclohexane and pentane have very low surface tensions [74], stiction is prevented with a high degree of success. After removal from the last solvent, the sensors were left on a cleanroom wipe for 2-3 seconds to remove excess fluid from the backside (preventing in this way “popping” due to boiling liquid) and then placed on a hot plate with a glass slide at 60^{o} C until the liquid dried out.

Using a handle wafer in the DRIE tool did not produce high quality results in terms of etching uniformity. It is important in microfabrication to interfere with the device layer as little as possible and sticking the processed device layer onto another wafer can cause damage to the delicate device layer. The harsh dicing of devices was prevented by introducing dicing features but the release was a very involved process that had to be done individually for each sensor. For these reasons, the fabrication process had to be developed further to address these issues.

5.2 Final fabrication process

As described previously, the SOI process used to fabricate the sensors was rather complicated with only moderate success. Nevertheless, the process evolved and eventually matured through the improvement of the individual steps. The use of the new cleanroom facilities in the University of Southampton provided a higher success rate mainly due to the clean and stable environment and the new improved equipment used during lithography and release. In addition, the DRIE recipe had been tweaked during different runs and eventually produced nearly ideal conditions for the process. A HF Vapour phase etcher (VPE) [75] was used for the release step eliminating the stiction issue. It also allowed a new die separation process without conventional dicing. This increased the overall yield to more than 95%.

The final fabrication process is based on the work presented in [76] and [77]. The improvements introduced are based upon the removal of parts of the handle layer behind the devices and the separation of devices during the release process. In order to accomplish this, the design of the amplified accelerometer had to be modified to include special features. Etch holes were used for the release of the proof mass and compliant parts. The release of the handle wafer parts and device separation was achieved by using a set of trenches and etch holes on the device and handle layers. The etched features on the front and backside of the wafers are designed such that they do not overlap at areas larger than $50x50\mu m^2$. This design consideration effectively eliminated the wafer rupture issue during DRIE.

In the final fabrication process, the handle wafer area below the largest part of the microlevers and output comb-fingers was removed to allow for out-of-plane and tilt motions, and to alleviate any issues related to stiction and debris accumulation. This proved to be a necessity inferred from initial test results of the previously fabricated devices where in many cases, stress-induced tilt or out-of-plane motion prevented operation. When the microlevers moved more than the allowed 2μm (distance between device and handle layer defined by the buried silicon dioxide layer) out-of-plane, the device became dysfunctional either due to friction or stiction to the handle wafer.

For the conventional accelerometer used as reference (described in Chapter 4), it was possible to remove the entire handle wafer block underneath the proof mass [77]. In contrast, the design geometry of the mechanically amplified accelerometer did not allow the entire area to be removed. This is due to the stator anchors located between the proof mass and the output system. The handle wafer was only removed behind the microlevers and the output comb-fingers but not the proof mass as shown in the diagram of Figure 5-8. This proved to be sufficient since the motion of the proof mass is substantially smaller than the amplified motion of the microlevers, hence there was no observed friction or stiction of the proof mass.

5.2.1 Final fabrication process description

This section describes the final fabrication process used for the implementation of the mechanically amplified accelerometer. The wafers used were 6 inch SOI wafers. The thickness of the device layer was 50±1μm, the buried silicon dioxide layer was 2μm±5%, and the handle layer 530±25μm. The device layer resistivity was 0.001-0.005Ωcm. The fabrication process steps are as follows:

1. The handle layer was patterned with a 6μm thick AZ9260 type positive photoresist. This was followed by DRIE etching of the handle layer up to the silicone dioxide layer (Figure 5-7a) to form the handle layer patterns.

2. After striping the backside photoresist, the device layer was patterned with a 6μm thick AZ9260 type photoresist and etched using DRIE down to the silicon dioxide layer to define the device and release features (Figure 5-7b).

3. The wafers were processed (device layer down) in a HF VPE system to remove the sacrificial silicon dioxide layer (Figure 5-7c).

4. The chips were separated and a part of the handle wafer was removed during the release step (Figure 5-7d).

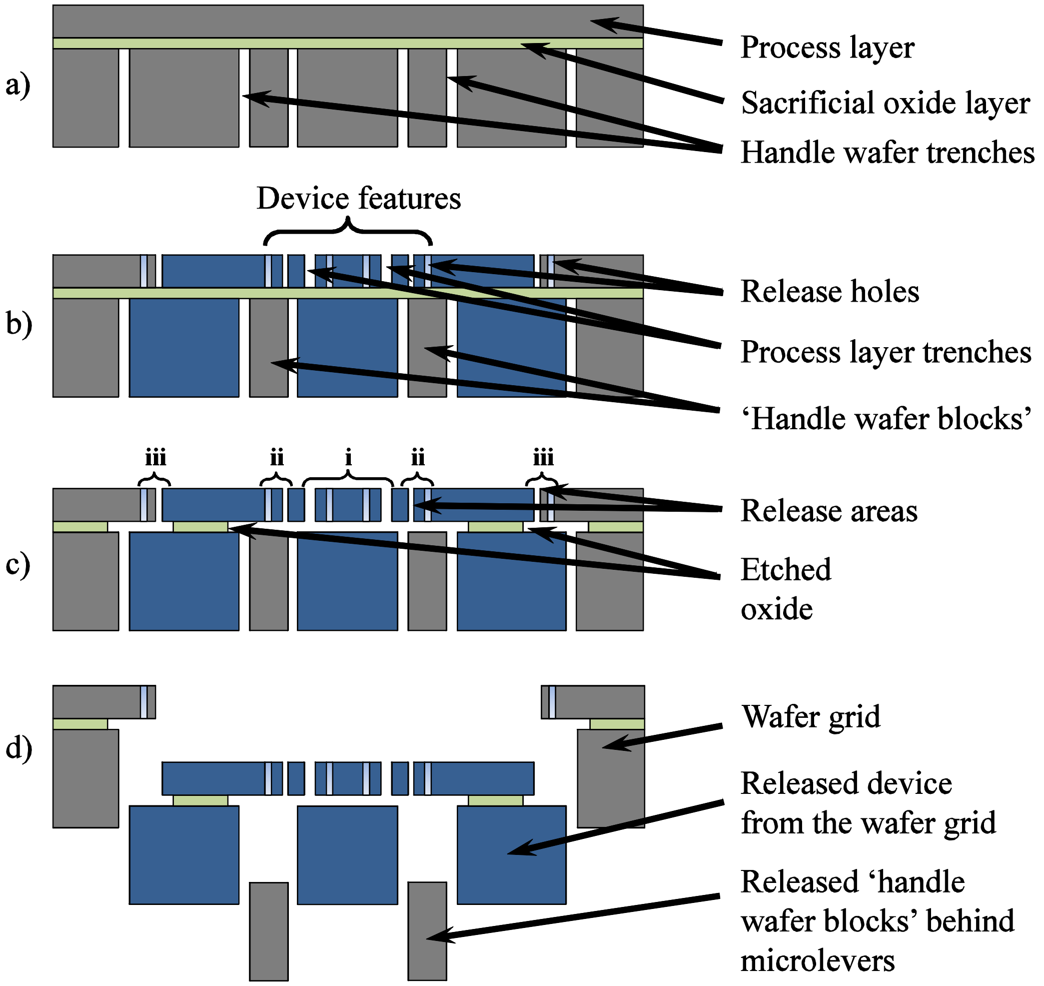

Figure 5-7 Fabrication flow of the amplified accelerometers: (a) Backside etching using DRIE to define the backside trenches. (b) Front side DRIE to pattern the device features, release holes, and front side trenches. (c) The three release regions i) device, ii) handle wafer blocks release features and iii) the area defined by the outer trenches on the front and backside, are etched consecutively in HF VPE (Hydrofluoric acid Vapour Phase Etching). (d) Device separation after release; devices can now be unloaded with the handle wafer blocks left behind.

Design modifications

The design of the devices was modified by introducing special features to accommodate the improved release process. The aim of the improved release process was to remove parts of the handle wafer beneath the microlevers and achieve the separation of the sensors without dicing but also to alleviate the issue of wafer eruption during DRIE. To achieve this an additional set of etch holes and trenches was introduced in the design. Etched areas were defined such that they do not overlap for more than 50x50μm^2. Three areas were defined from the additional features as shown in Figure 5-7c. Those were: i) the device area, ii) the handle wafer blocks area, and iii) the area defined by the outer trenches on the front and backside.

The first area (i in Figure 5-7c) includes features that allow for the release of the proof mass. The release of the proof mass is achieved by a set of etch holes, on the device layer, in a hexagonal arrangement with a maximum distance between holes being 20µm. This allows the proof mass to be released from the silicon dioxide layer first in the process due to the small undercut needed. The remaining compliant and movable features of the device were designed with a maximum undercut of 25µm from each side and are thus released after the proof mass.

The second area (ii in Figure 5-7c) includes the features for the release of the handle wafer blocks beneath the microlevers. For the release of the handle wafer blocks, 50µm wide trenches were designed on the backside of the wafer to surround the area behind the output comb-fingers and the microlevers. These trenches were formed by DRIE of the backside. The release trenches for the handle wafer are shown in Figure 5-8 in black for a device. During the release process, the etchant medium (HF), penetrated from the etched areas of the device layer and undercut the silicon dioxide up to the release trench. Thus, the front side of the device was no longer anchored to the backside block and hence this was removed. The release of the handle wafer block was timed to happen after the release of the compliant structures.

The process features the separation of the chips as the final timed step. This is achieved by the inclusion of trenches and etch holes (area iii in Figure 5-7c) in a similar manner to that used for the handle wafer blocks release. A 50µm trench was designed on the device layer and this surrounded the devices as shown in white in Figure 5-8. The front side of the devices is limited to the inner edge of the device layer trench. Next to the trench, a rectangular frame of etch holes was included on the device layer, and a trench on the handle layer defined the backside dimensions of the device. The trench on the front side served as the separating point for the device layer. The etch holes for device separation in Figure 5-8 were used to define the undercut that was needed to separate the devices but also it served as a resting point for the die since the wafers were processed with the device face down.

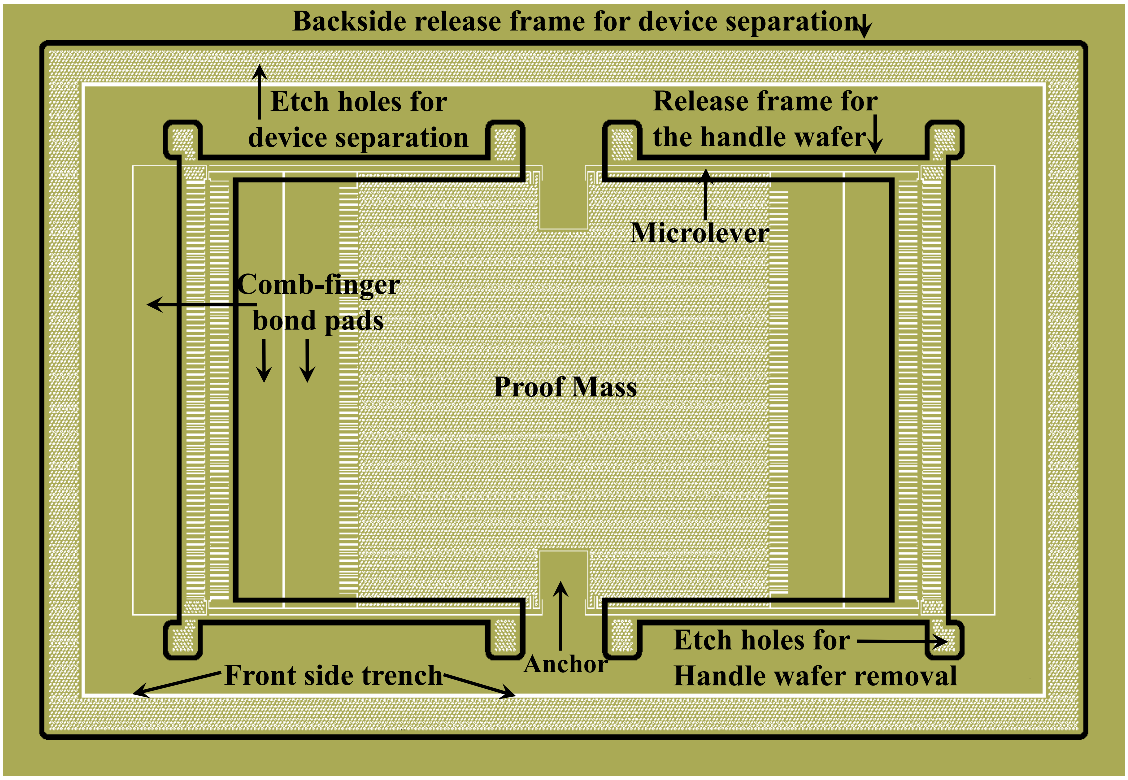

Figure 5-8 Layout of a single device as designed for fabrication. The black frames are etched on the backside of the SOI wafer enabling the removal of the handle wafer blocks behind the microlevers. The trenches also allow for device separation during the release process eliminating in this way the need for dicing.

The release features were defined in such a way so that the three areas were consecutively released. It is crucial that the silicon dioxide beneath the movable parts is etched away first to ensure the release of the device even when the removal of the handle layer blocks underneath the microlevers and comb-fingers fails. More importantly, since the wafer is processed with the device layer facing down during release, by releasing the movable parts first, it ensures that the handle wafer blocks will not be resting on the sensitive compliant parts. If the handle wafer blocks were released before the compliant structures they would then be supported by them and hence induce high stress and probably failure of the devices. Thus, the release of the handle wafer blocks was timed to happen after the release of the compliant structures. To achieve the timed silicon dioxide etch process the undercut needed for the backside blocks to be released was 50µm (plus 10um introduced by the etch holes for handle wafer removal, Figure 5-8). This ensured that the blocks were anchored while the device features were being released (maximum total undercut 50µm) and that they were released immediately after. In order to prevent the handle wafer blocks from trapping due to rotation or tilt and hence from sticking on the backside, special features such as the etch holes for handle wafer removal shown in Figure 5-8 were included. These features were released with a slight delay (increasing the undercut needed for the release of the backside blocks to 60μm) and prevented the block from getting stuck on the handle layer. They additionally offered a resting point area for the backside blocks during processing. In a similar manner, the third area was the last to be released. The etch holes for device separation Figure 5-8 were used to delay the release of the dice to happen right after the release of the handle wafer blocks. The etch holes frame served as a resting point for the die since the wafers were processed with the device face down.

After the release process, the wafer was placed with the device layer facing up in a single wafer box. A pair of tweezers was used to remove the wafer grid, which was separated from the devices after the final release step. This left the separated devices on the wafer box ready for collection. Finally, the devices were removed one by one leaving behind the released handle wafer blocks as depicted in Figure 5-7d.

Photolithography

For the transfer of the patterns on the wafers, a double side photolithography process was used. The backside patterning (handle layer) was performed first, while the front side (device layer) was done after the DRIE etching of the backside, imposing an increased processing complexity due to the already processed handle wafer.

The backside process steps when using SOI wafers were:

1. 5 minutes Fuming Nitric acid dip to remove organic contaminants
2. Quick dump rinsing to remove the Nitric acid
3. 1 minute HF dip to remove the surface silicon dioxide
4. Quick dump rinsing and spin drying
5. Dehydration of the wafers for t_{dh}= 30min in a 120°C oven
6. Spin and bake of TI Prime adhesion promoter on the backside of the wafers
    a. Spin speed of 3000rpm
    b. Baking on a hotplate at 120°C for t_{tib}= 120s
7. Spin of AZ9260 aiming to achieve the nominal 6μm thickness using the settings of Table 5-2 and with the time graph shown in Figure 5-9

Table 5-2 Settings of the spinner for the application of a 6μm thick AZ9260 uniform photoresist layer on a 6inch wafer

	Start-up	**Main**	**Slow down**	**Stop**
Rotation speed (rpm)	500	4000	500	0
Rise time (s)	$t_{r1} = 2$	$t_{r2} = 3$	$t_{r3} = 2$	$t_{r4} = 2$
Spin time (s)	$t_{s1} = 7$	$t_{s2} = 60$	$t_{s3} = 2$	$t_{s4} = 0$

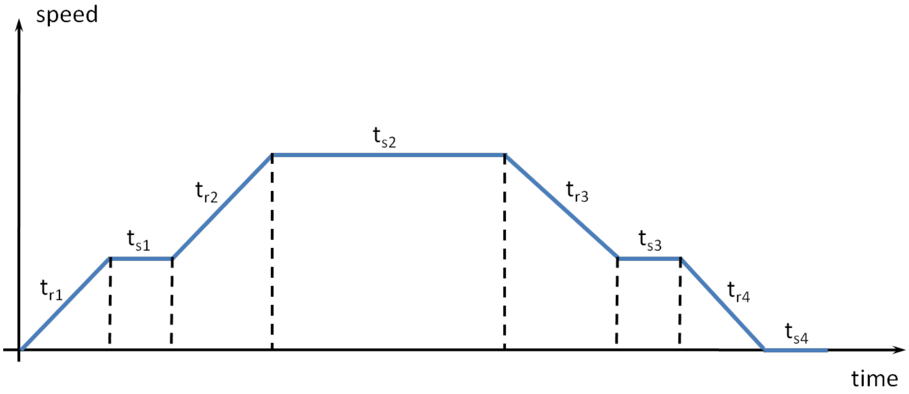

Figure 5-9 Time graph of the AZ9260 photoresist spinning

8. Softbake on hotplate at 110°C for t_{prb}= 150s
9. Rehydrate for t_{rh}= 30min
10. Exposure of the photoresist
    a. Exposure time for EVG 620T (without the i-line filter the intensity of the UV light is 20mW/cm^2) t_{exp} = 11s
11. Development in a solution containing 3 parts AZ400K and 1 part of DI water for t_{de}= 150s
12. DI water rinsing and nitrogen drying

The front side photolithography followed the same procedure, as the backside, apart from the fact that the backside etched patterns had to be covered during spin coating. In order to achieve that, the wafer was attached to a handle wafer using double sided thermal release tape before spinning. Covering the patterned side is imperative for using the vacuum chuck of the spinner. The double-sided thermal release tape can hold the wafers firmly attached for spinning at the required 4000rpm. The thermal tape was released easily during softbake without residues on the processed side. The attachment of the wafers proved to be a very delicate process since the etched parts of the handle wafer exposed areas of the 50μm thin device layer.

DRIE

For etching the patterns, the DRIE process step was performed using the SPTS Pegasus DRIE equipment. The recipes used are based on standard recipes provided by SPTS, which were then improved based on previous experience to produce the desired results for the specific design. Table 5-3 and Table 5-4 present the key parameters of the back and front side etching recipes, respectively.

Table 5-3 Backside DRIE process

	DEPOSITION CYCLE			**ETCH CYCLE**		
	delay	**Boost**	**main**	**delay**	**boost**	**main**
SF6 (sccm)	0	0	0	0	0	600
t (s)	0	0	4	0	0	4.5
O2 (sccm)	0	0	0	0	0	60
t (s)	0	0	4	0	0	4.5
C4F8 (sccm)	0	0	200	0	0	0
t (s)	0	0	4	0	0	4.5
Pressure (mT)	0	0	25	0	30	100
t (s)	0	0	4	0	1	3.5
Coil (W)	0	0	2000	0	0	4000
t (s)	0	0	4	0	0	4.5
Platen (W)	0	0	0	0	70 (HF)	35 (HF)
t (s)	0	0	4	0	2	2.5
Cycle time (s)	4			4.5		
Platen temperature	5°C at 10T back cooling pressure					

Table 5-4 Front side DRIE process

	DEPOSITION CYCLE			**ETCH CYCLE**		
	delay	**boost**	**main**	**delay**	**boost**	**main**
SF6 (sccm)	0	0	0	0	0	390sccm
t (s)	0	0	2s	0	0	1.7 s
O2 (sccm)	0	0	0	80	0	39sccm
t (s)	0	0	2s	1	0	0.7s
C4F8 (sccm)	0	0	250sccm	0	0	30 >> 0 (ramped down)
t (s)	0	0	2s	0	0	1.7s
Pressure (mT)	0	0	24mT	0	0	30mT
t (s)	0	0	2s	0	0	1.7s
Coil (W)	0	0	2000W	0	0	2800W
t (s)	0	0	2s	0	0	1.7s
Platen (W)	0	0	0	0	0	40W
t (s)	0	0	2s	0	0	1.7s
Cycle time (s)	2s			1.7s		
Platen temperature	5^{o}C at 10T back cooling pressure					

Release

The release of the structures was performed with the Idonus vapour phase etcher [75] shown in Figure 5-10. The wafer was placed on the chuck of the tool and clamped using mechanical clamping. The mechanical clamping was preferred over electrostatic clamping since the latter would induce forces that could lead to device stiction under certain circumstances. The etching time was found to be optimum at 50 minutes at a temperature of 40^{o}C.

Removed for copyright reasons.
Please find image on the cited source.

Figure 5-10 Idonus Vapour phase etcher. Taken from [75].

It must be noted that the etch rate can vastly change with parameters such as HF solution level, vapour pressure, ambient temperature, thickness and quality of the silicon dioxide. Failure to control these parameters may not only lead to under or over-etched oxides but also to device stiction. Although Vapour Phase Etching (VPE) systems are known to overcome device stiction, it nevertheless can easily occur under certain circumstances. This can be explained by considering the reaction that happens while etching silicon dioxide using HF vapours:

$$SiO_2 + 2H_2O \rightarrow Si(OH)_4$$
$$Si(OH)_4 + 4HF \rightarrow SiF_4 + 4H_2O$$

As shown in the two steps of the reaction proposed in [78], water is used in the etching process in its condensed form. The more water, the more reactive species are formed which leads to a quicker reaction. Decreasing the temperature of the wafer would accumulate more condensed water and the etch rate would increase. Conversely, when the temperature is increased the water evaporates quicker so the reaction slows down. The reaction formula shows that water is also a product of the process. Therefore, excess water formation due to low temperatures or due to large amounts of etched silicon dioxide would result in subsequent accumulated water. The surface tension of the accumulated water would lead to stiction of the compliant features. This phenomenon was observed when instead of 2µm, 5µm buried silicon dioxide SOI wafers were used. Excessive stiction was noticed although the rest of parameters were the same. The solution to this issue is to increase the temperature so that the remaining condensed water produced from the reaction evaporates before it exerts high enough surface tension to result in stiction. Another solution is to stop the process just before the release of the compliant parts, let the wafer dry on the thermal chuck for a few minutes and then resume the process to etch the remaining silicon dioxide. In this way, the excess water evaporates before there are any structures that can actually move so that during the final release step there is not enough time for the water to accumulate on the surfaces.

5.2.2 Process fluctuations

Process variation and fluctuations may cause poor yield and drastically affect device performance. This section examines the possible process deviations for each step of the final fabrication process as described in section 5.2.1 and the effect that those have in the device yield and performance.

Photolithography

Photolithography was performed to pattern the device and handle layer of the SOI wafers. The photoresist spinning was performed with an automated spinner and hence the repeatability of this step is excellent. The thickness deviation from the nominal value of 6μm of the photoresist layer was found to be consistently less than 400nm. Variation of the photoresist along the wafer was found to be less than 5% excluding the outer rim of the wafers. The photoresist thickness for both front and backside was chosen to be thick enough to withstand the DRIE process without being etched trough prior to its conclusion. Although the spinning process was very well controlled, in many occasions debris in the processing area was found to deposit on the wafers. This is believed to be mainly from the lid of the spinner and it caused an average of 5 devices having defects due to masking. Nevertheless, as the largest area of the devices is occupied by the proof mass and the debris masking was at the order of less than 10μm none of the tested affected devices seemed to have operational issues.

The soft bake of the wafers after photoresist spinning was performed on a high performance hot plate with temperature fluctuating less than 1% hence this step is not considered to have affected the yield and quality of the devices.

Exposure of the photoresist was performed with an EVG 620 series aligner. Prior to exposing the actual wafers, test wafers were used to verify this step. The ultraviolet lamp used in the aligner has a varying performance through its life therefore verifying the exposure time prior to processing is imperative. By verifying the aligner performance prior to each batch, defects and process variation due to over- or under-exposure were eliminated.

The development of the photoresist was performed manually in a beaker. This photolithography step is very critical and the conditions are not ideal when performed manually. In order to make the development more controllable and reduce variation between wafers due to fluctuations in development time the photoresist developer was diluted in DI water. This increased the development time so that small variations in the development did not cause drastically different results between wafers.

By inspection of the wafers after the photolithography, it was found that the misalignment between the front and backside patterns was less than 2μm. This does not affect the device performance or yield as the tolerance was set to 50μm at the design stage. Misalignment results in increased etching time for the silicon dioxide, which was found to be 2 additional minutes for the processed wafers. As the device features are released well before the release of the dice, this had no effect on the yield. By microscope inspection, the 1μm test features on the wafer were found to be a minimum of 0.7μm wide. This implies over-etch of the photoresist of 150nm from each feature side. The thinning of device members results in a decreased stiffness at the compliant parts (increased deflection, decreased natural frequency, decreased robustness) and a lower capacitance at the comb-fingers.

DRIE

The handle layer DRIE was designed to have a very high tolerance and a deviation from a 90 degrees profile would only have as a result the quicker release of the dice, which does not affect performance or yield. Conversely, the deviation from 90 degrees at the device layer affects device performance. The gap around critical compliant parts of the devices was fixed to 20μm in the design. The process was then optimised for producing optimum results for these critical features. The sidewall angle at these features was found to deviate less than 1 degree from being vertical. A 1-degree deviation from vertical would result at shrinkage of 1.75μm at the bottom of the features. Thus, on average the features would be 875nm narrower along their thickness. This was taken into account during the design phase. The critical compliant features were designed to be 1μm wider than the desired value to compensate for photoresist and DRIE over-etching.

Release

As presented in the release section, although vapour phase etching of silicon dioxide offers substantially higher success than liquid form HF etching there are many variables that can affect the etch performance. Parameters such as HF solution level and quality, vapour pressure, ambient temperature, thickness and quality of the silicon dioxide can vastly affect the etch rate and subsequently the yield. The effective release of the devices was ensured by designing such that the critical device features release first and the dicing of the chips occurs last. A completed etching can be verified by inspecting the wafer. When the wafer is held with the device layer facing upwards, if the silicon dioxide has effectively been etched, the chips rest at a lower level (2μm) than the wafer frame. This can easily be observed as shown in Figure 5-11 for the conventional accelerometer. The etching time was adjusted accordingly where needed after the inspection of the wafers. During tests, it was found that in certain circumstances a very thin silicon dioxide layer might remain on the backside of the devices. This induces stress to the device layer and hence the devices become warped. This was successfully prevented by prolonging the etching time by 10%.

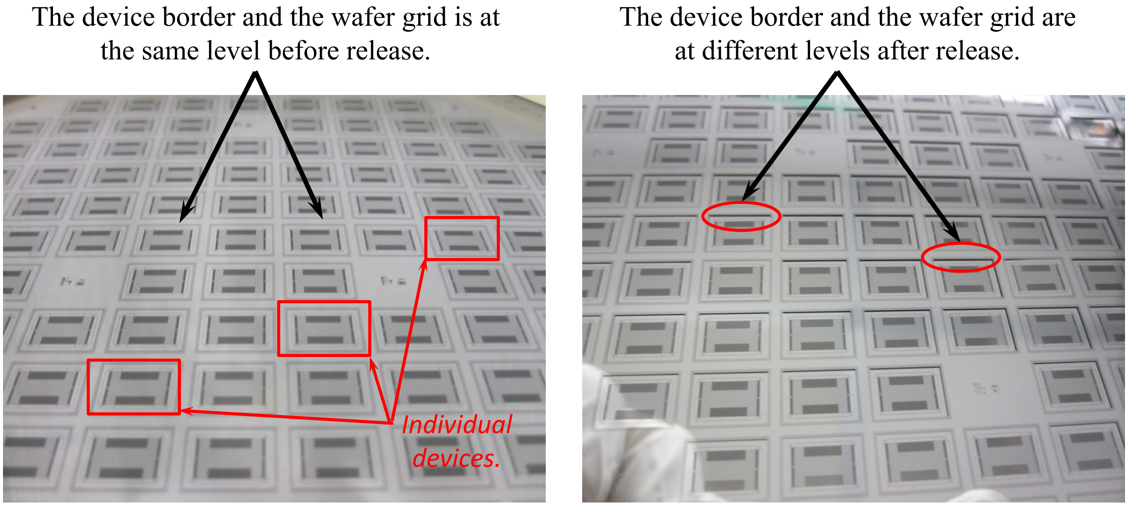
The device border and the wafer grid is at the same level before release.

The device border and the wafer grid are at different levels after release.

(a) Devices before release.

(b) Devices after release.

Figure 5-11 Part of the conventional accelerometer wafer a) before and b) after release. The devices rest at a lower level than the wafer grid after release. Taken from [77]

Although not a big sample of the particular devices was inspected to give strong statistical evidence for the yield, the yield performance was considered to be matching that of the conventional accelerometer, which was fabricated on different wafers at the same batch as the mechanically amplified design. As stated in [77] 135 out of the 143 were successfully released and were not found to have any defects after inspecting them under a microscope. The yield is therefore considered to be 95%.

The few devices that were tested do not offer an adequate sample for device performance variation. Nevertheless, an estimated theoretical assessment can be performed. As will be shown in Chapter 7, the maximum deviation of a measured parameter from the expected value was 20%. Although, this percentage includes a large number of error sources such as simulation and measurement errors it provides an estimate of the expected device performance variation. The performance sensitivity to parameters variation analysis presented in 4.4.1 may also be used as a guide to device performance dependence on size variations.

As the fabricated devices were used to prove the concept of mechanical amplification and not to adhere to a particular specification set, parameter variation due to fabrication imperfections did not affect the outcome of this research. Nevertheless, a commercial device based on the concept presented in this thesis should comply with certain tolerances according to the specifications. The fabrication process presented in this chapter offers a well-controlled procedure and hence it may be used to produce devices with specified performance and tolerance.

5.3 Conclusions on the fabrication

Although it was not optimised for these devices, the well-established SoG fabrication process developed in the University of Peking, China proved to produce functional prototypes. In order to establish a robust microfabrication process at Southampton Nanofabrication Facility, several steps were undertaken. The first was to explore the use of a very basic single mask SOI process. This helped in optimising the DRIE process for a range of device geometries. The limitations imposed by the handle SOI layer behind moving parts were alleviated by introducing a second mask in the process to etch the backside of the SOI wafers. With the second mask, a system of connecting bridges was introduced between the chips in order to simplify and reduce the risk of failure from dicing. In the meantime, the release step was evolved from a simple HF-water-IPA-cyclohexane dip to a more sophisticated substitution of the fluids increasing in this way the yield of the released devices. This release process gave much better results in terms of stiction but is rather complicated and dangerous due to the uncontrollability of the acid traces remaining in the solution. Problems with the release process were solved by using a vapour phase HF etcher. The vapour phase etcher offered the ability to safely remove parts of the handle wafer without risking failure during the DRIE. It also completely eliminated the need for dicing since the devices were separated during release due to specially designed front and backside trenches. The final fabrication process presented here was subsequently used for the fabrication of many different devices. Although not used for the mechanically amplified accelerometers a final refinement of the process, implemented after the fabrication of the sensors presented here, was to include a hard mask (1μm Plasma Enhanced Chemical Vapour Deposition (PECVD) silicon dioxide mask etched in an Inductively Coupled Plasma (ICP) etcher) for the device features etching. This eliminated the use of a handle wafer during spinning since the mask was defined before the etching of the SOI handle wafer and can be directly applied at the mechanically amplified sensors designs without modification of the fabrication masks. Apart from reducing the possibility of failure due to user mishandling, the additional steps constitute a process compatible with automatic tools such as robotic spinners and aligners. The development of the process constituted a considerable part of this research project and allowed to efficiently produce prototypes of a wide range of devices at the Southampton Nanofabrication Centre. The fabrication process was published for the reference sensor in [77]. Figure 5-12 shows a detail of the output of a fabricated sensor from the final stable SOI process presented in this chapter.

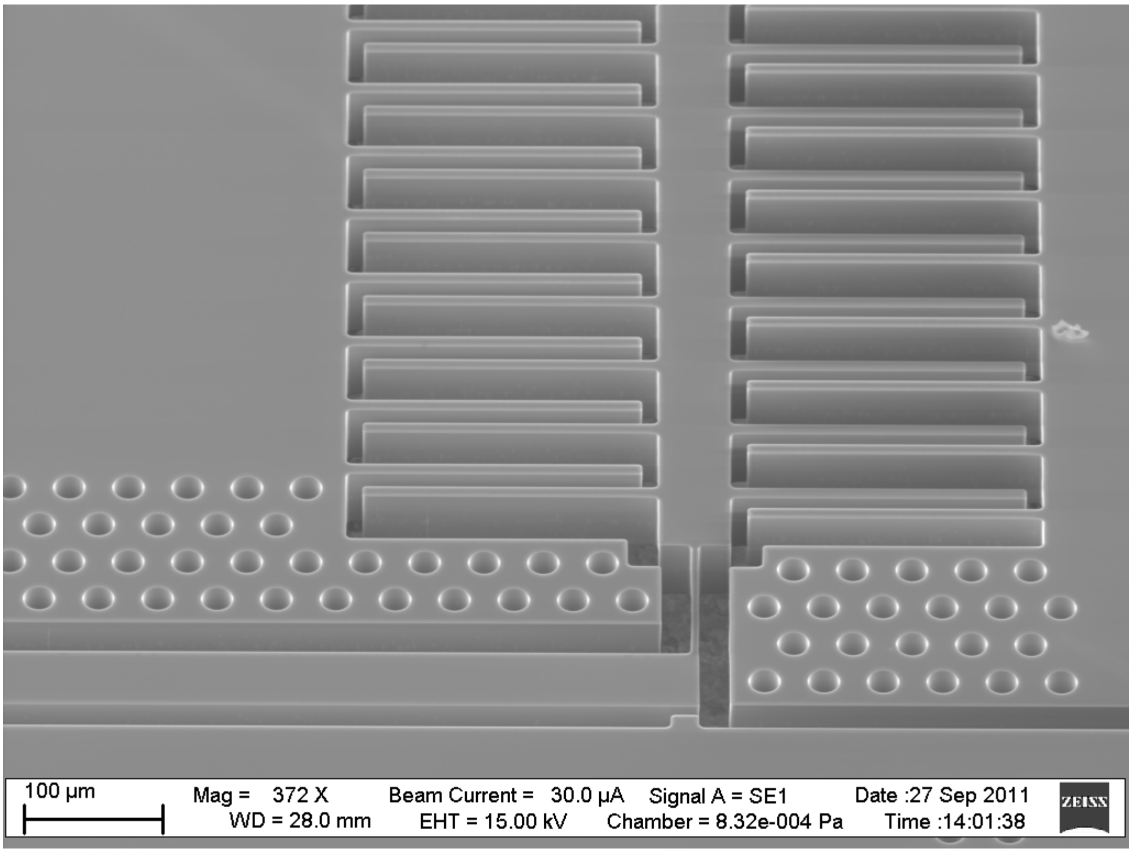

Figure 5-12 SEM detail from the output of the mechanically amplified accelerometer using the Zeiss EVO scanning electron microscope [79].

Chapter 6 Interface electronics

6.1 Pick-off circuit design

In order to electrically test the mechanically amplified accelerometers a capacitive pick-off circuit is needed. As the focus of the research presented here was the mechanical part, a rather simple circuit design with well-defined operation was used. The accelerometer can be used with a more sophisticated circuit in the future to meet specific application demands such as closed loop operation. The circuit used was based on charge amplifiers as presented in [80].

The pick-off circuit was implemented on a Printed Circuit Board (PCB) using surface mount components. The sensors were connected to the circuit through a specially designed PCB holder with gold contacts such as the one shown in Figure 6-1. The PCB holder offered a quick and inexpensive way to test and compare various sensor chips. The devices were attached to the PCB holders using crystalbond. The F&K Delvotec 5430 wedge aluminium wire wirebonder [81] was used to electrically connect the sensors to the gold pad connections of the holder board. The advantage using an aluminium wedge wirebonder over a gold wirebonder is that the wires can be bonded directly onto the silicon surface, thus it was not required to deposit gold on the devices. An additional advantage of the aluminium wedge wirebonder is that the samples do not need to be heated up for the bonding process, alleviating the necessity of using a special adhesive for attaching the chips on the board. Crystalbond can be released by heat (67^{o}C) so any damaged sensors could be removed easily.

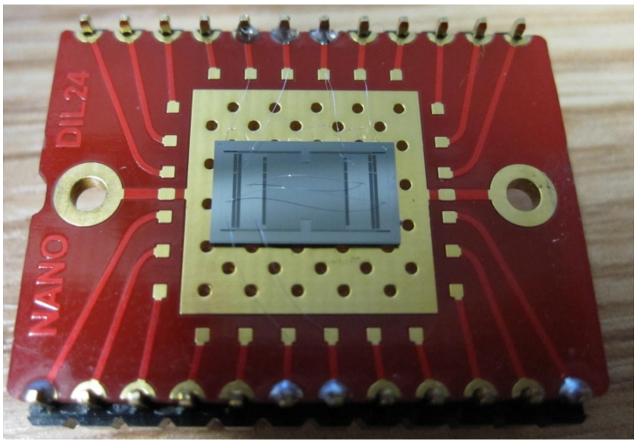

Figure 6-1 Designed PCB device holder with a sensor bonded with crystal bond and wired with a wedge aluminium wirebonder.

As mentioned earlier, the sensors also include comb-fingers at the proof mass for comparative signal pick-off. To achieve a fair comparison of the proof mass deflection to the mechanically amplified output deflection, the circuit that capacitively measures the motion has to be identical for the two sets of comb-fingers. For this reason, the sensor was wirebonded in such a way that both sets of comb-fingers could be measured (individually) by the same circuit by simply connecting the sensor holder in an inverted way to the pick-off board. The following sections aim to briefly discuss the operation of the pick-off circuit based on the mechanically amplified output of the 1HAN accelerometer.

6.2 Circuit operation

The circuit was simulated in Orcad Spice [82]. In order to simulate the capacitance variation of the sensors, an XY variable admittance block from the analogue behavioural modelling library was used. The sensor has large parasitic capacitances. The largest parasitic capacitance is the proof mass to handle wafer capacitance. It also imposes a 200Ω electrical resistance between its terminals. The parasitics were measured through Agilent CV IV tools [83] and were included in the electrical model of the sensor as shown in Figure 6-2. It was important to include the parasitic components in order to match the measurement results. It also proved crucial to include the exact amplifier models that were used in the circuit for the simulation.

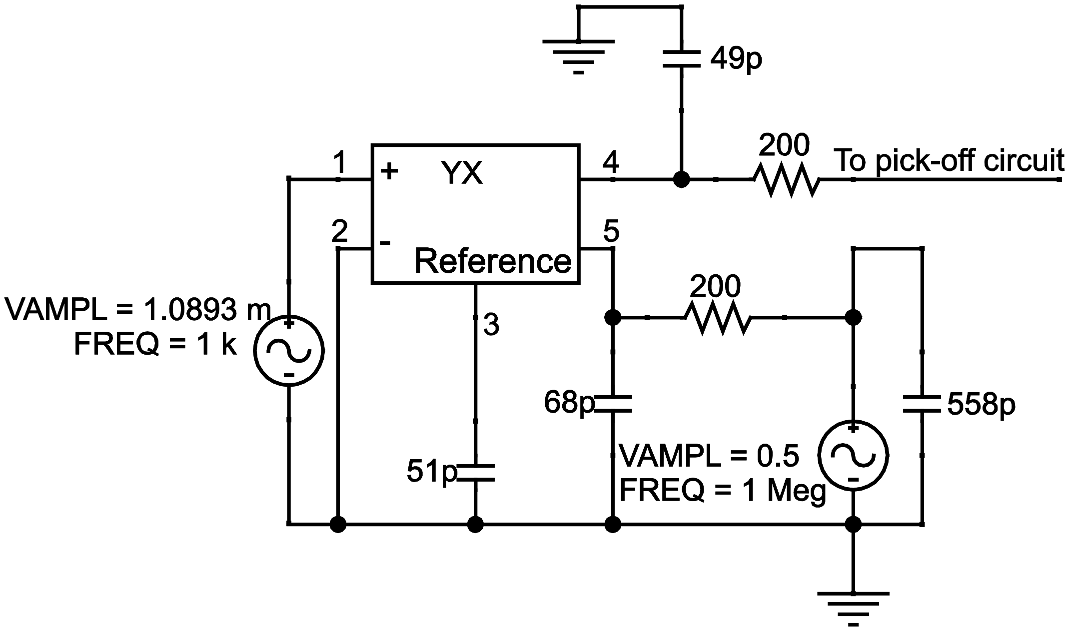

Figure 6-2 XY variable admittance block to simulate the change of capacitance of the mechanical element of the sensor in Orcad Spice. The model includes parasitic elements to model the parasitics of the actual sensor. The most prevalent parasitic is the 200Ω resistor between the sensor and circuit terminals. The model follows standard Orcad Spice notation.

The pick-off circuit shown in Figure 6-4 is based on charge amplifiers such as the one shown in the schematic of Figure 6-3. Two charge amplifiers were used for the two differential sides. A 1Vp-p carrier at 1MHz signal is connected to the proof mass of the accelerometer. When the sensor is subjected to acceleration, the carrier signal is modulated through the gap variation of the comb-fingers.

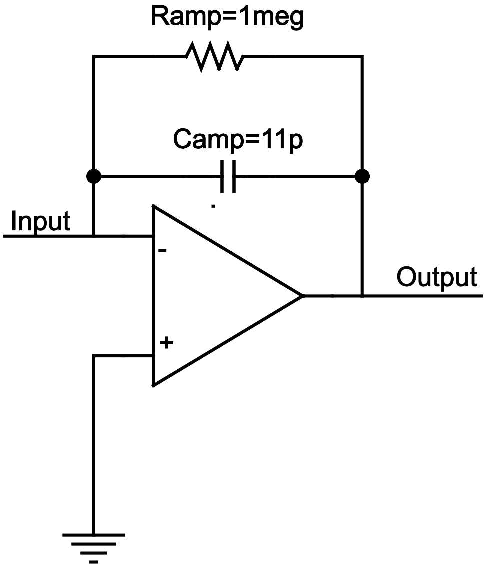

Figure 6-3 A charge amplifier with the component values used in the implemented circuit. The model follows standard Orcad Spice notation.

While the comb-fingers move under acceleration their capacitance changes by ΔC. This change produces a proportional charge ΔQ. When the voltage of the carrier applied on the proof mass is V then the charge at the comb-fingers output terminal is $\Delta Q=V*\Delta C$. A charge amplifier connected at this terminal will translate the charge change to a voltage at its output. If the capacitor of the charge amplifier is denoted as C_{amp} then the voltage change will be $\Delta V=-V*\Delta C/C_{amp}$. Since the variation of the capacitance of the comb-fingers will be orders of magnitude lower than the nominal capacitance C_s, it may be considered that the gain of the charge amplifier is approximately $G=C_s/C_{amp}$. The sensor was excited with a sinusoidal acceleration of 1g amplitude at 1kHz (the excitation signal was set higher than the natural frequency of the 1HAN sensor (740Hz) to increase the simulation speed but the results are also valid for lower excitation frequencies.) ΔC =57fF in this case.

The demodulation of the charge amplifier signal is obtained by a simple diode demodulator and a low pass filter system reduces the high frequency components.

After the demodulation of the signal, the two differential parts are fed into an instrumentation amplifier in a differential arrangement. The differential amplifier subtracts the two inverted signals, amplifies them, and rejects any common mode signals.

The signal is then further filtered by low pass filters and a final inverting amplifier stage amplifies the differential and filtered signal. Figure 6-4 presents the discussed signal path.

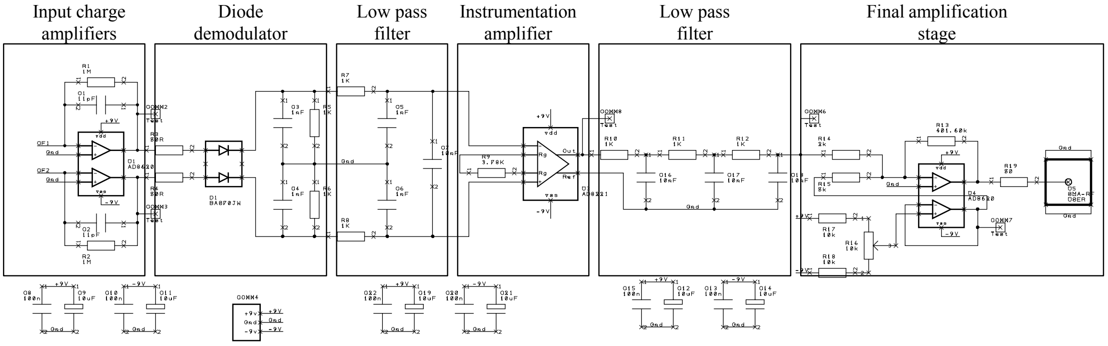

Figure 6-4 Schematic of the capacitive pick-off circuit. The differential output of the mechanical sensor is connected to the inputs (CF1, CF2) of the charge amplifiers, it is then demodulated and filtered by a diode demodulator. After the demodulation, an instrumentation amplifier amplifies the difference in the signal path. Finally, after further filtering the signal is provided to the output through an inverting amplification stage.

As mentioned earlier the circuit was simulated in Orcad Spice. The simulation model was identical to the schematic of Figure 6-4 apart from the addition of the electrical model of the sensor shown in Figure 6-2 that was connected to the input of the circuit. The output of the pick-off circuit for a simulation with a 1g sinusoidal acceleration for the 1HAN accelerometer is shown in Figure 6-5. As it will be shown in the next chapter, this agrees very closely to the experimental measurements.

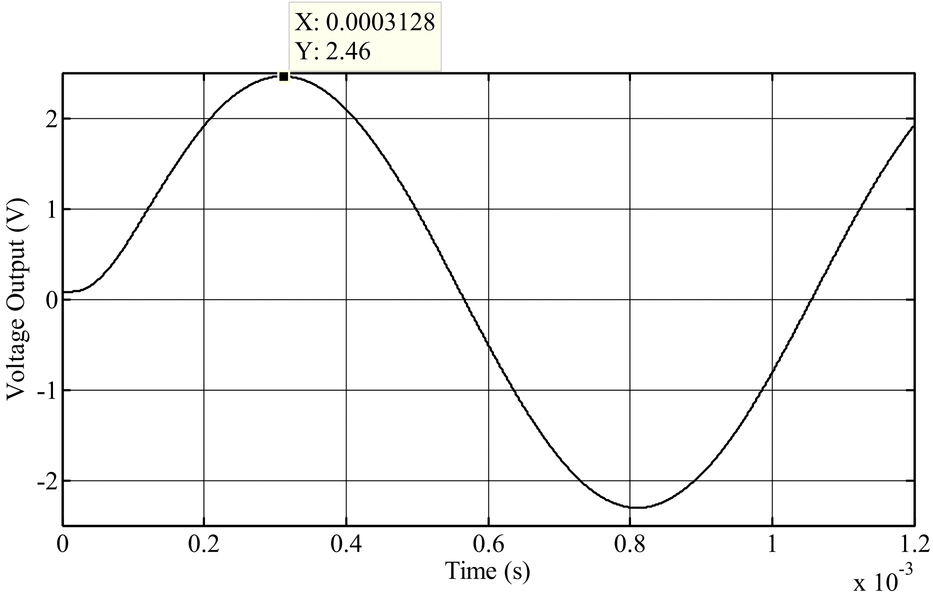

Figure 6-5 Output of the Orcad Spice simulated capacitive pick-off circuit. In this simulation, the excitation signal was equivalent to 1g at a frequency of 1kHz and a carrier of $1V_{p\text{-}p}$ at 1MHz was used. The output reaches 2.46V at the peak, which agrees very well with the experimental data shown in Chapter 7.

6.3 Electromechanical simulation

As mentioned earlier, the Architect module of Coventorware can simulate coupled electromechanical systems. The pick-off circuit was also simulated in Architect. It was then possible to include both mechanical and electronic designs into one simulation as shown in Figure 6-6. The simulation results verified the Spice simulations. Whereas the individual simulations in Architect take an insignificant amount of time the entire electromechanical system simulation demands requires very high computational power. This is due to the signals present over a very wide bandwidth (500Hz acceleration, 1MHz carrier). The results of the entire system simulation were obtained after 3 hours for a 1.5ms transient analysis.

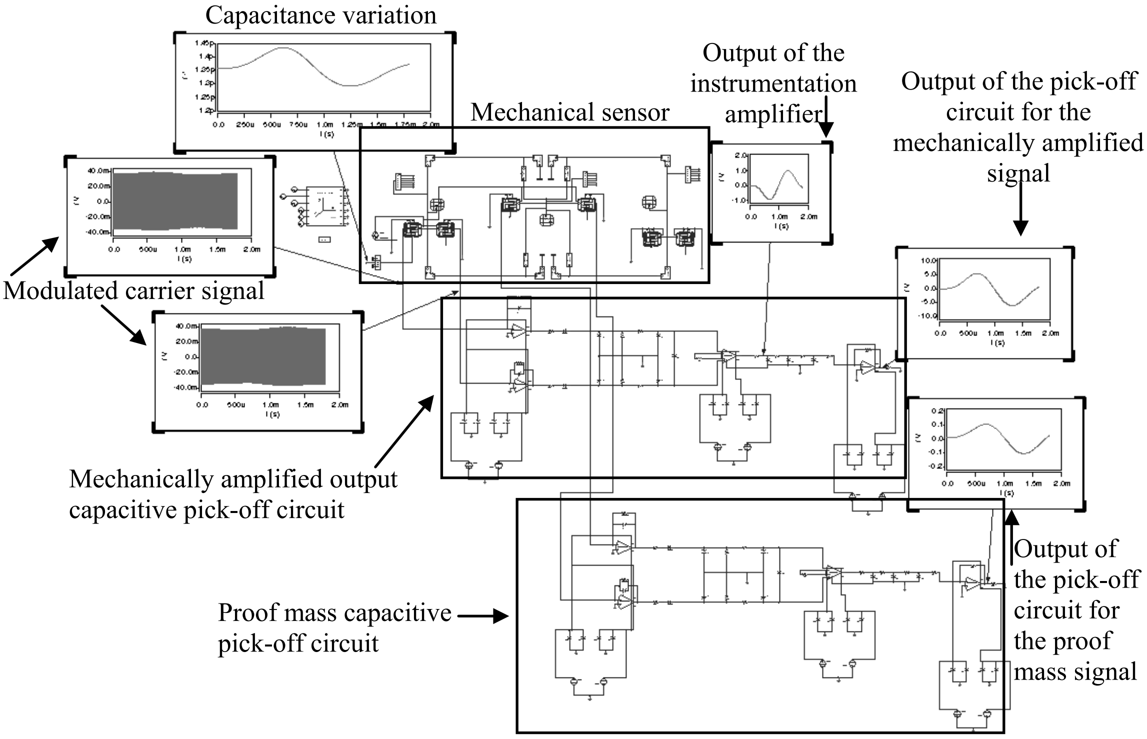

Figure 6-6 Architect simulation of the entire system. The simulation model shown in Figure 4-4 was connected to capacitive pick-off circuits to provide a full electromechanical simulation model. The two modelled circuits were connected to the amplified output and the proof mass respectively. The simulation results show the electrical output signals from the microlevers and the proof mass but any signal in the signal path (mechanical or electrical) can as well be displayed providing a very thorough electromechanical simulation.

6.4 Conclusions

The operation of the charge amplifier based pick-off circuit was discussed in this chapter. The open loop circuit offers simplicity of implementation and use. Additionally, the hardware was easy to debug. The compact PCB design offered relatively low noise, which can further be improved by optimising the design in the future. The same circuit was used to resolve the proof mass and the amplified motion. This is owed to the special PCB holder that was used and the way that the sensor was wirebonded. During the circuit simulation, it proved vital to use exact spice models of the amplifiers and include a model of the parasitic capacitance and resistance of the sensor. As will be shown in the next chapter the simulations predict the measurement results very well. An electromechancial simulation model was implemented in Architect. It provided estimation of the entire system operation, but proved highly computationally intensive. The implemented circuit is generic and hence with slight modifications can be used for a variety of capacitive accelerometers.

Chapter 7 Measurement results

7.1 Introduction and methodology

The mechanically amplified accelerometers were characterised both optically and electrically. The optical characterisation was performed with Polytec Micro System Analyser (MSA400) system [84], whereas the electronic measurements were performed with the use of the interface electronics circuit of Chapter 7 and a shaker system from Labworks [85]. The optical methods preceded the electronic measurements. Optical surface topography measurements were used to verify the successful fabrication of the sensors and reveal the static out-of-plane deflections due to gravity and stress. Laser Doppler vibrometry was used to evaluate the out-of-plane modes of the sensors. Optical planar motion analysis offered a means to compare the motion of the proof mass to the mechanically amplified output. Static measurements were performed by connecting the sensors to the interface circuit and employing a dividing head. The static measurements returned results for the noise performance of the sensors, the static mechanical amplification, and the static linearity. Measurements with the shaker system revealed the in-plane natural frequency of the sensors, the mechanical amplification factor, and the linear dynamic range. The results from the optical and electronic measurements were compared to each other to verify their validity and sources of errors are discussed. This chapter aims to present the measurement results, compare them with the simulations, and assess the operation of the sensor.

7.2 Optical measurements

The accelerometers were characterised optically under the Polytec MSA400 measuring system. MSA400 is an optical system that provides the ability to characterise out-of-plane motions using laser Doppler vibrometry, in-plane motions using stroboscopic imaging, and to take topography measurements by a white light interferometry method. The advantage of optical measurements is that the use of a pick-off circuit is not required. This greatly decreases the measurement time and helps avoid issues related to pick-off circuit such as electronic noise and non-ideal behaviour of the shaker system. The sensors in this case are excited by an electrical signal rather than acceleration and hence the measurement results have to be interpreted carefully, as will be discussed in the following sections.

7.2.1 Topography measurements

The effective fabrication of the sensors was verified using the white light interferometer of the MSA400. The sensors were investigated for defects before further measurements. When the sensors are placed flat on the measurement chuck, they are subjected to 1g constant out-of-plane acceleration due to gravity. As it was shown in Chapter 4, the sensors are sensitive to out-of-plane acceleration. It was possible to measure the out-of-plane static deflection using the interferometer. The results showed that the microlever outputs of the 1HAN and 2LAN overhung (lower than the frame of the sensor) by 430nm and 520nm respectively as shown in Figure 7-1 and Figure 7-2.

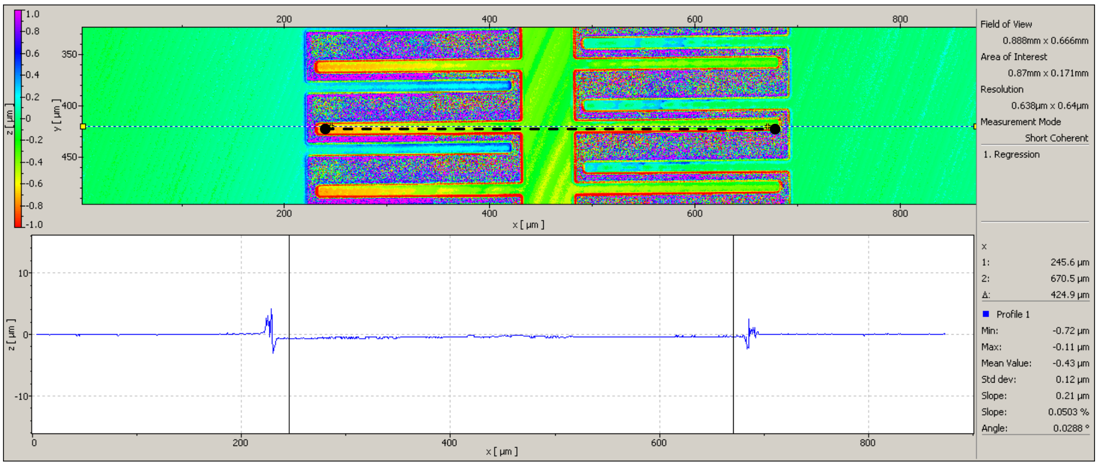

Field of View
0.888mm x 0.666mm
Area of Interest
0.87mm x 0.171mm
Resolution
0.638µm x 0.64µm
Measurement Mode
Short Coherent
1. Regression

x
1: 245.6 µm
2: 670.5 µm
Δ: 424.9 µm
■ Profile 1
Min: -0.72 µm
Max: -0.11 µm
Mean Value: -0.43 µm
Std dev: 0.12 µm
Slope: 0.21 µm
Slope: 0.0503 %
Angle: 0.0288 °

Figure 7-1 Interferometer measurement results for the 1HAN accelerometer. The figure shows the surface of the device coloured according to its height. The graph represents the height measurements across the vertical profile in the picture. The out-of-plane deflection of the mechanically amplified output is measured as the mean value of the height difference between the sensor frame and the mechanically amplified output. The frame top surface was set to z=0 and the mean value for the output is calculated between the two vertical lines in the graph (comb-finger tip at left to comb-finger tip at right side). For 1HAN, the amplified output deflects downwards and the mean height difference is 430nm.

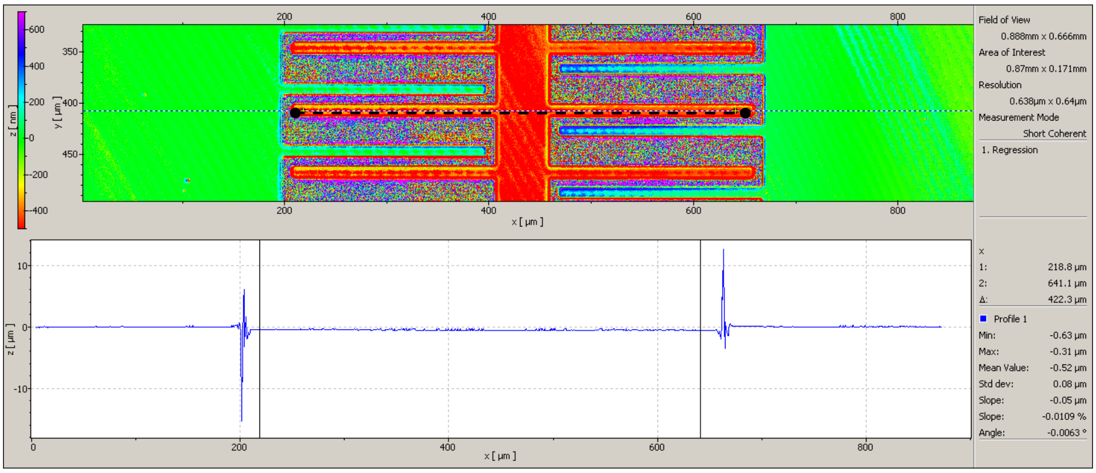

Field of View
0.888mm x 0.666mm
Area of Interest
0.87mm x 0.171mm
Resolution
0.638µm x 0.64µm
Measurement Mode
Short Coherent
1. Regression

x
1: 218.8 µm
2: 641.1 µm
Δ: 422.3 µm
■ Profile 1
Min: -0.63 µm
Max: -0.31 µm
Mean Value: -0.52 µm
Std dev: 0.08 µm
Slope: -0.05 µm
Slope: -0.0109 %
Angle: -0.0063 °

Figure 7-2 Interferometer measurement results for the 2LAN accelerometer. The figure shows the surface of the device coloured according to its height. The graph represents the height measurements across the vertical profile in the picture. The out-of-plane deflection of the mechanically amplified output is measured as the mean value of the height difference between the sensor frame and the mechanically amplified output. The frame top surface was set to z=0 and the mean value for the output is calculated between the two vertical lines in the graph (comb-finger tip at left to comb-finger tip at right side). For 2LAN, the amplified output deflects downwards and the mean height difference is 520nm.

Although the Z-axis deflection of 1HAN agrees well with the simulation results (Table 4-1, FEM 415nm, Architect 521nm), the 2LAN deflection is half than expected (Table 4-2, FEM 1.11µm, Architect 1.47µm). This is attributed to stress induced from the fabrication process to the devices, as it will be explained later. This effect is more evident on the devices with the out-of-plane suppressing springs. 3HAS and 4LAS mechanically amplified outputs deflect upwards by 290nm and 430nm respectively according to the interferometric measurements as shown in Figure 7-3 and Figure 7-4.

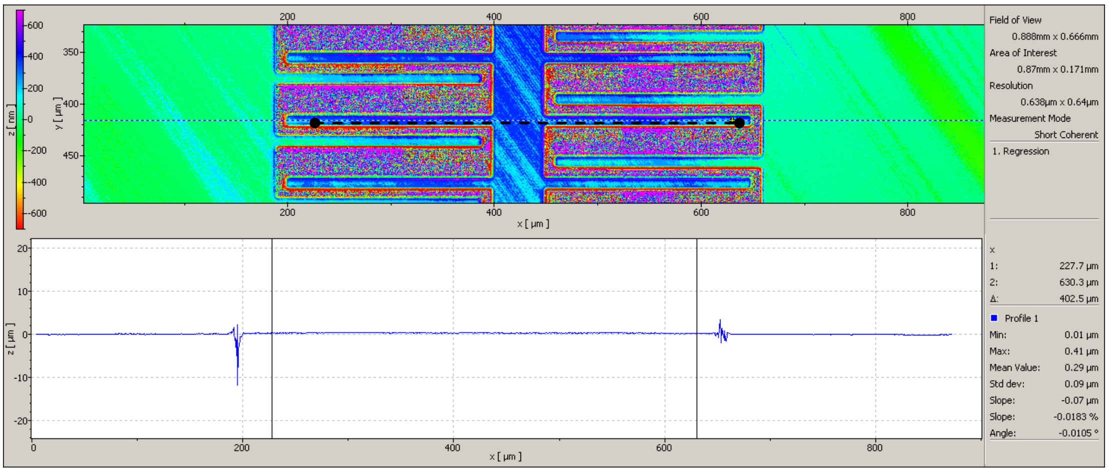

Field of View
0.888mm x 0.666mm
Area of Interest
0.87mm x 0.171mm
Resolution
0.638μm x 0.64μm
Measurement Mode
Short Coherent
1. Regression

x
1: 227.7 μm
2: 630.3 μm
Δ: 402.5 μm
Profile 1
Min: 0.01 μm
Max: 0.41 μm
Mean Value: 0.29 μm
Std dev: 0.09 μm
Slope: -0.07 μm
Slope: -0.0183 %
Angle: -0.0105 °

Figure 7-3 Interferometer measurement results for the 3HAS accelerometer. The figure shows the surface of the device coloured according to its height. The graph represents the height measurements across the vertical profile in the picture. The out-of-plane deflection of the mechanically amplified output is measured as the mean value of the height difference between the sensor frame and the mechanically amplified output. The frame top surface was set to z=0 and the mean value for the output is calculated between the two vertical lines in the graph (comb-finger tip at left to comb-finger tip at right side). For 3HAS, the amplified output deflects upwards and the mean height difference is 290nm.

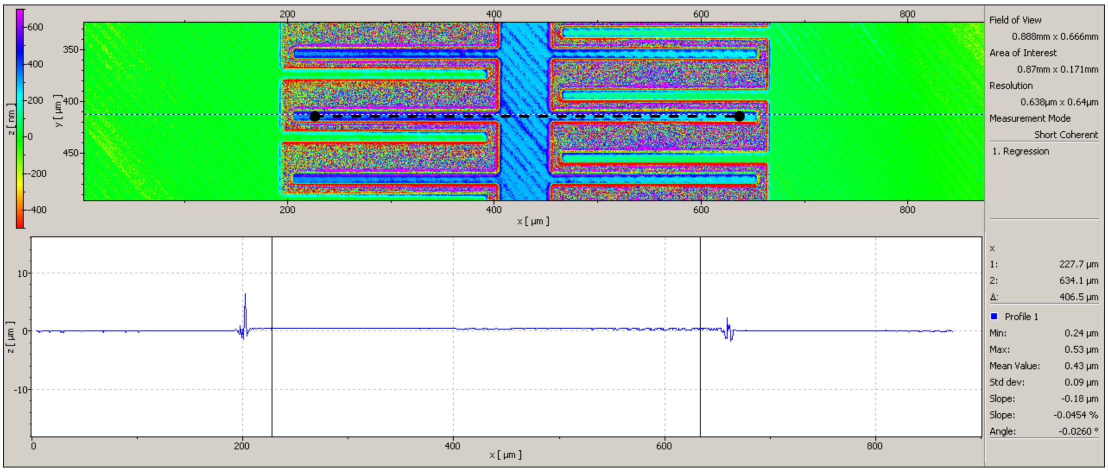

Field of View
0.888mm x 0.666mm
Area of Interest
0.87mm x 0.171mm
Resolution
0.638μm x 0.64μm
Measurement Mode
Short Coherent
1. Regression

x
1: 227.7 μm
2: 634.1 μm
Δ: 406.5 μm
Profile 1
Min: 0.24 μm
Max: 0.53 μm
Mean Value: 0.43 μm
Std dev: 0.09 μm
Slope: -0.18 μm
Slope: -0.0454 %
Angle: -0.0260 °

Figure 7-4 Interferometer measurement results for the 4LAS accelerometer. The figure shows the surface of the device coloured according to its height. The graph represents the height measurements across the vertical profile in the picture. The out-of-plane deflection of the mechanically amplified output is measured as the mean value of the height difference between the sensor frame and the mechanically amplified output. The frame top surface was set to z=0 and the mean value for the output is calculated between the two vertical lines in the graph (comb-finger tip at left to comb-finger tip at right side). For 4LAS, the amplified output deflects upwards and the mean height difference is 430nm.

The simulation results (Table 4-3) showed a downward deflection of 11.6nm (FEM) and 17nm (Architect) for the 3HAS. For the 4LAS (Table 4-4) the values were 51nm (FEM) and 52nm (Architect). High stress levels were evident during the fabrication process. In the two fabricated wafers these devices came from, some devices sprung off the wafer before the final step. This reveals that the wafers were highly stressed. The fabrication step responsible for the high stress seems to be the backside DRIE etch since the wafers presented defects, such as sprung devices, right after this step. Another possible cause for stressed and deformed SOI MEMS devices is residual silicon dioxide. If during the release process there is even a small amount of silicon dioxide left at the back of the devices (which proved common with the HF vapour etcher used) this will make them deform due to uneven stress, which can explain the results obtained for the devices examined here. Since the anchors of the devices are large enough to withstand longer release times this should be considered in later fabrications by prolonging the release time to avoid residual silicon dioxide induced stress.

7.2.2 Laser Doppler vibrometer measurements

Since the sensors have out-of-plane modes close to the in-plane sense modes it is important to know if these modes are correctly predicted by the simulation. Most importantly, it has to be investigated whether those modes are below or above the natural frequency of the sense mode. Being below the sense natural frequency would result in a bandwidth limitation. For this purpose the sensors out-of-plane modes were evaluated under the laser Doppler Vibrometer. To induce a vibration on the sensor the handle wafer below the proof mass was biased with a DC voltage whereas the proof mass was driven with a periodic chirp signal as shown in Figure 7-5.

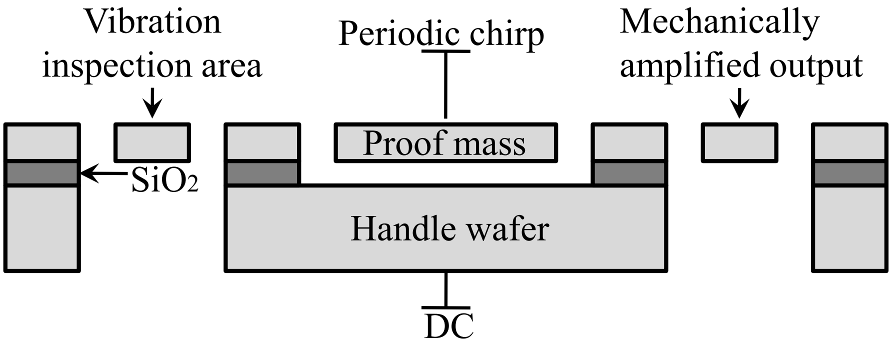

Figure 7-5 For the laser Doppler vibrometer measurements the handle wafer was biased with a DC voltage whereas the proof mass was driven with a periodic chirp signal. As mentioned in Chapter 5 the handle wafer behind the mechanically amplified output had been removed during fabrication thus the output could not be directly excited out-of-plane.

The measurement data did not show the out-of-plane modes clearly for all sensors types. This is due to the way the sensors were excited. There is no implemented mechanism to electrostatically excite the mechanically amplified output out-of-plane. Nevertheless, for the 1HAN two clear out-of-plane modes were apparent at 850Hz and 982Hz. Those were within 7% of the predicted values (Table 4-1 in Chapter 4 Mode2 786Hz, Mode 3 914Hz). They are also at least 100Hz higher than the in-plane mode (740Hz) hence they do not restrict the sense bandwidth. Although not entirely clear, for the 2LAN there were two out-of-plane modes, one at 594Hz, and another at 810Hz. Those agree within 10% of the predicted values (Table 4-2 in Chapter 4 Mode2 625Hz, Mode 3 724Hz) and are above the sense mode frequency (Table 4-2 553Hz). For the 3HAN, there was only one measurable out-of-plane mode at 4.67kHz, which is within 1% of the second mode predicted from the system level simulation but double from the FEM (Table 4-3 in Chapter 4). Finally, for the 4HAS accelerometer there was evidence for an out-of-plane mode at 5.18kHz, which is much higher than any predicted value (Table 4-4 in Chapter 4). Although the measurement results do not agree entirely with predicted behaviour by simulation they clearly show that the out-of-plane modes are higher than the in-planes in all the sensor types, hence the sense bandwidth is not restricted by these modes.

7.2.3 Planar motion analysis

The dynamic in-plane operation of the sensors was evaluated using stroboscopic image correlation. In this method, a stroboscopic camera is used to obtain a predefined number of images of a distinct pattern of the sensor during each cycle for each frequency of excitation used in the test. Then, the images are correlated and hence the deflection of the sensor for different frequencies may be extracted.

Although this method of evaluation is entirely optical and there is no need for a pick-off circuit the sensor has to be excited by an electrostatic force since excitation using vibrations (i.e. shaker) cannot be obtained at the same reference frame as the stroboscopic camera. In order to drive the sensor a bias voltage was applied at the comb-fingers whereas a sinusoidal signal was fed to the proof mass through its anchors. The unused comb-fingers and the handle layer were connected to the proof mass signal to prevent floating nodes that could affect the operation of the sensor. The electrical connections used in the planar motion analyses are shown in Figure 7-6.

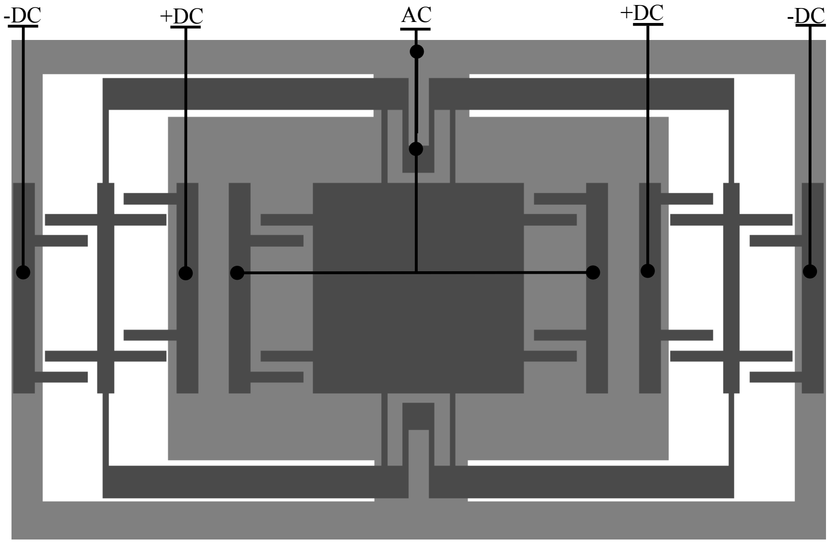

Figure 7-6 Electrical connections of the mechanically amplified accelerometers for planar motion measurements. An AC signal is applied at the proof mass and the output comb-fingers are biased with a DC voltage. The remaining comb-fingers and the handle wafer are connected to the proof mass signal.

It must be noted that electrostatic excitation of the sensors is not equal to subjecting them to vibration. Acceleration induces an inertial force experienced by the entire mechanical structure. For a simple sensor with a single proof mass suspended on springs, it would be adequately accurate to assume that electrostatic excitation would produce an equivalent effect to an inertial force. However, this is not a valid assumption for the sensors under test. The microlevers and the output system add an appreciably amount of mass to the mechanical structure which is not directly subjected to the electrostatic force.

Electrostatic excitation adds another issue. The noise floor of the stroboscopic system is quite high. This is due to various noise sources such as random vibrations, acoustic noise, chosen objective magnification, camera resolution, optical contrast between features, and selected feature distinctness. Due to this, and as it will be discussed in the next paragraph, the sensors have to be excited with a large force in order to detect the small motion of the proof mass. Large electrostatic forces in mechanical systems with parallel plate translational capacitors result in electrostatic spring softening [86]. The large electrostatic forces used during the measurements (~150μN) resulted in a softer overall spring constant hence, a lower natural frequency was observed for all sensors. In order to justify the effect different electrostatic force amplitudes were used. It was found experimentally that when the sensors were excited so that the comb-fingers at the lever ends moved a distance smaller than an order of magnitude less than the comb-finger gap (<1μm) the natural frequencies were matching the modal analysis results within less than 5%. Unfortunately, for such an output deflection magnitude the motion of the proof mass could not be measured by the equipment.

The early SoG prototypes had an amplification factor of 60 and comb-finger gap of 4μm with 1μm stoppers. Therefore, the maximum that the amplified output could deflect was 3μm. Dividing this by 60 gives the maximum deflection of the proof mass, which is 50nm. The nominal sensitivity of the measuring equipment is 5nm Root Mean Square (RMS) when this is used with optimal settings [84], whereas the actual peak-to-peak noise at low frequencies (<500Hz) achieved with the experimental setup varied from 100nm to 500nm. Apart from the excessive damping, this is another reason that the comb-fingers gap of the final designs was designed to be 10μm. The lower amplification factors of the later designs also helped with the measurements. The maximum amplification factor is 40 and the comb-finger gap is 10μm with a 1μm stopper. The maximum deflection of the proof mass when the comb-finger gap at the output closes completely (equivalent to moving the amplified output 9μm) for an amplification factor of 40 is 225nm which is well within the measurement capabilities of the equipment.

The figures that follow (Figure 7-7 to Figure 7-14) present frequency sweeps using an AC excitation signal for the sensors and the extracted amplification factors for the four designs.

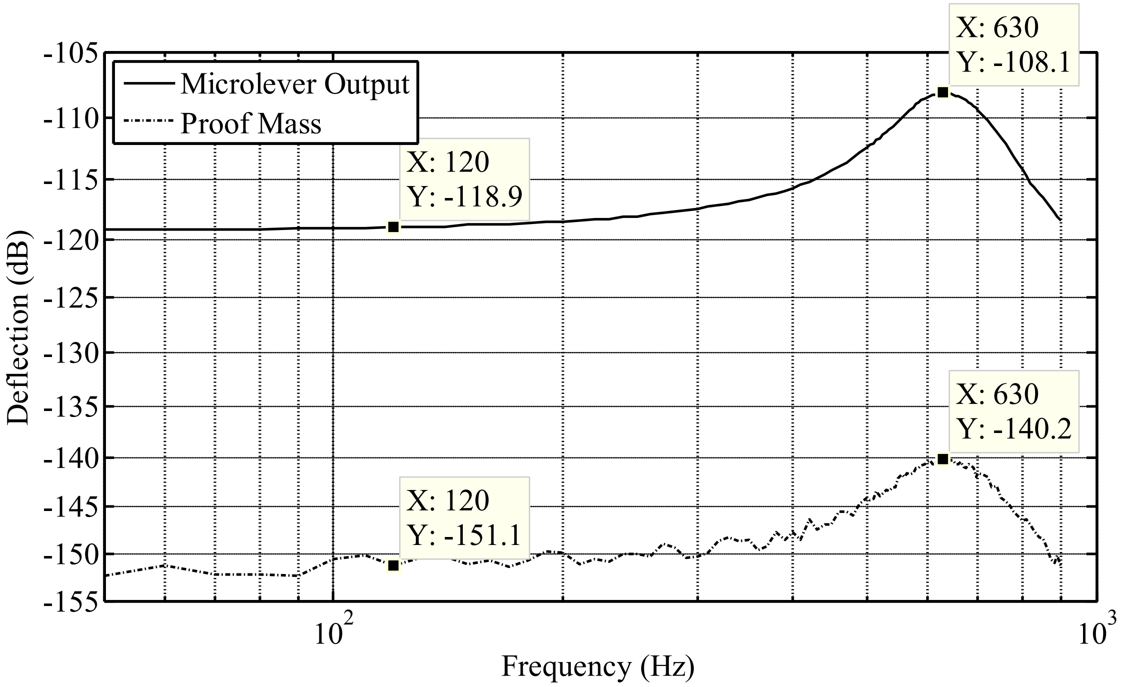

Figure 7-7 Device 1HAN frequency response of the output of microlevers and the proof mass motion using stroboscopic image correlation (0dB=1m).

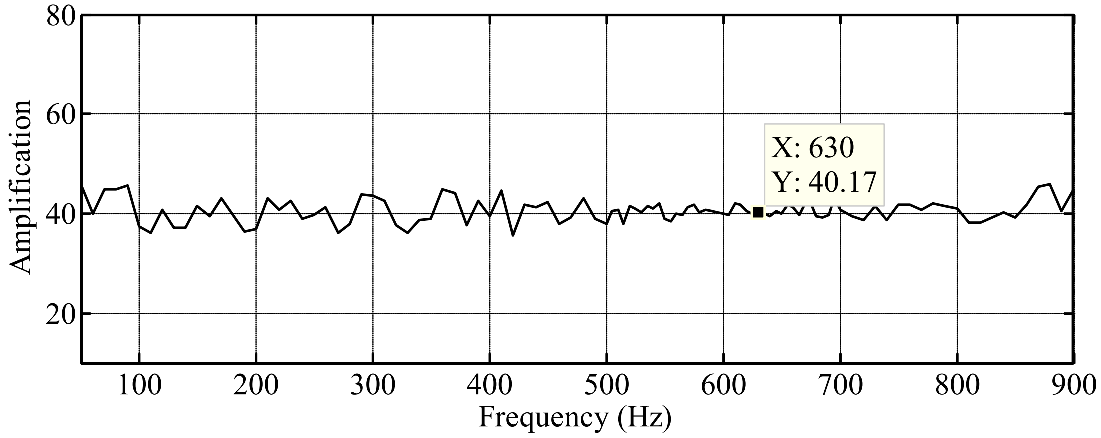

Figure 7-8 Device 1HAN amplification factor extracted from the individual displacements of the proof mass and output of microlevers. The small variation of the amplification factor is mainly due to the noise floor of the equipment when measuring the proof mass deflection.

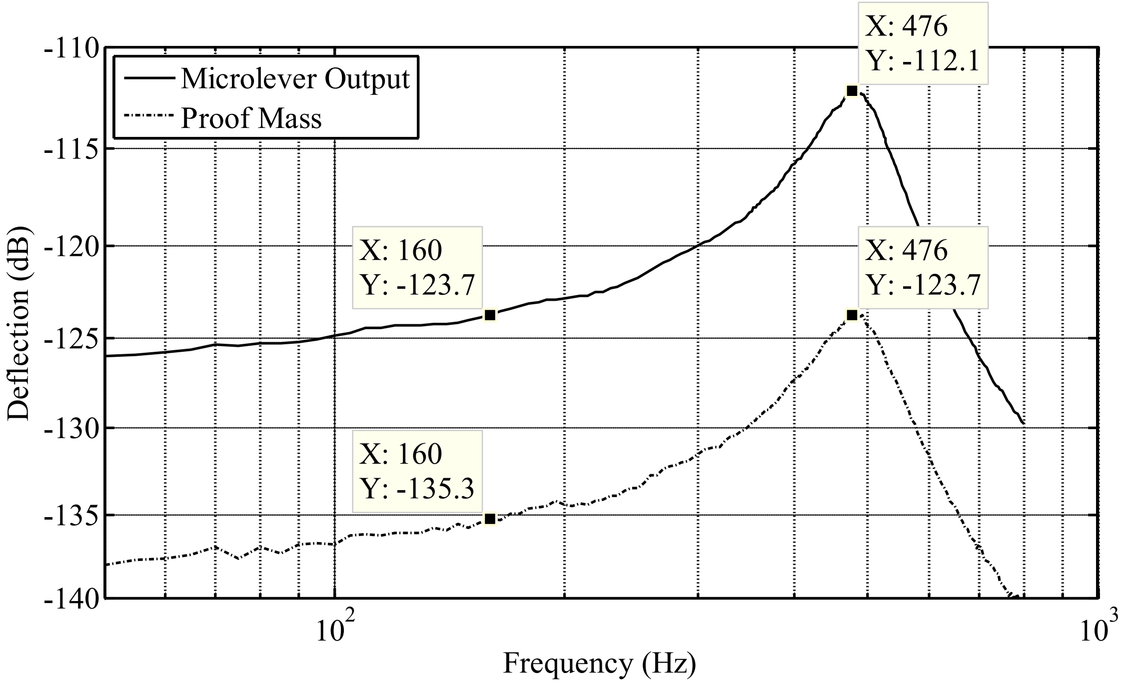

Figure 7-9 Device 2LAN frequency response of the output of microlevers and the proof mass motion using stroboscopic image correlation (0dB=1m).

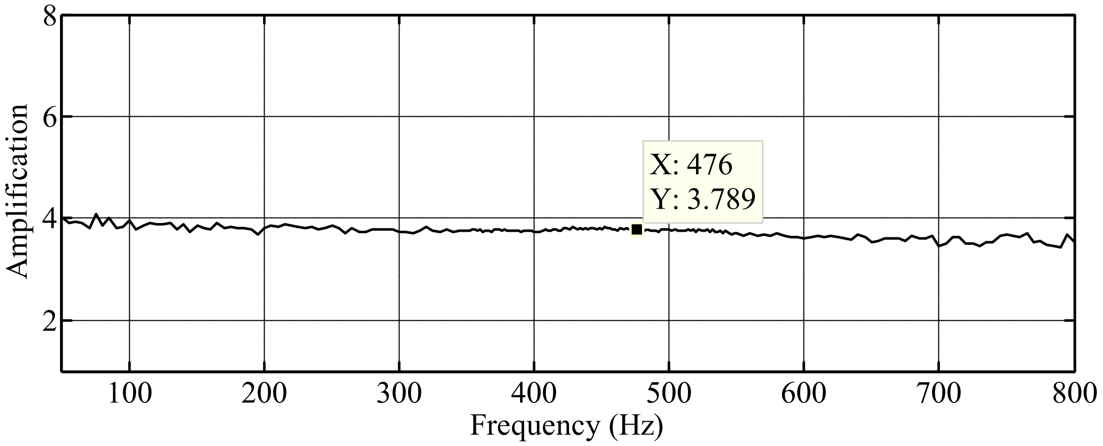

Figure 7-10 Device 2LAN amplification factor extracted from the individual displacements of the proof mass and output of microlevers. The small variation of the amplification factor is mainly due to the noise floor of the equipment when measuring the proof mass deflection.

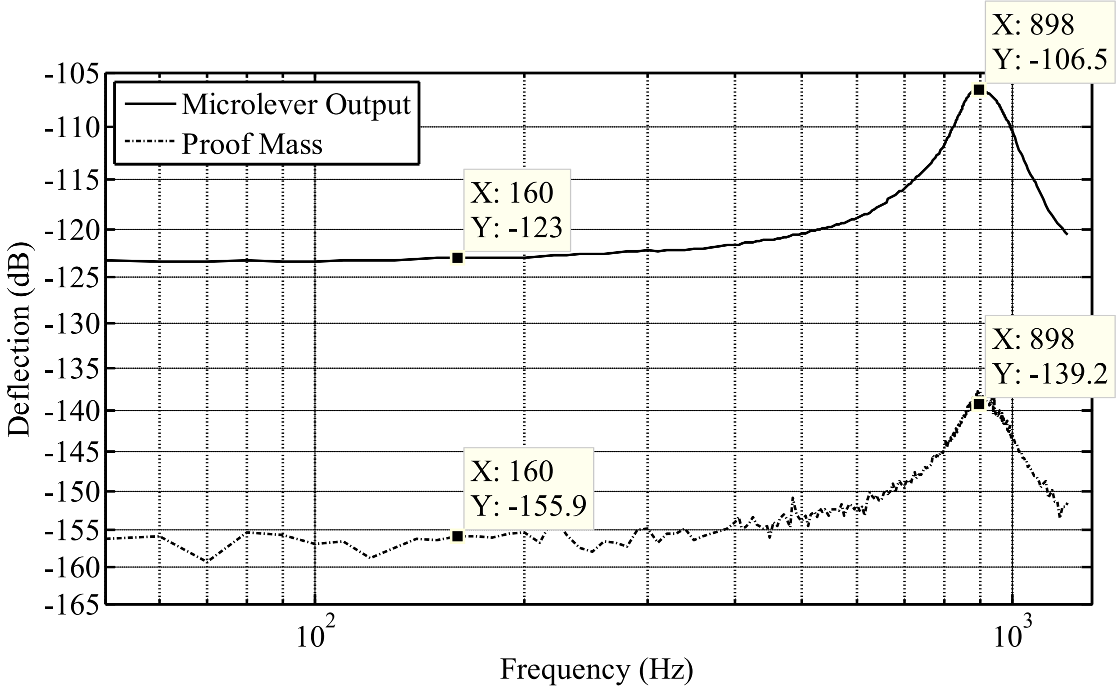

Figure 7-11 Device 3HAS frequency response of the output of microlevers and the proof mass motion using stroboscopic image correlation (0dB=1m).

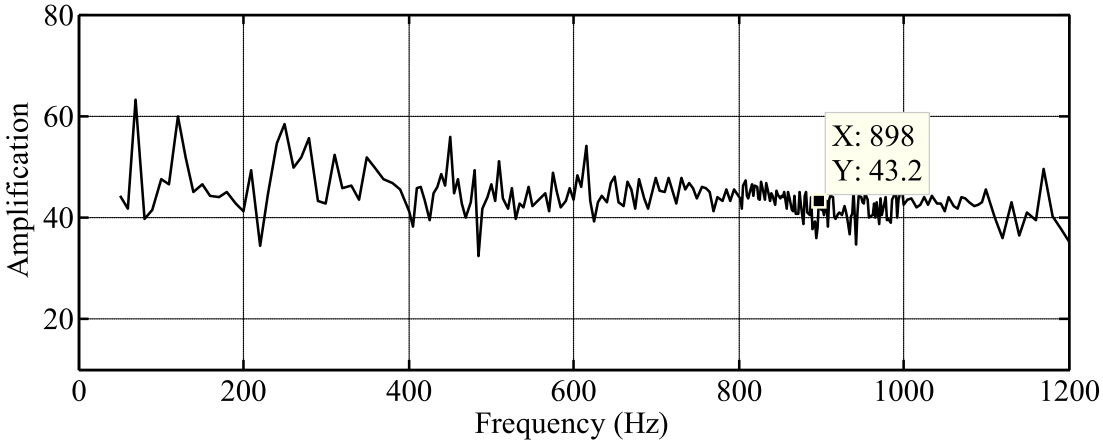

Figure 7-12 Device 3HAS amplification factor extracted from the individual displacements of the proof mass and output of microlevers. The small variation of the amplification factor is mainly due to the noise floor of the equipment when measuring the proof mass deflection.

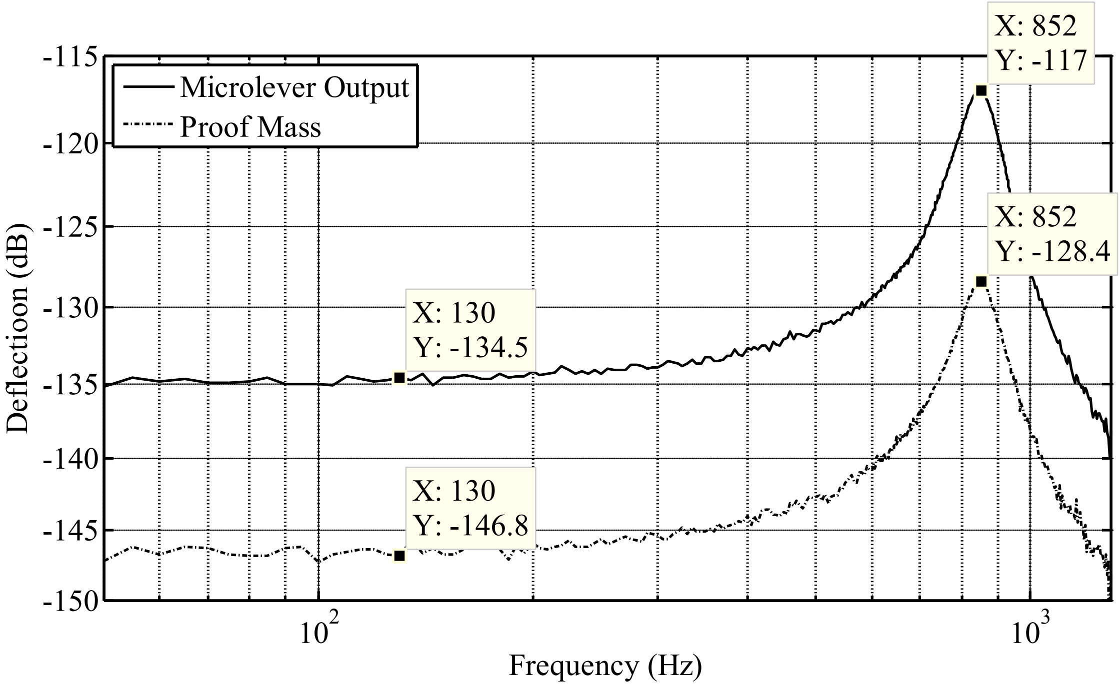

Figure 7-13 Device 3LAS frequency response of the output of microlevers and the proof mass motion using stroboscopic image correlation (0dB=1m).

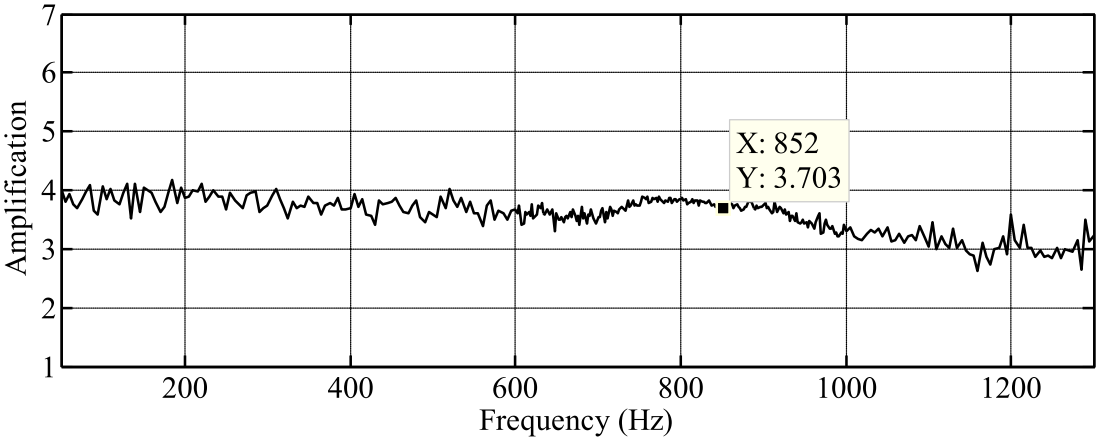

Figure 7-14 Device 4LAS amplification factor extracted from the individual displacements of the proof mass and output of microlevers. The small variation of the amplification factor is mainly due to the noise floor of the equipment when measuring the proof mass deflection.

From the above graphs, it is evident that the amplification factors were predicted quite accurately. The results are compared to the simulated values from Chapter 4 in Table 7-1. The lowest discrepancy is 1.36% and the highest is 20%.

Table 7-1 Optical planar motion analysis mechanical amplification factor results comparison to simulations of Chapter 4

Device	***Simulated mechanical amplification factor***		***Measured mechanical amplification factor***	***Percentage of discrepancy***	
	Ideal	FEM		Ideal	FEM
1HAN	36.5	41.7	40.17	11.5%	3.7%
2LAN	3.65	3.61	3.79	3.8%	4.9%
3HAS	36.5	36	43.2	18.4%	19.8%
4LAS	3.65	3.08	3.70	1.36%	20%

The noise in the signals is due to the deflection of the proof mass being close to the noise floor of the measurement equipment as discussed earlier. The natural frequency of all sensors was measured to be lower than what was expected by an average[6] of 20%. This is due to the electrostatic spring softening effect. This was verified with additional measurements with smaller signals, which showed the correct frequencies but resulted in proof mass motions that could not be detected by the measurement equipment. The results from these measurements verified the operation of the mechanical amplification mechanism implemented on sensors with the amplification factor being closely predicted as shown in Table 7-1 and the natural frequency being within 20% of that predicted by the simulation results of Chapter 4.

7.3 Electrical measurements

The sensors were electrically tested by connecting them to the interface circuit presented in Chapter 6. To investigate the effect of mechanical amplification the same physical circuit was used for the proof mass and amplified output. If two separate circuits were used, differences due to component tolerances between the circuits would invalidate the comparison. The circuit gain was set so that it does not saturate for the large amplified deflection but at the same time providing sufficient gain to sense the small deflection of the proof mass of sensors with high mechanical amplification. The output signals of the measurements were then compared to determine the amplification factor. Both dynamic and static tests were performed.

---

[6] The discrepancy was calculated for both FEM and Architect simulation results and then it was averaged for each sensor design.

7.3.1 Static and impulse response measurements

The sensors were first excited using earth gravity (1g). Table 7-2 shows the results for the output of the sensors for 1g acceleration. Those outputs were also verified with a 100Hz 1g acceleration. The number of comb-fingers at the output of the microlevers is roughly a factor of two larger compared to the number of comb-fingers on the proof mass. This leads to a twice as high value for the nominal capacitance at the microlevers output, thus increases the scale factor by a factor of two. Therefore, this is taken into account when calculating the amplification factors shown in the table. The discrepancies to the simulation results present in Table 7-2 are mainly due to equipment misalignment.

Table 7-2 Scale factor evaluation for the amplified accelerometers for 1g constant acceleration

Sensor	***Proof mass output (mV/g)***	***Amplified output (V/g)***	***Amplification***	***Discrepancy to Ideal***	***Discrepancy to FEM***
1HAN	30.8	2.39	38.8	6.3%	7%
2LAN	928	7.69	4.14	13.4%	14.7%
3HAS	14.3	0.94	32.9	9.86%	8.6%
4LAS	392	3.12	3.98	9%	29%

The response of the 1HAN to an impulse signal generated with a shaker allows to measure two important parameters; the natural frequency of the first mode and the damping ratio. It can be seen from Figure 7-15 that the natural frequency is 735Hz, which agrees within less than 1% of both the FEM (740Hz) and Architect (731Hz) simulation results. The damping ratio is found using the logarithmic decrement method [87]. For two successive peaks, the damping ratio ζ is 0.126, which agrees very well with the calculated value of 0.128 in Chapter 4 and with the under-damped behaviour that the sensors were designed to have. The damping measurement was verified with the bandwidth method applied [87] at the optical measurements.

The impulse response measurement was taken only for the 1HAN accelerometer as a verification measurement. The natural frequencies of the remaining accelerometers were evaluated during the dynamic measurements presented in section 7.3.4. The damping is the same for all sensor types and hence the damping ratio can be easily estimated from the critical damping[7] of each device.

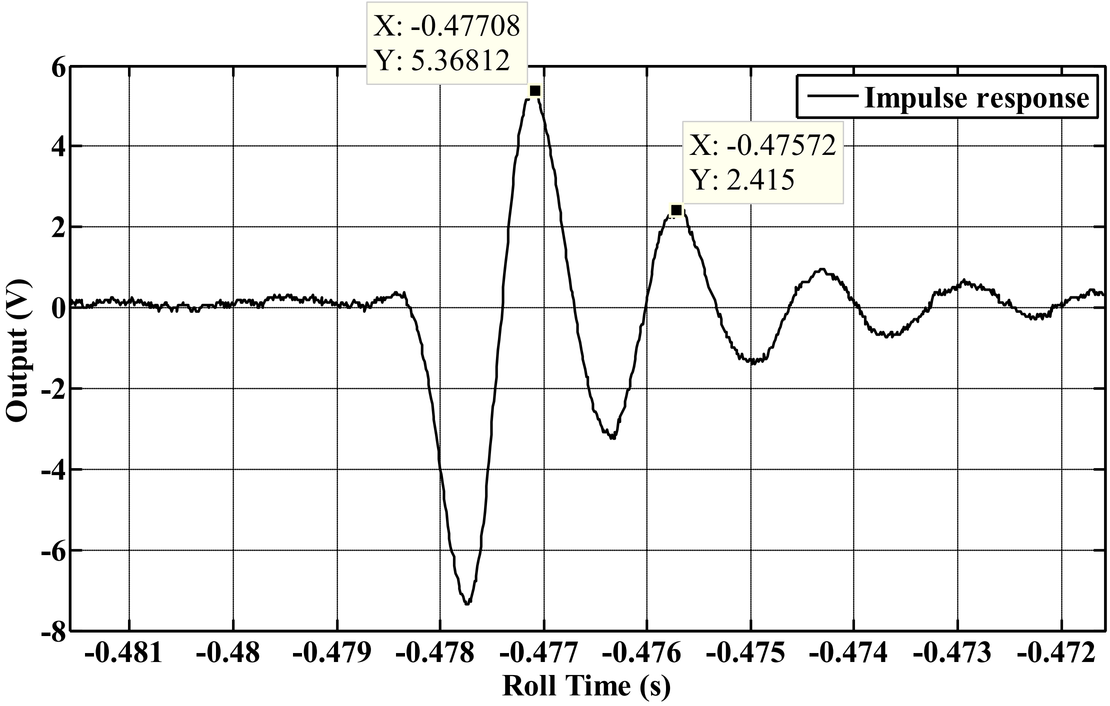

Figure 7-15 Impulse response obtained by exciting the 1HAN amplified accelerometer on a shaker. Using the output to an impulse excitation, the first natural frequency and the damping ratio were evaluated to be 735Hz and 0.126 respectively.

7.3.2 Noise measurements

The use of the amplifying mechanism aims to provide a higher SNR compared to conventional devices by increasing the signal level. Since there are no additional electronics involved when using a mechanical amplifier it is expected that the electronic noise will not be affected by the increase of the signal. To verify this argument, the output of the pick-off circuit was connected to a spectrum analyser. Low accelerations were used to omit the use of a DC block connector without saturating the input of the spectrum analyser. Figure 7-16 a and b show the power spectral density of the 1HAN for the proof mass and the mechanically amplified output, respectively, for a frequency range of 1kHz. A resolution of 1Hz is used in the spectral analyser, thus the average noise power is normalized over a 1Hz bandwidth. The measurement gives a

---

[7] The critical damping and therefore the damping ratio is different for each device since the effective mass is different for each sensor due to the different lever ratio as shown in section 4.4.3.

spectral noise density of 121.8µV/√Hz for the proof mass output (Figure 7-16a) and 120.3µV/√Hz for the mechanically amplified output (Figure 7-16b). This validates the argument that the mechanical amplifier does not change the electronic noise and therefore provides a higher SNR at the mechanically amplified output. From the scale factor of the 1HAN (2.39V/g) and the spectral noise density (120.3µV/√Hz) the 1HAN accelerometer noise floor can be derived as 50.3µg/√Hz. This is a rather high value compared to reported high performance accelerometers [9]. The system is dominated by electronic noise from the circuit. Decreasing the electronic noise will decrease the noise floor of the system. A more sophisticated low noise circuit needs to be implemented with the sensor to take advantage of its mechanically amplified output. This will be considered in future work.

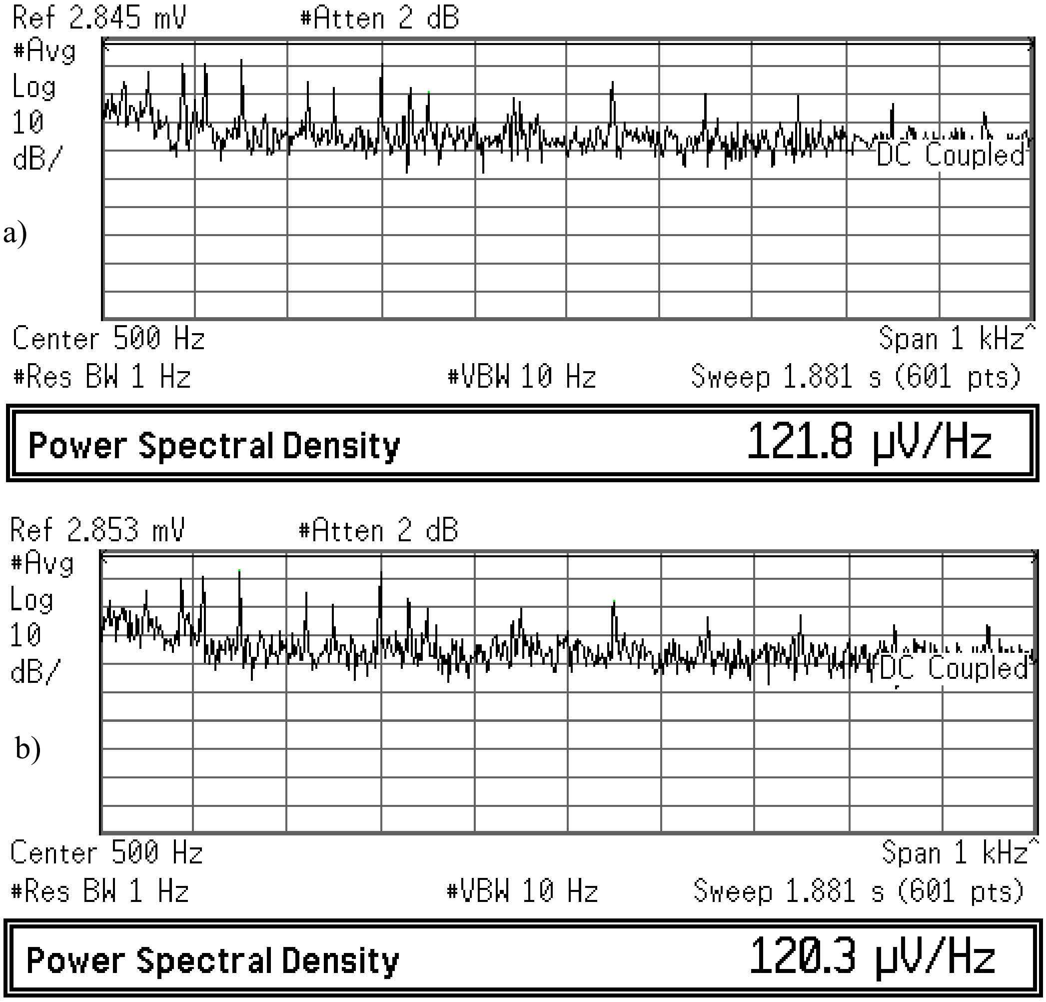

Figure 7-16 Spectral noise density for low acceleration from the same circuit for the a) Proof mass output (121.8µV/√Hz) and the b) mechanically amplified output (120.3µV/√Hz) of the 1HAN accelerometer. The noise floor is approximately the same in both cases revealing that the mechanical amplifier does not affect the noise of the system, which is dominated, by electronic noise.

7.3.3 Linearity measurements

The linearity of the amplified output of the 1HAN sensor was evaluated for static and dynamic acceleration. Figure 7-17 shows a static linearity test performed at the amplified output for a range of ±1g using a dividing head to accurately tilt the sensor. The nonlinearity was calculated as the maximum deviation of the mechanically amplified output voltage from a best-fit line (*y* in Figure 7-17), as a percentage of the full scale of measurements (-1g to 1g). This revealed a maximum nonlinearity of 1.8% (including apparatus misalignment) for the amplified output within this range.

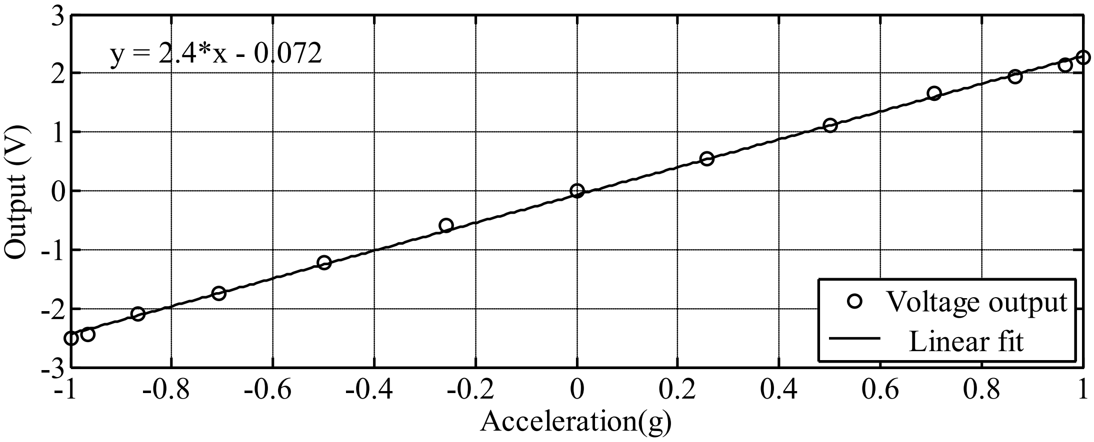

Figure 7-17 The amplified output of the 1HAN sensor for a range of ±1g. The linear fit was plotted using the least squares method. The nonlinearity is 1.8% using the "worst case" method.

In order to quantify the open loop linear dynamic range of the sensors the scale factor of the electronic circuit was significantly reduced to be able to support the large signal output of the sensors at high accelerations without saturating. The measurement was performed on a mechanical shaker setup for a range of measurements from 0.5g to 15g at 100Hz with a step of 0.5g for the 1HAN sensor. The voltage amplitude from the mechanically amplified output was measured and plotted for each acceleration step. Figure 7-18 shows the results from the dynamic test. A linear best-fit line was also plotted for accelerations up to 7g. The full-scale maximum nonlinearity measured at the full dynamic range of ±7g is 2%, which is found at 7g where the sensor output deviates the maximum from the linear best-fit line. This nonlinearity is attributed to the differential capacitance nonlinearity. If the deflection is considered linear, when the sensor is excited with 7g the deflection is close to 4.4μm. This deflection is indeed in the linear region since it is at least 10 times smaller than any length of parts that deflect in the design. Therefore, the nonlinearity in the measurement results originates solely from the nonlinearity introduced by the parallel plate capacitive comb-fingers. It is therefore a valid approximation to assume that for all the designs the sensors will have a linear output signal for deflections below 4.4μm. The dynamic range is significantly reduced by the nonlinearity in open loop operation therefore the sensors would best serve applications that demand for large dynamic range in a closed loop mode. This may be considered in future implementations of the mechanically amplified accelerometers.

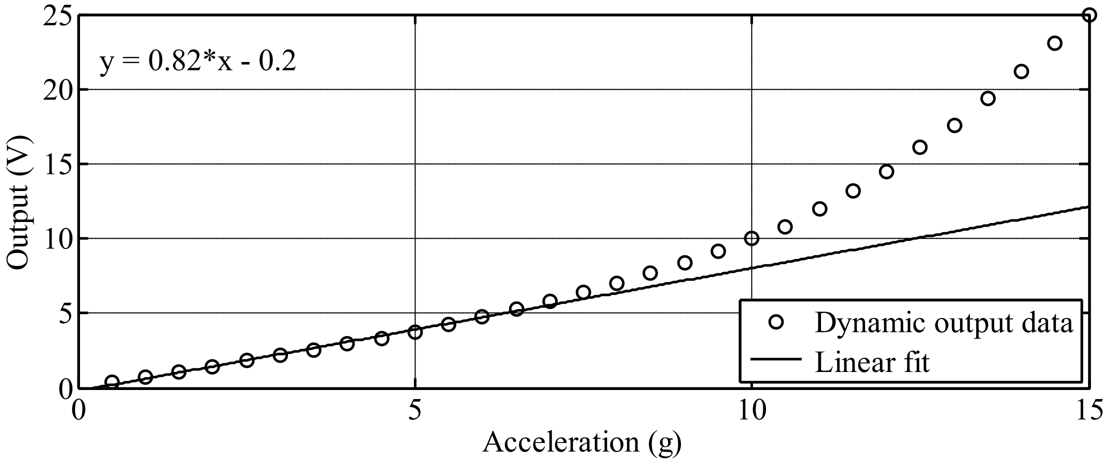

Figure 7-18 Dynamic range linearity test using a mechanical shaker varying the 1HAN acceleration amplitude from 0.5g to 15g at 100Hz with a step of 0.5g. The results show that the device is approximately linear up to about ±7g with a maximum nonlinearity of 2%.

7.3.4 Dynamic measurements

Frequency response measurements were carried out using the shaker system. The natural frequency of the 1HAN was found to be at 732Hz, which validates the impulse response measurement. The value from the shaker frequency sweep matches closely the FEM simulation value of 740Hz and the Architect result of 731Hz. It has to be noted that the shaker system used does not compensate for out-of-plane vibrations hence the measurements include coupled cross-axis motions. Figure 7-19, Figure 7-22, Figure 7-25, and Figure 7-28 show frequency response measurements of the mechanically amplified output of the four accelerometer designs (1HAN, 2LAN, 3HAS, 4LAS respectively) in Volts for 1g acceleration. Figure 7-20, Figure 7-23, Figure 7-26, and Figure 7-29 show the electrical output signals from the comb-fingers on the proof mass for the same excitation for the four accelerometer designs (1HAN, 2LAN, 3HAS, and 4LAS respectively). As previously mentioned the amplified output has double the nominal capacitance of the non-amplified proof mass, thus the measurements for the amplified output include a doubling of the scale factor. The measurements were taken with the same pick-off circuit for both the proof mass and the mechanically amplified output. The amplification factors of the four accelerometer designs, extracted from the measurements, are shown in Figure 7-21, Figure 7-24, Figure 7-27, and Figure 7-30. Those exclude the doubling of the scale factor and are in good agreement with the simulated and optical results.

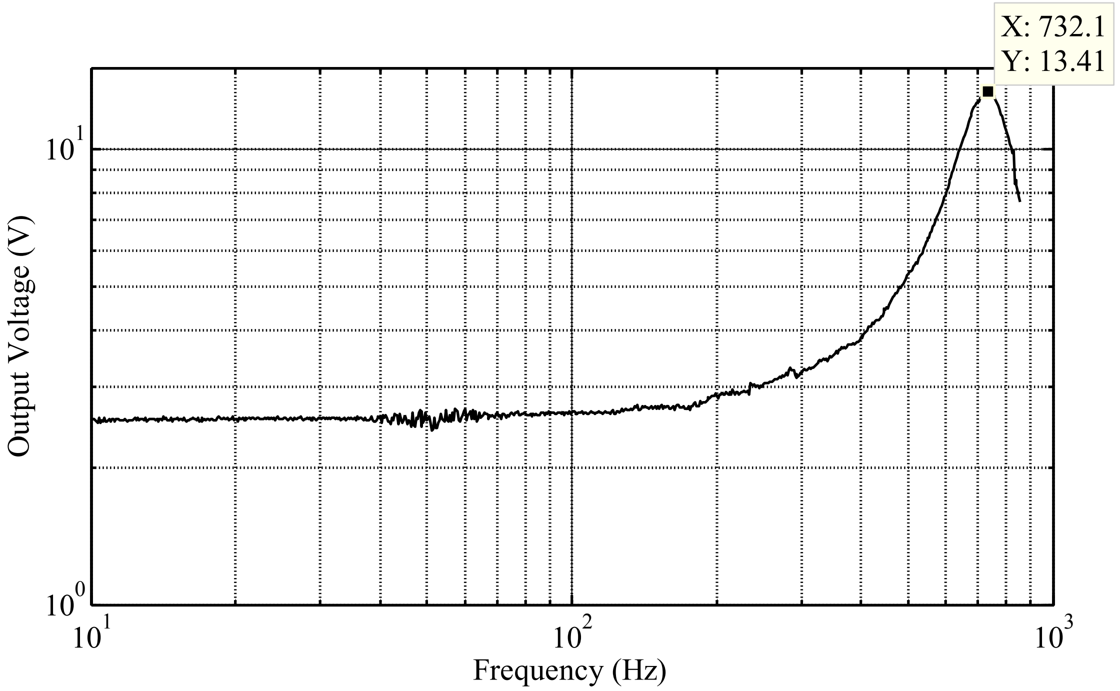

Figure 7-19 Frequency response of the amplified output of the 1HAN sensor to 1g of acceleration measured with a mechanical shaker system. The natural frequency of the in-plane mode is 732Hz. The noise between 50 and 200Hz is due to mechanical cross-coupling in the shaker system. It is more prevalent in the 2LAN accelerometer as it is the most sensitive but it is also visible for 1HAN.

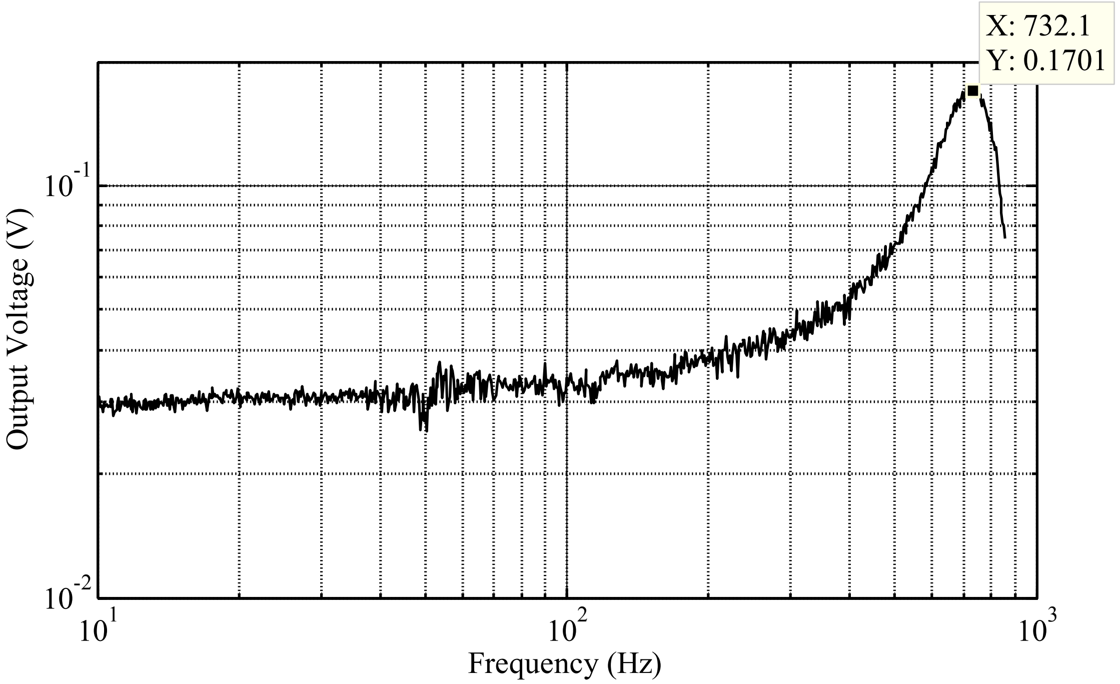

Figure 7-20 Frequency response of the proof mass of the 1HAN sensor to 1g of acceleration measured with a mechanical shaker system. The noise between 50 and 200Hz is due to mechanical cross-coupling in the shaker system. It is more prevalent in the 2LAN accelerometer as it is the most sensitive but it is also visible for 1HAN.

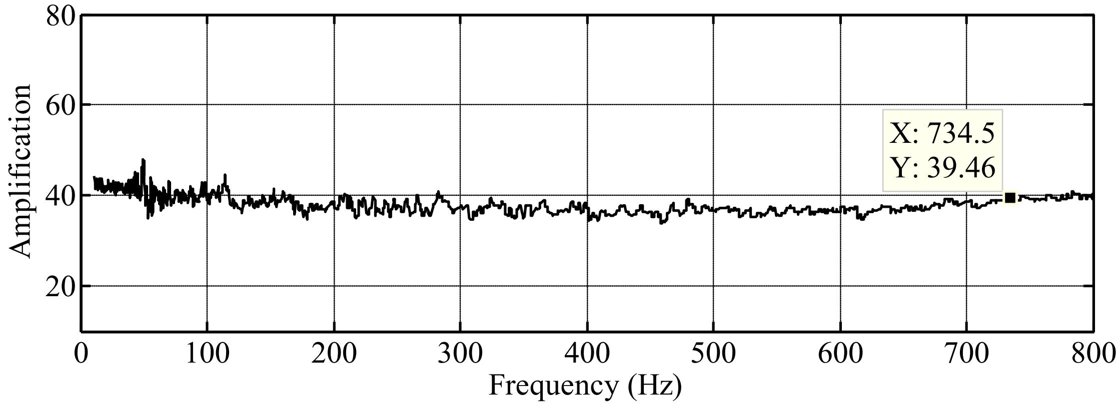

Figure 7-21 Amplification factor of the 1HAN (approximately 39) extracted from the shaker frequency sweep.

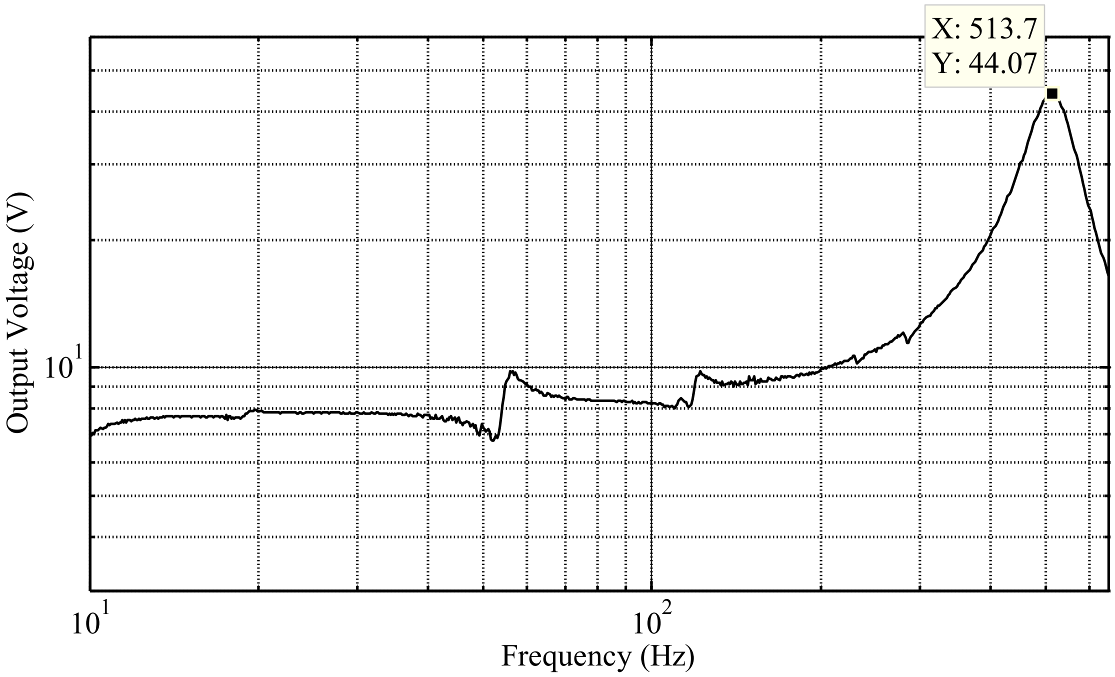

Figure 7-22 Frequency response of the amplified output of the 2LAN sensor to 1g of acceleration measured with a mechanical shaker system. The natural frequency of the in-plane mode is 513Hz. The steps between 50 and 200Hz are due to mechanical cross-coupling in the shaker system. These were also present in the reference sensor signal. They are more prevalent in the 2LAN accelerometer as it is the most sensitive. Since the feedback loop of the shaker system could not compensate for these, it was regarded that they are caused by out-of-plane motion of the shaker mounting stage.

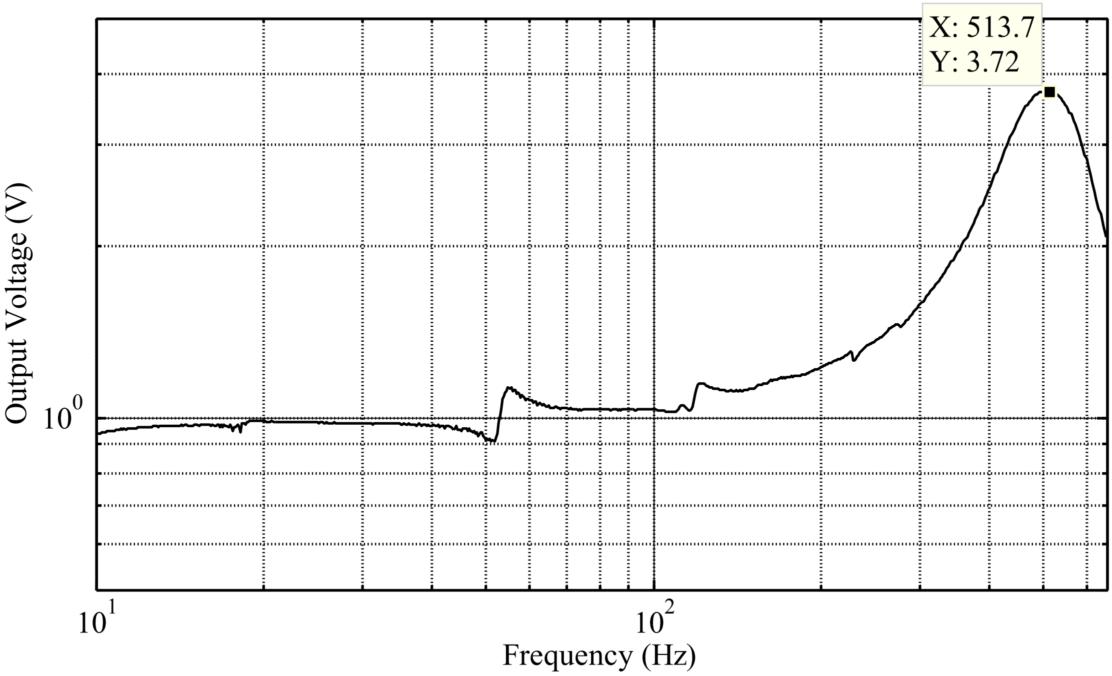

Figure 7-23 Frequency response of the proof mass of the 2LAN sensor to 1g of acceleration measured with a mechanical shaker system. The steps between 50 and 200Hz are due to mechanical cross-coupling in the shaker system. These were also present in the reference sensor signal. They are more prevalent in the 2LAN accelerometer as it is the most sensitive. Since the feedback loop of the shaker system could not compensate for these, it was regarded that they are caused by out-of-plane motion of the shaker mounting stage.

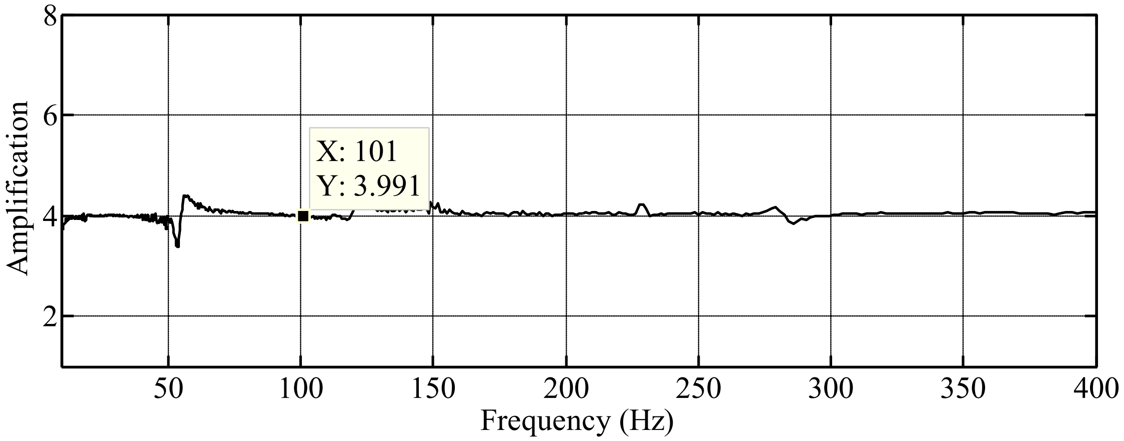

Figure 7-24 Amplification factor of 2LAN (approximately 4) extracted from the shaker frequency sweep.

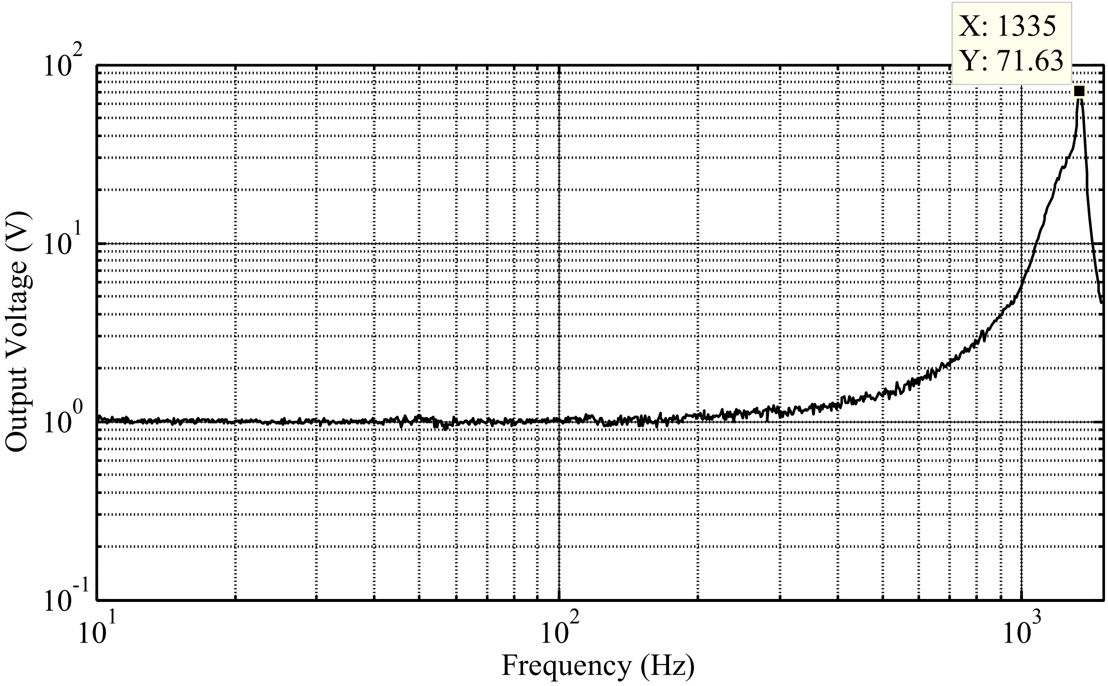

Figure 7-25 Frequency response of the amplified output of the 3HAS sensor to 1g of acceleration measured with a mechanical shaker system. The natural frequency of the in-plane mode is 1335Hz. 3HAS is the stiffest accelerometer so the noise between 50 and 200Hz is not very pronounced in the graphs although it is still present.

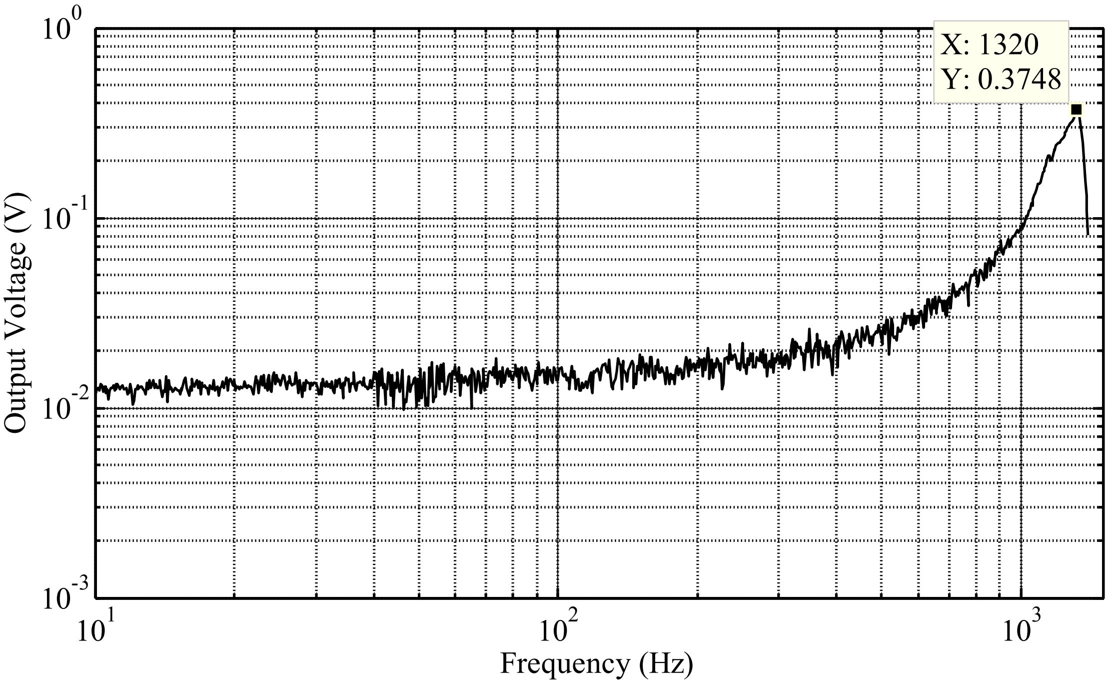

Figure 7-26 Frequency response of the proof mass of the 3HAS sensor to 1g of acceleration measured with a mechanical shaker system. 3HAS is the stiffest accelerometer so the noise between 50 and 200Hz is not very pronounced in the graphs although it is still present.

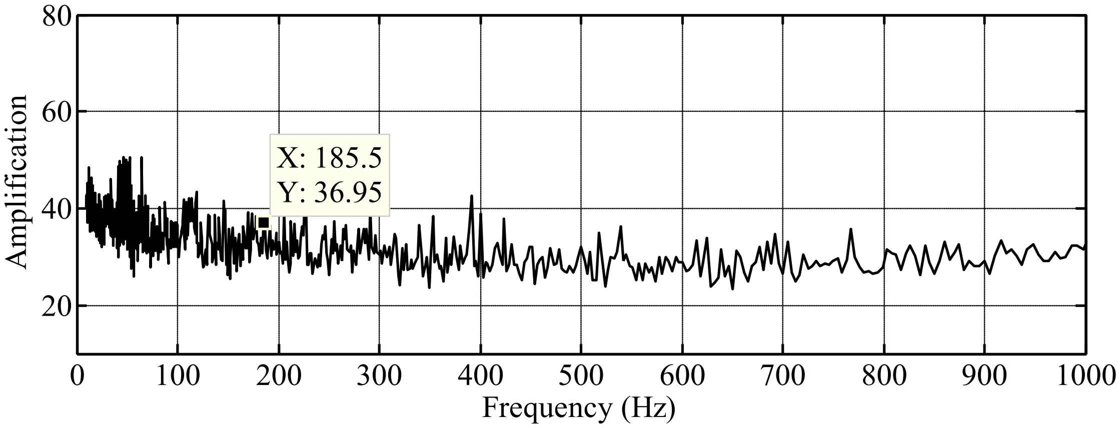

Figure 7-27 Amplification factor of the 3HAS (approximately 37) extracted from the shaker frequency sweep.

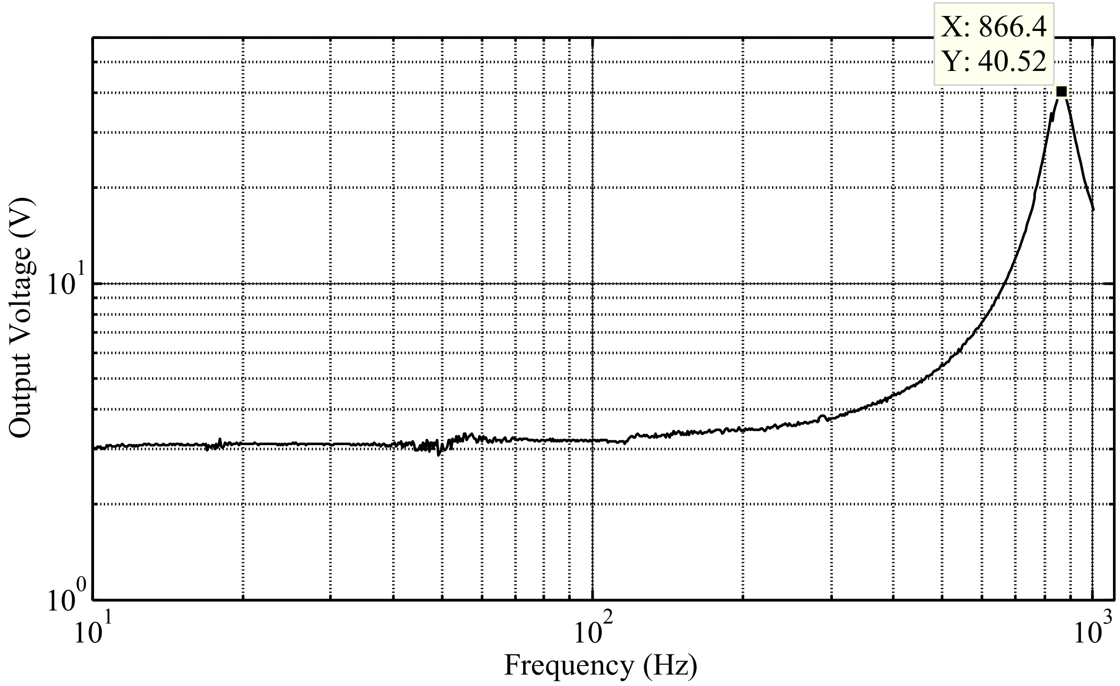

Figure 7-28 Frequency response of the amplified output of the 4LAS sensor to 1g of acceleration measured with a mechanical shaker system. The natural frequency of the in-plane mode is 866Hz. 4LAS is the second stiffest accelerometer so the noise between 50 and 200Hz is not very pronounced in the graphs although it is still present and more obvious than 3HAS which is the stiffest.

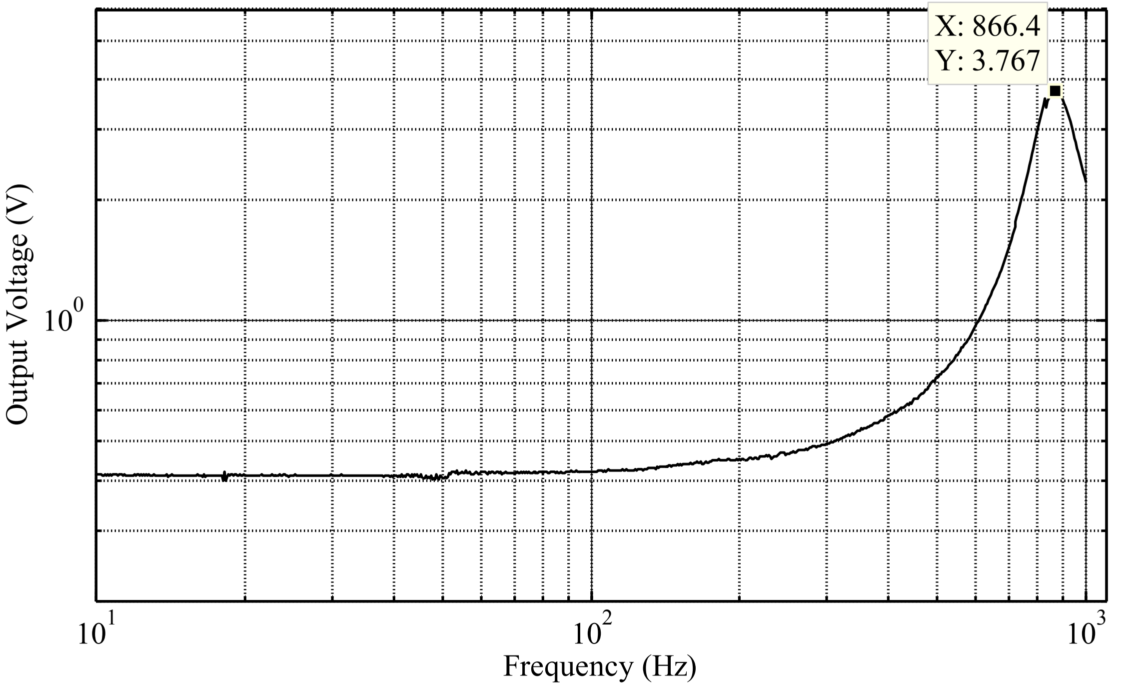

Figure 7-29 Frequency response of the proof mass of the 4LAS sensor to 1g of acceleration measured with a mechanical shaker system. 4LAS is the second stiffest accelerometer so the noise between 50 and 200Hz is not very pronounced in the graphs although it is still present and more obvious than 3HAS, which is the stiffest.

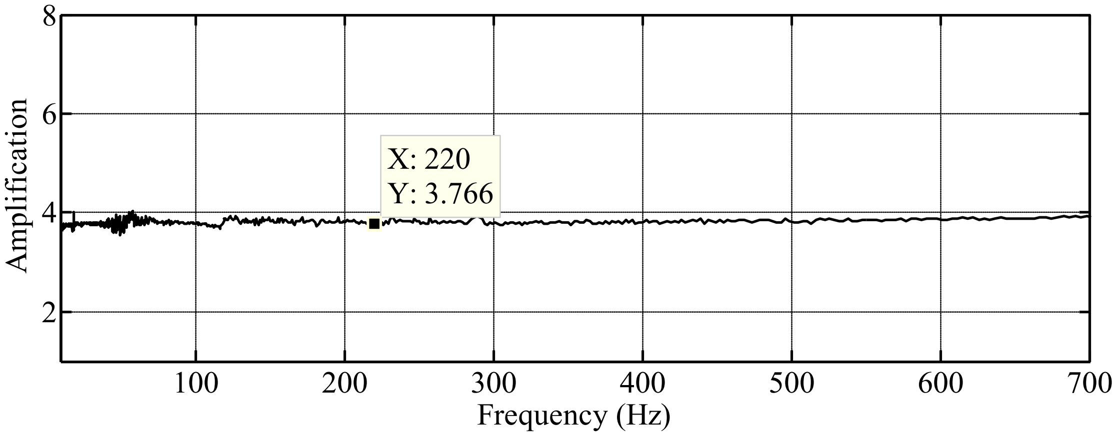

Figure 7-30 Amplification factor of the 4LAS (approximately 37) extracted from the shaker frequency sweep.

The graphs above show that the operation of the sensors was in general accurately predicted by simulation. Table 7-3 offers a comparison of the results for the in-plane natural frequency to the simulations. The results for the in-plane natural frequency much within 18% the simulation results for all the sensor designs. This verifies the validity of the FEM and system level simulation models of Chapter 4, which can therefore be used as a framework to simulate different versions of the mechanically amplified accelerometer. The measured and simulated mechanical amplification factors are compared in Table 7-4. The results are within 10% of the simulated values apart from the FEM result of 4LAS, which is 22%. The measured amplification factor never deviates more than 10% from the ideal, thus the geometrical parameters of the microlevers can be used in preliminary studies to closely predict the amplification factor. The output voltages obtained were in the predicted range. Specifically, the output voltage for 1g for the 1HAN sensor was 2.39V as shown in Table 7-2, which matches the value of 2.46, obtained by Orcad Spice very closely. The frequency response measurements include various sources of noise that can be eliminated by a better isolated and decoupled shaker system. This was considered in this work and improvements based on decoupling mechanisms are currently being implemented on the shaker system.

Table 7-3 In-plane mode natural frequency measured with shaker system and compared to the simulation results.

Device	***Simulated in-plane mode natural frequency***		***Measured In-plane natural frequency***	***Percentage of discrepancy to simulations***	
	FEM	Architect		FEM	Architect
1HAN	740Hz	731Hz	732Hz	1.08%	0.13%
2LAN	561Hz	625Hz	514Hz	8.37%	17.74%
3HAS	1456Hz	1285Hz	1335Hz	8.31%	3.89%
4LAS	1047Hz	936Hz	866Hz	17.28%	7.47%

Table 7-4 Mechanical amplification factor measured with shaker system and compared to the simulation results.

Device	***Simulated mechanical amplification factor***		***Measured mechanical amplification factor***	***Percentage of discrepancy to simulations***	
	Ideal	FEM		Ideal	FEM
1HAN	36.5	41.7	39.46	8.11%	5.37%
2LAN	3.65	3.61	3.99	9.32%	10.53%
3HAS	36.5	36	36.95	1.23%	2.64%
4LAS	3.65	3.08	3.77	3.28%	22.4%

7.4 Measurement errors

This section aims to describe and quantify measurement errors introduced during the optical and electrical evaluation of the sensors. Measurement errors were mainly introduced by the equipment used during evaluation and are responsible for variations between predicted and measured quantities but also between individual devices results. In order to find the origin of the errors a short description of the measurement setup is included in the following.

The optical measurements were initially performed on a passive optical table. The results from these measurements were polluted by noise components introduced mainly due to the inadequacy of the setup to fully damp vibrations. Vibrations not only affect the actual sensor operation but also the equipment performance. During discussions with Polytec [49] and assessment of the optical measurement equipment, frequency components were found to be introduced in the measurements by internal and external parts of the MSA400 being excited by environmental vibrations. The optical table was later upgraded to an active vibration isolation table with a substantially larger mass. This reduced the ambient vibrations and produced results of lower noise. The improvements were mainly prevalent at the in-plane measurements where the resolution was improved due to a reduced noise floor. The peak-to-peak noise of the in-plane measurements before introducing the improved optical table was larger than 500nm. With the introduction of the new optical table, the peak-to-peak noise was reduced down to 100nm.

Another source of error is ambient acoustic vibrations. The optical measurement equipment were enclosed in a metal measurement box without any sound damping. During experimentation, it was found that the peak-to-peak noise of the equipment could be reduced down to 20nm at specific conditions. Those conditions were met during late night at non-working days when the acoustic noise in the building where the measurements were performed was significantly reduced.

Finally, an additional error source was introduced at the optical measurements by the electrical excitation. The signal generator producing the excitation signals was found to provide an output signal with an error of 2%. This affected the overall deflection of the sensors. As the optical measurements were used to extract the amplification factor by the ratio of the proof-mass and microlever deflection this error was cancelled out.

The electrical measurements setup comprised of a mechanical shaker, a dividing head, the pick-off circuit, a signal generator, an oscilloscope and a spectral analyser. The static 1g deflection and linearity measurements were performed using the dividing head. The dividing head used is designed for mechanical workshop applications such as drilling holes at specific angles it therefore did not include a mounting chuck for attaching sensors. A custom-made chuck was used in these measurements. Due to the very high tolerance of the chuck, the static deflection measurements have an unknown error introduced. As shown in Figure 7-17 the worst-case non-linearity of the sensor is 1.8%. This means that, in the worst case, the measurement deviates by 1.8% of the full range from the best-fit line. It can therefore be concluded that the error introduced by the experimental setup is lower than 1.8%. This reveals that the actual linearity of the sensor is better than what extracted by the measurements. As it can be seen in Figure 7-17 although the measurement point of zero acceleration is very close to zero the best-fit line appears shifted by 0.072V on the Y-axis. It can therefore be assumed that the equipment introduced a shift during the transition between measurement points, which accumulated to an overall shift of 1.5% of the full measurement range.

The dynamic measurements were performed with a mechanical shaker. The mechanical shaker did not have a chuck for mounting the sensors with their sensitive axis along its actuating axis. The first method was to mount the sensor using a single bolt at the centre of the armature of the shaker. This resulted in a first series of measurements but with very high levels of noise due to various vibrations. The second method was to use a custom two-part plastic-printed chuck. This method did not improve the measurements as the complicated chuck structure introduced more mechanical noise to the system. Finally, a single block of aluminium was machined to produce a device holder that can be mounted on the armature. This method reduced the noise contribution enough to measure the performance of the sensors. As it is shown in the graphs of the previous section, there are two peaks visible at 50Hz and 200Hz. Those originate from the shaker itself rather than the chuck. By using a low cost 3-axis commercial accelerometer it was found that the shaker had erroneous frequency components in all three axes that the feedback sensor could not compensate for. Those were not quantified or compensated due to restriction in time and equipment. The shaker system was later updated with an advanced chuck system based on a probe rod, which improved the noise performance and reduced cross-axis components but was not used in this research.

The electronic parts involved in the measurements introduced measurement errors. In particular, due to poor capacitive tuning between the differential pairs of the pick-off circuit the measurements are considered to include an error of 1% at the output between positive and negative accelerations. Finally, using a high performance Agilent [83] oscilloscope it was found that the shaker acquisition card was introducing a factor of 2 in the measurements. This was verified as being due to a fault in the card by the manufacturer and as this was consistent between measurements, it was compensated by adjusting the scale factor at the software.

The setup of the measurement equipment proved to be a challenging task during this research. The time and budget limitation did not allow for improving the setup further. Therefore, the quality of results against time ratio had to be balanced for the successful completion of this thesis.

7.5 Discussion

The measurement results for the sensors presented in this chapter prove that their operation can be accurately predicted (within 10% for the majority of measurements) by the mechanical simulations of Chapter 4 and the simulations for the interface electronics of Chapter 6. Sensors implementing mechanical amplification can therefore be designed, simulated, fabricated, and tested by following the methodology presented in this thesis. Ultimate goal of this work is to improve the performance of capacitive accelerometers, thus the performance and the improvements that the sensors offer is discussed in the following.

As discussed in section 4.4.4 of Chapter 4 the main performance improvement that the mechanically amplified accelerometers offer over conventional devices is the higher deflection for sensors of the same sense mode natural frequency. The comparison of the simulation models of the conventional and mechanically amplified designs in Chapter 4 showed that the mechanically amplified accelerometer deflects more than the reference conventional accelerometer for the same natural frequency. In this chapter, it was shown that the simulation results agree very well with the measurement data, thus a comparison of a fabricated mechanically amplified accelerometer to a conventional sensor can be performed. As shown in Table 7-3 the Architect model predicts the natural frequency of 1HAN more closely than the FEM (0.13% as opposed to 1.08%). The model of the sensor used in the electrical simulation shown in Figure 6-2 is based on the results from the Architect simulation of 1HAN. Since the voltage output for 1g acceleration predicted in Figure 6-5 matched the measurement shown in Table 7-2 it is considered that Architect predicts the deflection of the sensor accurately. The natural frequency of 1HAN predicted in Architect is 731Hz and the deflection 640nm (Table 4-1). Those can be used to offer a comparison with a conventional sensor. The model shown in Appendix F gives a 1g deflection of 465nm for a conventional sensor when the in-plane sense mode natural frequency is 731Hz. The comparison of these results yields a 1.38 higher deflection (for 1g acceleration) for the mechanically amplified sensor compared to the conventional reference design. This effectively means that if the two sensors are designed with the same nominal capacitance and damping then the sensitivity of the mechanically amplified accelerometer will be higher within the same bandwidth.

Furthermore, if the Brownian noise for both sensors is considered to be lower than the electronic noise, which is a valid approximation for the technology used, then the mechanically amplified accelerometer (1HAN) has a higher SNR than the conventional sensor when connected to the same interface circuit. The SNR of the amplified accelerometer is 1.38 times higher over that of the conventional design. This is because the electrical signal at the output is directly proportional to the deflection of the sensor.

The electronic noise of the interface circuit used is 120.3μV/√Hz as shown in Figure 7-16. The scale factor of the 1HAN accelerometer is 2.39V/g (Table 7-2). The noise floor can be calculated from the electronic noise and the scale factor. For 1HAN, the noise floor is 50.3μg/√Hz. Since the scale factor is directly proportional to the deflection for a capacitive accelerometer, a conventional accelerometer with the same natural frequency, comb-finger capacitance and interface circuit would have a noise floor of 69.5μg/√Hz, which is 1.38 times higher than that of the mechanically amplified accelerometer.

From the results presented in this chapter and the simulations of Chapter 4 it is evident that the mechanically amplified accelerometer has a higher sensitivity and lower noise floor compared to a conventional sensor with the same sense mode natural frequency and comb-finger capacitance. If the damping is designed to be the same as well then the conventional and amplified designs will have the same bandwidth. This leads to the conclusion that the mechanically amplified sensor will have a higher sensitivity and SNR within the same bandwidth. The proposed design methodology can therefore be used as a guide to produce sensors of higher sensitivity and SNR over the same bandwidth compared to a conventional design.

7.6 Conclusions on the evaluation of the sensors

This chapter presents the results from the experimental evaluation of the sensors. The evaluation was performed both optically and electrically. The optical measurements verified the successful fabrication of the sensors, the predicted amplification factor, and the first two modes of the sensors. The electrical measurements served as a cross verification method for the natural frequency and the amplification factor of the devices. Additionally, through the electrical measurements the damping ratio, the electrical noise, and the scale factor were determined.

The optical results showed that the amplification factors were close to the predicted values. Nevertheless, special care has to be taken when evaluating sensors by electrostatically exciting them since large electrostatic forces introduce a spring softening effect. The electrical measurements verified that the mechanical amplifiers do not alter the noise of the system; hence, they can provide a higher SNR. Apart from the noise floor measurement for the 1HAN, other specific SNR measurements are not present in this work since the electronic circuit is not optimised and has a high level of electronic noise therefore this would lead to unfair comparisons. Referring to Figure 4-8 it is evident that the SNR will be higher for the mechanically amplified accelerometer compared to a conventional design as many times as the deflection is higher within the same bandwidth (natural frequency) and nominal capacitance.

The natural frequencies and the amplification factors were very close to the predicted values with the highest discrepancy for the electrical measurements being 22%. This verifies the simulations of Chapter 4. Those simulation models can be used to optimise the amplified sensors for specific application or to apply the mechanism to other micromachined devices. The highly under-damped nature of the sensors is evident in the graphs of this chapter and hence further improvement of the sensors should include damping optimisation to maximise the bandwidth of the accelerometers.

Chapter 8 Conclusions and future work

8.1 Conclusions

In the work for this thesis, mechanical amplification was applied to inertial sensors. Its particular focus is on the application of deflection amplification in capacitive accelerometers. Non-resonant capacitive accelerometers rely on the deflection of their proof mass to produce an output. It was aimed to increase the sensitivity and hence the SNR by mechanically amplifying their motion. For the improvements to be advantageous over conventional accelerometers the sensitivity and noise had to be improved compared to the ones from a conventional sensor within the same bandwidth.

After the introduction chapter, the literature, that was presented, reports on various methods of applying mechanical amplification in MEMS devices. Some state-of-the-art devices use computationally intensive optimisation algorithms to produce the design of the mechanical structure. In this work, the amplifying mechanism is based on micromachined levers without employing shape, size, or topology optimisation methods. As a result, it is simple, easy to comprehend and apply to other MEMS devices.

The mechanism was chosen to comprise Type 3 microlevers as those can amplify deflection without inverting their direction of motion at the lever output. The microlevers are consisted of a lever arm, a pivot, an input, and an output beam. To describe their operation an analytical model based on superposition of the individual stiffness of its compliant components was constructed. Using the schematic model shown in Figure 3-3, eq. 3-22 was derived. This equation can estimate the amplification factor and the deflection at the input and the output of a Type 3 microlever and hence it can be used for a first order optimisation of the microlevers. Eq. 3-22 was further improved by including a load at the output of microlever, which led to eq. 3-29. The derived equations were compared to FEM and system level simulation results and proved to be highly accurate.

Following the analytical model of the microlevers, the accelerometers designed comprise four symmetrically arranged Type 3 microlevers that suspend a proof mass. The device operation is as follows: When the proof mass deflects under acceleration the motion is amplified through the microlever based mechanical amplifier and can be detected at its output by differential capacitive comb-finger structures.

As the fabrication process allowed it, the proof mass was designed to be large weighting 1.9mg to provide a high force to the microlever inputs when subject to acceleration. The pivots of the microlevers were found to be the most important performance defining parameter. In particular, the width of the pivot affects the compliancy of the entire structure more than any other parameter as shown in Table 4-5. Although 5µm could be achieved in the fabrication process, the thickness was designed to be 10µm in order to make the device more robust for testing. As the input beams of the microlevers are almost equally affecting the compliancy and robustness of the sensors those were also designed to be 10µm wide. The width of the output beam affects compliancy but not robustness as it undergoes lower forces during operation and handling, hence it was designed to be 5µm. The lengths of those beams were optimised using parametric system level simulations. The length of the arm of the microlevers was designed to be 3650µm long, which was mainly dictated by the topology and size of the proof mass. Its thickness is 50µm to prevent bending and allow for fabrication. Two amplification factors, one order of magnitude apart, were implemented (36.5 and 3.65) by varying the distance between the input and pivot beams. Since the sensors are prone to out-of-plane motions an additional out-of-plane motion suppressing spring system was implemented in two of them effectively reducing the out-of-plane motion an order of magnitude more than the in-plane. Finally, there were two sets of differential comb-fingers implemented on the sensors. The BEM simulation shows 2.93pF for the output and 1.44pF for the proof mass comb-fingers. The comb-fingers gap is 10µm to accommodate large motions at the output as this was found to improve measurement results but also to prevent over-damping the device. The overall damping was calculated to be 2.61×10^{-4}N/(m/s) and the damping coefficient 0.0128 which was closely verified by measurements. The design and simulation chapter (Chapter 4) finishes by defining a Figure of Merit with which the mechanically amplified accelerometers can be compared to conventional accelerometers. The Figure of Merit is defined as the deflection natural frequency product. This reveals the fundamental advantage of the mechanically amplified accelerometers over conventional devices, which is the higher deflection over the same bandwidth.

A SOI based process was developed in several stages for the fabrication of the sensors. It is a dual mask process that is able to release the devices and part of the handle wafer while concurrently separating the individual dice during the sacrificial silicon dioxide layer etching step. To accommodate the fabrication process, the design incorporates a set of trenches and etch holes on the handle and device layers to achieve the timed release of the structures, handle wafer, and dice. The process starts with the patterning and etching, using photolithography and DRIE, of the release structures on the handle layer. It is then followed by the patterning and etching of the device layer that also includes structures for the release process. Finally, the wafers are released using an HF vapour phase etching technique. The process offers fundamental advantages over other SOI processes. The main ones are the release of suspended structures of virtually any size, the removal of part of the handle wafer without design restrictions, the separation of the dice without dicing and the very high yield of over 95%. This was achieved through many design and fabrication iterations for the sensors presented in this thesis but also for MEMS within the rest of the research group. The result is a design methodology with relatively high tolerances and a fabrication process with highly predictable and controllable results. The fabrication process development constituted a considerable part of this research project and it now offers a stable platform for the fabrication of various other MEMS devices within the research group.

A generic capacitive pick-off circuit was designed to accommodate the electrical measurements on the sensors. The circuit uses two input charge amplifiers to translate the capacitance variation of the differential comb-fingers to a voltage. The signal is then demodulated and filtered using a diode demodulator and RC filters. The instrumentation amplifier following at the signal path subtracts the two differential signals and hence rejects any common mode signals. After three low pass RC filters the signal is amplified and balanced from a set of operational amplifiers. The behaviour of the circuit was simulated in Orcad Spice [80] and it was found to match measured data.

The sensors were connected to the circuit through an inexpensive custom package made by using PCB technology.

The operation of the sensors was verified using both optical and electrical means. The optical measurements were performed by using white light interferometry, laser Doppler vibrometry, and stroboscopic image correlation. The effective fabrication of the sensors was verified by white light interferometetry. These measurements also revealed the out-of-plane deflection of the output of the sensors due to gravity and intrinsic stress. Laser Doppler vibrometry measurements showed that the out-of-plane natural frequencies were higher than the in-pane sense mode, for all the sensors, hence those did not hinder operation or affected the performance. An electrostatic signal is needed to excite the sensors during stroboscopic image correlation measurements, which resulted in an electrostatic spring softening effect at high amplitudes. Nevertheless, the functionality of the sensors was verified and the amplification factors were within 20% of the predicted values.

The electrical measurements were performed using the pick-off circuit, a dividing head, a shaker system, a signal generator, an oscilloscope, and a spectral analyser. The static deflection of the sensors was predicted within 15% of the FEM simulation values, when omitting extreme values. The impulse response measurement on the 1HAN sensor showed the first natural frequency of the sensor at 735Hz which is within 1% of the predicted value. From the same measurement, the damping coefficient was calculated by the logarithmic decrement method and was found to be 0.126 which matches the calculated at Chapter 4 result of 0.128. Measurements using a spectral analyser showed that the 1HAN accelerometer has a spectral noise density of 121.8μV/√Hz at the proof mass and 120.3μV/√Hz at the output when connected at the same pick-off circuit. This result means that by using mechanical amplification the electronic noise is not altered. Static linearity measurements showed a nonlinearity of 1.8% using the “worst case” method whereas dynamic linearity measurements showed 2% nonlinearity up to ±7g for the 1HAN accelerometer. The electrical measurements using a shaker system matched the simulation results within 18% for the natural frequency and 22% for the amplification factor. If the extreme results are omitted then the majority of results from the electrical evaluation matched within 10% the simulations proving that the methods used can accurately predict the fabricated results.

The measurement results proved that the mechanically amplified sensors behaviour can be accurately predicted and that they can be successfully fabricated using the reported fabrication process. The results therefore validate that by using mechanical amplification, sensors of higher deflection within the same bandwidth as conventional sensors may be designed and fabricated with the techniques presented in this Thesis. The scheme therefore provides means to produce sensors of higher sensitivity and lower noise compared to conventional designs. This offers substantial performance improvements on MEMS capacitive accelerometers without additional cost.

8.2 Future work

The mechanically amplified sensors fabricated and presented here are research prototypes. They are not optimised for specific applications yet they prove the concept of mechanical amplification. The first aspect that has to be optimised is the damping of the sensor. In order to avoid over-damped structures, with affected operation, and to be able to measure the small motion of the proof mass, the current devices are highly under-damped. The comb-fingers define the dominating squeeze film damping hence the under-damped behaviour is due to the large gap between them. The damping of the fabricated sensors was measured giving a good insight of what to expect when designing a mechanically amplified accelerometer. Since it was proven that the damping can be predicted closely the designs can be improved to be critically damped and hence maximise their bandwidth.

The number of comb-fingers at the output of the devices is not optimum. There can be fitted more comb-fingers increasing in this way the nominal capacitance of the sensors and hence their sensitivity. This has to be considered in future implementation of the sensors. The comb-fingers on the proof mass were only needed for the evaluation of the prototypes. In future implementations they can be removed giving space for a larger proof mass or more comb-fingers at the output.

The designs may also be considered for a closed-loop operation. Closed-loop operation will offer an even wider dynamic range but will not improve on the noise floor due to the additional electronics required. In this case, the comb-fingers on the proof mass have to be included in the design. Through the proof mass comb-fingers, the system can be electrostatically forced to keep its null position during operation in a closed-loop. Since the proof mass moves less than the amplified output the voltage at the opposing comb-fingers, that need to be energised to bring the proof mass back to its initial position, will not need to be as large as for a wider motion (the opening gap will be smaller, thus the electrostatic force will be larger). Nevertheless, if the stiffness of the amplified mechanism is considered a combination of its stiffness at its input and output then the input stiffness would be much higher (since it moves less compared to the output). This means that the force required to bring the sensor back to its initial position when electrostatically forcing the proof mass is higher than when forcing the mechanically amplified output. These points should be carefully taken into account when designing a mechanically amplified accelerometer in a closed-loop arrangement.

During the simulation of the sensors, a system level model was implemented. This highly parameterised model can be optimised using computational algorithms such as a Genetic Algorithm (GA) to produce optimum designs for specific applications. This optimisation technique is vastly different compared to topology and shape optimisation techniques since the structure maintains its basic shape. Contrary to other types of optimisation yielding devices of distributed compliance, the advantage of this kind of optimisation is that the mechanism will maintain its simple and well-understood operation.

Finally, when the mechanical design is optimum for an application the interface circuit has to be reconsidered. In this study, the pick-off circuit is not optimised for low noise operation. In a future iteration, the sensor has to be encapsulated in a proper ceramic package and the circuit has to be adequately electromagnetically shielded. With a more compact circuit design and by electromagnetically shielding it, the electrical noise can be further decreased. Certainly, an integrated version of the pick-off circuit will produce the optimum noise performance that the sensor can produce. For applications that demand a very large range the sensor can be implemented in a closed loop system, as discussed earlier. The produced prototypes can readily be implemented in a closed loop system since they provide comb-fingers for the electrostatic force feedback on the proof mass.

This research has proven that deflection amplification can be advantageous for micromachined accelerometers. It can therefore be extended to other inertial sensors such as gyroscopes and even further expanded to be included in completely different devices such as actuators that demand large deflections. By no means, has this research finished and the intention of the author and those involved is to expand the concept and produce micromachined devices of higher performance using this approach. Through this study, it was also proven that the evolvement of micromachined sensors is not reaching an end soon; in contrast, considerable research potential was revealed that will offer the community greater understanding of micromachined structures and expand on further applications for future technology.

Appendix A Matlab script for the analytical calculations of Type 3 lever deflections and amplification

```
%----------------------Model of a Type 3 microlever-----------------------%
%This model uses the superposition of the individual deflections and
%deformations of the pivot and lever arm of a Type 3 microlever to find the
%deflection at its input and output, the amplification factor and how those
%are affected from stiffness variations of the pivot.
%Two forces are applied. One at the input and a load at the output.
%The input force represents the force from a proof mass whereas the load at
%the output represents the force from the mass of the comb-fingers attached
%at the output. All units in the model are standard SI units.
%----------------------Created by Ioannis Zeimpekis-----------------------%

clc;
clear all;
syms ta l

%---Constants---%

E=169e9; %Young's Modulus
F=18e-6; %Input Force
a=100e-6; %Point of the arm where the input force is applied
L=3650e-6; %Length of the arm
tb=50e-6; %Thickness of the arm
Ib=(50e-6*tb^3)/12; %Moment of inertia of the arm
Ia=(50e-6*ta^3)/12; %Moment of inertia of the pivot

%---Deflection_Equations---%

M0=F*a; %Moment at point a
theta_CURV=(M0*l)/(E*Ia); %Angle at the end of the curve of the pivot
Yrot=L*sin(theta_CURV); %Deflection at the output due to rotation of the pivot
DL=(F*l)/(ta*(50e-6)*E);%Axial deformation of the pivot
Yb3= F*(a^2)*((2*a)+(3*(L-a)))/6/E/Ib ;%Bending of the arm at the output tip
Ybld = (F*a^3)/3/E/Ib ;%bending deflection at the input load
Yrotin = a*sin(theta_CURV) ;%Deflection due to rotation at the input

In = Yrotin+Ybld+DL ;%Input deflection due to pivot rotation, arm bending and axial
deformation of the pivot
Out5 = Yb3+ Yrot+DL ;%Output deflection due to pivot rotation, arm bending and axial
deformation and axial deformation of the pivot
Ag=Out5/In ;%Geometrical amplification factor

%-----Additional Weight at the Tip of the Microlever---%

F2=6.22e-7; %Force at the end by the comb-fingers
M2=F2*L; %Moment at pivot from additional force
```

```
theta_CURV2=(M2*l)./(E*Ia); %Rotation of the pivot due to additional force
Yrot2=L*sin(theta_CURV2); %Deflection at the output due to additional rotation
Yrotin2 = a*sin(theta_CURV2); %Deflection at the input due to additional rotation
Wa=(F2*a^2)*(3*L-a)/(6*E*Ib); %Additional deflection at the input due to arm bending
WL=(F2*L^3)/(3*E*Ib); %Additional deflection at the output due to additional force
DL2=(F2*l)./(ta*(50e-6)*E); %Additional axial deformation of the pivot due to load

InC = Yrotin+Ybld+DL+Yrotin2+Wa+DL2; %Input deflection due to pivot rotation, arm
bending and axial deformation of the pivot
OutC = Yb3+ Yrot+DL+Yrot2+WL+DL2; %Output deflection due to pivot rotation, arm bending
and axial deformation and axial deformation of the pivot
AgC=OutC ./InC; %Geometrical amplification factor of the full model

%---Parameterisation---%

Agw = subs(AgC,l,110e-6);
Out5w = subs (OutC,l,110e-6);

Agl = subs(AgC, ta , 10e-6);
Out5l = subs (OutC, ta, 10e-6);

dAg=diff (Agw,'ta') ;%differentiate Agw function
dAgin =inline (vectorise(dAg )) ;% Vectorise it

dOut = diff (Out5w, 'ta'); %differentiate Out5w function
dOutin = inline (vectorise(dOut)); %Vectorise it

Agin = inline (vectorise (Agw));
Outin = inline (vectorise(Out5w));

ta=2e-6:0.1e-6:15e-6; %Set value for pivot thickness
Ampdiff = dAgin(ta); %Give values to differentiated and vectorised Amp function
Outdiff = dOutin(ta); %Give values to the differentiated and vectorised Out function


%----------------Pivot width variation-----------------%

Agv = Agin(ta);
Outv = Outin (ta);

figure(1) %plot Amplification over width
p1=plot(ta,Agv);grid
xlabel('Pivot Width (m)')
ylabel('Deflection Amplification Factor')
set(p1,'Color','black','LineWidth',2)

figure(2) %Plot dAmp/dta
p2=plot(ta,Ampdiff);grid
xlabel('Pivot Width (m)')
ylabel('dAMP/dta')
set(p2,'Color','black','LineWidth',2)

figure(3) %plot Output deflection over width
p3=plot(ta,Outv);grid
xlabel('Pivot Width (m)')
ylabel('Output Deflection (m)')
set(p3,'Color','black','LineWidth',2)

figure(4) %Plot dOut/dta
p4=plot(ta,Outdiff);grid
xlabel('Pivot Width (m)')
ylabel('dOUT/dta')
set(p4,'Color','black','LineWidth',2)

Outvp = zeros (0,130);
for i = 1:1:130;
Outvp(i) = (Outv(1,i+1)-Outv(1,i)).*100./Outv(1,i);
end

figure (5)
```

```
 bar((2e-6:0.1e-6:14.9e-6),abs(Outvp),'histc');
%plot ((2e-6:0.1e-6:14.9e-6), Outvp);grid
xlabel ('Pivot Width (m)')
ylabel ('Absolute Output Deflection Change (%)')



Agvp = zeros (0,130);
for i = 1:1:130;
Agvp(i) = (Agv(1,i+1)-Agv(1,i)).*100./Agv(1,i);
end

figure (6)%Absolute Amplification Change over width
bar((2e-6:0.1e-6:14.9e-6),abs(Agvp),'histc');
xlabel ('Pivot Width')
ylabel ('Absolute Amplification Change (%)')

%-------------------------------------------------------------------------%

%------------------------------Length Variation---------------------------%

dAgl=diff (Agl,'l') ;%differentiate Agl function
dAginl =inline (vectorise(dAgl)) ;% Vectorise it

dOutl = diff (Out5l, 'l'); %differentiate Out5l function
dOutinl = inline (vectorise(dOutl)); %Vectorise it

Aginl = inline (vectorise (Agl));
Outinl = inline (vectorise(Out5l));

l=(5e-6:1e-6:2e-4); %Set value for pivot length
Ampdiffl = dAginl(l); %Give values to differentiated and vectorised Amp function
Outdiffl = dOutinl(l); %Give values to the differentiated and vectorised Out function

Agvl = Aginl(l);
Outvl = Outinl (l);

figure(7) %plot Amplificaiton over length
p7=plot(l,Agvl);grid
xlabel('Pivot Length (m)')
ylabel('Deflection Amplification Factor')
set(p7,'Color','black','LineWidth',2)

figure(8) %Plot dAmp/dl
p8=plot(l,Ampdiffl);grid
xlabel('Pivot Length (m)')
ylabel('dAMP/dl')
set(p8,'Color','black','LineWidth',2)

figure(9) %Plot output deflection over length
p9=plot(l,Outvl);grid
xlabel('Pivot Length (m)')
ylabel('Output Deflection (m)')
set(p9,'Color','black','LineWidth',2)

figure(10) %Plot dOut/dl
p10=plot(l,Outdiffl);grid
xlabel('Pivot Length (m)')
ylabel('dOUT/dl')
set(p10,'Color','black','LineWidth',2)

Outvpl = zeros (0,195);
for i = 1:1:195;
Outvpl(i) = (Outvl(1,i+1)-Outvl(1,i)).*100./Outvl(1,i);
end

figure (11)%Absolute Output Deflection Change over length change
bar((5e-6:1e-6:1.99e-4),abs(Outvpl),'histc');
xlabel ('Pivot Length (m)')
ylabel ('Absolute Output Deflection Change (%)')
```

```
Agvpl = zeros (0,195);
for i = 1:1:195;
Agvpl(i) = (Agvl(1,i+1)-Agvl(1,i)).*100./Agvl(1,i);
end

figure (12)%Absolute Amplification Change over length
bar((5e-6:1e-6:1.99e-4),abs(Agvpl),'histc');
xlabel ('Pivot Length')
ylabel ('Absolute Amplification Change (%)')

%----------------------------------------------------------------------%
```

Appendix B Analytical model based on the analysis from [36]

For a type 3 microlever.

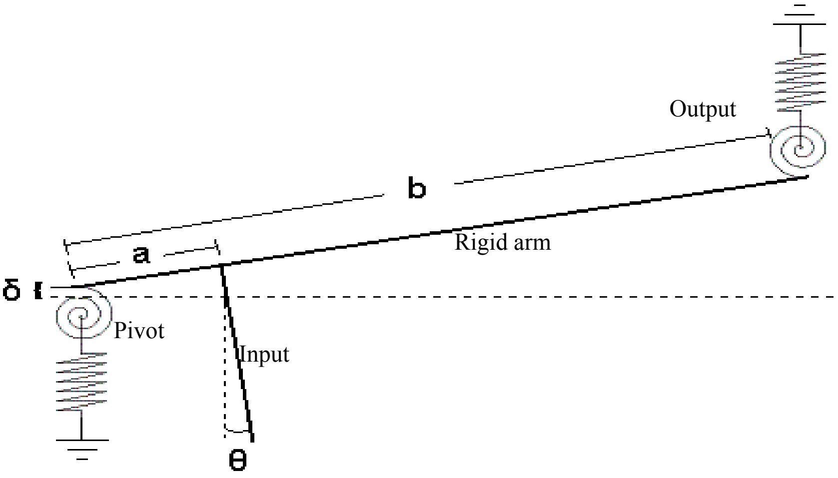

Figure B-1 model of a type 3 microlever

The model shown above contains the axial stiffness of the pivot and output link and can be used to derive a first approximation of the displacement amplification factor of a microlever. The application of force and moment equilibrium yields:

$$Fin = K_{axo}(bsin\theta + \delta) + K_{axp}\delta \qquad \text{eq. B-1}$$

$$F_{in}a = K_{axo}(bsin\theta + \delta)b + K_{roto}\theta + K_{rotp}\theta \qquad \text{eq. B-2}$$

Where F_{in} is the input force, K_{axo} and K_{axp} are the axial stiffness of the output and the pivot, respectively; K_{roto} and K_{rotp} the rotational stiffness of the output, and the pivot, respectively; *a* the distance from the pivot to the input, *b* the distance from the pivot to the output, *δ* the axial deflection, and *θ* is the angle of rotation.

Since the lever arm is considered rigid, the geometrical advantage of the microlever A_G is the ratio of the output deflection U_{out} to the input deflection U_{in} that can be easily calculated by the equations above if small angles of deflection are considered:

$$A_G = \frac{U_{out}}{U_{in}} \qquad \text{eq. B-3}$$

Where

$$U_{out} = b \sin\theta + \delta \qquad \text{eq. B-4}$$

$$U_{in} = \alpha \sin\theta + \delta \qquad \text{eq. B-5}$$

The angle of rotation *θ* and the axial displacement *δ* can be derived from eq. B-1 by considering small deflection angles as shown below.

$$\delta = -\frac{\mathrm{F_{in}}\left(\mathrm{bK_{axo}(a-b) - K_{roto} - K_{rotp}}\right)}{\mathrm{b^2K_{axp}K_{axo} + \left(K_{axo} + K_{axp}\right)\left(K_{roto} + K_{rotp}\right)}} \qquad \text{eq. B-6}$$

$$\theta = -\frac{\mathrm{F_{in}}\left(\mathrm{K_{axo}(b-a) - aK_{axp}}\right)}{\mathrm{b^2K_{axp}K_{axo} + \left(K_{axo} + K_{axp}\right)\left(K_{roto} + K_{rotp}\right)}} \qquad \text{eq. B-7}$$

Appendix C Dual stage microlevers analysis

The following table includes different combinations of Type 1 and 3 microlevers in compound arrangements. The number in the code represents the type of lever and the letter the relative to the lever position of the pivot, for the output and input stage respectively. The models were constructed and simulated in Synple system level simulator of Intellisuite [88].

Table C-1 Amplification factors for different compound microlever structures

No.	Code	Dual stage microlever configuration	A1 (1st stage amplification factor)	A2(2nd stage amplification factor)	A(Overall amplification factor)
1	1D-1D		4.27114	7.90352	33.7570
2	1D-3D		4.97855	7.31392	36.4127
3	1D-1S		4.49775	7.31370	32.8952
4	1D-3S		5.02712	7.31309	36.7638
5	1S-1D		1.29602	7.10273	9.20528
6	1S-3D		1.53469	7.11207	10.9148
7	1S-1S		1.71550	7.16548	12.2924
8	1S-3S		5.33147	7.17242	38.2395
9	3D-1D		3.98059	10.0511	40.0095
10	3D-3D		4.49103	10.0509	45.1393

11	3D-1S		4.00905	10.0402	40.2517
12	3D-3S		4.52054	10.0408	45.3901
13	3S-1D	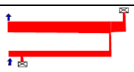	1.87223	9.87562	18.4895
14	3S-3D		2.06516	9.87078	20.3847
15	3S-1S		1.45014	9.79980	14.2111
16	3S-3S	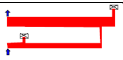	1.61706	9.79484	15.8389

Appendix D Dual stage parametric sweeps

The following value sweeps were obtained for model No. 10 of Table 8-1 using Synple [88]. They show how the amplification factor changes by varying the dimensional parameters of a mechanical amplifier based on a dual microlever stage. The dimensions of all X-axis are in meters.

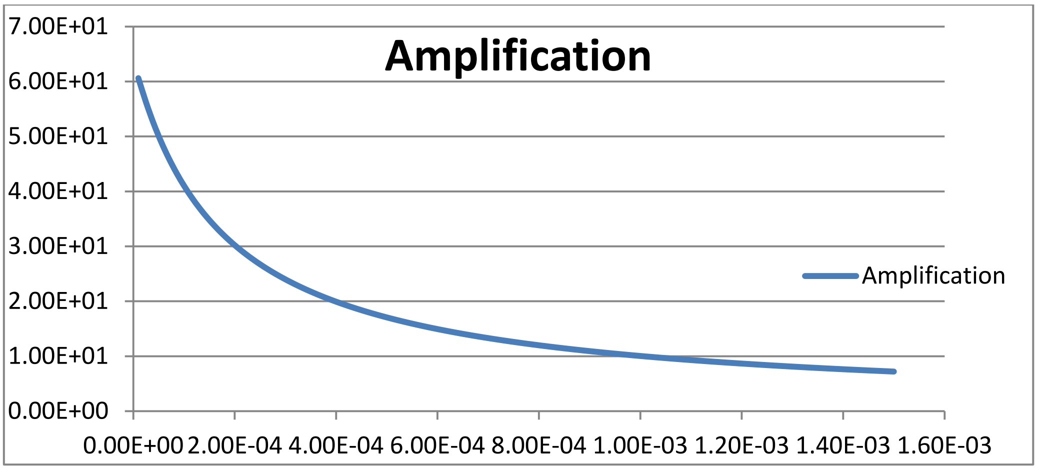

Figure D-1 1st stage pivot length sweep

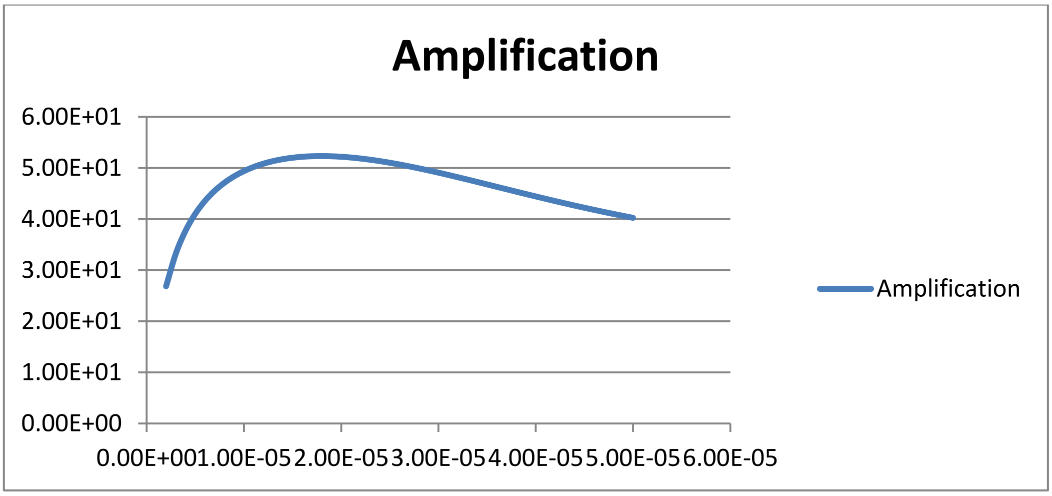

Figure D-2 Width of 1st stage pivot sweep

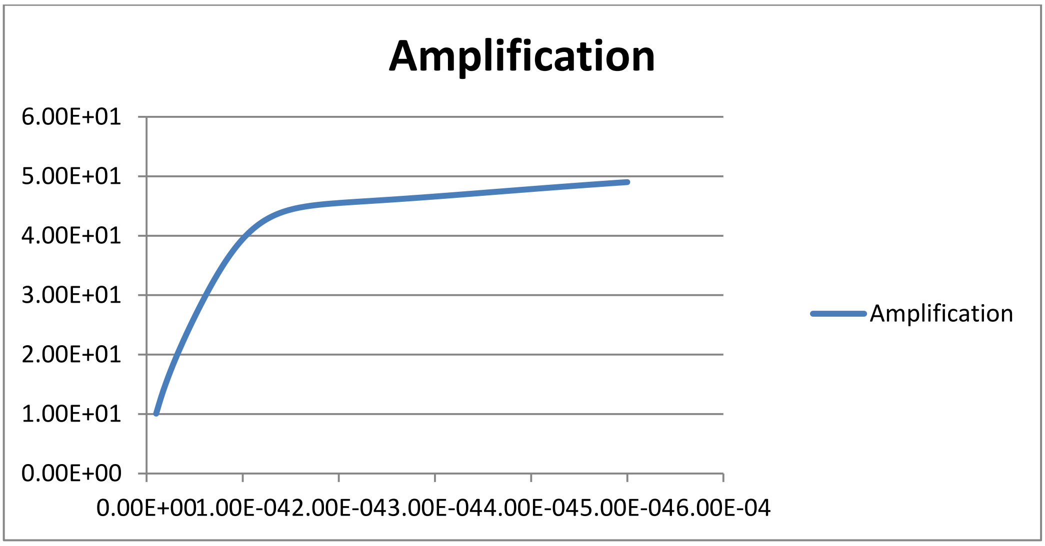

Figure D-3 Connecting beam length sweep

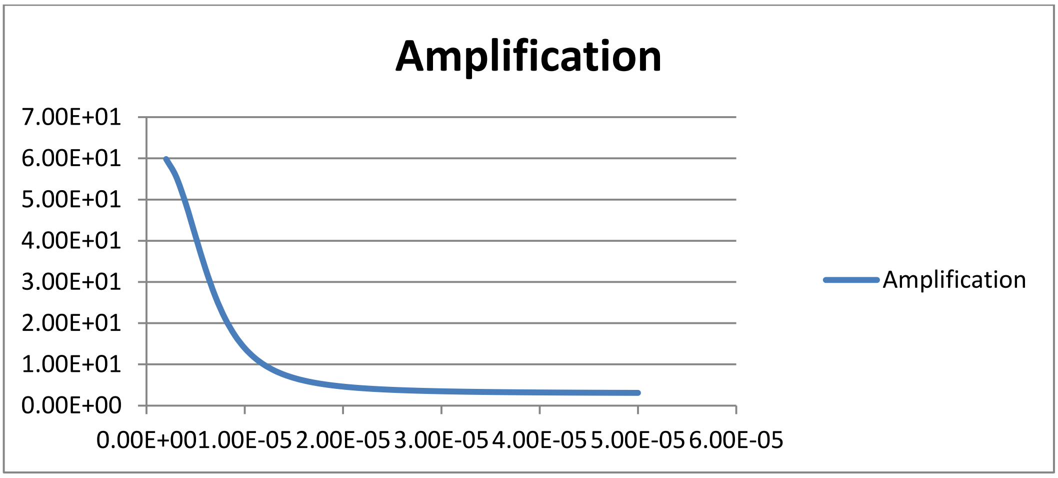

Figure D-4 Connecting beam width sweep

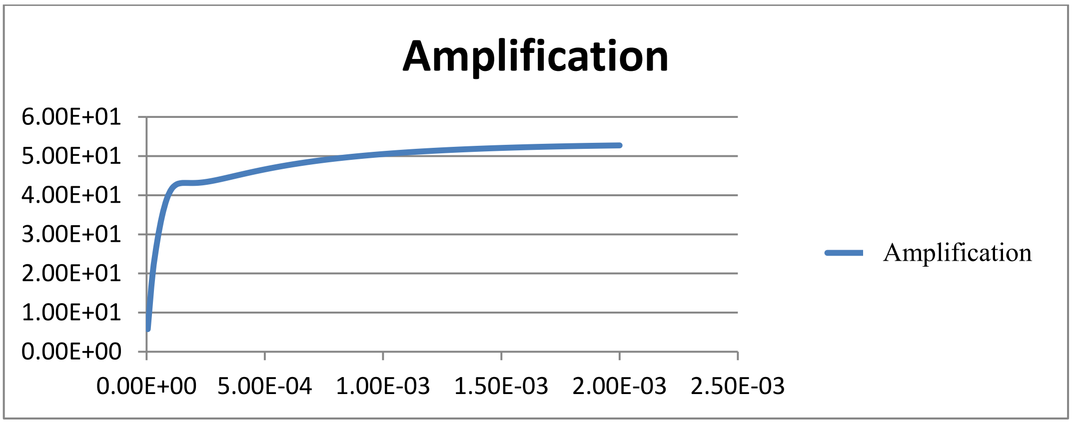

Figure D-5 Length of 2nd stage pivot

Appendix E Dual stage mechanical amplification in single axis accelerometers

E.1 Dual-stage amplification

In the preliminary study for the application of microlever based amplification mechanisms in inertial sensors, compound structures were also considered. Those were designed and simulated but never fabricated and so they are included in this report only for clarity.

To further evaluate the use of microlevers in inertial sensors dual-stage amplification is considered in this work. A dual-stage amplifying mechanism is defined as the mechanism that comprises two serially connected amplification mechanisms in such a way that the output of the first is connected at the input of the second. Apart from the apparent advantage of higher amplification, dual-stage amplification mechanisms can also offer designs that are more compact where this is needed.

The results from the analysis presented in Chapter 3 were used as an optimisation process for the dual leverage mechanism that was implemented in the capacitive accelerometer. It must be noted that these were optimised to provide maximum geometrical advantage rather than higher deflection. This choice was taken considering it will provide results that prove the validity of the concept. Equations presented in Chapter 3 can also be used to optimise the design for maximum deflection.

E.1.1 Deflection-deflection dual-stage amplification

To further investigate the deflection amplification concept a dual-stage capacitive accelerometer was designed. This is implemented with 4 compound microlevers. Every compound microlever uses two Type 3 microlevers in a serial arrangement designed to amplify deflection as shown in Figure E-1.

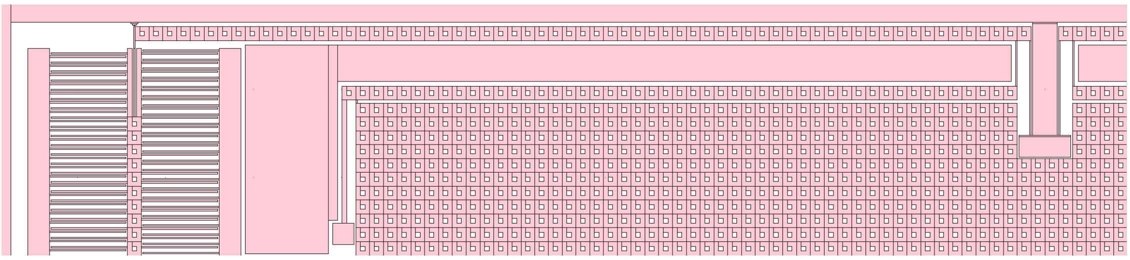

Figure E-1 Dual-stage deflection-deflection amplification. The dual-stage deflection amplification mechanism was optimised using nodal analysis

The dimensions of pivots and input/output links as well as the type of levers used were optimised by nodal analysis using Synple (Appendix C and Appendix D). The structure uses the same output system as the single stage amplified mechanism and comprises read-out and feedback comb fingers at the proof mass.

Table E-1 Dual-stage deflection-deflection mechanically amplified accelerometer specifications

Property	***Value***
Die area	6.64x5.03(mm)2
Proof mass	2.09mg
Proof mass deflection for 1g	$6.54\text{x}10^{-4}$µm
1^{st} Stage deflection for 1g	$3.81\text{x}10^{-2}$µm
Comb-fingers deflection for 1g	2.52µm
Deflection amplification	58.2 (1^{st}) x 66.1 (2^{nd})=3847
Input stiffness	34931N/m
Output stiffness	9.07N/m
Resonance frequency	323Hz
Nominal capacitance	22.94pF
Static sensitivity	10.9pF/g
1g Deflection BW product	814µm Hz

As it can be seen in Table 8-2 the proof mass is 17% smaller than that of the single-stage accelerometer (this refers to an accelerometer simulated for the preliminary study) while the deflection is 14.3% larger. The amplification factor calculated by FEM simulations is 58.2 and 66.1 for stage one and two respectively. The overall amplification factor is calculated as the ratio of the comb-fingers deflection versus the deflection of the proof mass and was found to be 3853 matching exactly the product of the two amplification factors. The figure of merit here shows that the single-stage amplified accelerometer has slightly better overall performance than the dual-stage. This is because, as mentioned before, the accelerometers are optimised to provide higher amplification than higher deflection and this is affecting the compound microlevers more than the single-stage ones. The amplification optimisation is reflected on the design as a very high input stiffness and very low output stiffness as shown in Table 8-2. Although this design is not benefited by higher deflection-bandwidth product as the single-stage, the motion of the proof mass is smaller than that of the single stage one. This may be useful in applications where the input has to preserve a small distance deviation from its initial position.

E.1.2 Operating principles of the dual-stage deflection-deflection capacitive accelerometer

The operation of the dual-stage deflection-deflection mechanically amplified accelerometer is similar to the single stage accelerometers and can be described with the help of Figure E-2. Like the single stage accelerometers, it detects acceleration in one axis. Acceleration in the sense axis will result in the deflection of the proof mass due to inertial forces. This motion of the proof mass will force the input of the first stage of levers deflect in the same direction, as the proof mass. The output of the first stage will move in the opposite direction, since the levers have an inverting characteristic, forcing the inputs of the second stage to move also in this direction. As a result, the outputs of the second stage will move along the sense axis and in the same direction as the proof mass. The comb-fingers structure will deflect due to the deflection of the outputs of the second stage. In this operation, the deflection of the proof mass is amplified in two stages through the dual amplification stage. The output result will equal the deflection of the proof mass amplified by the product of the amplification factors of the two stages.

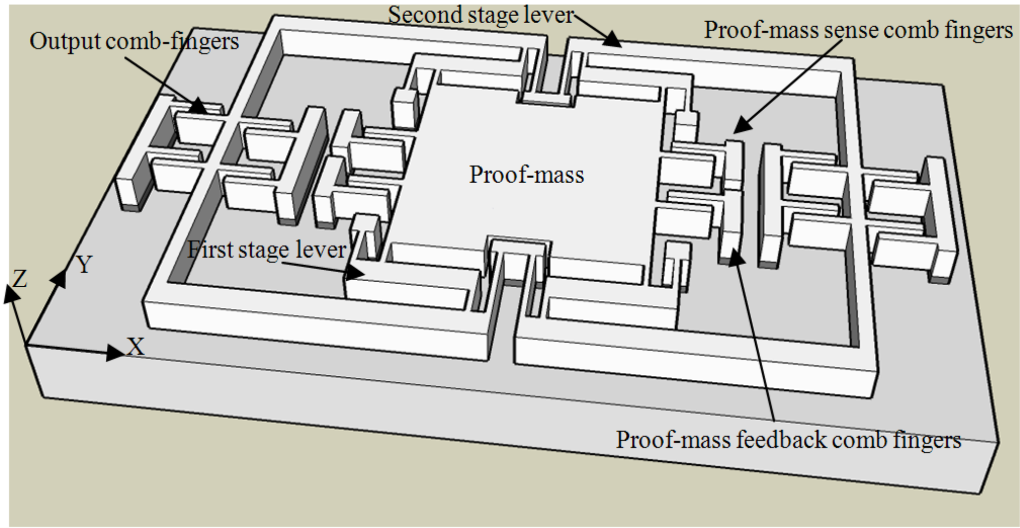

Figure E-2 Dual stage deflection-deflection mechanically amplified accelerometer 3d schematic. Y is the sense axis. Schematic not in scale

E.1.3 Simulation of the dual stage deflection-deflection mechanically amplified accelerometer

The microlevers of the dual stage deflection-deflection mechanically amplified accelerometer were simulated using nodal analysis and they were optimised using parameter versus amplification diagrams (Appendix D). After the dimensions of the microlevers parts were decided they were implemented with the proof mass, which was lumped with the comb-fingers to give the FEM model. The results are shown in Table 8-2.

As discussed previously the dual-stage deflection-deflection mechanically amplified accelerometer does not present any significant improvement over the single stage amplified accelerometer in terms of the deflection bandwidth product (here the bandwidth is considered to expand up to the natural frequency of the device). This is due to the optimisation for large amplification factor, which gives a very high input stiffness, and hence a low output independently of the large amplification factor. The improvement of the dual-stage deflection-deflection mechanically amplified accelerometer though is in this exact large stiffness and amplification factor. The low proof mass motion provides the ability to control it without the need of high voltages.

E.1.4 Force-deflection dual-stage amplification

In order to further investigate the capabilities offered by compound dual-stage microlevers a scheme including force amplification as a first stage was considered. This was implemented in the same proof mass (slightly larger) as the dual-stage deflection-deflection mechanically amplified accelerometer. The first stage is used to amplify the force induced by the proof mass in acceleration. Then the second serially connected deflection amplification stage takes over to amplify the deflection. Since the desired result is increased displacement the deflection amplifying microlevers have a much larger amplification ratio than that of the force amplifying microlevers.

The use of a force-deflection mechanism can be found useful on the optimisation of an amplified micromachined device. With this, the designer has more options to optimise the amplification since he can also define the amount of force that will be present at the input of deflection amplifying microlevers. This may also be used in the frequency tuning of the device.

The dual-stage force-deflection amplifying accelerometer was optimised and simulated the same way as the other amplified accelerometers mentioned before. Figure E-3 shows the mask designed while Table 8-3 shows the specifications of this sensor.

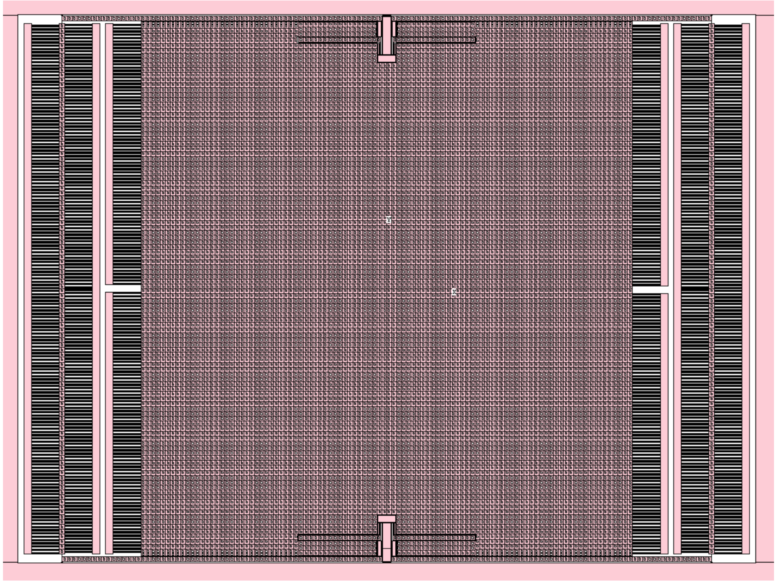

Figure E-3 Mask of the dual-stage force-deflection design.

Table E-2 FEM results for the dual-stage force-deflection mechanically amplified accelerometer

Property	***Value***
Mass deflection for 1 g acceleration	0.298μm
Comb fingers deflection for 1 g acceleration	0.912μm
Deflection amplification	3.05.
Input stiffness	109N/m
Output stiffness	35.6N/m
Sensitivity	1.82pF/g
Bandwidth	774Hz
1G deflection bandwidth product	705.8μm pF
Mass deflection for 1g acceleration	0.298μm

E.1.5 Amplified asymmetric accelerometer

The effort to obtain a capacitive accelerometer with lower input stiffness without sacrificing the deflection at the output gave the idea for an asymmetric accelerometer. By using a compound microlever and a suspension beam, the asymmetric accelerometer shown in Figure E-4 was designed.

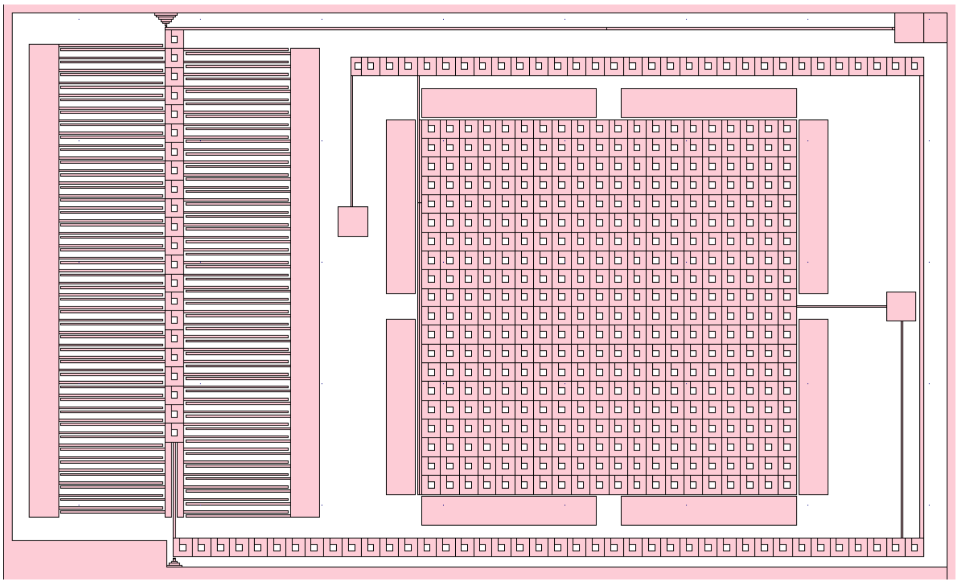

Figure E-4 Amplified asymmetric capacitive accelerometer

The asymmetric capacitive accelerometer uses a substantially smaller mass than the other accelerometers but provides high deflection at its output due to the use of the dual-stage microlevers system. The proof mass is suspended at the middle of its one side by one straight anchored beam. This inherits the characteristic of circular motion to the accelerometer when it is subjected to acceleration along one axis or tilted along the normal axis. This motion which is more pronounced at the unanchored side of the proof mass provides the input to the first type 3 microlever which is serially connected to the input of a type one microlever. The output of the second microlever is connected to a differential comb finger output. The proof mass motion can also be read and controlled by 8 planar capacitors located at its four sides.

Owing to its smaller size, such a structure can be used in an array to provide accurate measurements while it can also be used on its own as an accelerometer or a tilt sensor.

For coherence with the previous dual-stage amplified accelerometers the asymmetric accelerometer was also designed with a force-deflection compound microlever but the geometrical characteristics did not give any further improvement. This was due to the fact that the force amplifying microlever could not be freely tuned to provide us with the desire result because of space restrictions.

E.2 Conclusions on dual-stage amplification

The preliminary study presented in this Appendix for dual-stage deflection amplification did not prove to introduce substantial improvements. The main reasons are the very high stiffness and the complexity of the compound mechanical amplifier. Nevertheless, the mechanisms can probably be optimised to bring forward advantages. This would have opened new investigation routes, which would lead the research to be less concentrated in one goal and hence not complete successfully in the required time frame. Dual-stage mechanical amplification was therefore not applied at the fabricated accelerometers. It is evident that the simpler structure of single-stage accelerometers can be tuned to comply with a wide range of applications and hence the research of this thesis was concentrated in single-stage mechanical amplification.

Appendix F Conventional accelerometer Matlab script

```
%---High performance Accelerometer.      ---%
%---This file calculates the performance ---%
%---Specifications of a High performance ---%
%---Accelerometer                        ---%
%---Created by Ioannis Zeimpekis         ---%
%----MODIFIED FOR FOM---%

clc
clear

load Frequencies.mat
load FOM_Arch.mat
load Yuacc_Arch.mat
FOM=[];
deflection=[];
Frequency=[];
length=[];
% for l=1080e-6:0.5e-6:1870e-6
for i=1:1:38
%---Constants---%
Ds=2331; %Density of silicon in Kg/m^3
E= 169e9; %130.1800e9 %Young's Modulus in Pa
Ez= 130e9; %130.1800e9 %Young's Modulus in Pa
t= 50e-6; %Structural layer thickness
w= 10e-6; %Springs width
% l=800e-6 %Spring length in m
Nall = 924; %1260 %Number of combs
lcomb= 60e-6; %Combs length OVERLAP
da = 6e-6; %Small combs gap
db = 30e-6; %Large combs gap
a = 1; %acceleration in acceleration units
g = 9.81; %acceleration unit in m/s^2
T = 300; %Absolute temperature in Kelvin
Kb=1.38e-23; %Boltzman constant in Nm/K

%___Proof mass mass with comb-fingers___%
%Am=1.29854e-5 %Area of proof mass with etch holes in m^2
%Ac=1.647157e-6 %Area of combs attached to the proof mass in m^2
%A = Am+Ac %Total area in m^2
A = 1.49737e-5; %1.47488e-5 %Total area in m^2 calculated with L-Edit
V=A*t; %Volume of Proof mass with combs in m^3
% m=Ds*V %Proof mass mass with combs in Kg
m=1.91e-6;

%---Spring Constant---%
% Ks=4*E*t*(w/l)^3; %spring constant for straight beam Y-Axis
% Ksz=4*Ez*w*(t/l)^3; %spring constant for straight beam Z-Axis
Ks=((Frequencies(i).*2*pi).^2).*m;
l=((4*E*t*w^3)/Ks)^(1/3);
Ksz=4*Ez*w*(t/l)^3;
%---Combs capacitance---%
Ca=(Nall*8.85*(10^-12)*t*lcomb)/da; %Capacitance a
Cb=(Nall*8.85*(10^-12)*t*lcomb)/db; %Capacitance b
C=Ca+Cb; %Overall capacitance
%This is the overall nominal capacitance.
%if you connect it in a differential amplifier what you will affectively
%get is half of it.

%---Simple accelerometer model (no damping)---%
f=m*a*g; %Force due to acceleration in N
Fy = f/A; %Distributed load in N/m^2
```

```
x= f/Ks; %Deflection due to acceleration in m
% Wr=sqrt(Ks/m); %Natural frequency in rad/sec
% Freq=Wr/(2*pi); %Natural frequency in Hz
Df=Frequencies(i); %for critically damped (Cut-off ~equal to natural frequency)

%---Static Sensitivity---%
Sens=(C*g*m)/(da*Ks); %F/g (da= small gap cap, C=Ca in F)

%---Damping and Mechanical Quality Factor---%
c=t/lcomb;
P=(c^2/((c^2)+1))+(2*(c^2)/(9*((c^2)+9)));

D=Nall*0.8*0.895*(1.86e-5)*(50e-6)*((lcomb/da)^3)*P; %N/m Damping coefficient,l= finger
overlap
Q=(sqrt(m*Ks))/D;

%---Thermal Noise Equivalent Acceleration---%
TNEA=(1/g)*sqrt(4*Kb*T.*Frequencies(i)./(m*Q)); %g/Hz

%---Signal to Noise Ratio---%
SNR=(a^2)*(1/(TNEA))*1/(D*Df); % df=cut-off freq ONLY FOR CRITICALLY DAMPED!!!

deflection (end+1)=x;
length(end+1)=l
end

FOM_acc(:,1)=Frequencies;
FOM_acc(:,2)=deflection;
figure(1)

plot (FOM_acc(:,1),FOM_acc(:,2));

figure(2)
plot (FOM_Arch(:,2), FOM_Arch(:,1));

figure(3)
plot (FOM_acc(:,1), FOM_Arch(:,1)./FOM_acc(:,2));

figure (4)
plot (Yuacc_Arch(:,2), Yuacc_Arch(:,1));
figure (5)
plot (Yuacc_Arch(:,2), (FOM_Arch(:,1)./Yuacc_Arch(:,1)));
```

Appendix G Damping study

G.1 Damping study

Due to the miniature size of the geometry of MEMS devices the damping forces that they are facing due to the air that surrounds them governs their dynamic operation. Air can be modelled as a viscous fluid in these dimensions since the mean free path of its particles is two orders of magnitude smaller than the smaller dimension of a typical bulk micromachined MEMS device. The two main types of damping that those are subject to are slide film damping and squeeze film damping. The Navier-Stokes equation, which is used to describe the motion of a fluid, can be used to model the effects of damping in MEMS devices. [89]

In a device like the amplified accelerometer presented in this work squeeze film damping is dominant due to the large number of comb fingers moving in a translational motion towards each other. Slide film damping is a diminished effect on these devices due to their high aspect ratio (The damping study was performed in the SoG prototypes hence the slide film damping is orders of magnitude lower than the squeeze film). Thus the frequency response and hence the dynamic operation of the sensor can be evaluated by calculating the squeeze film damping forces applied to the sensor.

The main studies for squeeze film damping in microstructures were carried out by [90] and [91], they describe models of isothermal squeeze film damping for parallel plates of various shapes moving perpendicularly to their surfaces in respect to each other. Under certain assumptions, the Navier-Stokes equation can be reduced to a simpler linear Reynolds equation. These assumptions are: a) The gap between the plates is small compared to their linear dimensions. b) The air between the plates is facing a viscous and laminar flow [90], c) The plates are good thermal conductors and their relative velocities are leading to an isothermal process [90]. d) The distance covered by the motion of the plates is small compared to the gap (small pressure variation) [90, 91]. Those assumptions reduce the Navier-Stokes equation to the linearised Reynolds equation for isothermal compressible gas-film. The non-dimensional form of this equation is

$$\nabla^2\psi - \sigma\frac{\partial\psi}{\partial\tau} = \sigma\frac{\partial e}{\partial\tau} \qquad \text{eq. G-1}$$

$$\sigma = \frac{12\mu W^2\omega}{P_a h_0^2} \qquad \text{eq. G-2}$$

Where $\tau=\omega t$ is the non-dimensional time, $e=e_0 \cos \omega t$ the non-dimensional variation of the plate spacing, $\psi=\Delta p/P_a$ is the non-dimensional linearised pressure, ω is the oscillation frequency, Δp is the variation of pressure, P_a the ambient pressure, W the width of the plate (smaller dimension), h_0 the gap between the plates, μ the viscosity of air and σ is the squeeze number. For structures moving slowly or at a very low frequency, hence the gas flows instead of being compressed ($\Delta p/P_a<<\Delta h/h_0$), eq. G-1 can be further reduced by omitting the second term (pressure term).

The solution of eq. G-1can be assumed to be of the form: [91]

$$\psi = \psi_1 cos\,\tau + \psi_0 \sin\tau \qquad \text{eq. G-3}$$

The first term of equation eq. G-3 is in phase with the velocity component while the second term is in phase with the film thickness disturbance [91]. Another very useful explanation for this solution first given by [92] is that for small frequency or speed, σ is very small and the result for the damping force may be approximated by $(\sigma/12)e_0 \sin \omega t$ while the elastic force becomes negligible. For the case of high frequency or speeds, σ is large and the elastic damping force may be approximated by $\delta \cos \omega t$ while the damping force is negligible. In the first case the gas film follows a nearly incompressible viscous flow and hence acts as a damper (ψ_1) whereas in the second case the film cannot escape from the gap and acts like a spring ($\psi 2$). The squeeze film damping cut-off frequency is lying at the point where the damping and spring forces are equal in magnitude. [92-95].

Since the mechanically amplified accelerometer operates at low frequencies (<400Hz) the damping component is the dominant term while the spring component is negligible hence without affecting the accuracy of the result and for simplifying the analytical calculations, only this force will be taken into account in the following analysis. The damping coefficient (with dimensions) of the force extracted by the solution of the linearised Reynolds equation for rectangular plates with length much longer than width is [91]

$$C_d = \frac{64\sigma P_a A}{\pi^6 h_0 \omega} \sum_{\substack{m,n \\ odd}} \frac{m^2 + (n/\beta)^2}{(mn)^2 \left[\left(m^2 + \left(\frac{n}{\beta} \right)^2 \right)^2 + \frac{\sigma^2}{\pi^4} \right]} \qquad \text{eq. G-4}$$

Where A is the area of the face and β the ratio of the length versus the width (always long over short dimensions). A solution using the first few eigenvalues of this equation gives an adequately accurate result (the present analysis showed that the result is accurate to the second decimal point after the 9th eigenvalue). There are many other forms of this solution in the literature usually given in complicated series the most commonly used of which is the simplified solution given in eq. G-5 [93]

$$Capr = \frac{\mu L W^3}{h_0^3} \gamma(\beta) \qquad \text{eq. G-5}$$

Where $\gamma(\beta)$ is a correction factor. For a very long plate ($W<<L$) $\gamma(0)=1$, for a square plate ($W=L$) $\gamma(1)=0.42$. Figure G-1shows the dependence of the correction factor to the aspect ratio of the plate [93].

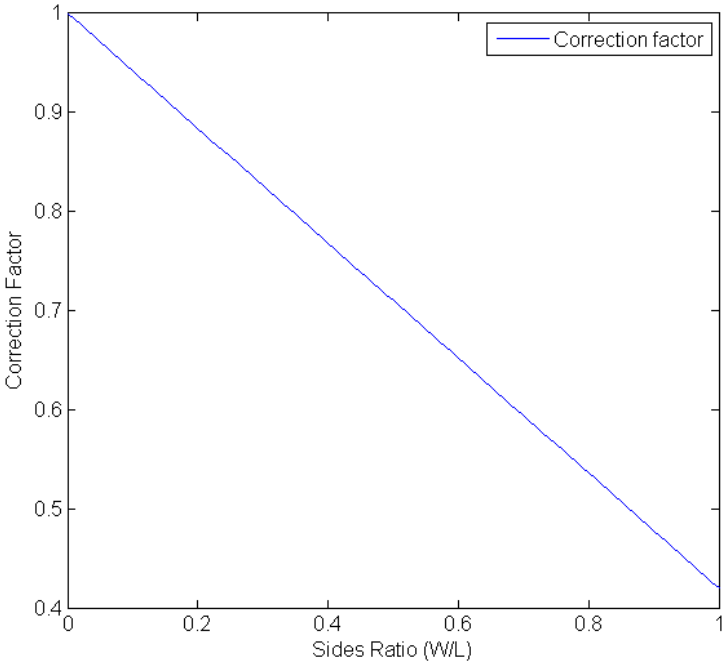

Figure G-1 Dependence of the correction factor *γ* used to calculate the damping in parallel plates to the ratio of the sides of the plates *β= L/W*

G.1.1 Cut-off frequency

The cut-off frequency of the damping is defined at the point where the amplitudes of damping and spring pressure forces are equal [91]. Equating the two forces gives a value for the squeeze number at the cut-off frequency eq. G-6. The cut-off frequency can be found by solving the squeeze number expression for ω by substituting the value of σ for the cut-off frequency eq. G-7. [90, 91]

$$\sigma_c = \pi^2(1+\frac{1}{\beta^2}) \qquad \text{eq. G-6}$$

$$\omega_c = \frac{\pi^2 P_a h_m^2}{12\mu}(\frac{1}{L^2}+\frac{1}{W^2}) \qquad \text{eq. G-7}$$

G.1.2 Effective viscosity

When the mean free path of air molecules becomes comparable to the gap dimensions where it is contained, the energy of the molecules is transferred by direct interaction with the environment rather than through molecular interaction (continuous medium).

This effect can be observed when the gap is small or when the pressure of air is well below one atmosphere [93, 94]. The first method suggests considering this effect, without invalidating the Reynolds equation, by substituting the viscosity with an effective viscosity. In order to do that the Knudsen number K_n is introduced. This is the mean free path versus the gap distance. This method renders the Reynolds equation valid for gap sizes down to an order of magnitude larger than the mean free path of air. For dimensions smaller than that or at very low pressures ($K_n>1$) the air stops behaving as a viscous fluid and hence a free molecular model has to be considered [93].

The effective viscosity of air is a function of the Knudsen number. There can be found many different functions of Knudsen number based on different considerations. The comprehensive review reported in [96] led to the derivation of a simple but accurate enough empirical approximation for the effective viscosity (eq. G-8) which will be used in this study.

$$\mu_{eff} = \frac{\mu}{1 + 9.638 K_n^{1.159}} \qquad \text{eq. G-8}$$

G.2 Damping on the mechanically amplified accelerometer

The damping evaluation of the sensor is performed on the single stage mechanically amplified accelerometer that was fabricated in the SoG process. The main source of damping is due to the translational motion of the comb-fingers normal to their surfaces hence in the following analysis the damping coefficient will be extracted for the comb-fingers of the structure.

As stated earlier in this appendix the damping cut-off frequency is located at the frequency where the damping and spring components of the squeeze film damping are equating. Figure G-2 shows a plot of these forces. The cut-off frequency is located at 3.5MHz. This validates that the damping forces are dominant in the region of operation (<400Hz) and hence spring forces due to squeeze film damping can be neglected without affecting the result.

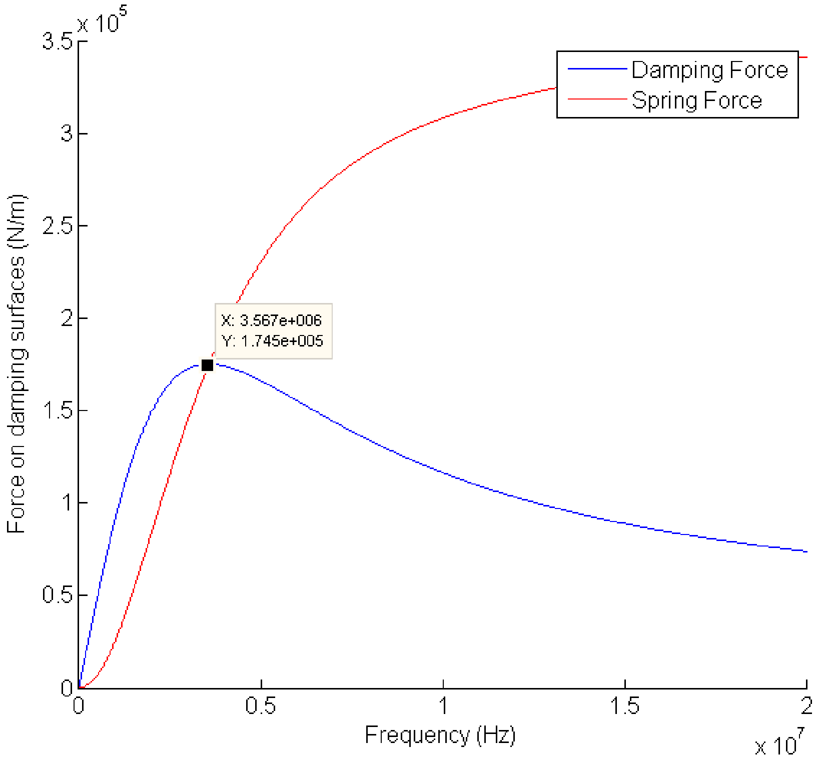

Figure G-2 Damping and spring components of the squeeze film damping forces of the accelerometer. The equation point is where the damping cut-off lies.

The squeeze film damping coefficient was calculated by an iterative process using the full solution given in eq. G-4. For a single finger including both positive and negative motion (small and large gap) this was found to be 1.265x10^{-5}(N/(m/s)). The simplified solution of eq. G-5 gives very close results (1.297x10^{-5}N/(m/s)) to the solution obtained using the iterative process, proving that this is adequately accurate for frequencies much lower than the damping cut-off frequency.

To clarify these results a simulation using the DampingMM solver of coventorware was conducted. In this simulation ideal boundary conditions were set for all surfaces to include the effect of damping on the edges, these are also included in the analytical model used as described by [91]. Figure G-3 shows a comparison of the graphs obtained by the analytical solution and the simulations, the two solutions are of very close agreement.

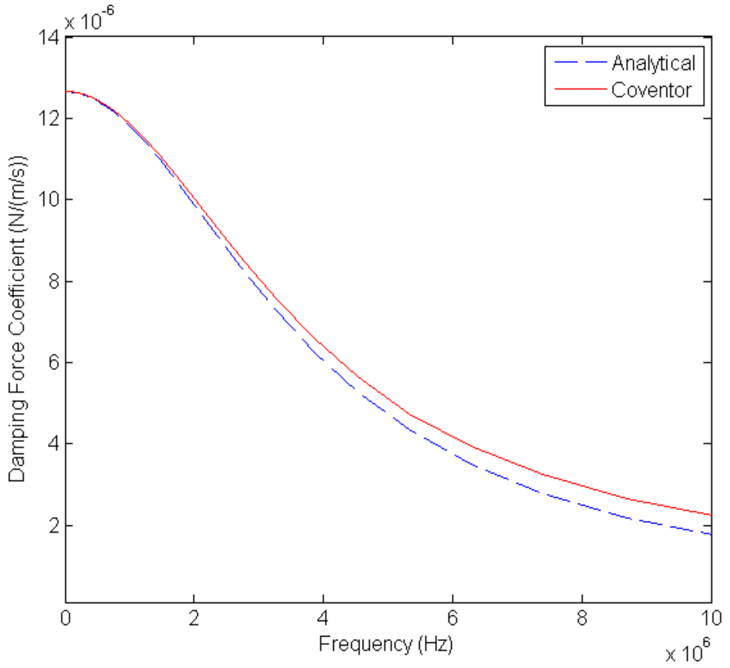

Figure G-3 Graphs showing the variation of damping force coefficient with frequency. The solid line shows the results obtained by the FEM simulation while the dashed line shows the analytical results.

In order to obtain the full damping of the accelerometer the damping coefficient for a single comb-finger calculated analytically was multiplied by the number of comb-fingers included in the structure. This gives a damping coefficient of 1.410×10^{-2}(N/(m/s)). To validate this method a quarter model of the device was constructed. The simulation of this model showed that the result obtained by multiplication is identical to that of the quarter model (by exploiting the symmetry to include the full damping). Figure G-4 shows the results for the complete damping of the accelerometer.

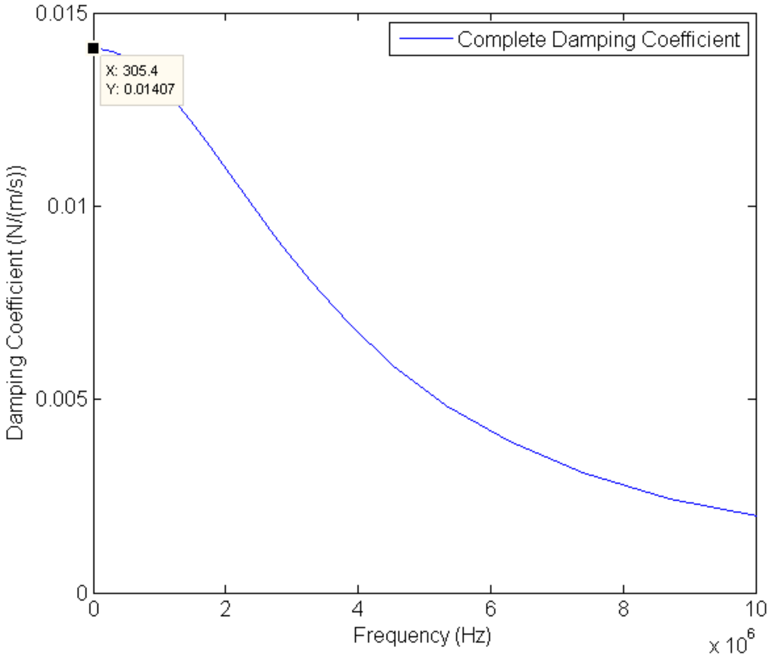

Figure G-4 Graph showing the complete damping of the accelerometer. This was obtained by using a quarter model in Coventorware.

G.2.1 Damping ratio

When damping is introduced in a spring-mass system, the shape of the output in the frequency domain is changing. The damping ratio given in eq. G-9 gives a figure of that change.

$$\zeta = Cd/2m\omega_0 \qquad \text{eq. G-9}$$

Where ω_0 the natural frequency of the undamped oscillation

Figure G-5 shows the output of a spring-mass-damper system for different damping ratios.

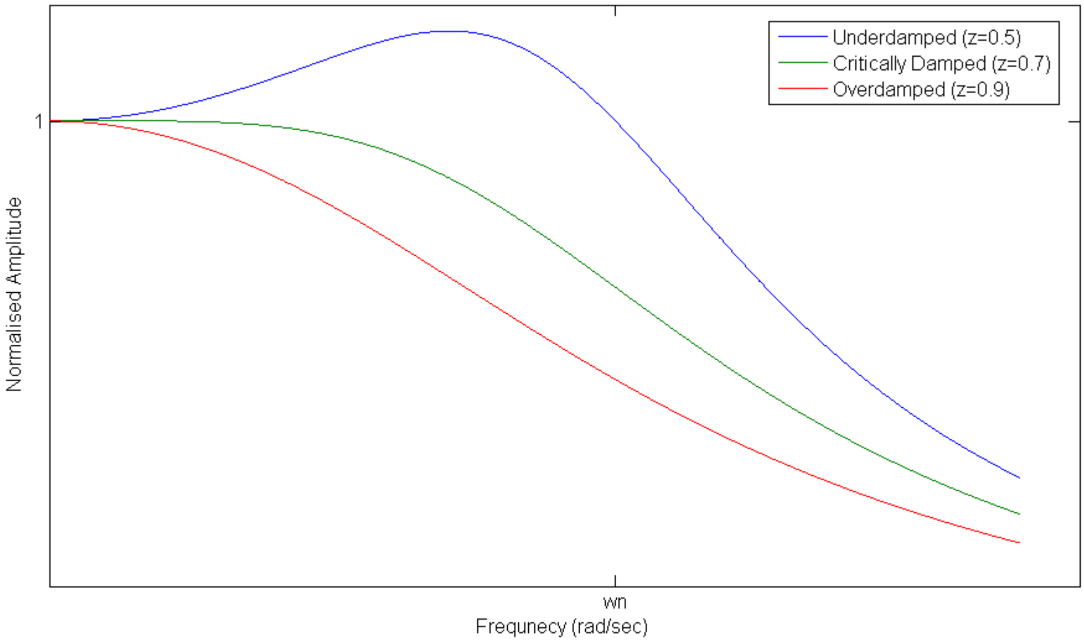

Figure G-5 Graph showing the non-dimensional output of a spring-mass-damper system in the frequency domain for different damping ratios. The red line shows a system with excessive damping, the green line shows a system, which is ideally damped (flattest response with higher cut-off frequency), while the blue line shows a system, which has very low damping.

From the analysis of the accelerometer, the damping ratio is calculated to be 14 (if it is considered as a 1-DOF mechanism). This value indicates that the designed accelerometer is highly damped. This will result in a dynamic operation with reduced amplitude and cut-off frequency. The reasons the sensor was designed in this way was to include a very high capacitance, to evaluate the usage of long and thin comb-fingers (aspect ratio of 50), and to evaluate the capabilities of the fabrication process. Moreover, according to this damping study, the initial calculation of the damping ratio conducted at the preliminary stage of this design proved to give rather underestimated results. Owing to that the sensor proves to have a poor performance when excited dynamically while still serves as a proof-of-concept model when operates statically. Nonetheless, the particular sensor could provide very high performance when it is operated at a low ambient pressure.

In order to get a figure of the dynamic operation of the accelerometer coventorware was employed to conduct a harmonic analysis including the damping ratio. Figure G-6 shows how the sensor should operate if it was critically damped (ζ=0.7) while Figure G-7 shows the operation of the over-damped sensor.

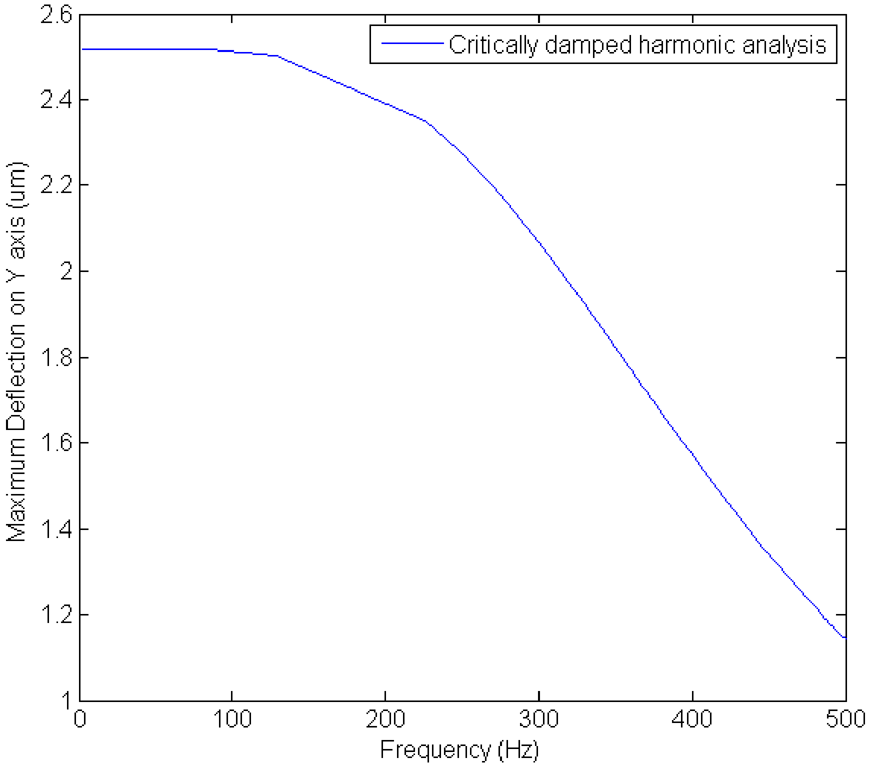

Figure G-6 Frequency response of a hypothetically critically damped amplified accelerometer

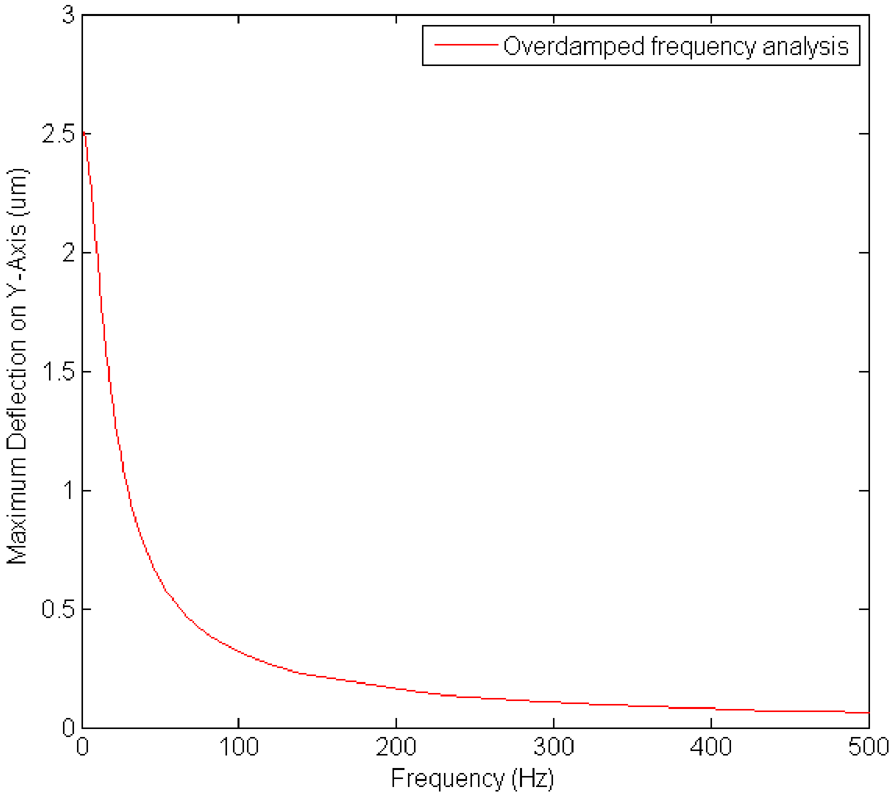

Figure G-7 Frequency response of the over-damped amplified accelerometer

G.2.2 Conclusions on damping

The evaluation of damping in microstructures proves to be very important for their dynamic operation, yet challenging enough to match with the actual experimental data. Although the underline literature has been well established over the past 40 years, it seems that different approaches and forms of the solution have complicated the evaluation. Moreover, the accuracy of the solutions proved to be highly dependent on the geometry of the structure. Hence, the use of approximations and simplified forms of the solutions should be carried out with great care taking into consideration ambient conditions and the distinct geometry of the structure under investigation.

The analysis indicates that optimisation of the damping ratio of the amplified accelerometer will improve the dynamic operation of the sensor. This will be performed at the next generation of amplified accelerometers by decreasing the overlapping area of comb-fingers, their number and by increasing the gap between them. Such prototype sensors were fabricated to test the second generation of the SOI microfabrication technology used.

A Matlab script to calculate the overall damping of the final prototypes is presented in Appendix H.

Appendix H Matlab script for the analytical calculation of damping coefficient for the amplified accelerometers

```
%--------------Mechanically amplified accelerometer damping---------------%
%This script calculates the squeeze and slide film damping of a
%mechanically amplified accelerometer. It then finds the equivalent mass
%and spring stiffness at the point of measurement (output) and calculates
%the damping ratio to compare with the measurement results. All units in SI
%----------------------Created by Ioannis Zeimpekis-----------------------%


clc
totalsingle=[];

%---Constants---%
Xn=1%13.6381817; Length of finger parametrisation
Yn=1%13.6381817; Width of finger parametrisation
L=Xn*190e-6 %Length of finger overlap
W= Yn*50e-6 %Width of finger
A=L*W %Area of finger's face
b=L/W % Overlap/width ratio
P=101.3e3 %Ambient pressure
h=11e-6 %Small gap film thickness including over-etch
h2=31e-6 %Large gap film thickness including over-etch
w=2*pi*10; %Frequency of the measured damping
Kn=0.067e-6/h; %Knudsen number
mu=1.86e-5; %Viscosity of air

%----Squeeze film damping calculation---%

mueff=mu/(1+9.638*Kn^1.159); %Effective viscosity of air
s=(12*mueff*(W^2)*w)/(P*h^2); %Squeeze number for small gap

%---Small gap---%

small_gap=0;
for M=(1:2:9);
    for N =(1:2:9);
CA=(64*s*P*A/(w*(pi^6)*h));
Cd=(M.^2+(N./b)^2)/(((M.*N).^2).*((((M.^2)+((N./b).^2)).^2)+((s^2)/(pi^4))));
CDA=CA*Cd;
small_gap=small_gap+CDA;
    end
end
SMALL_GAP_DAMPING=small_gap;

g=(-0.58/b)+1; %Plate shape coefficient
wc2=(1+(1/(b^2)))/(12*mueff*(W^2))/(P*h^2); %Simplified model for comparison
```

```
%---------------%

%---for the large gap---%

s2=(12*mueff*(W^2)*w)/(P*h2^2) %Squeeze number for large gap

large_gap=0;
for M2=(1:2:99);
    for N2 =(1:2:99);
CA2=(64*s2*P*A/(w*(pi^6)*h2));
Cd2=(M2.^2+(N2./b)^2)/((M2.*N2).^2.*((M2.^2+(N2./b).^2).^2+((s^2)/(pi^4))));
CDA2=CA2*Cd2;
large_gap=large_gap+CDA2;
    end
end
LARGE_GAP_DAMPING=large_gap
%-----------------------%

totalsingle(end+1) = (SMALL_GAP_DAMPING + LARGE_GAP_DAMPING); %Total squeeze film
damping for one finger


total = 452*(SMALL_GAP_DAMPING + LARGE_GAP_DAMPING)%Total damping for all the comb-
fingers



%---slide film damping---%
e=2.71828; %Euler's number
Am=15.37e-6 %Effective area of the proof mass
hmass=2e-6 %Gpa between the proof mass and the handle layer
Kn2=0.067e-6/hmass

mueff2=mu/(1+2*Kn2) %Effective viscosity
J0= mueff2*Am/hmass %Slide film damping from proof mass



%----Equivalent mass---%

Na=4;%Number of levers
da=2330; %Density of silicon Kg/m^3
ta=50e-6; %Thickness of structural layer
wa=50e-6; %Width of the arm
La=3650e-6; %Length of Lever arm
ba=3550e-6; %Output-Input distance
aa=100e-6; %Pivot output distance



%Equivalent mass at the output from microlevers
Lever=Na*(((da*ta*wa*(2*La - La)*La)/(2*La))-((da*ta*wa*(2*La - 0)*0)/(2*La)))

Pmass=1.91e-6; %Mass of Proof mass including comb fingers
AmpFact=36.5 %Deflection amplification factor
Sup=6.2211e-8 %Mass of comb finger support arm and output comb fingers
meq=(Pmass/AmpFact)+Lever+2*Sup% Total equivalent mass at the output



Keq= ((2*pi*740)^2)*meq %Equivalent spring constant
Cc=2*sqrt(Keq*meq) %Critical damping
z=(total+J0)/Cc %Damping ratio

%------------------------%
```

References

[1] E. Mounier, L. Robin, and J. Mouly, "Emerging MEMS: Technologies & Markets," Lyon, France, Market Report 2010.

[2] J. Bouchaud and R. Dixon, "MEMS Q2 2011 Market Tracker," iSupply, California, Market Report 2011.

[3] G. Krishnan, C. U. Kshirsagar, G.K. Ananthasuresh, and N. Bhat, "Micromachined high-resolution accelerometers," *Journal of the Indian Institute of Science*, vol. 87, no. 3, pp. 333-361, Jul. 2007.

[4] N. Najafi and K. Yazdi, "An all-silicon single-wafer micro-g accelerometer with a combined surface and bulk micromachining process," *Journal of Microelectromechanical Systems* , vol. 9, no. 4, pp. 544–550, Dec. 2000.

[5] P. Monajemi and F. Ayazi, "Design optimization and implementation of a microgravity capacitive HARPSS accelerometer," *IEEE Sensors Journal*, vol. 6, no. 1, pp. 39- 46, Feb. 2006.

[6] S. Chen et al., "A new type of MEMS two axis accelerometer based on silicon," in *3rd IEEE International Conference on Nano/Micro Engineered and Molecular Systems, 2008. NEMS 2008.* , 2008, pp. 959-964.

[7] R. Abdolvand, B. V. Amini, and F. Ayazi, "Sub-micro-gravity in-plane accelerometers with reduced capacitive gaps and extra seismic mass," *Journal of Microelectromechanical Systems*, vol. 16, no. 5, pp. 1036-1043, Oct. 2007.

[8] C. P. Hsu, Y. C. Hsu, M. C. Yip, and W. Fang, "A novel SOI-based single proof-mass 3-axis accelerometer with gap-closing differential capacitive electrodes in all sensing directions," in *IEEE Sensors*, Kona, HI, Nov. 2010, pp. 1188-1191.

[9] J. Chae, H. Kulah, and k. Najafi, "An in-plane high-sensitivity, low-noise micro-g silicon accelerometer with CMOS readout circuitry," *Journal of*

Microelectromechanical Systems, vol. 13, no. 4, pp. 628-635, Aug. 2004.

[10] B. V. Amini, R. Abdolvand, and F. Ayazi, "A 4.5-mW closed-loop micro-gravity CMOS SOI accelerometer," *IEEE Journal of Solid-State Cirrcuits*, vol. 41, no. 12, pp. 2983-2991, Dec. 2006.

[11] X. Jiang, F. Wang, M. Kraft, and B. E. Boser, "An integrated surface micromachined capacitive lateral accelerometer with 2μg/√Hz resolution," in *Solid-State Sensor, Actuators and Microsystems Workshop*, Hilton Head Island, South Carolina, 2002, pp. 202-205.

[12] H. Qu, D. Fang, and H. Xie, "A monolithic CMOS-MEMS 3-axis accelerometer with a low-noise, low-power dual-chopper amplifier," *IEEE Sensors Journal*, vol. 8, no. 9, pp. 1511-1518, Sept. 2008.

[13] S. S. Tan et al., "Design of low-noise CMOS MEMS accelerometer with techniques for thermal stability and stable DC biasing," in *IEEE Custom Integrated Circuits Conference*, 2010, pp. 1-4.

[14] Y. Dong, M. Kraft, and W. Redman-White, "Higher order noise-shaping filters for high-performance micromachined accelerometers," *IEEE Transactions on Instrumentation and Measurement*, vol. 56, no. 5, pp. 1666-1674, Oct. 2007.

[15] Y. Dong, P. Zwahlen, A.-M. Nguyen, F. Rudolf, and J.-M. Stauffer, "High performance inertial navigation grade sigma-delta MEMS accelerometer," in *IEEE/ION Position Location and Navigation Symposium (PLANS)*, Indian Wells, CA, 2010, pp. 32-36.

[16] H. Kulah, Junseok Chae, and K. Najafi, "Noise analysis and characterization of a sigma-delta capacitive silicon microaccelerometer," in *TRANSDUCERS, 12th International Conference on Solid-State Sensors, Actuators and Microsystems*, 2003, pp. 95-98.

[17] T. Kajita, Un-Ku Moon, and G. C. Temes, "A two-chip interface for a MEMS accelerometer," *IEEE Transactions on Instrumentation and Measurement*, vol. 51, no. 4, pp. 853- 858, Aug. 2002.

[18] L. L. Howell, *Compliant Mechanisms*. New York, U.S.A.: John Wiley & Sons, 2001.

[19] L. A. Oropeza-Ramos and K. L. Turner, "Parametric resonance amplification in a MEMGyroscope," in *IEEE Sensors*, Irvine, CA, 2005, pp. 660-663.

[20] R. I. Shakoor, S. A. Bazaz, M. Kraft, Y. J. Lai, and M. M. UL Hassan, "Thermal

actuation based 3-DoF non-resonant microgyroscope using MetalMUMPs," *Sensors*, vol. 9, no. 4, pp. 2389-2414, Apr. 2009.

[21] S. Kota, J. Joo, Z. Li, S. M. Rodgers, and J. Sniegowski, "Design of Compliant Mechanisms: Applications to MEMS," *Analog Integrated Circuits and Signal Processing*, vol. 29, no. 1-2, pp. 7-15, Oct-Nov 2001.

[22] J. P. D. Hartog, *Mechanical vibrations*. New York, U.S.A.: Courier Dover Publications, 1985.

[23] C. Acar and A. M. Shkel, "Nonresonant micromachined gyroscopes with structural mode-decoupling," *IEEE Sensors Journal*, vol. 3, no. 4, pp. 497- 506, Aug. 2003.

[24] G. Krishnan and G. K. Ananthasuresh, "Evaluation and design of displacement-amplifying compliant mechanisms for sensor applications," *Journal of Mechanical Design*, vol. 130, no. 10, p. 102304 (9), Oct. 2008.

[25] G. Arunkumar and Srinivasan P. S. S., "Design of displacement amplifying compliant mechanisms with integrated strain actuator using topology optimization," *Proceedings of the Institution of Mechanical Engineers, Part C: Journal of Mechanical Engineering Science*, vol. 220, no. 8, pp. 1219-1228, Aug. 2006.

[26] D. Clements, "Implementing Compliant Mechanisms in Micro-Electro-Mechanical Systems (MEMS)," Brigham Young University, Utah, Thesis (M.S.) 2000.

[27] J. M. Paros and L. Weisbord, "How to design flexure hinges," *Journal of Mechine Design*, vol. 25, pp. 151-156, Nov. 1965.

[28] N. Lobontiu and E. Garcia, "Analytical model of displacement amplification and stiffness optimization for a class of flexure-based compliant mechanisms," *Computers & Structures*, vol. 81, no. 32, pp. 2797-2810, Dec. 2003.

[29] N. Lobontiu, J. S. F. Paine, E. Garcia, and M. Goldfarb, "Corner-filleted flexure hinges," *Journal of Mechanical Design*, vol. 123, no. 3, pp. 346-352, Sep. 2000.

[30] N. Lobontiu, J. S. F. Paine, E. Garcia, and M. Goldfarb, "Design of symmetric conic-section flexure hinges based on closed form compliance equations," *Mechanism and Machine Theory*, vol. 37, no. 5, pp. 477-498, May 2002.

[31] N. Lobontiu, *Compliant mechanisms: design of flexure hinges*. USA: CRC Press, 2003.

[32] L. L. Howell and A. Midha, "A loop-closure theory for the analysis and synthesis of compliant mechanisms," *Journal of Mechanical Design*, vol. 118, no. 1, pp. 121-125,

Mar. 1996.

[33] A. A. Zeid, "Mathematical modeling of planar mechanisms with compliant joints," *Mathematical and Computer Modeling*, vol. 11, no. 3, pp. 1144-1150, 1988.

[34] L. C. Lin, J. W. Sheu, and J. H. Tsay, "Modeling and hierarchical neuro-fuzzy control for flexure-based micropositioning systems," *Journal of Intelligent and Robotic Systems*, vol. 32, no. 4, pp. 411-435, Dec. 2001.

[35] M. Carricato, V. Parenti-Castelli, and J. Duffy, "Inverse static analysis of a planar system with flexural pivots," *Journal of Mechanical Design*, vol. 123, no. 1, pp. 43-50, Mar. 2001.

[36] X.-P. S. Su and H. S. Yang, "Single-stage microleverage mechanism optimization in a resonant accelerometer," *Sructural and Multidisciplinary Optimisation*, vol. 21, no. 3, pp. 246-252, Apr. 2000.

[37] G. K. Lau, H. Du, and M. K. Lim, "Systematic design of displacement-amplifying mechanism for piezoelectric stacked actuators using topology optimization," in *Proceedings of SPIE—The International Society for Optical Engineering, Smart Structures and Materials*, 2000, pp. 583-591.

[38] S. Kota, J. Hetrick, Li Z, and L. Saggere, "Tailoring unconventional actuators using compliant transmissions:design methods and applications," *IEEE/ASME Transactions on Mechatronics*, vol. 4, no. 4, pp. 396-408, Dec. 1999.

[39] F. E. Scire and E. C. Teague, "Piezodriven 50-μm range stage with subnanometer resolution," *Review of Scientific Instruments*, vol. 49, no. 12, pp. 1735-1740, Dec. 1978.

[40] N. Takeshima et al., "Electrostatic Parallelogram Actuators," in *International Conference on Solid-State Sensors and Actuators, 1991. Digest of Technical Papers, TRANSDUCERS '91.*, San Francisco, CA , USA, 1991, pp. 63-66.

[41] X. T. Huang, M. T. Saif, and N. C. MacDonald, "A Micromotion Amplifier," in *The Ninth Annual International Workshop on Micro Electro Mechanical Systems, 1996, MEMS '96, Proceedings. 'An Investigation of Micro Structures, Sensors, Actuators, Machines and Systems'. IEEE*, San Diego, Jan. 1996, pp. 424-428.

[42] Wu MC Tsai JC, "Design, Fabrication, and Characterization of a High Fill-Factor, Large Scan-Angle, Two-Axis Scanner Array Driven by a Leverage Mechanism," *Journal of Micromechanical Systems*, pp. 1209-1213, 2006.

[43] V. Milanovic, G. A. Matus, and D. T. McCormick, "Tip-tilt-piston actuators for high fill-factor micromirror arrays," in *Solid-State Sensors, Actuators and Microsystems Workshop*, Hilton Head Island, 2004, pp. 232-237.

[44] V. Milanovic, G. A. Matus, and D. T. McCormick, "Gimbal-less monolithic silicon actuators for tip-tilt-piston micromirror applications," *IEEE Journal of Selected Topics in Quantum Electronics*, vol. 10, no. 3, pp. 462-471, Aug. 2004.

[45] D. Lopez et al., "Monolithic MEMS Optical Switch with Amplified out-of-plane angular motion," in *International Conference on Optical MEMs, 2002. Conference Digest. 2002 IEEE/LEOS* , Murray Hill, NJ, USA, 2002, pp. 165-166.

[46] H. Y. Lin and W. Fang, "Tortional mirror with an electrostatically driven lever-mechanism," in *Optical MEMS, 2000 IEEE/LEOS International Conference on*, Kauai, HI , USA, 2000, pp. 113-114.

[47] D. Hah, S. T.-Y. Huang, J. C. Tsai, H. Toshiyoshi, and M. C. Wu, "Low-voltage, large-scan angle MEMS analog micromirror arrays with hidden vertical comb-drive actuators," *Journal of Microelectromechanical Systems*, vol. 13, no. 2, pp. 279-289, Apr. 2004.

[48] H. W. Ma, S. M. Yao, L. Q. Wang, and Z. Zhong, "Analysis of the displacement amplification ratio of bridge-type flexure hinge," *Sensors and Actuators A: Physical*, vol. 132, no. 2, pp. 730-736, Nov. 2006.

[49] B. J. Pokines and E. Garcia, "A smart material microamplification mechanism fabricated using LIGA," *Smart Material and Structures*, vol. 7, no. 1, pp. 105–112, 1998.

[50] M. J. Madou, *Fundamentals of Microfabrication: Science of Miniaturization* , 2nd ed.: CRC Press, 2002.

[51] J. Paine and Z. Chaudhry, "The impact of amplification on efficiency and energy density of induced strain actuation," in *ASME Aerospace Division International Mechanical Engineering Congress and Exposition*, Atlanta, GA, U.S.A., 1996, pp. 511-516.

[52] M. B. Parkinson, B. D. Jensen, and K. Kurabayashi, "Design of compliant force and displacement amplification micromechanisms," in *Proceedings of DETC'01, ASME 2001 Design Engineering Technical Conferences and Computers and Information in Engineering Conference*, Pittsburgh, Pennsylvania, 2001, pp. 1-8.

[53] S. Bharti and M. I. Frecker, "Topology optimization and detailed finite element

modeling of piezoelectric actuators: effects of external loads and detail geometry on actuator output," in *Proceedings of SPIE—The International Society of Optical*, San Diego, CA, USA, 2002, pp. 124-135.

[54] B. W. Pedersen and A. A. Seshia, "On the Optimization of Compliant Force Amplifier Mechanisms for Surface Micromachined Resonant Accelerometers," *Journal of Micromechanics and Microengineering* , vol. 14, no. 10, pp. 1281-1293, Oct. 2004.

[55] C. W. Dyck, J. J. Allen, and R. J. Huber, "Parallel-plate electrostatic dual-mass resonator," in *Proc. SPIE 3876*, 1999, pp. 198-209.

[56] M. P. Bendsøe and O. Sigmund, *Topology optimization: theory, methods, and applications*. Berlin, Germany: Springer Verlag, 2003.

[57] A. A. Seshia et al., "A vacuum packaged surface micromachined resonant accelerometer," *Journal of Microelectromechanical systems*, vol. 11, no. 6, pp. 784-793, Dec. 2002.

[58] O. Sigmund and J. Petersson, "Numerical instabilities in topology optimization: a survey on procedures dealing with checkerboards, mesh dependencies and local minima," *Structural optimization*, vol. 16, pp. 68-75, 1998.

[59] H. D. Hibbitt, B. I. Karlsson, and P. Sorensen, "ABAQUS/Standard User's Manual, version 6.2," 2001.

[60] X.-P. S. Su and H. S. Yang, "Two-stage compliant microleverage mechanism optimization in a resonant accelerometer," *Structural and Multidisciplinary Optimisation*, vol. 22, no. 4, pp. 328–336, Jun. 2001.

[61] P. Davidovits, *Physics in biology and medicine*, 3rd ed.: Academic Press, 2007.

[62] S.P. Timoshenko and J.M. Gere, *Mechanics of materials*. New York: Van Nostrand Reinhold Company, 1972.

[63] X.-P. S. Su and H. S. Yang, "Design of compliant microleverage mechanisms," *Sensors and Actuators A: Physical*, vol. 87, no. 3, pp. 146-156, Jan. 2001.

[64] R.C. Hibeler, *Structural Analysis*, SI edition ed. Singapore: Prentice Hall, 2005.

[65] Coventor. [Online]. www.coventor.com

[66] Tanner. [Online]. www.tanner.com

[67] Synopsys. [Online]. www.synopsys.com

[68] R. Houlihan and M. Kraft, "Fringe capacitance models for MEMS devices," in *MME 2004*, 2004, pp. 71-74.

[69] T. Veijola and M. Turowski, "Compact damping models for laterally moving microstructures with gas-rarefaction effects," *Journal of Microelectromechanical Systems*, vol. 10, no. 2, pp. 263-273, Jun. 2001.

[70] Y. Dong, M. Kraft, C. Gollasch, and W. Redman-White, "A high performance accelerometer with a fifth-order sigma-delta modulator," *Journal of Micromechanics and Microengineering*, vol. 15, no. 7, pp. S22-S29, Jun. 2005.

[71] SPTS. [Online]. www.spts.com

[72] H. Ding et al., "A bulk micromachined Z-Axis Single Crystal Silicon Gyroscope for Commercial Applications," in *Nano/Micro Engineered and Molecular Systems*, 2008, pp. 1039-1042.

[73] Oxford Instruments. [Online]. http://www.oxford-instruments.com

[74] O. Raccurt, F. Tardif, F. Arnaud D'Avitaya, and T. Vareine, "Influence of liquid surface tension on stiction of SOI MEMS," *Journal of Micromechanics and Microengineering*, vol. 14, no. 7, pp. 1083-1090, Jul. 2004.

[75] Idonus. [Online]. www.idonus.com

[76] T. Overstolz, P. A. Clerc, W. Noell, M. Zickar, and N. F. Rooij, "A clean wafer-scale chip-release process without dicing based on vapor phase etching," in *17th IEEE International Conference on Micro Electro Mechanical Systems* , Maastricht, The Netherlands, 2004, pp. 717-720.

[77] I. Sari, I. Zeimpekis, and M. Kraft, "A full wafer dicing free dry release process for MEMS devices," in *Procedia Engineering, Vol. 5, Eurosensors XXIV*, Linz, Austria, 2010, pp. 850-853.

[78] M. Offenberg, B. Elsner, and F. Larmer, "Vapour HF Etching for Sacrificial Oxide Removal in Surface," *Extended Abstracts: Electrochemical Society*, vol. 94, no. 2, pp. 1056-1057, 1994.

[79] Carl Zeiss. [Online]. www.smt.zeiss.com/evohdmicrosite

[80] J. C. Lotters, W. Olthuis, P. H. Veltink, and P. Bergveld, "A Sensitive Differential Capacitance to Voltage Conerter for Sensor Applications," *IEEE Transactions on Instrumentation and Measurement*, vol. 48, no. 1, pp. 89-96, Aug. 1999.

[81] F&K Delvotec. [Online]. www.fkdelvotec.com/html_englisch/index.html

[82] Cadence. [Online]. www.cadence.com

[83] Agilent. [Online]. www.agilent.com

[84] Polytec, "Micro System Analyzer MSA-400," Hardware Manual.

[85] Labworks. [Online]. www.labworks-inc.com

[86] S. K. De and N. R. Aluru, "Full-Lagrangian schemes for dynamic analysis of electrostatic MEMS," *Journal of Microelectromechanical Systems* , vol. 13, no. 5, pp. 737-758, Oct. 2004.

[87] W. Clarence de Silva, *Vibration: Fundamentals and Practice*, 2nd ed. Florida, USA: CRC Press, 2006.

[88] Intellisense. [Online]. www.intellisense.com

[89] F. Braghin, E. Leo, and F. Resta, "The damping in MEMS inertial sensors both at high and low pressure levels," *Nonlinear Dynamics*, vol. 54, no. 1, pp. 79-92, 2008.

[90] W. S. Griffin, H. H. Richardson, and S. Yamanami, "A study of fluid squeeze-film damping," *ASME Journal of Basic Engineering*, vol. 88, no. 2, pp. 451-456, Jun. 1966.

[91] J. J. Blech, "On isothermal squeeze films," *Journal of Lubrication Technology*, vol. 105, no. 4, pp. 615–620, 1983.

[92] W. E. Langlois, "Isothermal Squeeze Films," International Business Machines Corporation, Research Laboratory, San Jose, 1961.

[93] H. Yang and M. H. Bao, "Squeeze film air damping in MEMS," *Sensors & Actuators A: Physical*, pp. 3-27, 2007.

[94] Coventor Inc, Coventorware Manual, 2008.

[95] J. Y.-J. Young, "Squeeze-film Damping for MEMS Structures," Massachusetts Institute of Technology. Dept. of Electrical Engineering and Computer Science, Massachusetts, Thesis (M.S.) 1968.

[96] T. Veijola, K. Heikki, J. Lahdenpera, and T. Ryhanen, "Equivalent-circuit model of the squeezed gas film in a silicon accelerometer," *Sensors and Actuators A:Physical*, vol. 48, no. 3, pp. 239-248, May 1995.

[97] K. S. Min, Choi W. C., S. H. Song, and E. J. Hwang, "Static and dynamic analysis of a nanopositioning flexure-hinge stage with a flexible lever mechanism," *Proceedings of the Institution of Mechanical Engineers, Part B: Journal of Engineering Manufacture*, vol. 219, no. 6, pp. 447-454, Jun. 2005.

[98] M. Jouaneh and R. Yang, "Modelling of Flexure-Hinge Type Lever Mechanisms," *Precision Engineering*, vol. 27, no. 4, pp. 407-418, Oct. 2003.